UNIVERSITY OF LEEDS

Fluid-based micropatterning for the fabrication of biomimetic functional surfaces

by

Francis James Dent

A Thesis submitted for the Degree of

Doctor of Philosophy

Faculty of Engineering and Physical Sciences
The University of Leeds

April 2024

Intellectual Property and Publication Statements

The candidate confirms that the work submitted is their own, except where work which has formed part of jointly authored publications has been included. The candidate confirms that appropriate credit has been given within the thesis where reference has been made to the work of others. The following papers are included throughout the thesis:

Dent, F. J. Harbottle, D. Warren, N. J. Khodaparast, S. *Temporally Arrested Breath Figure* (2022). ACS Applied Materials and Interfaces, 14, 23, 27435 - 27443.

Dent, F. J. Harbottle, D. Warren, N. J. Khodaparast, S. *Exploiting breath figure reversibility for in situ pattern modulation and hierarchical design* (2023). Soft Matter, 19, 2737 - 2744.

Dent, F. J. Tyagi, G. Estat, Faye. Cabral, J. T. Khodaparast, S. *Tuneable topography and hydrophobicity mode in biomimetic plant-based wax coatings* (2024). Advanced Functional Materials. 34, 1, 2024, 2307977.

Graffiedi, M. **Dent, F. J.** Khodaparast, S. Bucci, M. *Cryogenic Quenching Process Enhancement Through Coating and Microstructure Optimization* (2024). Journal of Physcis: Conference Series, 2766, 012139.

Chapters 5 and 6 are currently being drafted as further journal publications:

Dent, F. J. Khodaparast, S. *Pattern modulation of temporally arrested breath figure.*

Dent, F. J. Khodaparast, S. *Dynamic wetting states of breath figure and replica coatings.*

This research has also been disseminated through conference events and presentations that established further research and networking:

- John Fox Award Annual Lecture (2024), UK - oral presentation
- Leeds Institute for Fluid Dynamics 5th birthday (2024), UK - poster presentation
- International Soft Matter Conference (2023), Japan – oral presentation
- Bragg Centre for Materials Research Exchange (2023), UK - oral presentation
- American Physical Society Gallery of Soft Matter (2023), USA - graphical entry
- STEM for Britain (2023), UK - poster presentation
- International Conference on Bioinspired Materials (2022), Switzerland – poster presentation
- UK Fluids Conference (2022 and 2021), UK - oral presentation
- International Soft Matter Summer School (2022), France – poster presentation

Some work presented in this thesis is also a product of short placements undertaken at different international universities:

- Classical breath figure fabrication under supervision from Prof. Hiroshi Yabu. Yabu Laboratory - Advanced Institute for Materials Research. Tohoku University, Japan.
- Biological fouling studies under supervision from Asst. Prof. Benjamin Hatton. Functional and Adaptive Surfaces Group - Department of Materials Science and Engineering, University of Toronto, Canada.

Signed: 

Francis Dent

...to my loving family and dear friends

Acknowledgements

It is Sepideh Khodaparast to whom I owe the most thanks to as a foreword to this work. None of this would have been possible without her, and my muddled words can't begin to express my gratitude. The supervision, for which has made this project so successful, the mentorship, for the life advice and trust in my ever-ongoing applications, and of course the honey and lemon, for getting me through the tough times. Thank you! To my other supervisors and academic mentors including Nick Warren, David Harbottle, Mark Wilson and Robert Kay for the thoughts, perspectives and encouragement along the way. I would also like to extend my thanks to the staff and technicians in both the schools of Mechanical and Chemical and Process Engineering, in particular to Diane Cochrane, Rob Simpson, Chris Hodges and Sam Flint. A further thanks to the admin staff in Mechanical, as well as funding from the Engineering and Physical Sciences Research Council.

I would also like to thank my external collaborators for the interesting discussions throughout and for showing me the true opportunities of global academic research; including Maximilian Dreisbach, Jochen Kriegseis and Alexander Stroh at Karlsruhe Institue of Technology, Marco Graffiedi and Matteo Bucci at Massachusetts Institute of Technology, Sasaki-*san* and Yabu-*sensei* at Tohoku University and Desmond van den Berg and Benjamin Hatton at the University of Toronto.

Thanks to everyone at Leeds who has helped and supported me along the way. To Sophie, with whom I started my PhD with and ran the MedTech Foundation alongside, and to everyone in the office, including Ishmaeel, Piya and Fabian. The Fluid Dynamics Centre for Doctoral Training, for adopting me as an honorary member and to Yatin, Ciara, Emily, Danielle and Julie for the successful outreach collaboration. My housemates over the years, including Louis who would forever hold it against me if his name wasn't here. These last words, however, I save for my family. All of my grandparents, including the memory of my Grandpa for being the inspiring and inquisitive engineer that he was. Thank you to my parents for the endless love and encouragement and for providing me with the best upbringing, and to my big brother, Dom. But finally, it is to Lia for putting up with me during the long few months of writing this, thank you for your belief you have in me, and for the love that you show me.

Abstract

Intricate micro/nanoscale structural features common on biological surfaces provide evolutionary-optimised inspirations for the design of functional materials. Micropatterns engender enhanced collective properties from hydrophobicity to antifouling, enabling the exploitation of often overlooked interfacial phenomena, providing new material functionality beyond that of the intrinsic properties. However, drawbacks in conventional microfabrication approaches limit the widespread use of micropatterned surfaces due to the antagonistic pheneomena of manufacturing nano and microscale features over large areas. The realisation of desired properties can be emulated through biomimetic design approaches, in which we draw inspiration from the self-assembled designs and energy-efficient fabrication mechanisms manifested in natural systems.

This thesis looks toward fluid-based fabrication approaches, for inherently low-cost and scalable fabrication. To this end, the spontaneous nucleation and self-assembly of condensation water droplets are harnessed to dynamically pattern polymer films prior to polymer solidification and water evaporation. An adapted breath figure (BF) templating methodology is developed and characterised. In this novel approach, we de-couple condensation onset/growth and polymer curing mechanisms by using external cooling and photocurable polymers. Through *in situ* interrogation of the system physics, a phenomenological mechanistic model using the condensation kinetics describes and predicts the pattern growth. Systematic variation of highly packed porous patterns is achieved, attaining programmable average pore sizes ranging from 100's of nanometres to 10's of micrometres.

Modulation of the breath figure pattern beyond capabilities of the classical approach are explored. The inherent phase-change reversibility of the templating condensate is exploited, modulating the final surface architecture through regimes of condensation and evaporation. Surfaces with spatially diverse designs and bimodal distributions are manufactured. Spatial masking and gradiented patterning is created through experimental adaptations and inverse replica samples are fabricated in PDMS. Finally, characterisation of the pattern properties is tested in relation to wetting behaviour, and key applications relating to thermal efficiency, directional wetting and biofouling are introduced.

Keywords: Micropatterning, bottom-up fabrication, breath figure, self-assembly, dropwise condensation, biomimicry.

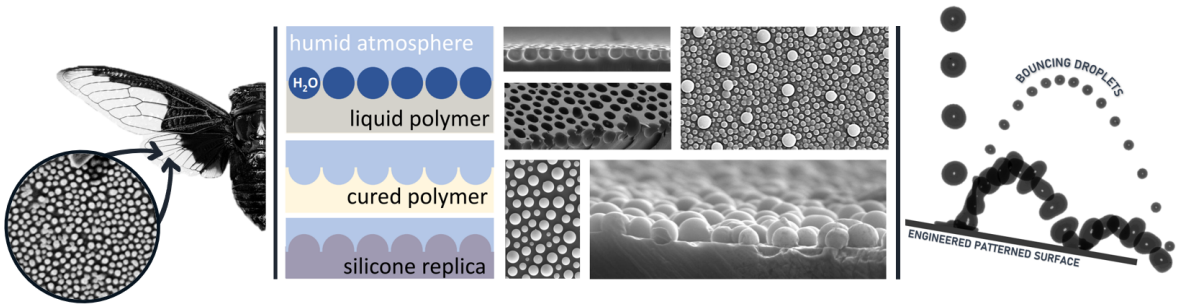

Figure 1. Graphical abstract showing the overview of the PhD from left to right; the route from biological inspiration, fabrication mechanism and examples of engineered surfaces created and potential applications.

Contents

List of Figures

List of Tables

Chapter 1

Introduction to surface patterning

The introduction to this thesis provides background to the inspiration and rationale of surface patterning at the nano/microscale. The main focus on the microfabrication methodology is introduced in full before summarising the contributions of this work and the breakdown of chapters.

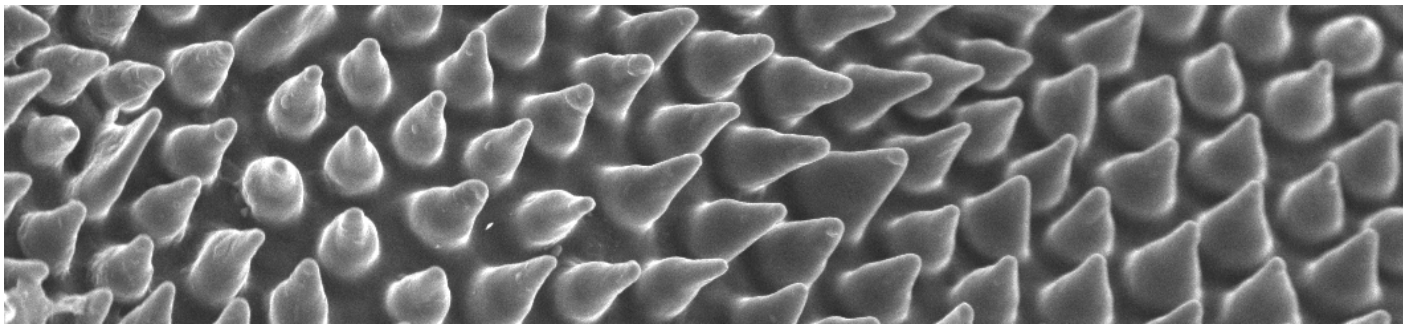

"The more our world functions like the natural world, the more likely we are to endure on this home that is ours, but not ours alone."

Janine Benyus

1.1 Motivation

If all surfaces have an inherent structure, pattern and texture, what is the objective of this work?

The same question was posed by Evans and Bryan in their 1999 review paper, defining for the first time what 'structured', 'textured' and 'engineered' surfaces are.[1] Within these definitions, patterned surfaces are differentiated from standard texture, with specific structural components that facilitate or enhance functionality beyond the intrinsic material properties. Although their initial example, a patterned mouse mat surface to provide the trackball with optimised frictional control, may now seem slightly outdated, their review classifying key terms in relation to production engineering and the manufacturing of functionalised surfaces still resonates. As functionality is often imparted through nano/microscale structural patterns, it is this ability to manufacture such small features over large areas for application exploitation that ultimately gives patterned surfaces value and motivates this work.

Surface texture denotes typical degrees of roughness or waviness, often characterised by the specific surface finish and quantified by standard parameters such as R_a (average roughness given by an arithmetic mean of absolute values over an evaluation length) and R_z (maximum peak to valley distance in a given length).[2] Engineered surfaces imply at a minimum an attempted design to relate the surface characteristics to functional performance, where specific alterations, often for example through surface finish, provide an intended benefit.[3] It is, however, patterned surfaces, designed with a certain degree of deterministic structure of high aspect ratio that provide surfaces with a targeted modification in functional properties. While not necessarily composed of regular, repeating arrays, patterned surfaces can vary from isotropic (homogeneity in all directions), periodic (recurring at fixed intervals), to stochastic (randomised distribution) assemblies of structures. This thesis hence summarises the state-of-the-art in fabrication approaches to create variable patterned surfaces, looking towards scalable manufacture.

The notion of imparting functionality through topographical surface modifications is not new, and is most visible in relation to fluid interactions and wetting. The knowledge and application of functionalised materials has been evidenced in archaeological finds dating back to the Mycenaean Greeks (1750 - 1050 BC).[4] Cooking equipment with engineered perforations for grilling and baking is thought to be some of the earliest examples of non-stick surfaces. The Bhagavad Gita, a Hindu scripture from around 200 BC, contains what is thought to be the first written mention of the hydrophobic properties of the lotus leaf being 'untouched by water'. Early scientists including Galileo (1564 - 1642) commented, 'How is it possible for those large drops of water to stand out in relief upon cabbage leaves without scattering or spreading.'[5] It was not until the mid to late 20th century and early

21st century, however, that the conceptual origins,[6,7] working mechanisms[8,9] and later, the development of fabrication techniques were introduced, giving rise to the scientific study of roughness-induced wetting effects.

Patterned surfaces in relation to hydrophobic wetting behaviour were first studied in the 1950s when different techniques were applied primarily to create wax coatings.[10,11] Superhydrophobic surfaces, however, only gained mainstream prominence after the 'lotus effect' was coined by Barthlott and Neinhus in 1997 in their paper describing the self-cleaning behaviour of the plant leaf.[8] Interestingly, their findings were initially published in the 1970s, following the commercialisation of scanning electron microscopy (SEM) which they used to characterise the microstructure of over 2000 plant species.[12] However, the niche, botany-centric nature of the paper, published in German, did not gain traction within the international physics and material science fields at the time. The term superhydrophobicity itself was also used prior to 1997, initially by Busscher *et al.* in 1991[13,14] and later by the now famous Kao Group experiments.[15,16] Nonetheless, since the turn of the century, widespread advancements in manufacturing technology, imaging equipment and computing power have firmly established the field of pattern-induced wetting manipulation.

Whilst often characterised in some regard or another to wetting and interfacial behaviour, pattern surfaces can give rise to a host of collective functionalities. In the natural world, hydrophobicity is just one of many properties achieved by surface patterning, with examples going far beyond the regularly cited lotus leaf. Shark skin has specialised ribbed scales called dermal denticles which reduce shear stress underflow, limiting boundary layer separation and decreasing drag.[17] The resulting hydrodynamics limits bacterial attachment and colonisation which is further strengthened by the inherent anti-biofouling properties of the skin's microstructure. Tightly packed nanoscale pillars on the wings of cicada insects have also not only been shown to exhibit excellent superhydrophobic and self-cleaning effects, but strong anti-biofouling and bactericidal properties.[18] The specific aspect ratio and density of these pillars both reduce potential adhesion to incident contaminants and mechanically rupture bacteria causing cell death.[19] In contrast, flexible fibrillar structures on the foot of the gecko exhibit excellent dry adhesive properties due to the amplification of van der Waals interactions from increased surface area.[20] The great variety of pattern-induced functional properties in nature has inspired a similar diversity in engineered analogues, in areas from tribology,[21] to optics[22] and biomedicine[23], to name a few.

Bio-inspired patterning demonstrated in research has attracted significant commercial interest. A number of government-backed initiatives, university spin-outs, and industrial startups have sought to exploit the opportunity and efficiency gains offered by engineered patterned surfaces. The UK government's Manufacturing Technology Catapult (MTC), an organisation operating at the nexus of research and industry, facilitates trials

and assessment of surface structuring technologies for companies' product development.[24] Sharklet technologies Inc. (Colorado, USA) claims to mimic the form and function of shark skin to inhibit bacterial growth through micropatterning alone. Similarly, AeroSHARK is a product of Lufthansa Technik (Hamburg, Germany) and manufacturer BASF (Ludwigshafen, Germany) for drag reduction in aerospace industries through microscale riblets. LiquiGlide (Massachusetts, USA), a university spinout to reduce food residue on packaging, has created a self-lubricating surface inspired by the *Nepenthes* pitcher plant. Despite the seeming lack of imagination when it comes to product naming, these companies offer unique and creative solutions by exploiting often overlooked interfacial phenomena beyond the intrinsic material properties.

The transfer of nature-inspired applications from theoretical research to practical use is contingent upon the ability to manufacture complex designs at scale. However, industrial-sized substrates oppose traditional microfabriction workflows, due to the inherent difficulties of manipulating and controlling nanoscale structures over large surface areas. Serial processes, where structured features are created sequentially are of limited use due to the disparate length scales at play. Further, common microfabrication techniques driven by the semiconductor industry are inherently expensive and scale-limited; long lead times with low throughput coupled with requirements for cleanroom facilities and limited materials limit their widespread use.

More recently, bottom-up self-assembling approaches have received interest due to their ability to create small and complex features with inherently scalable and low-cost processes.[25] While instabilities in classical engineering domains are regarded as failure mechanisms, harnessing them for the creation of intricate structures spontaneously over larger scales offers new potential. Further, manufacturing using intrinsic forces and instabilities mimics the biological inspiration's end function and formation mechanisms. Of central interest to this thesis is the fluid-based, self-assembly fabrication routes that facilitate low-cost and scalable manufacturing.

While surface patterning is not necessarily restricted to specific dimensional order or length scales, for the purpose of this work we narrow our focus to surface features in the micrometre range and below. This scale is most represented when we talk about natural functional surfaces and the bio-inspiration.[26] As such, this chapter summarises the rationale for surface micropatterning, delineating current trends and fabrication techniques before framing the novel understanding of this work. The fundamentals of wetting interactions are initially covered to preface key topics quoted throughout. Biological examples of surface functionalisation are discussed to provide insight into how nature has adapted to hostile environments and developed her own answers to many of the solutions we are trying to find today. Engineered analogues and conventional microfabrication techniques are outlined within the context of mass-market and scalable manufacturing methods.

Finally, self-assembly fabrication techniques using fluids are introduced and a proposed methodology, the temporally arrested breath figure approach, is summarised through the key contributions of this work.

1.2 Fundamentals of wetting

Wettability describes the behaviour and interactions of a liquid in contact with a solid surface, indicating the affinity between the respective phases. The first consolidated theory of wetting stems from the work of Thomas Young written in 1805.[27] When a liquid droplet contacts a surface, the balance between the adhesive forces between the liquid and surface, and the cohesive forces of the liquid determine the interaction. As the fluid interface is deformable, it aims to minimise the system energy determined by the spreading parameter S,

$$S = \gamma_S - (\gamma_{SL} + \gamma_L)\,. \tag{1.1}$$

If $\gamma_S > \gamma_L + \gamma_{SL}$, where γ denotes the interfacial tensions of the solid (γ_S) and liquid (γ_L) phases respectively, total wetting occurs. The total surface energy is minimised as the liquid spreads over the high energy surface into a thin film (Fig. 1.1a). For cases where $\gamma_S < \gamma_L + \gamma_{SL}$, only partial wetting occurs and the liquid forms an equilibrium droplet shape in the form of a spherical cap (Fig. 1.1b). The angle formed between the surface and the sessile droplet at the three-phase triple line is known as the contact angle, where this can be quantitatively measured to determine the extent of wetting. For $\theta < 90°$, the surface is deemed hydrophilic, and for $\theta > 90°$ the surface is hydrophobic.

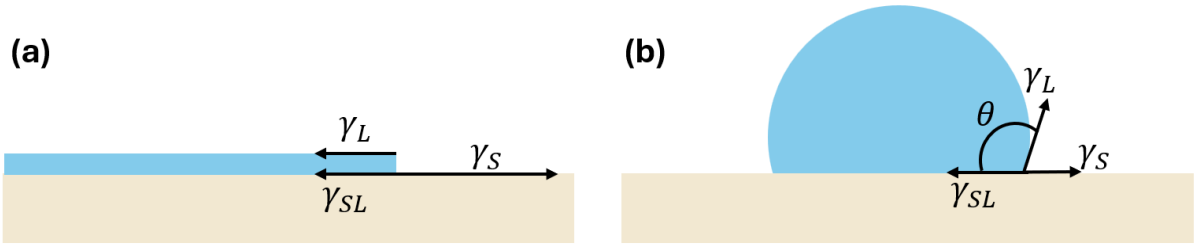

Figure 1.1. Two classical wetting scenarios on an ideal material. (a) Complete wetting and (b) partial wetting forming a sessile spherical cap with a contact angle θ.

For a droplet at equilibrium on an ideal surface, the Young equation sums the capillary forces acting at this contact line. By normalising the forces per unit length, in other words using the respective interfacial tensions between the phases, one obtains,

$$\cos\theta_e = \frac{\gamma_S - \gamma_{SL}}{\gamma_L}\,. \tag{1.2}$$

The equilibrium contact angle θ_e does not describe the full behaviour such as the dynamic properties for droplets on real surfaces. As pointed out in the work of Gibbs, the het-

erogeneity (both chemical and topographical) on almost every solid substrate can pin a droplet at the contact line.[28] As such, small droplets on an inclined surface can remain at rest due to the difference in Laplace pressure between the front and the rear of the droplet overcoming the force due to gravity. The maximum observable angles termed advancing, θ_a, and receding, θ_r, are the minimal corresponding angles upon depinning/retracting of the contact line at the front/rear of the droplet respectively.[29,30] The droplet can hence have a contact angle anywhere between θ_a and θ_r, depending on its history.[31] The difference in these angles ($\Delta\theta_H = \theta_a - \theta_r$) is termed contact angle hysteresis, and manifests across different surfaces as observable sticky or slippery behaviour.

In the real world, few surfaces can be considered ideal. The works of Wenzel (1936)[7] and Cassie and Baxter (1944)[6] derived models for wetting on rough surfaces, emphasising the surface geometry which can significantly increase/decrease the predicted wetting from Young's equation. The two distinct models refer to whether a droplet wets the entirety of a rough surface and increases its contact area (Wenzel) or remains on top of the surface roughness features, only in contact with the peak asperities in a solid-vapour composite contact (Cassie-Baxter). In the former, a roughness factor r can be determined equal to the specific surface area relative increase. This results in a modified contact angle to,

$$\cos\theta_w = r\cos\theta_e\,. \tag{1.3}$$

The Wenzel roughness factor amplifies the (non)affinity of the liquid to complete (non)wetting behaviour.[29] For example, hydrophilic surfaces ($\theta_e < 90°$) in the Wenzel state exhibit lower contact angles than predicted by Young (Eq. 1.2), and hydrophobic surfaces ($\theta_e > 90°$) exhibit larger contact angles.

If the liquid does not penetrate the surface roughness and instead bridges the gap between asperities, it is known as the Cassie-Baxter state. The resultant solid-vapour surface contact is hence taken into account with the solid fraction f_1,

$$\cos\theta_{CB} = f_1\cos\theta_e - (1 - f_1)\,. \tag{1.4}$$

In practice, these binary modes do not exhaust all possible wetting regimes.[9,29] Cassie-Baxter neglects the real-world roughness of highly textured and complex features,[32] and the overall models fail to account for the significant interactions at the three-phase contact line.[33,34] Transitional Cassie-Baxter to Wenzel regimes occur, leading to various modes of partial fluid infiltration observed on regular surfaces.[35] Further advancements in fabrication approaches in the design of complex and hierarchical structures have hence defined a range of potential wetting behaviours.[9,36]

For flat surfaces, the highest intrinsic water contact angles observed are on low surface en-

ergy fluorinated polymer substrates such as PTFE (*e.g.* Teflon®), giving contact angles of $\theta \approx 120°$.[37] Through the combination of topographical and chemical optimisation, superhydrophobic surfaces ($\theta > 150°$) can be created and modelled by the Cassie-Baxter state. Although superhydrophobicity is not the focus of this work, the idea of manufacturing topographical features that can modulate effects primarily relating to wetting behaviour is of central importance. As a result, the focus of this work surrounds the fabrication of these structures, and does not consider secondary surface coatings/functionalisation. To ensure functionality, designs will be inspired by nature and employ natural, self-assembling processes to ensure scalability.

1.3 Patterned surfaces found in nature

Surfaces represent the boundaries for solid materials, largely defining the interactions between that object and its environment through various physical, chemical and biological reactions.[38] As such, natural materials have developed some of the most intriguing, complex nano/microscale patterned features that have optimised their ability to function through millions of years of evolution and natural selection.[38] It is these surfaces that serve as a constant muse for designing and developing the best engineered materials. The morphology and assembly of these natural microstructures in relation to interfacial wetting behaviours have driven this research. While several reviews summarise a snapshot of what biological materials and bio-inspired materials have to offer,[38–40] three prominent effects relating to fluid interaction from hydrophobicity, oleophobicity and anti-fouling are highlighted here.

The classic example of the lotus leaf is composed of densely packed microscale papillae structures of varying heights (Fig. 1.2).[41] A secondary roughness scale of nano wax tubules composed of non-polar methyl groups strongly repels any incident water, making the leaf extremely efficient at shedding dirt to keep the surface clean, reducing the risk of disease and increasing photosynthesis efficiency.[8] The varying feature heights and nanoscale aggregations of wax keep incident water in a Cassie-Baxter suspended state, engendering ultra-low hysteresis effects with water roll off angles of less than 2°. Although the majority of plants require sophisticated means to hold onto water, the majority of studies has been on the rare superhydrophobic, self-cleaning cases. Rose petals exhibit interesting phenomena with similar features to those of the lotus. Depending on the pitch values of microstructures and density of nanostructure, different species of rose exhibit both low adhesive superhydrophobicity (like the lotus leaf), but also superhydrophobic structures with high adhesion (Fig. 1.2). The antagonistic wetting properties of high water contact angles but also high droplet adhesion has been termed the 'petal effect', where adhesion plays important roles in the precise transport and retention of microdroplets

over a surface.[42] In the low adhesive case, the smaller pitch of microstructures (distance between features) coupled with high density of nanostructure make the Cassie-Baxter wetting state very stable so that water droplets experience very low pinning and hysteresis effects. In the opposite case, it is thought that the lower density of nanostructure enables partial penetration of the water droplets into the asperities, resulting in strong pinning of the droplet (Fig. 1.2). Bhushan *et al.* measured the topographies of two roses, *Rosa* cv. Showtime and *Rosa* cv. Bairage which exhibit the contrasting behaviour.[43] The Showtime has taller microstructures at a smaller pitch than the Bairage. While both petals exhibit superhydrophobic static contact angles of $\theta > 150°$, the Showtime has a droplet roll-off angle of 6°, compared to no roll-off angle for the Bairage that could be turned through 180° and retain the droplet. Similar structures have since been emulated and applied to fields for precise fluidic manipulation in microfluidics and *in situ* detection scenarios with localised chemical reactions and biochemical separation.[40] However, the low hysteresis effects tend to break down and fail in high humidities or pressures from pinning effects, and the epidermal wax coating is oleophilic, causing oils to readily spread and contaminate the surface.[29] The oleophilic effects have since been used in functional materials for oil/water separation, for example in situations for cleaning oil spills.[44]

Specific animals have also developed their own mechanisms to remain clean and resist contamination. Fish scales have spaced microstructures which entrap secreted mucus to engender super oil repellent (oleophobic) qualities. Springtails are soil dwelling arthropods that inhabit demanding environments full of surface-active substances originating from decaying organic matter.[45] As these insects rely on epidermal respiration (cutaneous gas exchange through the skin), the prevention of cuticle wetting is essential for their survival. The spingtail cuticle consists of a hexagonal or rhombic patterns of granular structures forming nanocavities (Fig. 1.2). The micron-sized diameter patterns form overhanging geometry that creates re-entrant cavities, providing very stable air cushions (known as plastrons) to facilitate epidermal respiration in immersed environments.[46,47] The negative curvature creates effective non-wetting effects from water and oil at elevated pressures up to 4 atmospheres.[45] In fact, engineered omniphobic surfaces mimic this re-entrant geometry to create similar effects, overcoming limitations of lotus-inspired surfaces.[47,48] Variation of the size/morphology of the microstructure between samples of the same species indicate ecomorphological response adaptations to specific environmental conditions.

The wings of different insects also exhibit superhydrophobic effects from nanoscale features, where the low contact area with droplets exhibit similar low wettability, adhesion and friction effects.[49] Cicada wings have tightly packed features ranging from 200 nm to up to 2 µm in height, and aspect ratios from 0.5 to > 2.[50] Samples from different countries acquired from Etsy UK and imaged using SEM show the breadth of morphology across

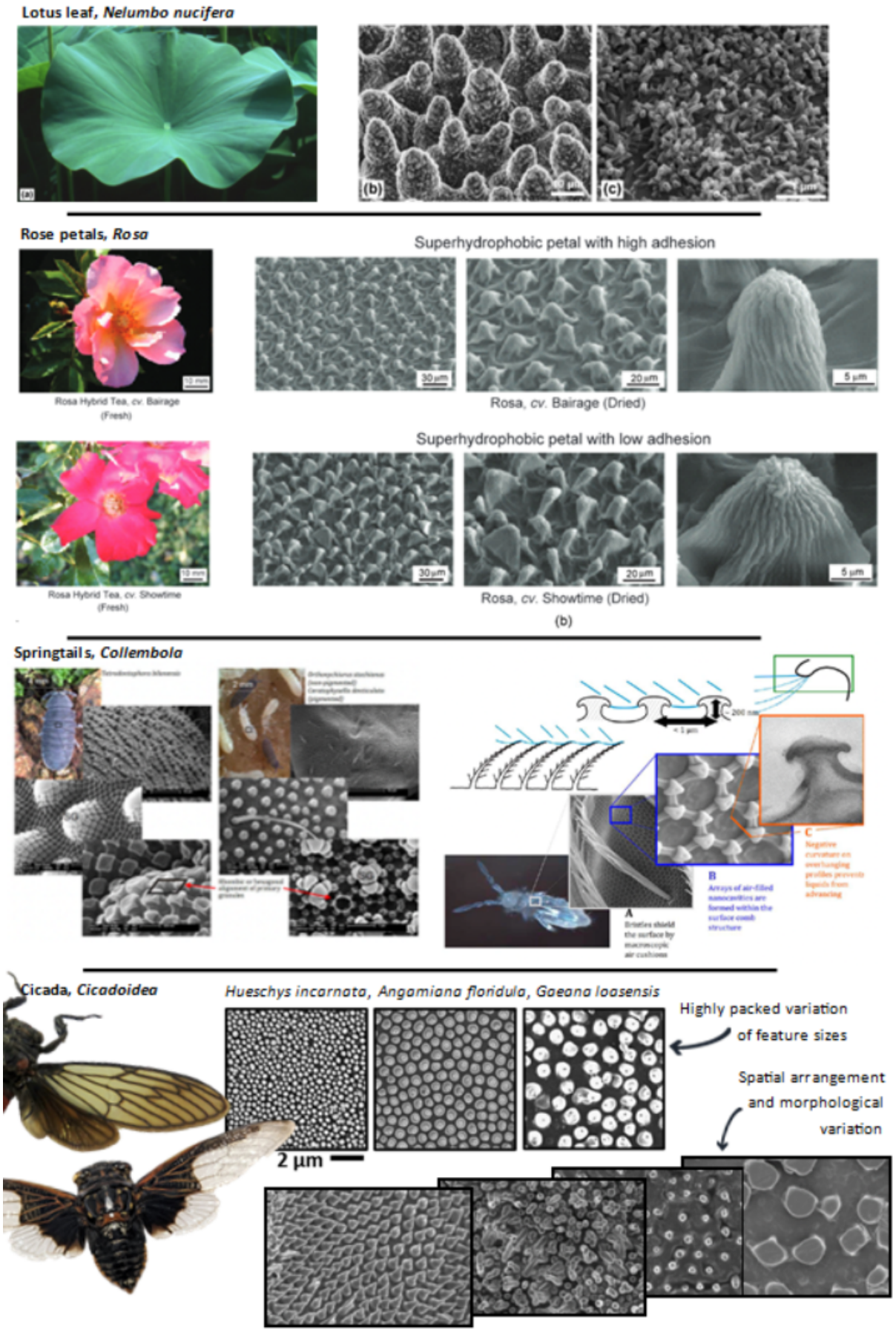

Figure 1.2. Nano/microscale features of biological functional surfaces. (top) Lotus leaf adapted from Ensikat *et al.*[41], (top-middle) rose petals adapted from Bhushan *et al.*[43] (bottom-middle) springtails adapted from Helbig *et al.*[45], and (bottom) wings of cicadas imaged as part of this project.

different cicada species' wings, with features extending from diamond shaped cones to spherically capped pillars (Fig. 1.2). Not only does the superhydrophobicity limit bacterial adhesion, but the morphology of the nanoscale patterning particularly in the wings of the cicada *Psaltoda claripennis* has been shown to exhibit bactericidal behaviour. The wings limit the bacterial colonisation and biofilm formation through two mechanisms - non-biofouling through low adhesion of contamination and bactericidal properties by killing and suppressing the growth of microbes.[51,52] Discovered by Ivanova *et al.* in 2012, this mechano-bactericidal effect causes the stretching and penetration of settled bacteria's cell walls, leading to rupturing and cell death of common bacteria such as *E. coli* and *P.aeruginosa.*[19] Although the bactericidal mechanism is debated,[53] the cell-killing efficacy on gram-negative (having thin cell walls) bacterial strains has been shown to be effective after only minutes of contact.[19]

While material function evidently changes across species and ecosystem, the reliance on nano/microstructures tailors the specific effects. Across specimens, it is the tightly packed, self-assembled morphology of structures where slight changes can drastically alter the properties (see the rose example above). Even within a singular species, variation in the average feature size, and polydispersity of the same features help to amplify the effects in many cases. With the breadth of functionality observed in nature, engineered designs are commonly inspired by natural materials and even named after their biological analogues. Designing mimics, however, relies on the ability to manufacture and control features across a range of length scales, predominantly from nano to micro size. The ability to tune the interfacial properties of the surface is further reliant upon the capacity to finely modulate the size, morphology and spatial arrangement of said features for specific applications.

1.4 Engineered patterned surfaces

A variety of manufacturing approaches exist to micropattern surfaces dependent on the specific design and material required. Although techniques are often combined or rely on simultaneous oxidation/reduction reactions, for the purposes of this summary, fabrication approaches have been broadly classified into top-down subtractive and bottom-up additive techniques. While this is not by any means an exhaustive list, focus is provided on the main techniques that facilitate the fabrication of features within the biological feature size range of 100's nm to 10's µm. Common and novel patterning approaches ranging from deterministic to stochastic features are discussed, emphasising on this length scale of structuring, where further molecular-scale methods and subsequent coating/grafting techniques are not considered.

1.4.1 Top-down manufacturing

Top-down manufacturing techniques encompass some of the most common techniques for obtaining specific surface modifications. Due to the required feature length scale, approaches harness the use of low wavelength light sources and chemical etchants to create patterns via the removal of material. The semi-conductor manufacturing industry has been the key driver of these microfabrication techniques, where the performance of integrated devices is reliant on the ability to miniaturise components, widely popularised by Moore's law. The approaches are typically completed in clean room facilities to avoid contamination from dust and debris and involve many repeated steps of patterning and removing material to create well-defined structures.

In photolithography, a light sensitive photoresist is spincoated on top of a silicon wafer.[54] The use of a chromium and quartz photomask with a computer aided design (CAD) of the pattern is used to selectively expose the resist upon UV irradiation. Both positive and negative photoresists exist and react differently upon exposure, enabling the transfer of the two dimensional (2D) geometrical design. Depending on the photoresist type, the more soluble part gets removed in developer solution, revealing the latent design (see Fig. 1.3). The remaining photoresist protects the substrate from subsequent removal or addition of material before being stripped itself. Other methods such as electron beam lithography (EBL) can be used to increase possible resolution by overcoming limitations from the wavelength of light used.[55] Pulsed high-velocity electrons directly expose the CAD pattern onto the photomask, mitigating the use of a photomask and decreasing the feature size from 100's nm to around 10 nm.

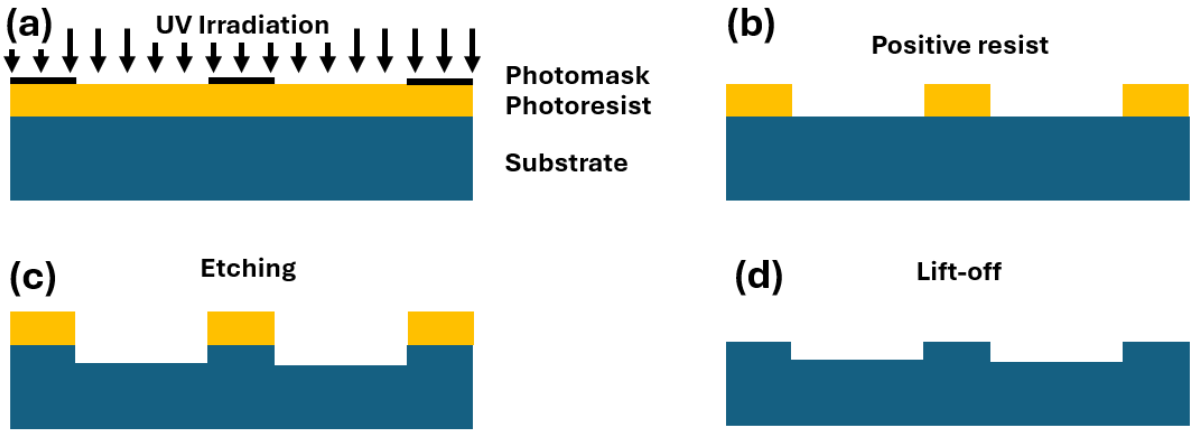

Figure 1.3. Schematic of a standard photolithography procedure. (a) Selective exposure of resist through photomask before (b) dissolution reveals the latent design. (c) Sequential etching and (d) lift-off steps create the design in the substrate material.

Etching procedures chemically remove the uppermost layers of a substrate that are not protected by a photoresist. Wet and dry etching methods use corrosive acids/bases or plasma to dissolve the substrate and produce the three-dimensional (3D) features. The

photoresist is stripped after etching, and successive iterations of the process are completed to create more complex or high aspect ratio designs, varying potential geometries from simple pillar arrays to undercut features (Fig. 1.4b).[56] Stochastic patterned surfaces across a full surface can also be created via etching processes without defining a larger macro design through a photoresist. Alkaline hydrothermal treatment of titanium etches via the dissolution of titanium producing titanium oxides to create nanospike arrays for functional biomedical materials and cicada-inspired antibacterial effects (Fig. 1.4c).[57] Ultra-low broadband anti-reflection black silicon can be created through different etching techniques to create high aspect ratio nano and microscale cones.[58]

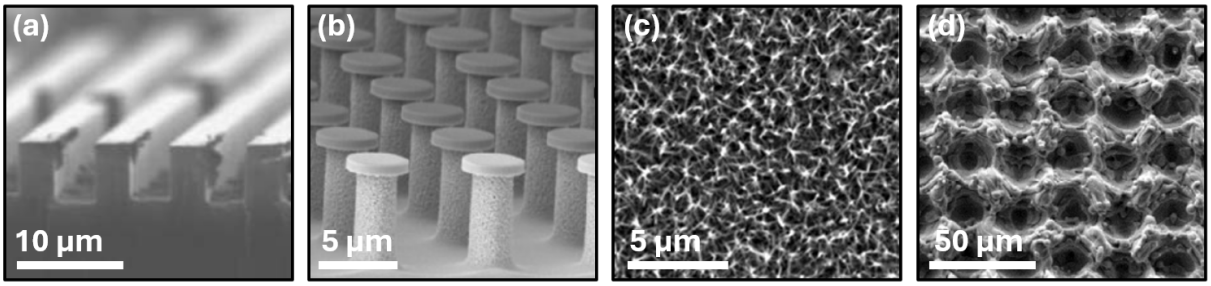

Figure 1.4. Patterns created via top-down processes. (a) Conventional photolithography[59] and (b) successive lithography and etching procedures to create more complex geometries.[60] (c) Titanium oxide (TiO_2) nanostructure formed from hydrothermal treatment (etching plus oxidation)[61] and (d) laser machined[62] surface.

Laser ablation is a common direct write technique that enables the translation of a CAD design to a surface (Fig. 1.4d).[63] Significant innovation with the use of ultra-fast lasers and direct laser interference patterning (DLIP) can create features down to hundreds of nanometres across different metallic, semiconductor and polymer surfaces.[64] Although restricted to the top-down removal of material from a surface (no complex or undercut geometries), DLIP can fabricate a range of geometrical features through the overlapping of coherent beams to produce periodic interference patterns. The single-step templateless approach offers significant benefits in terms of material independence and process speed, enabling the creation of structures that mimic the superhydrophobicity of the lotus leaf.[65] While this technique is deterministic in the sense it is derived from a programmed pattern, stochastic defects arising from ablated material re-solidifying cause a degree of non-uniformity.

Once a patterned surface is created with any of the above techniques, soft lithography can be employed to replica mould the inverse pattern from the 'master', assuming limited trapped or overhanging geometry.[66] The relief template is commonly made in elastomeric materials such as polydimethylsiloxane (PDMS) to allow removal from the mould. Providing an effective way to fabricate a master template, common imprinting and casting techniques can lead to the low-cost and high-throughput transfer of nanoscale designs to many subsequent replicas. Continuous imprinting from a master can be completed

via mechanical embossing with a continuous feed-stock material substrate provided an effective automated set-up (*e.g.* rolling device). However, typical manufacture lead time and costs associated with the expensive equipment to make the master template limit the adaptability of the process for variable design.

1.4.2 Botton-up fabrication

Bottom-up approaches involve the creation of a pattern from the assembly of constituent elements. These typically involve the growth of material, the aggregation or the assembly of particles that form via self-organising forces. Due to the serial, slow nature of additive manufacturing processes and the limited capability in the length scales of interest, these processes are not considered here. While some templating approaches, *e.g.* the use of self-assembled colloids, may not be purely bottom-up, they are considered here as they are built-up through self-assembled constituent parts. The regularity of structures created through instability-driven and non-equilibrium processes that harness self-assembling forces can generate designed architectures of long-range order without the serial addition of elements placed through mechanised intervention. The biomimetic structures created in such ways are not dissimilar to the biological methods employed in nature, harnessing the self-assembling mechanisms of instabilities that serve as a favourable guide for the fabrication of complex structures.[38]

Since the discovery of the lotus effect, the abundance of plant leaves with functional properties has guided significant development in engineered analogues. Epicuticular waxes can create 3D structures of varying morphologies, ranging in feature size from 0.5 to 100 µm. Depending on the wax chemistry, common structures ranging from tubules, platelets, rodlets and films are observed.[35] In fact, epicuticular waxes extracted from the leaves themselves have been successfully recrystallised into similar micropatterns using thermal and solvent evaporation approaches.[67,68] The earliest studies of artificial superhydrophobic surfaces were created on spontaneously formed fractal crystalline assemblies of alkyl ketene dimer (wax-like materials).[15] Recently published work within this project showed how through controlled solvent evaporation of wax solutions, the morphology of aggregated crystals can be varied (Fig. 1.5a), engendering variable wetting effects for different fluid-handling functionality.[69] By varying the type of solvent and temperature of the substrate, commonly discarded materials such as wax extracted from rice bran could be repurposed to create biodegradable superhydrophobic coatings in a single step.

Similarly, the growth of inorganic crystals can be used to generate oxide layers on metal or semiconductor substrates. Oxide layers can be tuned from vertical nanosheets to cubes and flower-like microstructures, where the chemical bonds dictate the morphology.[70] Elevated temperatures for prolonged periods of time are often required, where oxidation processes can be employed as a sequential process on pre-formed micropatterns to create

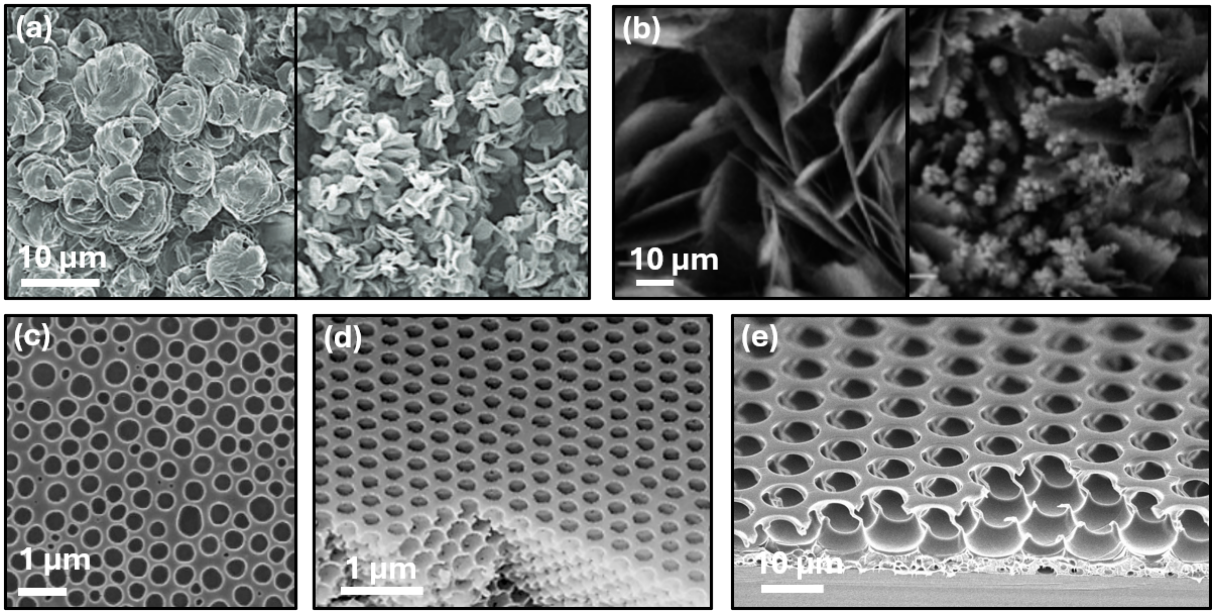

Figure 1.5. Varied patterned morphologies created via bottom-up techniques. (a) Rice bran wax crystals created within this work,[69] (b) Zinc carbonate crystals,[70] (c) phase separation,[71] (d) colloidal templating,[72] and (e) classical breath figure structures created within this work.

multi-degrees of roughness. Anisotropic crystal growth in high temperature and pressure plasma environments can lead to the formation of high aspect ratio filaments known as nanowires or nanograss.[73] Further, anodising electrochemical processes can be done where the patterning metal forms an anode electrode in an electrolyte solution under an applied voltage. Processes can also be combined with previously mentioned etching techniques to build up strong corrosion-resistant layers.[74]

Phase separation is a technique in which two distinct phases can form from a homogeneous mixture. A bi-continuous structure can be formed from the spinodal decomposition of block copolymers, a uniform de-mixing process where different domains form and solidify to create various nanoscale patterns.[75] If different blocks on a polymer chain are immiscible, solidification can result in chemically homogeneous domains in common lamellar, cylindrical and spherical morphologies (Fig. 1.5c).[76] Porous structures can be created through dissolution of one phase, with the domain size tuned by the rate of phase separation from temperature change or poor-solvent addition. This simple and low-cost patterning approach is widely used for generating polymer membranes and scaffolds,[29] and has even been used to create nanostructured light absorbers inspired by butterfly wings for photovoltaic applications.[77]

Colloidal templating methods rely on the self-assembly of nanoparticles from regular monolayer or multilayer structures. Assembly of latex, polystyrene or silica particles at the air-water interface is achieved through typical spin coating, drop casting and evap-

oration techniques to create close-packed arrays of spheres. The assembled structure can be further infiltrated with a polymer matrix material before the templating particles are dissolved or sintered out to create a porous structure (Fig. 1.5d). The uniform and monodisperse pattern is much more regular than phase separation techniques for example, where the feature size is easily regulated through input sphere size (often 10's nm to 100's µm).

Instead of nano/microscale spheres to pattern a substrate, the breath figure (BF) templating approach creates similar porous films to colloidal routes by using the spontaneous formation of condensation water droplets. The BF technique is a fast and simple single-step process that initiates condensation at the interface of an evaporating polymer solution. Through evaporation of a volatile solvent, droplets nucleate and assemble into a hexagonally packed array before solidification of the polymer. The droplets act as a dynamic template that evaporates at the end of the process, achieving feature sizes from 100's nm to 10's µm based on the solvent/polymer choice and environmental conditions. This method is one of the simplest, requiring only a polymer solution in a humid atmosphere, whilst still capable of producing highly ordered, regular patterns due to the stability of non-coalescing droplets at the interface. As a result, this method is investigated in more detail.

1.5 Overview

1.5.1 Discussions and perspectives

Interaction between material and environment in natural systems is optimised by virtue of the complex patterns at the nano and microscale. Not only do these abundant materials serve as an inspiration for our own engineered designs, but how they are realised demonstrates potential routes for fabrication. Simple organisms are able to generate, as well as continuously repair and re-generate,[78] complex hierarchical patterns in ambient conditions and via inherently energy efficient means. By harnessing molecular and interfacial interactions through instability-driven and self-assembling mechanisms, nature has her own solution to high-throughput/low-cost manufacturing. To further exploit what nature does so effortlessly, the need for predictable and scalable fabrication approaches inspired by biomaterials is evident.

To date, engineered materials fabricated through intensive top-down approaches or a combination of top-down and bottom-up techniques have surpassed the functionality of their bio-inspired analogues from a purely functional perspective. For example, Liu *et al.* demonstrated how complex doubly re-entrant and coated patterning can transform a completely wettable material (silica), and make it superomniphobic that even low surface

energy fluids bounce off the surface, further robust enough to withstand temperatures of over 1000°C.[56] The different top-down manufacturing routes summarised offer a diverse portfolio of patterns and capabilities, ranging from stochastic nanoscale needles in titanium oxide engineering cicada-like bactericidal effects, to doubly re-entrant nanometre-perfect arrays creating highly stable omniphobicity.[56,79] However, these methods often require substantial technical training in cleanroom facilities with multiple successive steps to create a pattern often constrained to the size of a silicon wafer. Further, the high capital investment of these machines and facilities, coupled with the use of extremely toxic and corrosive chemicals needed for etching metals make it not very feasible for the fabrication of adaptable, low-cost and scalable patterns. Bio-inspired design forming the basis of copying natural solutions is hence a primitive step toward the true mimicking nature, where both the end product and production means should take inspired routes for ultimate applicability.

Many bottom-up approaches partially bridge the gap between bio-inspired and biomimetic design, where relying on natural instabilities can create opportunity for sustainable patterning. As such, attractive advantages to these approaches manifest in large spontaneous patterning capabilities and low equipment cost, without sacrificing structural or property control. The creation of lotus leaf and rose petal-like patterning recently demonstrated here demonstrates how control over the pattern and properties is still attainable using low-cost methods, similar to natural fabrication pathways.[69]

The large-scale commercial implementation of microfabrication techniques provides exciting opportunities for the unprecedented development of functional materials. However, for wider applications to take hold, the need for manufacturing complex micropattern geometries at macro scales is required. Flexible and adaptable fabrication approaches facilitate the ability to readily prototype designs and alter the material properties. As one design does not fit all, the ability to create complex geometry, such as the re-entrant designs seen in nature, and control the size and spacing characteristics is imperative. What bottom-up approaches hence offer the most low-cost and flexible design? How can existing approaches be adapted to garner both greater control and scalability?

1.5.2 Contributions of this work

This work predominantly evaluates breath figure patterning as an effective patterning approach for the low-cost and scalable fabrication of micropatterned features. BF is low cost, requiring a polymer substrate and condensation as a template, and adaptable, using dynamic droplets which grow and shrink to create a range of feature sizes within the nano/microscale range of interest. Further, the basic laboratory equipment warrants minimal set-up, and as will be discussed has already showed scalable and commercial premise.

In particular, this thesis aims to clarify current drawbacks surrounding the classical BF approach through evaluation of the literature and experiments. Hence, an adapted approach for increased control and predictable BF patterning is presented, demonstrating novel levels of control and modulation. To this end, the chapters are structured around key elements of the adapted method, with each chapter containing a review of pertinent literature and perspectives, complimented by experimental work. The chapters are thus arranged as quasi-standalone pieces of work, organised as follows:

Chapter 1. Introduction to the project motivation, summarising the fundamental physics and key manufacturing techniques.

Chapter 2. Critical evaluation of the breath figure patterning method. Theory surrounding the forming mechanisms are presented alongside findings from complimentary experiments.

Chapter 3. The developed temporally arrested breath figure approach is introduced in full. Methods used throughout this work are summarised.

Chapter 4. Liquid-liquid studies on the condensation nucleation and growth of templating droplets are evaluated in the context of breath figure patterning.

Chapter 5. Pattern modulation capabilities are explored, elucidating the control handles in the process, resulting in the manufacture of varied breath figure samples.

Chapter 6. Initial functionality and wetting behaviour tests are performed on manufactured samples to characterise initial designs.

Chapter 7. This chapter summarises the findings and provides concluding remarks alongside future perspectives and ongoing investigations to explore functionalities.

Chapter 2

The breath figure patterning approach

The breath figure (BF) patterning approach harnesses the spontaneous nucleation, growth and assembly of condensation as a dynamic patterning medium. In this chapter, the foundation and process development is discussed alongside experimental studies to highlight key aspects of the process. Work elaborated upon here is a partial result of collaboration and a short research visit to Prof. Yabu of Tohoku University, Japan, whose work you will see extensively referenced throughout.

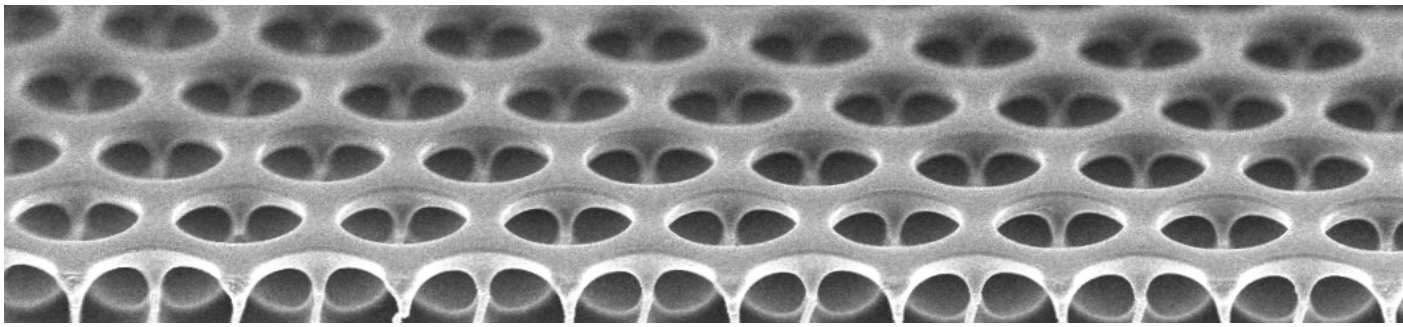

"I'd like to wash
By way of experiment,
The dust of this world
In the droplets of dew."
Matsuo Bashō

2.1 Introduction

The origin of the word breath figure (BF) stems from the phenomena observed with humid breathing upon a relatively cold surface. The ubiquitous formation of sessile water lenses from condensation pictured in Fig. 2.1 is the same process responsible for the formation of morning dew on grass to the droplets on a bottle drinks can, and was first reported in modern scientific literature by Aitken in the late 19th century.[80] With effect of a blow-pipe flame, Aitken demonstrated both drop-wise and film-wise condensation; dark images were observed due to the light scattering from a homogeneous array of plano-convex lenses (drop-wise condensation) on the non-treated surface.[80] The same idea was used in wet plate collodion photography, where photographers inspected their plates for contamination and cleanliness from the uniformity of condensation droplets.[81] Observations were elaborated upon by Rayleigh and later by Baker, with several other papers published throughout the next decade further describing the formation, morphology and contact angles of droplets.[81–83]

Figure 2.1. Breath figure examples in everyday life. From left to right, condensation forming inside my cracked double glazing, a water bottle, morning dew on a rose and droplets on the inside of a takeaway coffee cup.

The first quantitative studies of BF phase transition were completed by Beysens and Knobler, who elucidated the thermodynamic and kinetic underpinnings in a series of theoretical and experimental studies on dew formation.[84,85] This work explored the growth regimes of BF droplets, describing the monodisperse initial ordering and self-assembly of locally ordered hexagonally packed states. Characteristic self-similar scaling of droplet pattern growth laws was derived for coalescing droplets, introducing a polydispersity parameter. Similar notable studies and computational simulations were performed by Meakin and Family regarding metallic vapour deposition,[86,87] and Briscoe and Galvin understanding growth regimes and condensation impact on light transmission in greenhouses.[88,89] The formation of distinct growth regimes was established with explanations for the eventual rise of fractal droplet patterns and co-existing multi-generational droplet families.

It is, however, primarily the works of Widawski, Francois and Pitois in the mid 1990s who

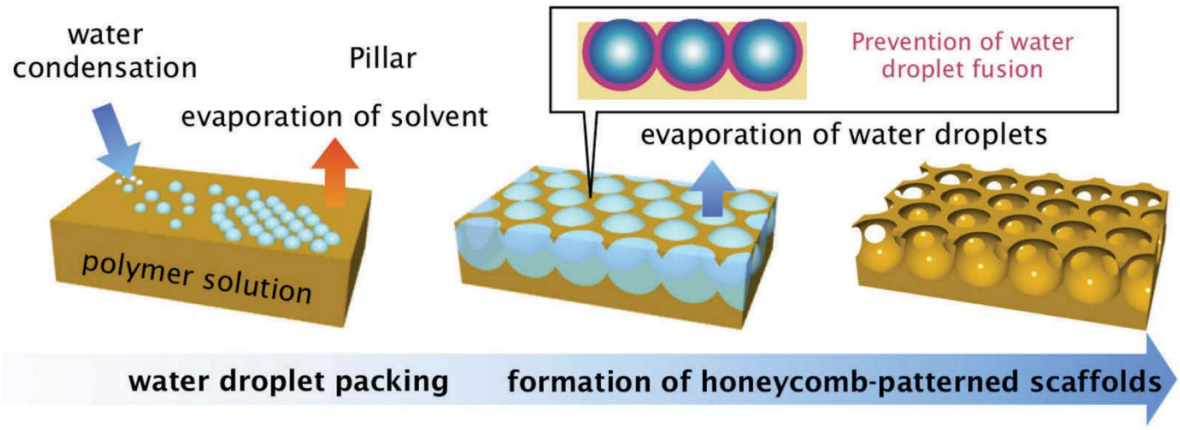

Figure 2.2. Schematic illustration of BF pattern formation adapted from Yabu.[90]

are accredited with the first demonstration of BF templating by using the arrangement of droplets as a patterning approach.[91,92] The method uses the nucleation and self-assembly of water droplets at an air-polymer interface to template a polymer film (Fig. 2.2). A low weight concentration polymer (often <10%wt) dissolved in a volatile organic solvent is drop cast onto a substrate.[92] Under the right humidity conditions (typically 50% $\leq$ Relative Humidity (RH) $\leq$ 90%), evaporative cooling decreases the temperature of the solution surface to below the dew point temperature of the system. At constant pressure conditions, this temperature corresponds to the temperature where the air becomes fully saturated with water vapour.[93] With continued cooling from solvent evaporation, the partial pressure of water vapour at the air-polymer solution interface is greater than the saturation pressure, facilitating the nucleation and growth of droplets. Droplets stabilise and grow at the polymer interface due to a balance of interfacial phenomena, organising into a quasi-crystalline hexagonal array characteristic of the BF honeycomb pattern. As the solvent completely evaporates, the polymer solidifies and the temperature raises back to ambient temperature. The imprinted droplet morphology is revealed upon droplet evaporation from the solidified film. Successful BF patterning classically hinges upon the formation of regular hexagonally packed arrays, gaining the name of honeycomb film formation due to the pattern resemblance.[90] To summarise, the process thus consists of several overlapping steps:[94]

1. Solvent evaporation from the polymer film
2. Condensation of water droplets onto the film interface with humid air;
   2.1. Nucleation of water droplets
   2.2. Growth of the water droplet array
3. Self-assembly of droplet array
4. Solidification of the polymer film

5. Evaporation the of water droplets

Since the turn of the century, advancements in polymer synthesis methods coupled with new interest in nano and micropatterned surfaces have increased with new developments and potential applications for BF fabrication.[90] Despite the wealth of empirical and context-based studies with several comprehensive reviews, many facets in the thermodynamics and kinetic underpinnings remain ambiguous.[95–100] BF patterning is a complex process relying on the synergistic interplay of environmental and physicochemical parameters, governed by heat and mass transfer in a non-equilibrium state. Although the formation process is generally accepted, no mechanistic theory adequately explains all experimental data from the actions of nucleation, droplet stabilisation and self-assembly, with many investigators failing to examine the importance of the governing physics from a quantitative standpoint.[101] The current literature comprises largely empirical data with conflicting results, describing the highly influential experimental parameters and perhaps the lack of control / natural variability in the casting conditions of many studies.[97] Battenbo *et al.* in their review summarised the current landscape as 'the haste for utilization of these structures has generated a wealth of experimental work, yet has overlooked utilising theoretical understanding...'[102]

The chapter reviews the underpinning theory and mechanisms of the BF process, detailing significant developments in materials and adapted techniques used since inception. Limitations and drawbacks to the classical technique are discussed alongside data and observations made as part of a secondment collaboration with Prof. Yabu of Tohoku University, Japan. This presents a general summary of the literature of BF method, with more pertinent studies covered in the following chapters.

2.2 Influence of physicochemical parameters

The BF patterning approach is a facile and accessible templating technique that requires only basic laboratory equipment. While advanced set-ups can include closed-loop environmental controls for methods of strictly controlling temperature and humidity, the basic principle merely involves a polymer solution (polymer dissolved in a volatile solvent), some sort of substrate and a humid environment to facilitate condensation. As such, these main components and their interlinking influences are discussed under respective headings before explaining their roles in the governing physics of the process. While the interplay and temporal evolution of competing effects ultimately dictate the resultant pattern formation, the key components are explained in isolation before providing a detailed overview of the formation mechanisms.

2.2.1 Polymer solution

Polymer. The polymer plays a crucial role in the non-coalescence and stabilisation regime of droplets, as highlighted in the literature.[95,97] Early research in the 1990s pointed to the polymer's architecture as the key to the formation process, with high segment density polymers, such as star or branched chain polymers, considered essential for homogeneous or monodisperse BF formation.[91,92] Pitois *et al.* first demonstrated the precipitation of functionalised polymers at the water-polymer interface, observing an enveloping layer of a block co-polymer of polystyrene (PS-b-PPP) around a droplet in a solution of carbon disulphide (CS_2).[103] X-ray scattering experiments supported this hypothesis, revealing precipitated micellar aggregates in BF architectures compared to flat films of the same formulation. This spontaneous encapsulation of droplets restricts coalescence between neighbouring droplets as they grow in size and interact with one another. More recent research by Li *et al.* corroborated Pitois's findings with *in situ* fluorescent imaging alongside theoretical and computational models, showing the aggregation and encapsulation process.[104]

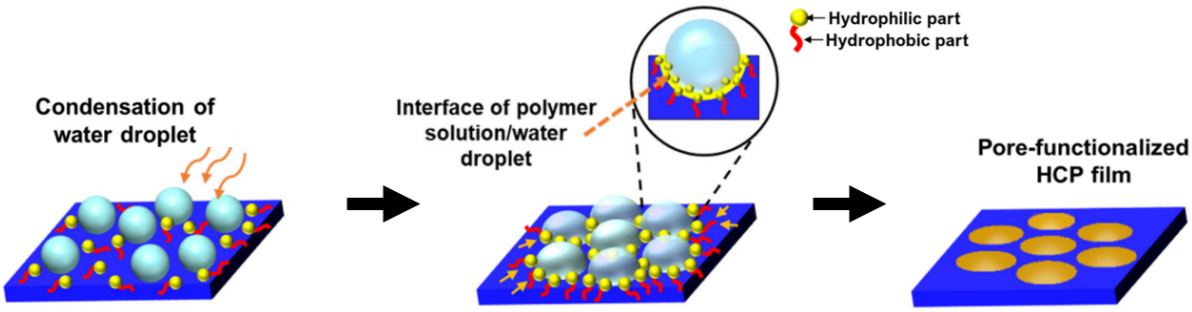

Figure 2.3. Amphiphilic polymer stabilisation effects showing the relative constituent system phases. Adapted from Falak *et al.*[105]

The formation of homogeneous BF patterns has also been linked to polymers containing polar end groups. Amphiphilic (high polarity) polymers act as surfactants and adsorb at the water-polymer interface, partially stabilising droplets by creating an amphiphilic-molecule emulsion (Fig. 2.3).[95] Linear polymers with specific functional groups have been shown to exhibit micelle-like behaviour leading to the formation of ordered arrays.[106] The surfactant adsorption at the interface has a strong steric stabilising effect, in some cases preventing coalescence for over one day.[107] The tendency of amphiphilic molecules to assemble in this manner has been confirmed through Raman spectrum mapping and dynamic light experiments, revealing enriched areas at pore boundaries.[108,109] Similar effects have been achieved for linear polystyrene with combinations of different additives from specialised block copolymers,[110] nanoparticles[111] and different surfactants[109,112]. Classical BF samples created within this work used linear polystyrene (230k Mw) with an additional surfactant, dodecylacrylamide and carboxyhexylacrylamide copolymer (CAP), mixed at a 10:1 ratio (Fig. 2.4b).[90] Not only does the preferential polymer orientation help

stabilise the templating droplets, the resultant porous structure can further be exploited for pore-specific functionalisation due to the locational chemical functionality. [105]

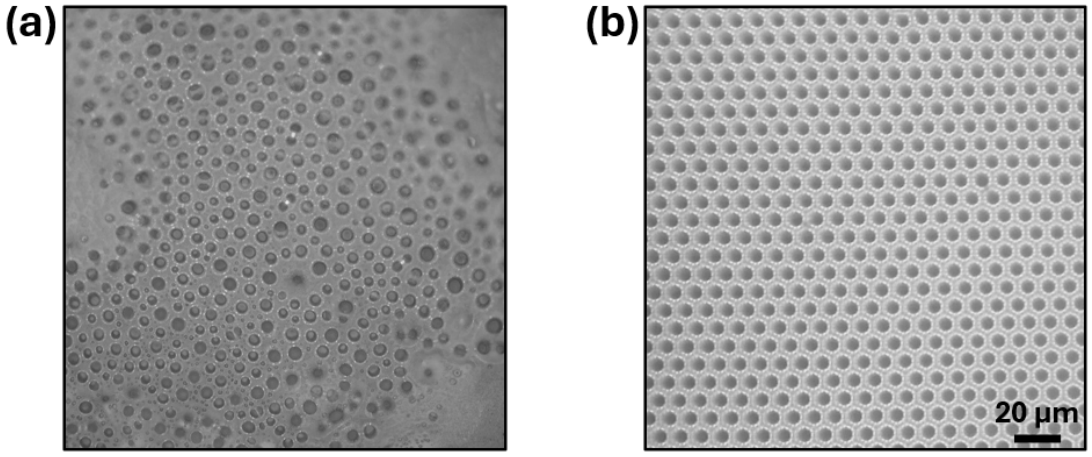

Figure 2.4. Fabricated surfaces made in this research. (a) Polystyrene polymer used independently and (b) with the use of CAP surfactant. The scale bar is consistent for both images.

The use of functionalised polymers and surfactants for use in BF formation often requires the precise control of block lengths, and significant multi-step synthesis methods. [105] Further studies have indicated that monodisperse BF formation can still be achieved with non-functionalised commercial linear isomers of polystyrene (PS) and poly(methyl methacrylate) (PMMA). [106,113–115 116] However, conflicting results over the feasible formation of monodisperse BF using these polymers indicate increasingly strict working conditions and the influence of other factors such as viscosity on droplet stabilisation. [112,113] Studies report a middle range M_w was effective ($M_w \approx 200$k) where smaller or larger M_w do not produce the same monodipserse arrangement. The polymer solution viscosity significantly increases with increased M_w, where other parameters such as the condensation working time become more significant. While the general honeycomb formation window is already small due to the balance of influencing factors, decreasing the range of working parameters further limits the fabrication control. A certain degree of polymer chain density or polarity (*i.e.* high branching from block-copolymers or amphiphilic polymers) can aid droplet stabilisation and increase the experimental resilience for the formation of honeycomb films.

Parametric studies investigating molecular weight and concentration show contrasting effects. Many studies report a positive correlation with polymer molecular weight M_w and pore size. [95,113,117] However, the common weight percentage variation of polymer in solution standardises for mass, but decreases the relative molar concentration and thus number of polymer chains in solution. These results can thus be interpreted as a decreased capacity for droplet stabilisation and delayed solidification resulting in larger droplets. Upon normalisation of the molar volume and hence polymer chain number, only a statistically

insignificant variance in pore size is reported.[95,115] The temporal element of droplet stabilisation and condensation duration appears to be the more significant variable in this case. This is evident in studies exploring the polymer concentration.[102] While the experimental time is inherently linked to the volume of solvent, the increased capacity to stabilise droplets faster and over a wider area is evidenced by a decrease in pore size. When the M_w is too low, the solution viscosity is too small and droplets cannot be adequately stabilised by the polymer to prevent coalescence. Conversely, if the viscosity is too high due to a large M_w or polymer concentration, the self-assembly of droplets is limited through restricted translation.[113] Hence, there exists an optimum balance specific to the polymer/solvent system used and the environmental parameters which dictate the working conditions window, explaining the empirical design rules from previous experimental studies.[118]

Solvent. The choice of solvent relies on its ability to completely dissolve the polymer whilst providing a sufficient amount of cooling to promote condensation.[90] Compared to the breadth of research on specialised polymers for fabrication, only a small number of organic solvents are generally used, including chloroform, dichloromethane and carbon disulphide.[97] Generally, the solvent should be non-polar to enable the aggregation of the polar moieties of the dissolved polymer to effectively stabilise the droplets. The solvent should also typically be water-immiscible to prevent droplet mixing and aid stabilisation through precipitation at the interface.[106]

The templating droplets nucleate and grow on the polymer solution until the viscosity of the solution passes a critical point (solidification) or the temperature rises back above the dew point.[97] As a result, high vapour pressures (low boiling points) and low enthalpies of vaporisation are required to initiate sufficient cooling.[106,119,120] At high evaporation rates, a greater temperature gradient is established between the surface and ambient, equating to increased condensation.[120,121] However, the faster solvent evaporation rate results in a greater viscosity increase rate, limiting droplet growth and further highlighting the importance of the temporal evolution of the formation process.[122] The size of the resultant pores, if there will be pores at all, is hence dictated by which regime dominates (Fig. 2.5). Gilemann *et al.* demonstrated that with too fast evaporation, regular pore formation does not occur due to large perturbations and the sudden vitrification of the non-equilibrium state in which the viscosity increase was too rapid for self-assembly.[113,123] The effective regime is thus a careful balance between achieving sufficient cooling for condensation, but not excess condensation where droplets grow until a stability imbalance results in coalescence and a non-monodisperse pore arrangement. Experimental adaptations can also increase the range of appropriate solvents by altering external factors. For example, toluene has a relatively high boiling point at 111 °C in which many studies have failed to achieve BF formation under their experimental conditions.[106,119,124] A later study by

Bormashenko *et al.* concluded that pre-cooling solutions were the decisive factor between successful and unsuccessful fabrication by facilitating condensation.[125]

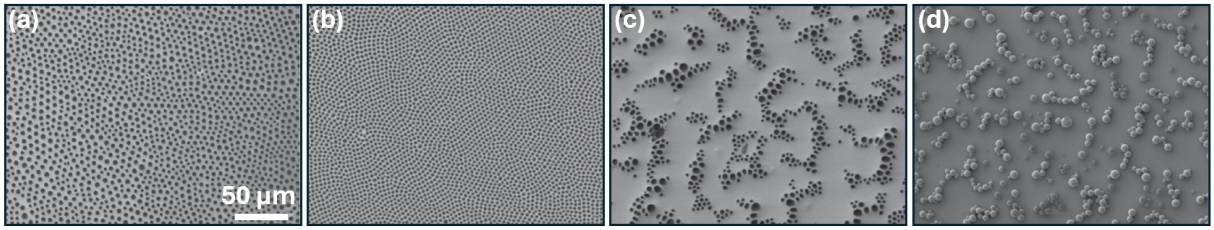

Figure 2.5. Polystyrene BF formed with different solvents on glass substrates. (a) chloroform, (b) dichloromethane, (c) carbon disulphide and (d) methyl ethyl ketone. Adapted from Ferrari *et al.*[106]

Temperature alone, however, is not enough to explain the formation in all empirical results. Ferrari *et al.* described the thermodynamic affinity in the solvent/polymer and miscibility as key parameters for BF formation as a criterion to discriminate solvents.[106] Hansen solubility parameters HSP, and the relative energy difference RED, were used to demonstrate how high solubility (thermodynamic affinity) affected results. The results were in agreement with a similar study by Tian *et al.* concluding that solvents with RED ≤ 1 (high affinity) created BF with the exception of toluene.[124] Toluene's behaviour can be explained as before where adequate cooling for condensation was not achieved from the low solvent volatility coupled with the experimental parameters (*e.g.* relative humidity). Further consideration in solvent choice has to regard the water miscibility and interfacial tension with water.[106] For example, acetone, a highly volatile solvent with a boiling point lower than chloroform but a similar vaporisation enthalpy, failed to obtain BF formation by many groups.[126] This can be explained by water miscible solvents such as THF and acetone which partially dissolve the condensed water droplets and thus create no stable pores. This, however, may not be a significantly dominating parameter as some studies have shown, contradicting feasibility with these solvents.[125] One explanation could be that the presence of polymer in solution may alter the solution miscibility to such an extent that dissolution of droplets does not occur.[99] This may be particularly prevalent given the rapidly changing relative concentrations of components throughout the process and the observed cold temperatures. The very matter of contradicting literature here suggests the need for the fine-tuning of experimental parameters, in particular when the inputs are seen as not ideal, such as with water miscibility and boiling point.

The impact of solvent density was initially regarded as an important parameter, particularly for the fabrication of multi-layer porous films. Studies initially hypothesised that multi-layer films could only be created when the density of water droplets was greater than that of the solvent, allowing the droplet to sink and reorder. However, subsequent studies have demonstrated various films created with solvents of densities above and below that of water,[127] indicated theoretically through the interplay of gravity and interfacial

forces by the capillary length and Bond number:

$$\lambda_c = \sqrt{\frac{\gamma}{\Delta\rho g}}\,, \tag{2.1}$$

$$\mathrm{Bo} = \frac{\Delta\rho g L^2}{\gamma} = \left(\frac{L}{\lambda_c}\right)^2 . \tag{2.2}$$

Where $\Delta\rho$ is the difference in density between the two phases, g is the gravitational acceleration, L the characteristic length, and γ the surface tension. Assuming standard numerical values for common inputs, the lateral characteristic length scale is in the nano to micro range ($10^{-9}\,\mathrm{m} < L < 10^{-6}\,\mathrm{m}$) with $Bo \ll 1$. When the Bond number is set to 1, the characteristic length is equal to the capillary length, hence due to the small characteristic length scale of the templating droplets resulting in a Bond number much less than unity, buoyancy and gravity effects can be neglected due to the dominant surface tension effects.[128] This is observed experimentally with BF formation using chloroform (relative density of 1.48), and in fabrication techniques such as dip coating and electrospinning, where pores form irrespective of a flat horizontal surface.[128–130] Further, the formation of multilayer porous structures seems to be an effect of dosage volume and high droplet stability upon complete packing, forcing the downward trajectory of the droplets.[94,103,131]

While the droplet stability is predominantly noted as a function of the polymer precipitation effect from the assembly at the water-polymer interface, further literature suggests that the solvent also plays an important role. Evaporative cooling from the solvent can both produce convection currents in the solution to drive effective re-ordering of the droplet array, but also separate droplets by a thin lubricating layer of air driven by the same gradients.[94,132] Daly *et al.* suggests that effective droplet stability is attained on pure solvent films irrespective of polymer, where the polymer role merely translates the shape into a solid form.[127,128]

2.2.2 Substrate

Due to the passive nature of the evaporation-driven BF process, the substrate can have significant effects depending on its thermal conductivity.[133] Further, with common drop-casting methods used, the molecular affinity of the polymer/solvent to the substrate (wetting behaviour) can significantly alter the spreading of the solution and hence pattern outcome.[106] Despite the significant role in the process dynamics, the substrate parameters are often substantially less reported than those of the polymer or casting conditions - investigators fail to report the type and thickness of material used, as well as cleaning history and other such parameters which can have significant impact.[102]

Standard glass cover slips or microscope slides, silicon wafer or polymer substrates such as polyethylene (PE), polyethyleneterephthalate (PET), polyvinyl chloride (PVC) are all commonly used substrates.[97] Generally, solid substrates form films with a bilayer structure, resulting in an upper porous layer and a solid polymer bottom layer.[92] Although water droplets nucleate at the air/polymer interface[134] and seemingly stay as an upper porous layer, the empirical data clearly suggests that the substrate affects the resultant film morphology.[106] Systematic substrate studies have been completed and come to similar conclusions; it has been shown that the hydrophilicity of substrates can aid in droplet nucleation and lead to enhanced periodicity and regularity of pores.[135,136] Cheng *et al.* found that mica was the most suitable substrate being the most hydrophilic that they tested, also concluding that the pattern generation is somewhat dependent on the water adsorbed onto the substrate surface before polymer deposition.[135]

Li *et al.*'s findings contradicted the previous study, stating that the substrate effectiveness is solution specific.[137] They claimed that polypropylene (PP) substrate (less hydrophilic) gave the best results under their set-up, leading to the conclusion that it is the wettability of the polymer solution with the substrate rather than the hydrophilicity of the substrate. Due to the affinity of the polymer solution to the substrate, if the solution spreads well and polymer chains freely move to aggregate and stabilise droplets, the pattern is more likely to be monodisperse. Ferrari *et al.* corroborated the important role of wettability, demonstrating that scarcely wettable fluorinated substrates led to unsuccessful BF attempts.[106] They concluded that the formation mechanism and role of substrate lies in the combined effect of solution characteristics and interaction. These claims further substantiate the polymer-droplet interface stabilisation theory that the polymer strands migrate and encapsulate the droplets in a colloidal-type stabilised assembly, indicating the importance of the polymer spreading effects.

The thickness of the substrate is also an important parameter when considering the purely evaporation-driven phenomenon and finite solvent volume. Bormashenko *et al.* demonstrated that the BF formation was strongly impacted by substrate thicknesses, with uniform self-assembly observed exclusively on substrates less than 150 µm thick.[138] This was attributed to the substrate acting as a thermal reservoir, particularly with thin polymer films and highly volatile solvents where the reaction working time was reduced. Due to the substrate's large mass relative to the small volume of polymer solution, the rate of heat transfer observed through solvent evaporation was reduced, in some cases completely mitigating any BF formation. The idea of the substrate acting as a thermal bath was also observed in a study by Onder *et al.*[133] Depositing their polymer solution by spin coating, the small area of the substrate under vacuum to keep the substrate attached during spin coating prevented BF formation. By backing the slide to a piece of cardboard to insulate from the vacuum, uniform BF was then formed. Battenbo *et al.* confirmed

the dependence on substrate thickness with a computational model describing the casting process.[102] A decrease in substrate thickness increases the evaporation rate due to an increased heat transfer rate through the system because of the proximity of the evaporating solution interface to the heat input (substrate) given no conduction.

2.2.3 Environmental Conditions

With BF patterning being predominantly a phase-change-driven phenomenon, measurement and control over the environmental conditions is essential. Although most often neglected in studies, the dew point temperature of the system is perhaps the most important parameter, defining the physical rates of condensation and pattern formation. Humidity control has conventionally been done with either ambient conditions, dynamic airflow or static closed systems of fixed humidity.[97] The most common method used since the development of the technique regulates the flow of humid gas with controlled rate/humidity.[92,103] Nitrogen gas is bubbled through water and mixed with pure nitrogen gas in desired quantities to achieve a specific relative humidity (RH) of humid airflow which continuously purges the casting environment. Static humid environments have also been established through sealed vessels that are left to reach saturation equilibrium for a sufficient period of time.[117,139,140] Different amounts of inorganic salts can be dissolved into the water to alter the vapour pressure and consequent RH.[141] The different techniques have varied advantages/disadvantages - dynamic gas flow has the potential to be highly regulated with closed loop control, however, this is not always the case and non-regular flow can cause disturbances in the ordering.[102] On the other hand, small vessel static environments can be somewhat uncontrolled and need time to equilibrate which makes sample deposition difficult.

The nature of finite solvent-evaporation means initial conditions are crucial for successful patterning. Previous literature demonstrates this importance with the initial polymer solution temperature having an effect[125] as well as the general relative humidity on overall pore size.[113] While dynamic environmental conditions can thus increase the versatility of the polymer/solvent choice, discrepancies across reported influences discussed could be due to poorly characterised environmental conditions. Some studies have also performed experiments in non-aqueous environments, where the type of vapour alters both the size and shape of pores (Fig. 2.6).[97,143] It is important to characterise both the evaporation enthalpy of the vapour due to it being a function of the resultant droplet size, and the relative interfacial tension in determining the shape and contributing effects of deformation due to gravity.[142]

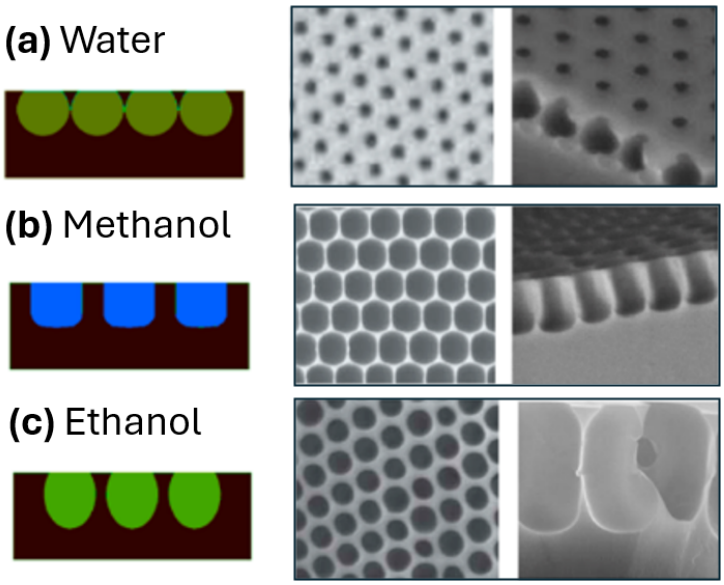

Figure 2.6. Aqueous and non-aqueous atmosphere effect on pore morphology. Adapted from Zhang *et al.*[97,142]

2.3 Governing physics and formation mechanisms

Successful BF patterning is contingent upon the formation of regular hexagonally packed arrays, gaining the name of honeycomb film formation due to the pattern resemblance.[90] The deceptively simple, passive self-assembly and formation process of honeycomb packed BF films, however, relies on the temporal evolution of the combined and competing effects from the constituent components. As shown schematically in Fig. 2.7, successful fabrication depends on the balance between nucleating droplets that grow and pack together before the eventual complete solidification and drying of the film. The formation mechanism is hence governed by the stabilisation and non-coalescence effects that maintain the monodisperse droplet arrangement through self-assembly into the lowest energy ordering configuration of a hexagonally packed array.

The temporal ordering of events is critical for successful monodisperse fabrication. As well described by Gurr *et al.*,[112] nucleation and growth of individual droplets first have to occur before assembling into a large surface coverage of highly packed order prior to complete solvent evaporation results in the polymer film solidification. If complete evaporation occurs too early, the viscosity increase of solution becomes too great for significant self-assembly (viscosity opposes the mobility and translation of droplets). On the contrary, if solidification occurs too late, droplets tend to coalesce or form multilayer films as interactions between neighbouring droplets become too large. As described in the interacting physicochemical parameters, it is the interplay of interfacial forces and interactions between water-solvent-polymer that govern the formation, but the kinetics of the process which dictate the resultant structure.[145] This section provides an overview of

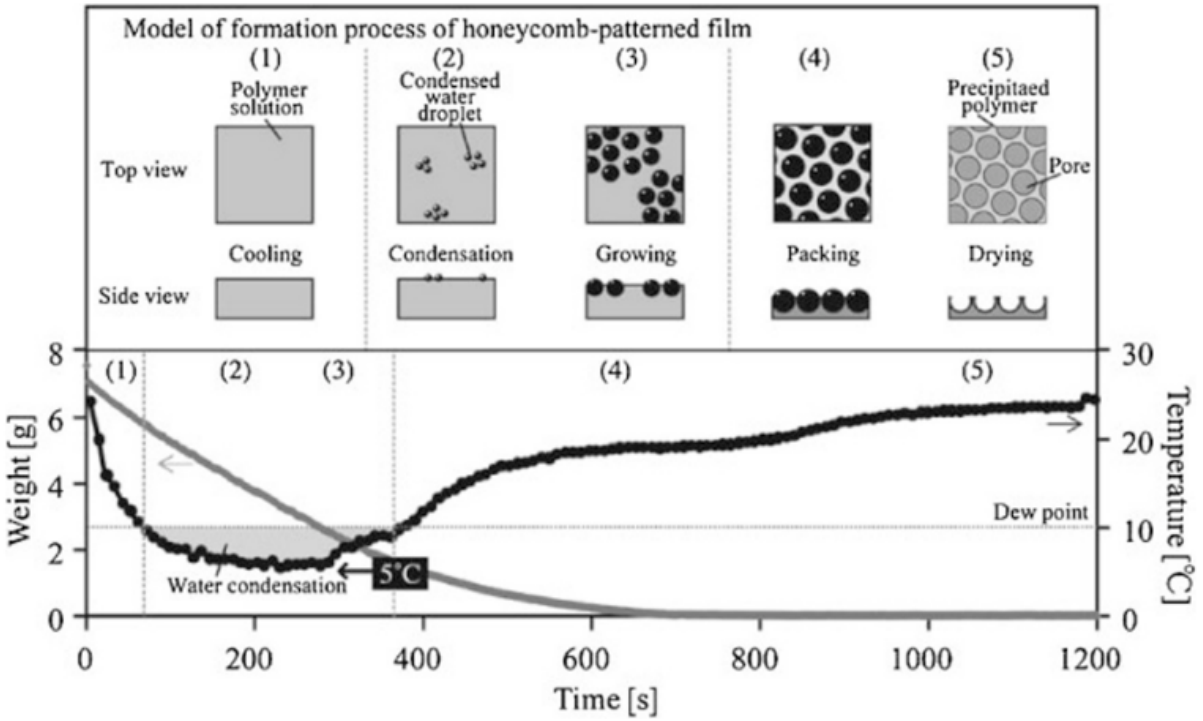

Figure 2.7. Process schematic plotted alongside the temperature and weight variation of the polymer film. Reproduced from Kojima *et al.*[144]

how the respective components of the BF casting facilitate this model formation process. Comments and analysis of critical theories are discussed alongside images and commentary from research undertaken.

2.3.1 Nucleation and droplet growth

As discussed in Sec. 2.2, the choice of solvent can dictate the difference between a pattern and no pattern, provided there is effective environmental conditions. The evaporation of said solvent leads to significant energy removal from the system due to the latent heat of vaporisation, decreasing the temperature of the solution and initiating the nucleation of droplets. Associated temperature drops have been reported from non-significant temperature changes and no condensation,[125] to upwards of a 25 °C below the ambient temperature.[94] While the evaporative cooling effect is the main driver for temperature change and condensation onset, environmental control further impacts condensation. As such, many reports show the relationship of increased pore size with relative humidity,[95] with some studies trying to quantify the minimum humidity required for which pattern formation occurs for a specific system.[97] For nucleation to occur, however, it is more about the combination of parameters that affect the dew point of the system and overall rate and absolute change in temperature. It is such parameters as the ambient system temperature and respective dew point, the initial temperature of the solution, relative airflow rates in dynamic set-ups, and even contributing insulative effects from the substrate that

lead to discrepancies noted within the literature.

With the polymer solution experiencing a temperature decrease from the ambient, it is widely accepted that droplets are created through heterogeneous condensation at the air-polymer interface.[99] The vapour pressure of water at the cooled interface will be greater than the saturation vapour pressure in the ambient, creating a thermodynamic driving force for nucleation to occur.[93] It has been shown that the presence of an interface,[146] and in particular the presence of a deformable soft or liquid interface[147,148] decreases the energy barrier for nucleation to occur, making the nucleation at this interface most likely. Empirical and theoretical studies show that this phase transition is a function of the wetting behaviour of the condensate at the polymer solution interface.[146] While condensation can occur as both film-wise and drop-wise as will be explained later in Ch. 4, the fundamental requirement for BF patterning is for discrete droplets to form rather than a film of condensate. As such, the spreading of water on the polymer (see Eq. 1.1) denoted by the spreading parameter S must be negative.[99] The high surface tension of water (cohesion) results in the water forming a spherical droplet lens shape rather than spreading into a thin film.

With the Bond number $\mathrm{Bo} \ll 1$, the dominance of interfacial forces determines the initial droplet shape. This is evidenced with the high spherical symmetry of pores produced, characteristic of the templated water drop. As the interfacial tension of the water and polymer solution is typically less than that of the surface tension of the water, the liquid lens tends to partially submerge below the free surface plane of the solution.[115] In a static solution, the lens shape can generally be predicted by analysing the relative interfacial tensions, however, with the dynamic temperature and viscosity changes throughout the experimental working time, the droplet shape readily changes.[149] Reports indicate different relative sinking depths, or aspect ratios, with rapid evaporation of solvents tending to 'levitate' the condensing droplets.[126,150] As a result, even with the reported pore size control of the process in literature, the range does not necessarily consist of systematically size-varied structures but a variation of the size of the surface hole.[145,151]

After the initial nucleation of water droplets at the interface, water droplets grow through continued net condensation. The growth of dropwise condensation on substrates was first explored in detail in the studies of Beysens and Knobler (BK).[84,85] In these works, three different growth regimes were reported: early, intermediate and late stage growth which correlated to the surface coverage of the droplets and working time duration. Briscoe and Galvin suggested similar regimes in terms of initial isolated droplet growth, growth through coalescence and significant interaction and thirdly a re-nucleation regime.[88,89] This is further corroborated in the computational simulations of Meakin and Family which included a further, final regime of coalescence and re-nucleation with removal of larger droplets[86].

For isolated droplets, growth via condensation occurs in a diffusion-limited regime.[152] Water molecules may diffuse directly from the gas phase to the droplet surface or adsorb molecularly on the substrate and diffuse towards the droplet. With a steady state of condensation flux, the volume of the droplet grows proportional to time ($V \propto t$), thus indicating a diametric growth rate of $D \propto t^{1/3}$.[85] Droplet coalescence is negligible until a critical surface coverage value is reached, beyond which inter-droplet interactions result in temporal and spatio-temporal variations in the surface coverage with geometric configurations.[153] As the surface coverage increases, droplet coalescence increases polydispersity within the system, forming non-monodisperse arrangements. The formation of hexagonally packed BF patterns thus requires solidification of the polymer before this stage.

Whilst the established growth rates were theoretically and experimentally verified on both solid and liquid substrates before BF as a patterning construct was conceived, few studies exist which quantify the pattern evolution on solvent-evaporating films. While the original reports studied the general formation of condensing water droplets, carrying out experiments under model conditions and in the absence of evaporated polymer solutions,[84] the more complicated physics and non-linear temperature control with evaporation alter the growth trends. $D \propto t^{1/3}$ occurs in ideal steady-state conditions where non-isothermal growth in this case can unpredictably change this growth. This manifests in size variation across the film due to the solvent evaporation front[140] and a range of different observable growth rates.[154,155]

The non-equilibrium solvent evaporation with non-linear solution temperature makes it difficult for studying the onset of condensation. Further, some systems achieve highly packed microscopic droplets in a matter of seconds, presenting experimental and analytical difficulty to both control and analyse the process.[156] The inability to properly modulate or control the process *in situ* due to the reliance upon the initial input conditions also demonstrates the decreased need for nucleation analysis and tracking as the outcome is almost pre-established. Despite the nucleation and growth of droplets playing a paramount role for BF patterning, few studies report on the effects of nucleation and overall growth rate. However, as postulated by Saunders *et al.*, the effect of nucleation density on resultant pore size could explain the contrasting results in the literature.[118] By attributing the increasing M_w in their case with increasing hydrophobicity of the polymer, they equated the increasing pore size due to a lower initial nucleation density that led to the few droplets growing larger with a net equal condensation flux.

2.3.2 Droplet stability and pattern formation

Successful fabrication of hexagonally packed BF structures depends on the temporal evolution of the droplet stability and self-assembly prior to polymer solidification. As such,

the droplets (or rather the overall pattern) need appropriate time to stabilise, grow and assemble together. Without adequate stabilisation or with too much droplet growth, the pattern exhibits a polydisperse structure as noted before. The non-coalescence behaviour, arising from contributions of many of the same fundamental mechanisms, is hence fundamental to proper fabrication.

For coalescence to occur, the polymer solution between two neighbouring droplets first has to drain. As a result, viscosity is a contributing factor where viscous forces work against the draining of this lubricating layer.[112] This is also a function of solvent evaporation time as the polymer concentration dynamically increases. Further theories suggest similar effects to what Dell'Aversana *et al.* demonstrated with two millimetric-sized droplets of different temperatures.[132] Thermocapillary flow gradients in air driven by the temperature gradient between the droplets result in hydrodynamic resistance opposing the draining of a thin lubricating air film. Srinivasarao *et al.* postulate that the temperature gradients of the condensing droplets and evaporating solvent from the solution create a lubricating film of solvent vapour which suppresses the coalescence.[94] With continued droplet growth duration, only systems with adequate stabilisation arising from the polymer encapsulation and surfactant effects will form a monodisperse arrangement.[112]

For non-coalescing droplets, it is the combination of short and long-range self-assembling forces which contribute to the minimum energy arrangement of a hexagonal packed array. As individual droplets grow nearer to one another in a diffusion-limited regime, they experience attractive capillary forces due to the deformation of the interface. While classical capillary forces due to gravitational bulk forces distorting an interface tend to become negligable at the Bond number of templating droplets (see Eq. 2.1, 2.2 where $L \ll \lambda_c$), deformation at the liquid surface triple line can still occur as a result of the wetting behaviour. To minimise the potential energy due to any slight menisci, the droplets attract one another and can form well-documented islands.[157] Some of the classic BF samples fabricated in this study show the initial formation of packed droplet islands (Fig. 2.8a) and the final packing of the droplets which is mediated by grain boundaries from the combining of islands (Fig. 2.8b).

Due to the relative temperature gradients that arise from solvent evaporation and droplet condensation, gradients in surface tension can occur, resulting in Marangoni convection or thermocapillary flow within the solution.[158,159] Due to the solvent evaporation, a temperature gradient exists in the polymer solution where the surface temperature is lowest at the solvent evaporating front. A resultant gradient in surface tension occurs ($\gamma \propto 1/T$) and can exert a force on the droplets, pulling them below the surface. The flow transports the droplets towards the evaporating edge of the polymer solution, packing the droplets closely together.[139] Further, the sinking of droplets from the solution surface can result in new droplet nucleation and the formation of multilayer porous films.[94,160–162] Another

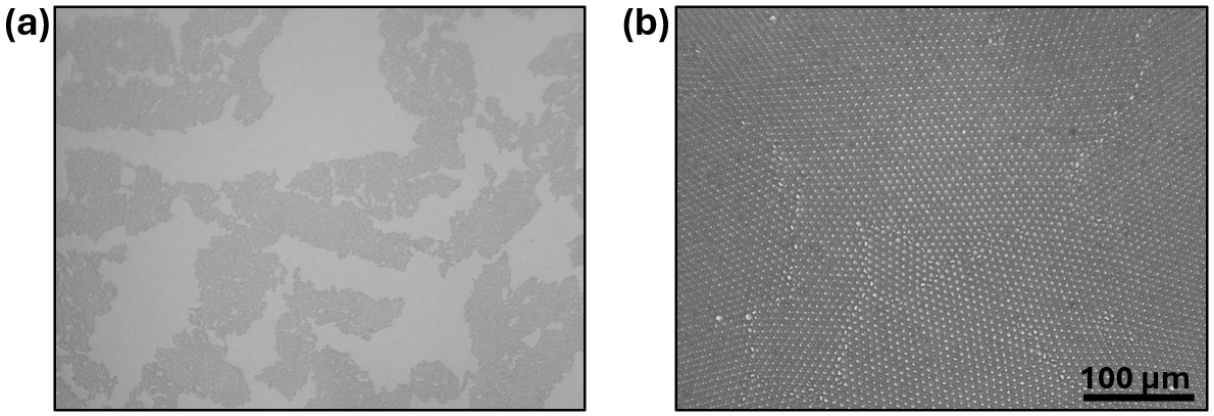

Figure 2.8. BF formed in this research. (a) Islands of packed droplets assemble togethor, (b) and resultant complete high packing mediate by grain boundaries.

explanation invokes the stabilisation of droplets due to the evaporating solvent escaping which partially levitates the droplets.[150] Re-ordering of the droplets then occurs through a combination of said convective currents in the solution and dynamic airflow when humid air is pumped into the system, before the eventual sinking and templating of the droplet shape occurs.[94] While de Gennes demonstrates that the concentration gradients will dominate over the classical temperature gradient convection,[163] ultimately, it is the varying combination of the respective densities, relative concentration/temperature gradients, dynamic airflow and opposing increasing viscous forces that are influenced by the temporal evolution of the patterning, dictating the pattern formation mechanism.

2.4 Breath figure adapted methods

In most classical BF studies, the process is predominantly driven by the passive solvent evaporation and modulated to some extent via environmental control. Similar to initial studies of dropwise condensation by Beysens and Knobler,[84] some patterning reports have added another control handle via the use of a Peltier cooling device below the substrate to readily influence the polymer solution temperature,[157,164] increasing the experimental tolerances and range of compatible solvents. Additional handles, such as a roll-to-roll process developed by Fujifilm allow the continuous production of such patterned films.[165,166]

The majority of adapted BF methods have stemmed from particular applicational perspectives. Farbod *et al.* developed a direct breath figure (DBF) approach by preparation directly onto a solid polymeric substrate;[167] the main difference being that no pre-prepared polymer/solvent solution is required due to the use of an organic polymeric substrate. The dissolution of poly(methylmethacrylate) (PMMA) slabs in a water and tetrahydrofuran (THF) solvent solution occur by sonication before being left to dry through evaporation in a non-humid environment. This method gave rise to the semi-direct breath figure

(sDBF) method in which pure solvent partially dissolves a polymeric substrate (creating the polymer/solvent solution) before evaporation of the solvent and subsequent condensation of water in humid conditions.[168] This had beneficial implications for biological analysis in which standard polystyrene Petri dishes could be directly post-fabricated with 3D honeycomb porous films to aid with antimicrobial properties and cell adhesion.[169]

Depending on the porous film application, a vast range of alternative materials have been utilised for both the bulk polymer and substrate. Surfaces have been synthesised with particular engineering polymers for specific qualities, such as stimuli responsive polymers,[170,171] fluorinated low surface energy polymers (superhydrophobic)[172,173] and photocrosslinkable polymers[174–176]. Casper *et al.* developed a method for patterning non-planar substrates and creating porous fibres through using the BF principles in the electrospinning process.[129] Ice and liquid substrates have also been used to aid the cooling process and create perforated through-holes for microfiltration applications.[177] New techniques have mitigated the use of solvent altogether, relying solely on active cooling through a Peltier device and solidifcation by UV crosslinkable polymer adhesives.[178,179] By combining active methods for cooling and curing the structures, the process was readily controllable in terms of final pore morphology, whilst negating the need for toxic solvents that are conventionally used.

The pattern morphology has previously been modulated in a number of ways. *In situ* dynamic airflow can force droplet configurations and surface pore shape, going from spherical to elliptical and rectangular,[170] and post-fabrication manipulation has been demonstrated via thermal shrinking to decrease the overall size.[180] The overall pore shape can be modulated through the use of non-aqueous vapours,[181] as well as altering the interfacial tension with solvent/polymer choice[128,182] or precise regulation of the phase change dynamics.[149] Depending on the type of polymer used, some BF samples can result in interconnected subsurface pores through bursting of the droplets with evaporation at the final stage.[126,183] The interconnections must occur in the final stages of polymer solidification, with rising temperatures promoting droplet evaporation from the stabilised pores.[126,183] Pillar, 'pin cushion' like structures can be created by peeling the top layer of the BF sample off with adhesive tape, creating superhydrophobic functional surfaces (Fig. 2.9).[184]

2.5 Challenges and limitations

Much of the appeal and beauty in the breath figure method relies upon the passive deposition and intrinsic self-assembling nature which reveals the surprisingly ordered structured state. The formation of such regular, hexaongally packed pore structures is more reminiscent of strictly controlled machined manufacturing methods than one would think of being created from the spontaneous onset and self-assembly of condensation droplets.

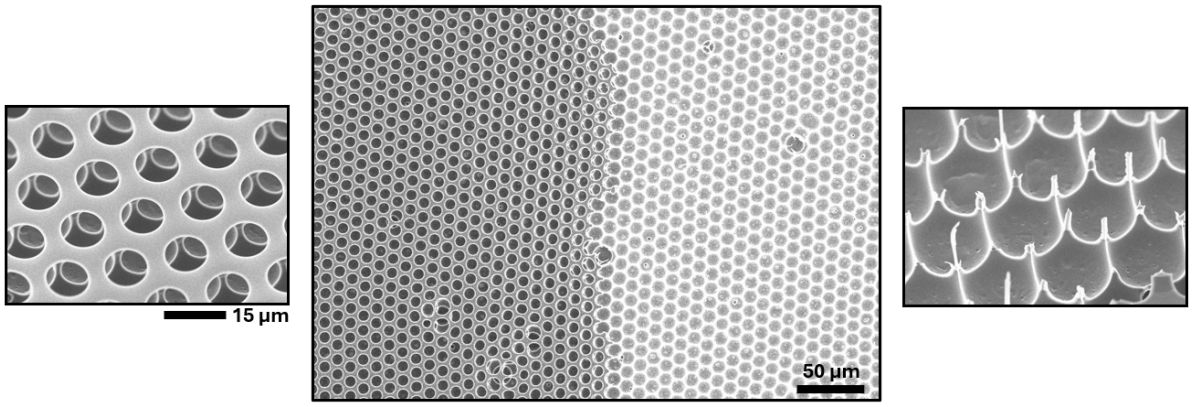

Figure 2.9. Breath figure sample fabricated from PS and CAP created in this study. Showing both BF (left) and pincushion (right) topography with highlighted views on either side.

The contrasting mechanistic theories and empiracle-based nature, however, is far from the elegance of the successful samples which make the cover images. Fundamental lack of control stems from the interplay of the competing mechanisms which counter-intuitively make the experimental process deceptively simple. As such, a trade-off exists between the passive process and a fabrication technique that offers true flexibility and control over the resultant samples.

The main challenges surround the temporal interplay of the influencing parameters. As reported by Yamazaki *et al.* the formation mechanism of assembly defects are caused by the 'tectonics' of assembling water droplet arrays.[157] Divergent defects arise when the condensation growth time is not long enough for complete pattern assembly, and solidification occurs prior to complete packing. Moreover, if the condensation growth time is too long, convergent defects form with the overlapping of multiple layers. If there is not adequate droplet stability, the converging droplets also tend towards coalescence, forming polydisperse samples.[112]

The majority of this review has attempted to explain 'ideal' formation with the creation of hexagonally packed porous samples. However, due to the complexity of achieving perfect packing and size, the literature is replete with varying degrees of disordered samples exhibiting non-perfect packing configurations and polydispersity.[97,126] Further, the widely reported feature range of hundreds of nanometres to tens of micrometres is far from systematic or ideal. To the best of the author's knowledge, no single input solvent/polymer solution combination can create that diverse range; rather, through empirical trial and error of material concentration input and environmental variation can the range of sizes begin to be explored, incidentally also modulating the pore morphology. This poses questions on how greater control of the process can be garnered and if it's possible to de-couple interacting phenomena to attain a more predictable design. Further, as seen

with natural feature polydispersity in biological systems even enhancing the effects, is some amount of polydispersity acceptable?

Only with effective pattern control, can the wide array of potential applications of these surfaces be fully explored. Over the next few chapters, a proposed technique for separately controlling the saturation level and cooling to control the condensation, and a further handle to control the solidification onset is investigated. By simplifying and de-coupling components of the method, the ability to link the condensation growth physics to gain predictable and understandable patterning is researched.

2.6 Summary

- The classical breath figure patterning approach harnesses the evaporation of a solvent from a polymer solution. The spontaneous formation and assembly of condensation droplets imprint the polymer solution before solidifcation of the film, leaving behind porous shapes after the evaporation of droplets.
- By employing water droplets as a dynamic template, the breath figure patterning approach is a versatile method for creating low-cost, scalable and adaptable micropatterned functional surfaces.
  - Scalable - unlike lithographical etching techniques or other top-down manufacturing methods, the spontaneous formation of condensation droplets over a wide area is inherently scalable.
  - Low-cost - bottom-up process with no templating material other than water droplets originating from humid air.
  - Adaptable - the formation of condensation droplets that grow in time enables a range of feature sizes to be created.
- The passive nature of the solvent-evaporation-driven approach creates a complex interconnection between the dynamic and non-equilibrium condensation/evaporation processes that restrict the direct translation of the mechanistic knowledge of dropwise condensation kinetics towards the predictive design of pattern morphology.
- By managing the temporal evolution of the pattern formation, can the kinetics of the process be controlled and translated into predictable and systematic feature variation?

Chapter 3

The temporally arrested breath figure approach

The full temporally arrested breath figure method is introduced here in its entirety. The rationale for the technique is summarised and the main technical aspects and methodology are described. Some of the content written here is published across two previous publications, '*Temporally arrested breath figure*'[185] and '*Exploiting breath figure reversibility for in situ pattern modulation and hierarchical design*'.[186]

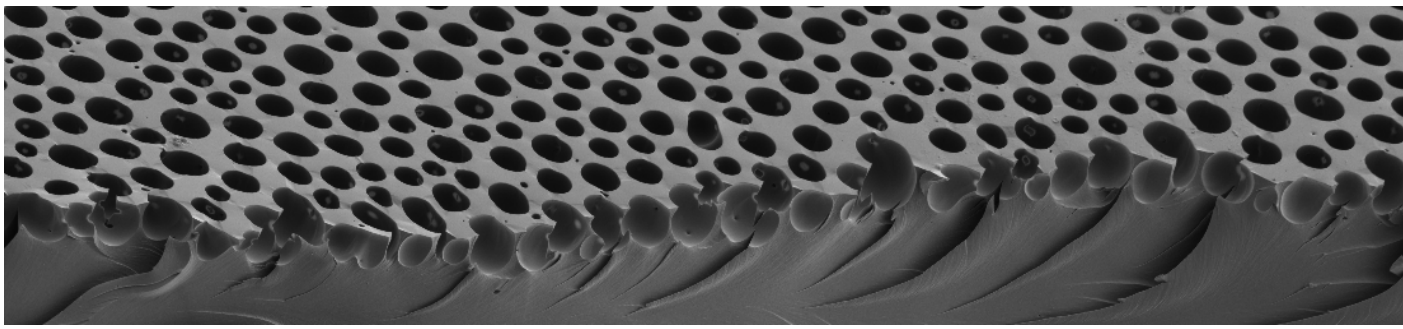

"The borders between great empires are often populated by the most interesting ethnic groups. Similarly, the interfaces between two forms of bulk matter are responsible for some of the most unexpected actions"

Pierre Gilles de Gennes

3.1 Introduction

The ability to readily create self-assembled patterns of features ranging from nano to microscale in a scalable and systematic manner has wide-ranging applications. However, as summarised in the previous chapter, the drawbacks to the classical, solvent-evaporation driven BF technique arise from the very same benefits; while BF patterning is seen as a facile templating technique due the passive nature of solvent-induced coupled phenomena, this does not allow systematic control over the resultant pattern.

From herein, the classical BF approach is defined as solvent-evaporation-driven as per the original studies.[91,92] In this approach, total evaporation of the solvent is essential to the creation of the final solid structure. It is the complete removal of the solvent from the polymer solution which controls not only the condensation rate, but the experimental time in which the composition of the polymer solution goes from $> 90\%$ solvent to solid polymer. If complete solvent evaporation and polymer solidification does not occur fast enough, the condensation droplets will either tend towards coalescence[164,187,188] or, given the right conditions, form multi-layer porous structures[94,160–162] due to the sinking of the droplet array. A specific output pore size and spacing is therefore achieved for given experimental inputs of material properties and environmental conditions. Consequently, relatively narrow system-specific working windows are often empirically derived to achieve regular BF patterns. Limited systematic control over the pore size is garnered due to the inability to control the exact moment the final pattern is arrested. This complex interconnection between the dynamic and non-equilibrium condensation/evaporation processes restricts the direct translation of the mechanistic knowledge of drop-wise condensation kinetics[189] towards the predictive design of pore size and spacing.

Proposed solutions to the key challenges are summarised below for the presented temporally arrested BF approach, with more technical information discussed in the following sections.

Challenge 1 - Droplet nucleation
In classical BF, the solvent evaporation is essential for initiating droplet nucleation. This leads to ambiguity around solvent compatibility - studies often have conflicting success or failure results because of the specific environmental conditions in their study. Depending on the ambient or set humidity, evaporation of the solvents in question may or may not yield the required energy removal to produce sufficient cooling for the nucleation of the droplets.[106] The temperature difference is further complicated by the insulative or conductive potential of the substrate.[106] Accurate prediction of the nucleation and subsequent pattern growth is thus not straightforward due to the non-linear temperature dynamics over the duration of the experimental working time (Fig. 3.1).[149]

In this adapted approach, we employ external cooling facilitated by a Peltier device situ-

ated below the polymer film. This enables regulation of the saturation regime and control over the droplet condensation. The subcooling level of the polymer film can thus be set by measuring the dew point of the environment and setting the respective temperature difference. By alleviating the need for solvent completely, the supersaturation level can be directly controlled in a linear fashion.

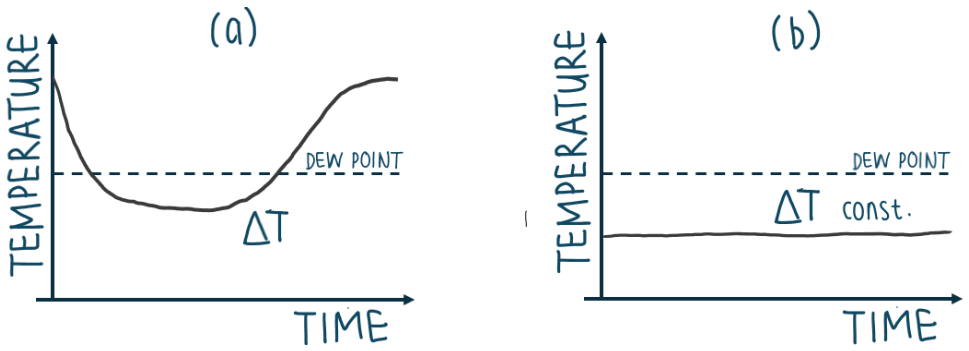

Figure 3.1. Polymer film temperature profile during the experimental working time for (a) the classical and (b) the temporally arrested BF approaches.

Challenge 2 - Pattern growth

Variation of the pattern size is classically attained through environmental control of temperature/humidity and the variation of the input parameters (*e.g.* polymer/solvent ratio).[106] This essentially modulates the condensation working time (droplet growth) through the amount of solvent removal. By altering the input conditions, the feature sizes can be somewhat modulated, however, this has combined effects on the pore morphology and sinking depth due to the variation of interfacial tension and viscosity with time. This undefined, non-linear variation of conditions is incompatible with control and prediction of the resultant pattern size (Fig. 3.2). Actively controlling the level of supersaturation through the substrate temperature facilitates direct translation of the environmental conditions and condensation physics to the resultant pattern, allowing prediction of the pattern growth rate.

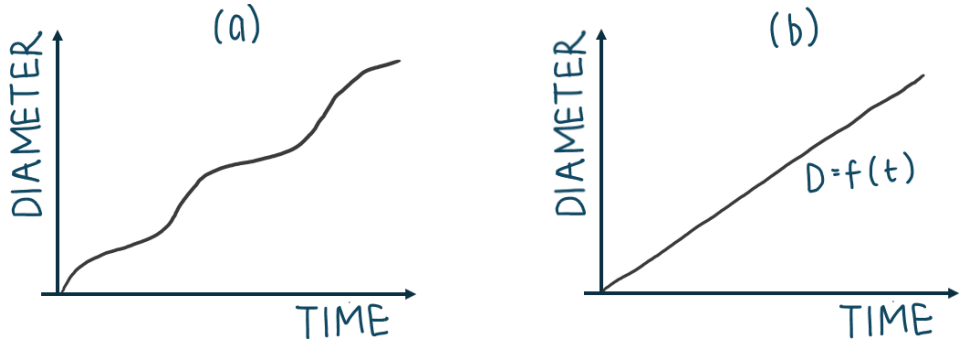

Figure 3.2. Average diameter of droplets forming the pattern. (a) non-linear growth vs (b) controlled growth in the adapted approach.

Challenge 3 - Film solidification

Only after complete solvent evaporation in the classical approach does one attain knowledge of the pattern feature sizes. This translates to an empirically-derived workflow that for every parameter / variable combination, a single final pattern is achieved. Much of the BF literature regards studies of this variation, with successful (monodisperse) or unsuccessful (semi-coalesced or incomplete coverage) patterning conclusions for variable conditions. By substituting the passive evaporation-driven polymer cooling and solidification with both UV-curable polymers and external cooling, we eliminate the coupling and enable *in situ* interrogation and modulation of the BF patterns through access to discrete intermediate designs within a single dynamic process. Instead of a predefined viscosity increase profile that is a function of the solvent volume, photopolymers enable on-demand quasi-instantaneous solidification (Fig. 3.3). As a result, the pattern evolution can be directly and systematically influenced in the temporal domain, facilitating better control and application of the condensation physics.

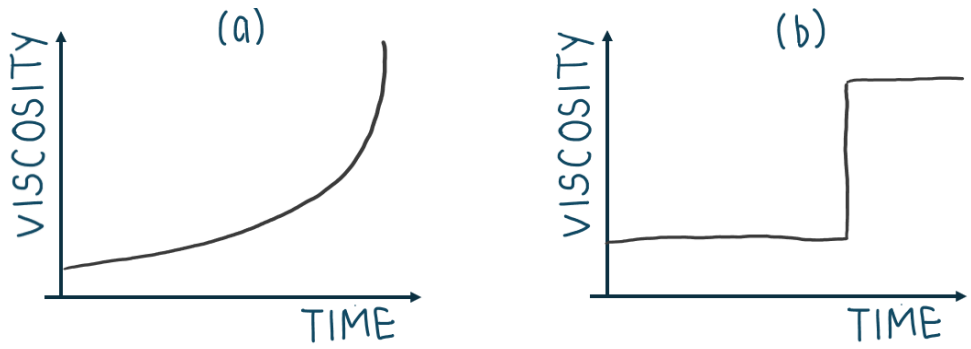

Figure 3.3. (a) Non-linear increase in viscosity until solidification vs (b) quasi-instantaneous solidification through photocurable polymers.

The adapted BF approach can be schematically summarised as per Fig. 3.4. (i) A thin polymer film is created by spincoating on a glass cover slip. (ii) After measuring the environmental conditions and implementing the required subcooling level on the Peltier device, the polymer film is placed on top and the subsequent pattern evolution is monitored with real-time image analysis. (iii) Once the desired pattern characteristics have been reached, the whole Peltier device is placed under the UV light source and cured for the designated curing time. (iv) The droplets evaporate after the film is cured and the sample returns to ambient conditions (v) where the pattern can either be used as is or further replicated. The following sections describe the technical methods used with this approach.

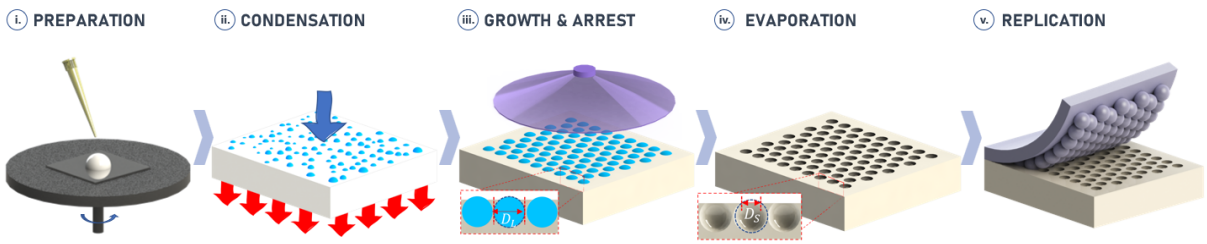

Figure 3.4. Schematic showing the main steps in the presented temporally arrested breath figure methodology.

3.2 Materials and characterisation

3.2.1 Materials

Substrate. Stainless steel, silicon wafer, borosilicate glass and polymer substrates were all used as substrates at different points throughout this study. The main pattern evolution characterisation, however, was carried out on standard glass cover slips of 24 mm × 24 mm with thickness of 0.15 ± 0.02 mm. These were cleaned prior to use by washing with isopropanol (IPA) and deionised (DI) water before being dried in the oven overnight at 80 °C. The cover slips were chosen due to their low-cost availability and optical transparency, enabling both transmission and reflected light optical microscopy analysis. The relative thinness facilitated effective heat transfer from the external cooling device below whilst providing a rigid support to maintain a flat, thin polymer film that is easy to cross-sectional fracture for further analysis. For a typical cooling cycle as shown in Fig. 3.5, the measured temperature responds quickly to programmed variation with a small difference between the absolute set temperature on the Peltier (red line) and substrate temperature (grey line) up to a maximum of ±2.5°C at extreme experimental parameters (*e.g.* largest set subcooling available in the warmest ambient conditions).

Polymer. Norland Optical Adhesive (NOA, Norland Products Inc.) polymers were purchased and used as received throughout this body of work. These single-component polymer resins are commercially available and widely used across industry and academia.[190] NOA60, -61, -63, -65, -68 and -81 products were trialled, comprising optically transparent and colourless pre-cursers in a range of different viscosities that cure when exposed to UV light. Their cross-linked, cured form exhibits varied mechanical properties with strong adhesion across different substrates from glass to metals.

The NOA polymers used consist of urethane-related base materials that are cross-linked upon UV exposure through radical-mediated thiol-ene chemsitry. Whilst the complete polymer composition is proprietary commercially sensitive information, the safety data sheet[191] references mercaptan (thiol or sulfur-containing analogue of alcohol, e.g. -SH) dopants alongside a monomer/oligomer mixture and photoinitiator. The photoinitiator enables the polymer precurser to absorb the UV light and create a reactive species to initi-

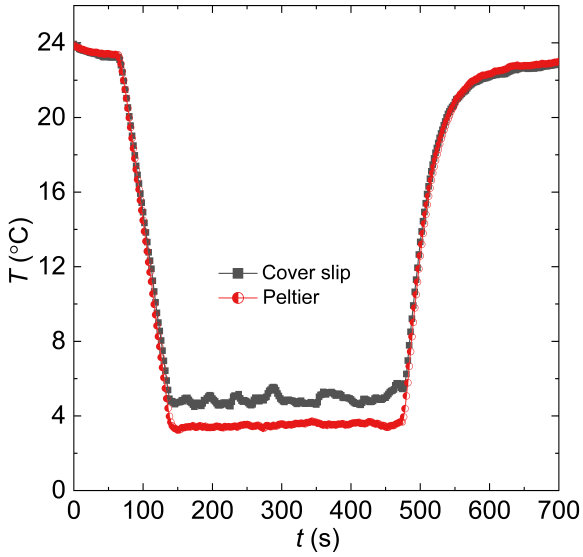

Figure 3.5. Temperature measurements of the Peltier device and mounted cover slip over a typical cooling cycle.

ate and propagate the polymerisation. Created photoiniator radicals abstract a hydrogen from the thiol, producing thiyl radicals which propagate and react with the C=C double bonds of the alkene (Fig. 3.6). This photo-induced crosslinking mechanism exhibits rapid curing in ambient conditions with low material shrinkage resulting in little change to surface features from pre to post cure. Further, the polymers exhibit high resistance to solvent, oxidative and UV degradation, making them excellent candidates for thin-film functional coatings.[190,192]

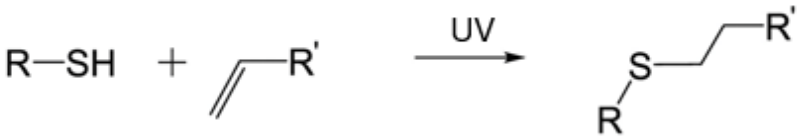

Figure 3.6. The click chemistry of a thiol–ene reaction. Adapted from Sticker *et al.*[190].

3.2.2 Polymer characterisation

Density. The density of the fluids was necessary for characterisation and further use within experiments such as interfacial and surface tension investigations. Due to the viscosity of some of the samples being as large as 5000 Pa.s, conventional techniques such as reverse pipetting with slow aspiration speeds could not be realised. Instead, a weighing strategy using a relatively large 1 mL (± 0.005 mL) disposable syringe was used with 0.5 mL of sample taken for each polymer. Ten measurements were completed on the digital mass balance (± 0.00005 g) by decreasing the volume by 0.05 mL after each reading. The results were repeated three times for each material at ambient lab conditions (22 ± 1

°C) and the average mass for each volume was plotted on a graph to attain the density by quantifying the gradient of the linear regression to the mass - volume data (Fig. 3.7). De-ionised water was also measured as a benchmark validity check.

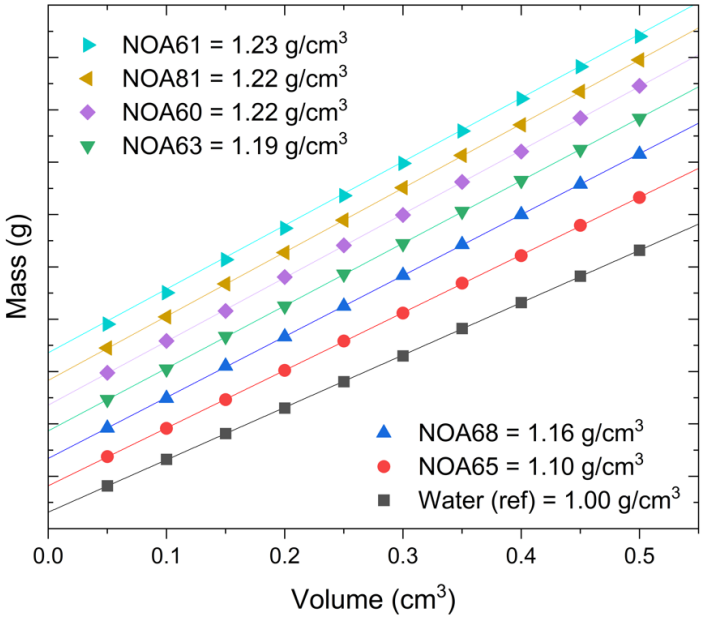

Figure 3.7. Density measurements of the NOA polymers used in this study and a de-ionised water reference. Data points are vertically offset for gradient comparison, with the major y-axis ticks representing 0.1 g increments.

Interfacial tensions. The shape and stability of droplets in the BF method is largely governed by the interfacial phenomena and resulting interactions between the polymer film, water droplets and air. Surface tension (SFT) of the NOA samples in air and interfacial tension (IFT) between the NOA and de-ionised water were thus measured using an optical tensiometer (Theta Attension, Biolin Scientific).

Pendant drop tensiometry apparatus was used in which a high-contrast image was taken of a droplet suspended from a dispensing syringe needle.[193] Pendant drop analysis was chosen in this experiment due to the simplicity of the experimental set-up and small sample volume required relative to other methods.[194] The interfacial tension between the droplet and the bulk fluid it is suspended in (where $\rho_{\text{droplet}} > \rho_{\text{bulk}}$) is then ascertained through geometrical analysis and the fitting of the Young-Laplace equation in the software. High-contrast imaging of the droplet with a backlight is hence important for accurate thresholding. The experiment was further optimised by maximising the Worthington number, Wo, a nondimensional number that scales the volume of the drop with the maximum volume that can be suspended.[195] Drops of volumes of 5 - 20 µL depending on the sample were created with a 22 gauge dispensing tip, with analysis taken just prior to detachment of the droplet from the tip to maximise the observable Wo. Five repeats were taken for each polymer measured, with a mean and standard deviation extracted

from the average data set. Interfacial tension (IFT) experiments in de-ionised water were completed with respect to time to monitor the variation and equilibrium values due to the dynamic trend in some of the polymers (Fig. 3.8). A 300 s average value was taken as the IFT data point, concluding this to be characteristic of a typical experimental run time. 3 hour tests were also run to find an equilibrium value on NOA61 and NOA81, however difficulties arose from the unstable disposable syringes used. The standard deviation provided refers to the variation across the repeats for comparison with the other data sets here, and thus does not account for the dynamic time values particularly for NOA61 and NOA81 (Fig. 3.8). A summary of the polymer data can be viewed in Table 3.1, where viscosity and curing energy values are taken from the polymer data sheets.[191]

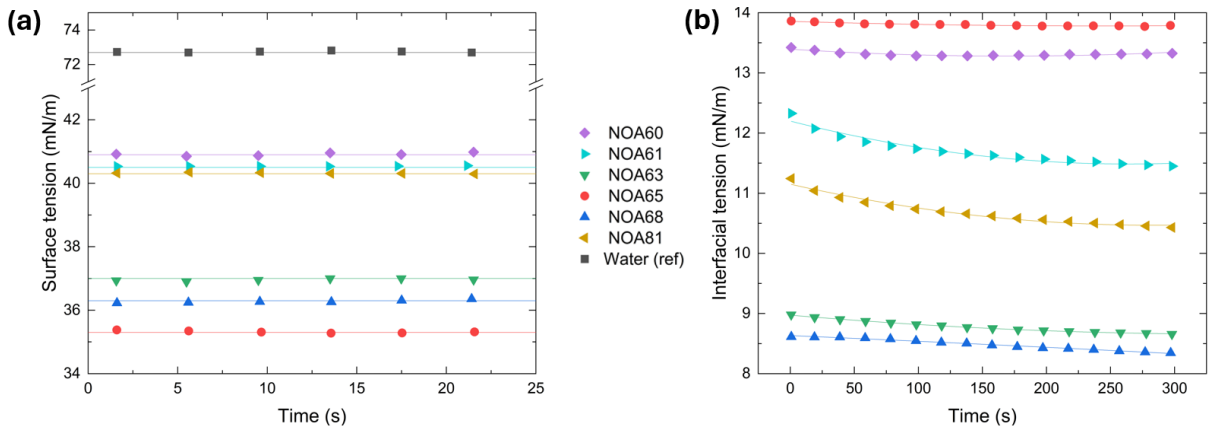

Figure 3.8. (a) Surface tension and (b) interfacial tension with water measurements for the NOA polymers used within this study.

The SFT results have good droplet pendant shapes and appear in good agreement with the limited published data.[191] However, the IFT in water validity is much more dependent on other factors, such as Bond number, due to the relative density differences between the two phases.[194] A small Bond number is a physical limitation in Pendant drop tensiometry, where interfacial forces dominate over gravitational forces, resulting in only small deformations from sphericity.[194] Small perturbations in droplet shapes reflect in large changes to the measured IFT, limiting the accuracy of the experiment. This is most evident in NOA65, where the relative density difference of 10% from water manifests in droplet volumes larger than double that of the other polymers with highly spherical droplet shapes.

Real force SFT measurements were also taken for NOA61 and NOA65 using a Kruss K100C and Wilhemy plate set-up. Contrary to optical tensiometry, this machine provides direct force detection measurements at the polymer-air interface for the surface tension of the polymer. An average of three repeats were made per polymer, with data showing the SFT to be within 2% of the optically measured values, validating the pendant drop approach. Due to this being an external service, no further samples were measured in this regard.

Table 3.1. Table of key parameters for the different polymers used in this study. Lab measurements are taken at ambient laboratory conditions varying from 20 °C - 25 °C.

Material	Viscosity‡ (mPa.s)	Density† (g/cm^2)	SFT (mN/m)	IFT (300s avg) (mN/m)	Curing energy‡ (J/cm^2)
NOA60	300	1.22	40.9 ± 0.3	13.3 ± 0.0	3
NOA61	300	1.23	40.5 ± 0.1	11.7 ± 0.2	3
NOA63	2000	1.19	37.0 ± 0.1	8.8 ± 0.1	4.5
NOA65	1200	1.10	35.3 ± 0.2	13.8 ± 0.5	4.5
NOA68	5000	1.16	36.3 ± 0.1	8.5 ± 0.1	4.5
NOA81	300	1.22	40.3 ± 0.3	10.7 ± 0.2	3

†Error in density regression calculation is insignificant relative to the significant figures provided.
‡Viscosity and curing energy values are taken from the respective polymer specification sheets.[191]

3.3 Patterned film generation

3.3.1 Spincoating

A thin film of polymer was used as the BF surface. A thickness of approximately 30 µm was chosen due to the relative thinness for effective heat transfer through the film whilst maintaining a larger depth than the condensation droplets considered here $\mathcal{O}(0.1-10\ \mu m)$ to assume negligible interaction between the droplets and the substrate. Constant NOA film thickness was controlled through modulation of the spin coating parameters.

The spin coating model developed by Emslie *et al.* demonstrates how the spin coated film thickness scales with $d_{polymer} \approx (\mu/t\omega^2)^{1/2}$, where μ is the polymer viscosity, t is the spincoating time and ω is the angular velocity.[196] Initial tests varied the spincoating time at constant speed, with polymers of viscosity 300 mPa.s spin coated at 1000 rpm and the polymers with viscosities from 1200 mP.s to 5000 mP.s spin coated at 2000 rpm. Polymers were spincoated on cover slips and cured for 5 s before being fractured to measure the film thickness. The spin coating times were selected from the graph to attain a $d_{polymer} \approx 30$ µm thickness, with trends showing good agreement with the model (Fig. 3.9).

3.3.2 Environment and set-up

A schematic of the full experimental set-up can be viewed in Fig. 3.10. The polymer-coated cover slip is placed atop the Peltier device, situated under either the optical microscope or UV flood curing system. The Peltier was stabilised at the desired subcooling temperature, ΔT, before placing the coated glass cover slip at time zero. Images were captured during the pattern progression at specific imaging frequencies and the film was cured with a short exposure to UV at t_c. In this set-up the image observation and curing mechanisms are differentiated processes, represented by the hashed line in Fig. 3.10. The pattern can be analysed in real-time, before placing the full Peltier stage under the adjacent curing

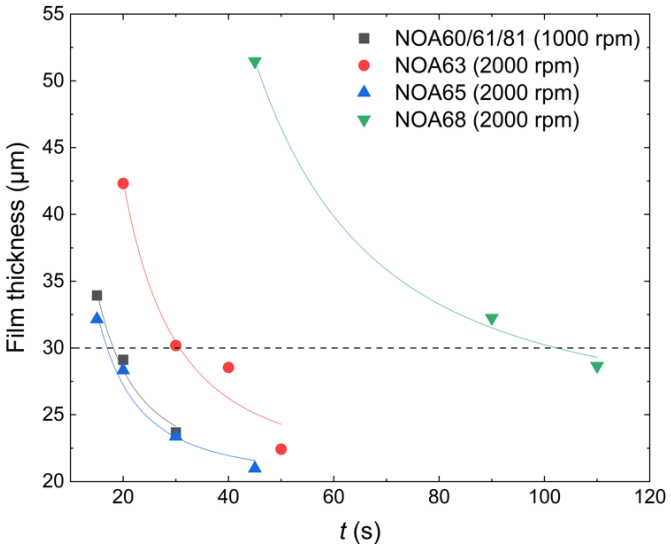

Figure 3.9. Polymer film thickness vs spin coating duration. Low viscosity (300 mPa.s) polymers were grouped together and spun at a lower rotational velocity.

system to create the final patterned sample.

As the simplest and easiest way to control the supersaturation, experiments were completed on a cooling/heating Peltier module (Linkham PE120) in ambient laboratory conditions. The temperature (T_0), relative humidity (RH) and saturation dew point were recorded using a hygrometer at the start of the experiment and monitored throughout the experimental progression. The corresponding saturation temperature (dew point) was calculated with the August-Roche-Magnus formula.[197] The level of supersaturation inferred from the subcooling, ΔT, was set on the Peltier stage at the start of each experiment. Based upon the corresponding measured parameters, the subcooling temperature range used varied between 0 - 15 °C. The set temperature was kept constant during each experimental test lasting hundreds of seconds, with fluctuations in conditions keeping the subcooling temperature on the Peltier accurate to within ± 0.5 °C. Fig. 3.5 shows the relative close tracking between the temperature of the Peltier device and the cover slip surface temperature using two thermocouples placed on the respective surfaces. There was consistent negligible temperature lag observed in response to the increase/decrease in Peltier temperature, with the relative difference being a function of the ambient conditions at the time of the experiment. As a result, the set Peltier temperature (T_P) and difference from the system dew point (T_DP) is referred to as the induced level of subcooling (ΔT) for experimental simplicity.

3.3.3 Polymer curing

The photosensitive polymers are mediated by thiol-ene based crosslinking through a free-radical induced 'click' chemistry pathway (Fig. 3.6).[198] This photopolymerisation mech-

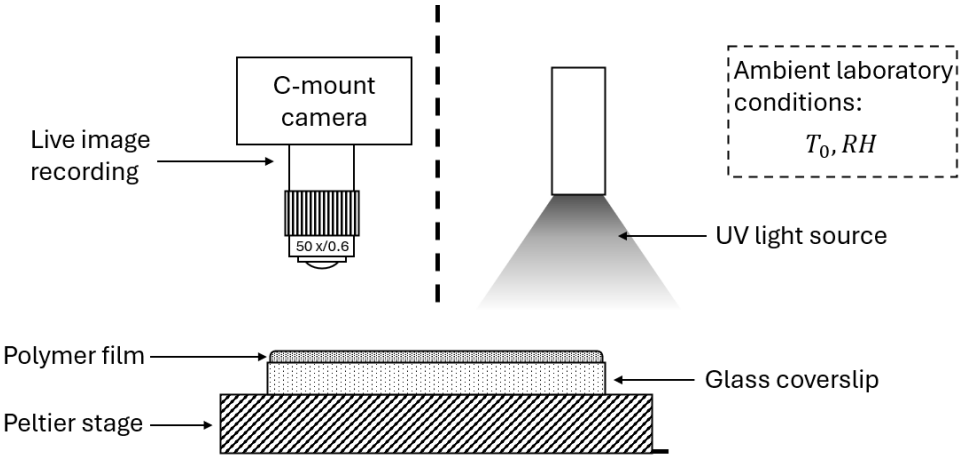

Figure 3.10. Schematic showing the experimental apparatus used. The hashed line represents the discrete live observation and curing mechanisms used.

anism offers benefits from traditional free-radial polymerisation including rapid curing speeds in ambient temperatures and atmospheric conditions regardless of material mass. Oxygen and water from the environment can typically retard and quench radical-mediated reactions, proving futile for BF fabrication. The NOA polymers, however, exhibit fast curing speeds in ambient conditions, with high conversion and crosslink densities, low shrinkage, and strong resistance to chemical, oxidative and UV degradation.

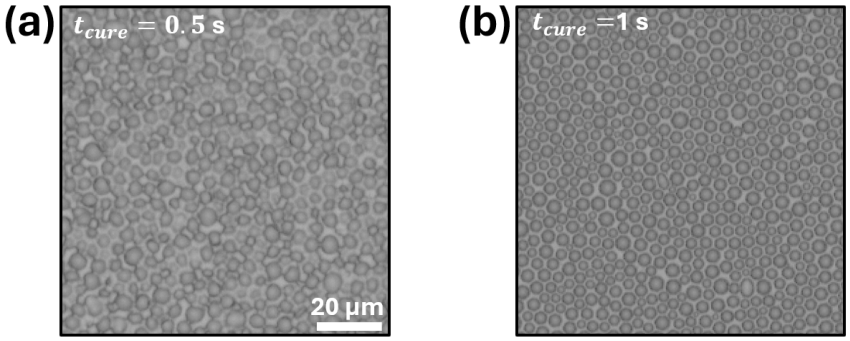

Figure 3.11. Pattern cured for (a) 0.5 s and (b) 1 s. If droplets are not fully stabilised, partial coalescence of the pattern occurs.

In this system, a UV flood curing device (Dymax Bluewave AX-550 Redicure) is used at a 25 mm working distance. The 650 mW/cm^2 system operating at 100% can thus provide the 3 J/cm^2 to 4.5 J/cm^2 dose required to fully cure the respective NOAs in 4 - 7 seconds. Preliminary tests concluded that the thin polymer films ($\approx$ 30 µm) could yield stabilised droplets after as little as 1 s curing at 650 mW/cm^2, sufficiently preserving the liquid-observed pattern to the cured film (Fig. 3.11). For the majority of characterisation, an irradiation time of 5 s was selected to ensure the film was cured whilst being insignificant compared to the condensation / experimental working time. Upon warming of the cured film to ambient conditions to allow for evaporation of the templated droplets, a further UV irradiation dose was completed to ensure the pore cavities were fully cross-linked.

The fabricated samples were then baked at 150 °C for 1 hour to remove any residual and unreacted functional groups at the interface.

3.3.4 Pattern replication

Many functional surfaces found in nature are composed of varied morphologies of self-assembled circular footprints. The ability to create both porous and protruding patterns is thus part of having a versatile fabrication method. Soft lithography replication of classical BF patterns often involves solvation of the BF film due to the brittle characteristics and the polymers often used.[199] As a result, each pattern can be templated once, and a further step is required to dissolve the pattern.

In this adapted approach, the highly cross-linked polymer has strong bulk properties and a high resistance to solvent degradation. The BF patterns created can thus be moulded and re-moulded continuously in an elastomeric medium such as silicone. Sylgard 184 (Dow Corning), a widely used low surface-energy and biocompatible polydimethylsiloxane (PDMS) derived polymer was selected as a suitable elastomer to enable the facile removal from the characteristic negative curvature within the cavities on the BF pattern. PDMS is a widely used silicone that has good transparency, chemical inertness and good bulk properties (*e.g.* mechanical flexibility) that make it one of the leading choices for rapid prototyping and soft lithography applications.[66] Base and hardener were mixed at a 10:1 ratio and degassed for 30 minutes. The liquid polymer was poured over the respective BF and further de-gassed to remove entrapped air from the cavities and ensure a high-fidelity replication. Slow peeling and separation of the PDMS / BF were done to ensure complete removal of the replica from the mould.

3.4 Pattern and morphology characterisation

3.4.1 Liquid film pattern analysis

Data surrounding the resultant pattern feature size was achieved through analysis of the water droplet growth on the liquid NOA. An Olympus BX53M optical microscope (OM) equipped with a long working distance objective (Olympus LMPLFLN 50x/0.50) and a digital CMOS camera (Basler ace acA2040-90uc) took images of the pattern progression at a rate of 1 Hz. The optical set-up provided an imaged area of 444 µm x 444 µm, corresponding to a nominal spatial resolution of 0.22 µm per pixel. Rayleigh's criterion can be used to establish the minimum resolvable distance between two points in the field of view, defined as $d = 0.61\lambda/NA$, where λ is the wavelength of light (commonly 400 - 700 nm) and NA is the numerical aperture.[200] For the aforementioned set-up, this corresponds to $d \approx 700$ nm. In reality, as the overall resolution is also affected by the image contrast,

this results in droplets of $D_L \approx 1$ µm being just about identifiable with round droplets of $D_L > 2$ µm in diameter being effectively measured.

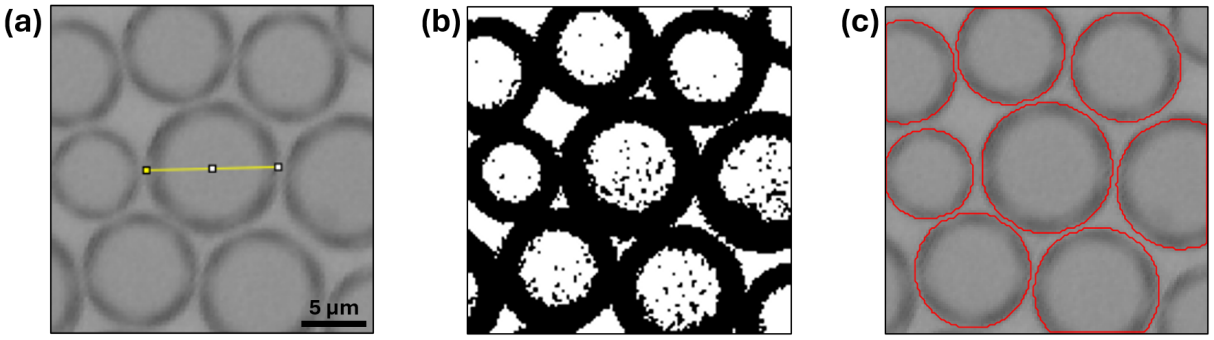

Figure 3.12. Analysis of a 10 µm diameter droplet. (a) Manual line measuring tool in ImageJ, (b) default threshold and (c) developed algorithm in Matlab using droplet perimeters.

Manual analysis of individual droplets on ImageJ[201] was not sufficient considering the polydispersity in diameters and the large number of images generated when analysing droplet growth rates (Fig. 3.12a). While this was useful for quick random analysis of droplets within a film due to accurate selection of boundary, significant time would have to be spent measuring a statistically representable sample size in each frame of a time series, taking too long and further introducing human error. Binary thresholding, where a threshold for pixel intensity value is chosen and the pixels greater/less than this value are coloured black or white was also largely ineffective at attaining the droplet data across the field of view (Fig. 3.12b). Due to the high transparency and relatively low refractive indices of the polymers (n = 1.56), the transmission of light through the centre of large droplets was relatively unobstructed, resulting in little greyscale variation between the droplet centres and free surface. Even with subsequent manipulation of the images, automated analysis of droplets could not be attained because of the inability to segment individual droplets within the pattern as well as the need for continuous variation in the thresholding parameters.

As the droplet perimeters exhibited the highest contrast in the images, these were used to identify and count droplets on the film using a circlular Hough Transform identification algorithm (Fig. 3.12c).[202] Fig. 3.13 shows the thresholding protocol developed in Matlab (Image Processing Toolbox, Matlab R2023b, Mathworks) to automatically analyse droplets across the film:

(a) The central region of interest is cropped to negate any uneven lighting and focus effects. This dynamic crop size varies depending on the size of droplets.

(b) An initial range of droplet radii is input into the algorithm. The image is scanned for circles within the specified range.

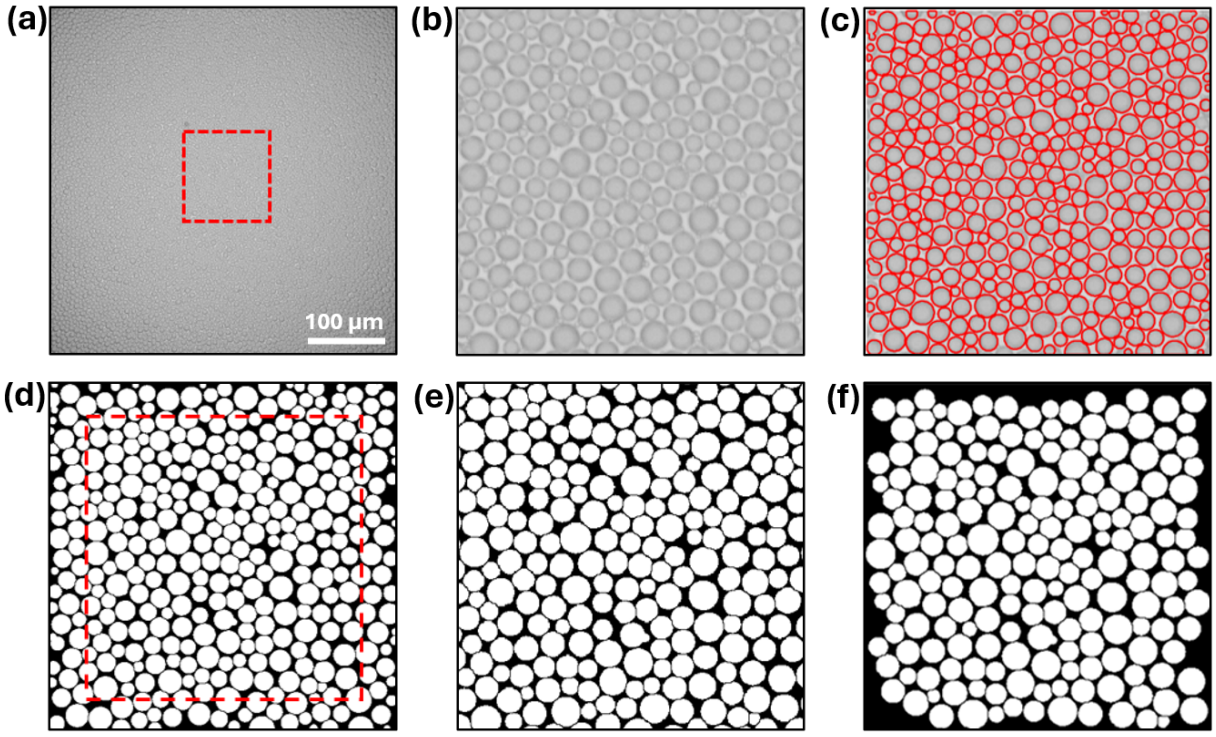

Figure 3.13. Droplet identification method in Matlab showing the transition from the greyscale raw image to binary mask.

(c) An image is produced highlighting the identified circles. Partially occluded droplets at the edge of the region of interest often get misidentified.

(d) The image is transformed into a binary mask representation (droplets coloured white) and binary operations such as watershedding of circles are completed to enhance the image. This ensures that all identified droplets have discrete, non-overlapping boundaries when measuring the key parameters.

(e) The outer region is cropped to eliminate the non or falsely identified edge circles. Area coverage data is taken from this binary representation containing a full frame of identified droplets.

(f) Any partially occluded droplets at the new boundary are excluded for analysis of the rest of the parameters.

For analysis on the liquid film, the droplet diameters, D_{L}, are identified (Fig. 3.13c). As highlighted in Fig. 3.14 only the projected droplet perimeters are completely visible and readily identifiable due to the film transparency. With the droplets stabilised at the air-polymer interface, the bulk of the droplet resides below the surface which enables the identification at this largest diameter. Other parameters such as area fraction, number density and polydispersity of the droplets were calculated based upon this data with the relationships $A_f = \frac{\sum_{i=1}^{N} DropletArea}{FrameArea}$, $N_d = \frac{n}{A}$ and $g = \frac{<|D-D_{\mathrm{L}}|>}{D_{\mathrm{L}}}$ respectively. n is the number of droplets identified in the analysis, and g is the polydispersity measure. Unless

otherwise specified, the image analysis frame and cropped region (Fig. 3.13b) was set to capture 100's droplets for statistically relevant data, however, the exact size was non-critical due to the low polydispersity ($g \approx 15\%$) across the observation window. For both manual and programmatic detection methods, while the diameter measurement for one droplet is within ±5% difference of each other (Fig. 3.12a compared to Fig. 3.12c), the automated process attains the average metrics for all droplets the image. Despite the fairly low polydisperstiy of droplets within each frame, the manual method is both time consuming, and compounds to a ±15% difference from the programmatic method when analysing 5 random droplets versus the whole frame.

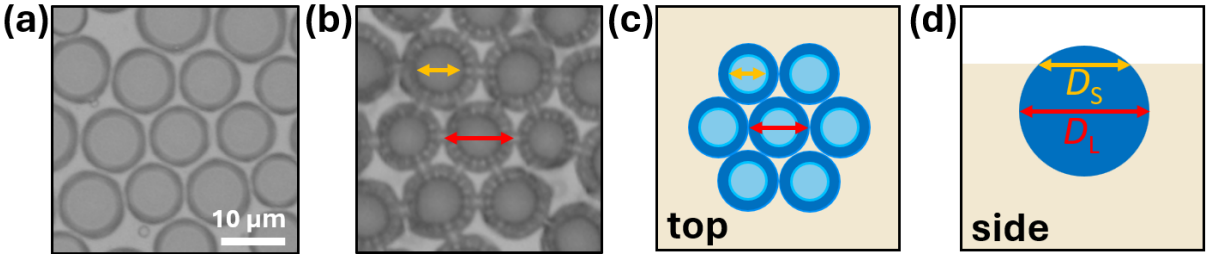

Figure 3.14. Diametric analysis of droplet patterns on the liquid films. Images showing the observable liquid droplet diameter, D_L in (a) liquid and (b) cured films. Schematic (c) top and (d) side view representations.

The average spacing between droplets (interdroplet spacing, L_c) was calculated by taking the average Euclidean distance between neighbouring droplets across the region of interest. After identifying the central coordinates for each droplet as per the droplet identification protocol, a Voronoi tessellation function was used to establish borders between neighbouring droplets.[150] A Voronoi diagram uses a dataset of discrete points (droplet centre coordinates) and divides the plane into a tessellation of space-filling but non-overlapping convex polyhedrons.[203] The polyhedron edges, or boundaries between central points, correspond to the bisecting plane that divides that point to the nearest neighbouring point, for all points in the dataset. In that regard, the interdroplet spacing is calculated by taking the linear distance between a singular central point and its neighbours (Fig. 3.15c). For all points in the dataset, this average distance was calculated for all points with a shared vertex with one another. In simple terms, for a perfectly hexagonally packed distribution of droplets (Fig. 3.15a), $L_c \rightarrow D_L$.

A measure of the droplet packing distribution was also completed using the Voronoi diagram. The Voronoi entropy, was calculated with the equation,

$$S_{vor} = -\sum P_z \ln P_z \, . \tag{3.1}$$

This conformational entropy uses the probability of a polyhedron with a specific coordination number P_z. For a perfectly ordered BF sample where all polyhedrons have a

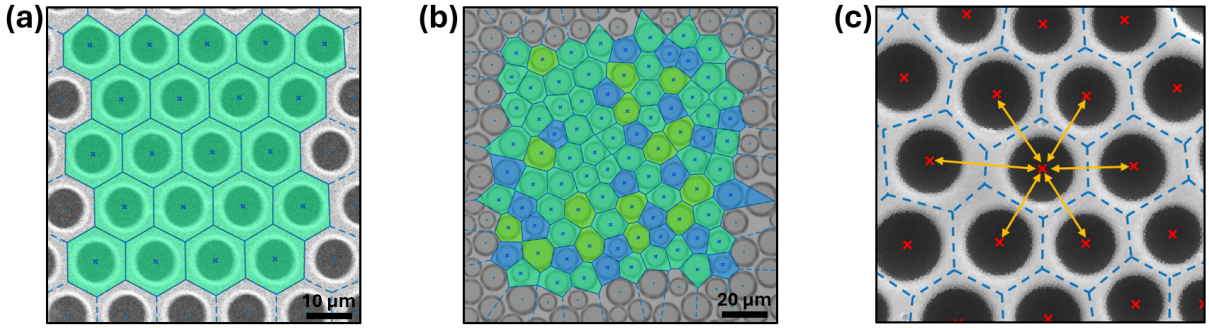

Figure 3.15. Voronoi tessellations overlaid on different sample images. (a) Voronoi entropy analysis on classical and (b) temporal BF. (c) Analysis method for average interdroplet spacing, L_c.

coordination number of 6, the entropy is equal to 0. The max entropy in this case for a random 2D distribution of points, $S = 1.71$.[154] Further, as this is an extensive property, contrary to thermodynamic entropy, the value does not depend on the number of points used.[150]

3.4.2 Cured film pattern analysis

In most of the cured pattern analyses, scanning electron microscopy (SEM) and laser scanning confocal microscopy (LSCM) were used, resulting in only the opening pore diameter being visible. In the pre-cured liquid films, image processing quantified the maximum overall diameter of the droplet D_L, due to the optical transparency and relative refractive indexes of water and NOA (Fig. 3.14). Compared to optical microscopy, the same film transparency is not observed with these techniques and so the visible diameter is the pore opening D_S, compared to the maximum submerged diameter D_L. Similar feature quantities and size distributions to the liquid analysis were extracted from the cured patterned films using the same algorithm process. While the same pattern characteristics were measured for comparison from liquid to solid films, D_S was attained as the diametric measurement in the solid film from top-view SEM images, corresponding to the three-phase contact line perimeter (Fig. 3.16).

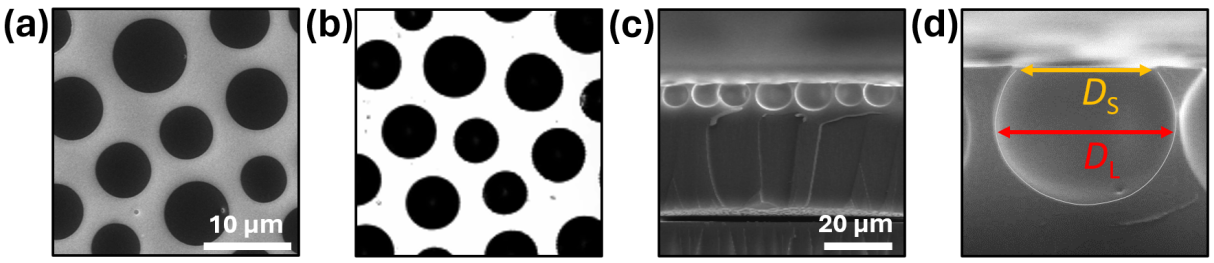

Figure 3.16. Diametric analysis of droplet patterns on cured films. Top view images taken with (a) SEM and (b) LSCM. (c, d) Cross-sectioned views of the patterned film, highlighting the physical form of the different measurements viewed in Fig. 3.14

Patterns with smaller than optically resolvable features ($D_L < 2$ µm) were imaged using SEM. Hitachi SU8230 and Zeiss EVO MA15 SEMs were used with carbon and irridium coated samples at accelerating voltages at 2 kV and 20 kV, respectively. Side profile droplet morphology analysis was also completed on cross-sectioned samples. Films of interest were fractured by hand after scoring the glass cover slip with a diamond tip and mounting the shards to 90° chamfered SEM stubs.

Laser scanning confocal microscopy (LSCM) performed on a Zeiss LSM800 was also used as an imaging technique for analysing feature sizes between that of SEM and optical microscopy (see example image in Fig. 3.16). The LSCM has a mechanised stage for automated image stitching and the 405 nm laser line provides a nominal resolution of around 30 nm/pixel, enabling high-resolution images of relatively large sample areas. LSCM increases the resolution attained from conventional OM through the use of a coherent laser light source and spatial pinhole, blocking out-of-focus light from a narrow and defined focal plane. Unlike OM where samples are totally illuminated in bright field, LSCM uses a scanning laser to raster and illuminate samples point by point. The low wavelength laser combined with a pinhole aperture and illumination mechanism eliminates out-of-focus light, and effectively increases image contrast.[204] This allows both high-resolution images of samples to be taken as well as 3D reconstructions by creating a z-stack of images at incrementally varied depths.

3.4.3 Error and uncertainty in image analysis

In the liquid-liquid growth analysis, uncertainty at early time frames results from the optical microscopy spatial resolution; due to the diffraction limit, the resolution of an optical microscope is typically that of half the wavelength of the illumination light source.[205] Using the aforementioned optical microscope and camera set-up, this results in a pixel size that is approximately 0.22 µm. However, the ability to accurately detect and identify circular shapes is unreliable due to the many square pixels needed to produce a circular shape. A 5 pixel diameter droplet ($D_L \approx 1$ µm) is therefore only just identifiable, with $D_L > 2$ µm often used as the limit in most analysis (Fig. 3.17).

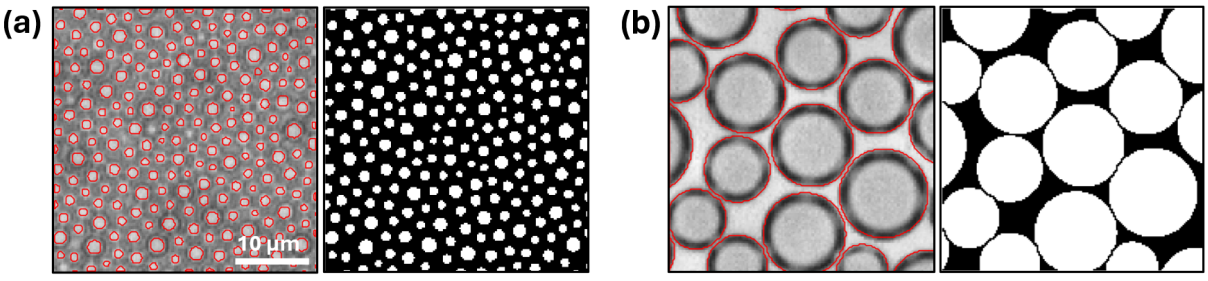

Figure 3.17. Error in image thresholding identification and binary representation. Length scale difference for droplets of (a) 2 µm compared to (b) 10 µm.

At this smaller length scale, the inner bright region of the droplet perimeter is selected as the resolution is too small to view the free space between the droplets and locate the dark outer perimeter. Fig. 3.17 shows the identified droplets (red outlines) touching one another in (b) and attaining the full liquid droplet diameter, D_L, whereas only central portions of the droplets are found in (a). This is clear in the binary masks where despite a good general identification of the droplet central coordinates, there is a significantly smaller area coverage due to non-touching droplets. In this regime, an arbitrary number of pixels are added to the diameter matrix until the droplet boundaries are just touching to get a measure of other parameters (Fig. 3.18).

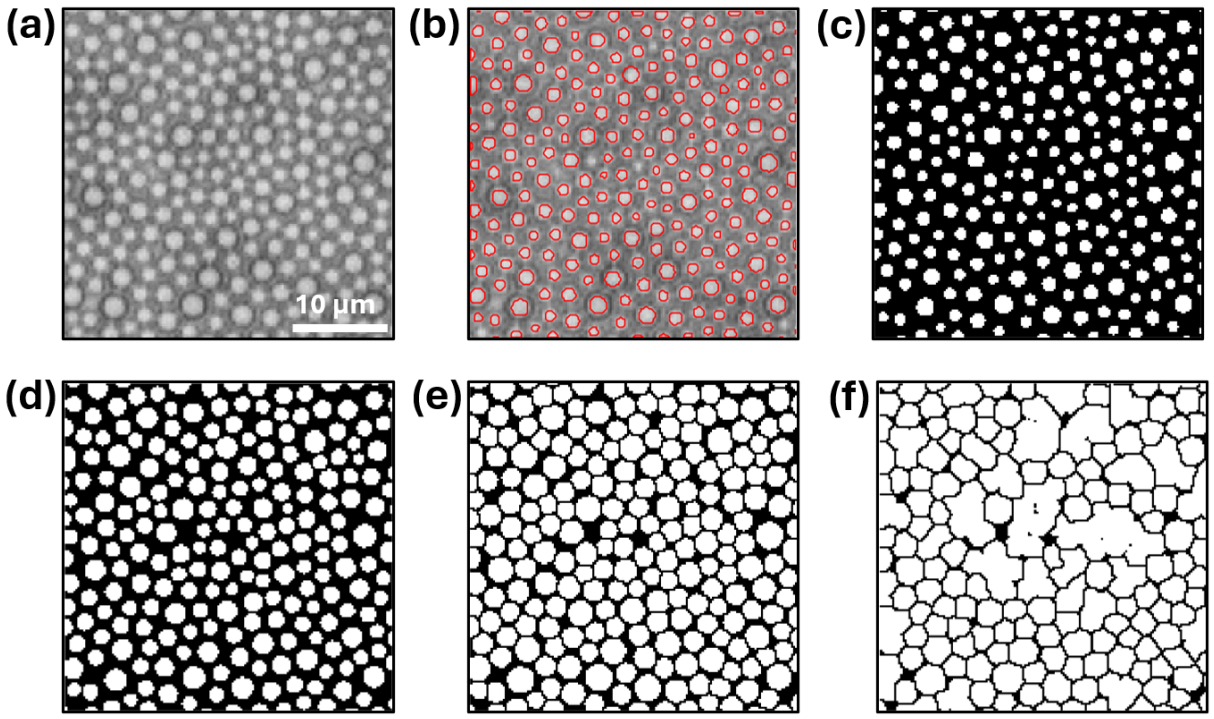

Figure 3.18. Image thresholding error at small length scales. (a) Raw cropped image, (b) identified droplet inner perimeters and (c) binary mask representation. Manipulated binary masks after (d) 1 pixel, (e) 2 pixels and (f) 3 pixels addition to the radii matrix.

Whilst it is clear that there is a high density of droplets in the raw image (Fig. 3.18a), attaining quantitative measurements relies on the addition of pixels to the identified diameters. The data needs to be manually checked, ensuring that the final mask has correctly thresholded discrete individual droplets at the maximum possible diameters. If too few pixels are added to the diameter matrix, the mask appears with an artificially low surface coverage of droplets (Fig. 3.18d). However, if too many pixels are added, the watershedding algorithm which ensures droplets have discrete boundaries starts to break down, forming large, nonphysical aggregations of identified droplets (Fig. 3.18f). As the droplet central coordinates are the only direct measurement made (*e.g.* without subsequent data manipulation through pixel addition), the visual representation of the final mask relative to the raw image can be used to infer the validity of the other inferred measurements.

In this case, the majority of droplet centres are well identified and the final mask (Fig. 3.18e) looks like a fair representative of the raw image. The interdroplet spacing is the only directly measured parameter - as long as the droplets do not appear aggregated (negating data from Fig. 3.18f), there is less than a 2% relative range in measured values, showing little variation across the measurements from each mask (Fig. 3.18c - e). Analysis of the inferred parameters on the chosen mask (Fig. 3.18e) then shows an area fraction in the expected high packing range and an average diameter measurement maintaining the same relationships to other parameters as derived in later Chapters. Despite the logical values, the mismatch of a small number of square pixels with circular object identification results in non-circular droplet thresholding and blank gaps from non-identified droplets. With poor initial droplet identification and limited success incrementally increasing the detected radii of the mask, the estimated error in this regime can be as large as 20%.

On larger 10 µm diameter droplet samples, a similar sensitivity analysis on the identified droplet boundaries shows a much smaller variation in parameters. Fig. 3.19a shows half an overlay of the general algorithm run an isolated droplet. The threshold readily attains a good measure of the droplet perimeter with the automatic grey scale gradient edge threshold used. When subtracting or adding 1 pixel to the radii matrix, the output results do not vary significantly, with the measured diameters varying less than ± 4% (Fig. 3.19b).

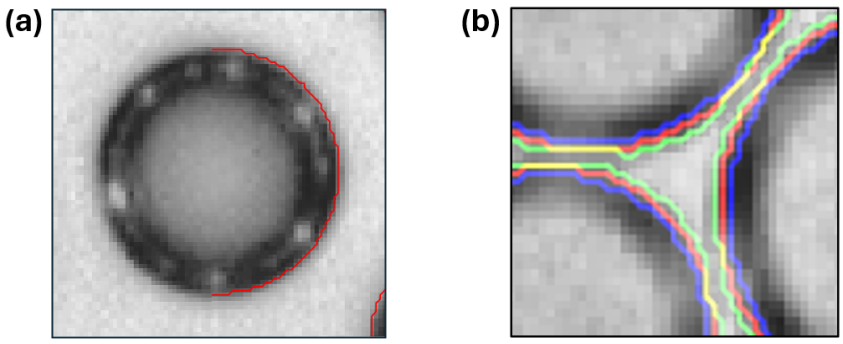

Figure 3.19. Overlays of droplet identification thresholding on larger droplets where $D_L \approx 10\mu m$. (a) isolated droplet with a half overlay and (b) perimeter sensitivity analysis of general (red), - 1 pixel (blue) and + 1 pixel (green) to the identified radii.

Errors can also arise from how the data is sampled. Using the 50x objective provides the greatest resolution to facilitate observation of the droplets, especially at the smaller length scales. However, the larger lens numerical aperture of this objective creates a shallower depth of field. Throughout the experimental run time, the focus has to be continuously updated to ensure high contrast and good edge definition of droplets. Random human error is introduced with the manual focus shift introducing a slight variation in image quality at times. To reduce the overall error, the growth of droplets is monitored to continuously adjust the focus, and later-time data with larger droplet sizes is used where

possible. Data taken to establish the growth rate trends in samples was captured and analysed at 1 s intervals over the course of the experimental run time (100's seconds). To negate effects from invariable focus and poor thresholding in specific frames, the analysed data was averaged every 5 - 10 frames, depending on the length of the experiment. Due to the range and polydispersity of droplets captured across this downsampled average, unless otherwise stated, the average plus or minus the polydipersity is plotted throughout as this quantity is more useful to the general analysis of data.

3.5 Summary

- The classical breath figure patterning approach provides little to no ability to readily modulate and control the patterning due to the interdependence of coupled solvent-evaporation cooling and curing dynamics.
- By readily controlling the set subcooling temperature and time of pattern arrest, systematically varied patterns can be fabricated using the proposed technique.
- The active control over the patterning environment requires monitoring and the setting of specific control parameters to influence the measured pattern characteristics. Real-time image analysis provides feedback and knowledge of the design. A summary of all the handles can be viewed in Table. 3.2.
- The following two chapters delineate the fundamentals of the pattern formation in the liquid state, comprising analysis of the droplet nucleation and growth regimes, and permutations of the technique to influence the final cured pattern. Challenges 1 and 2 of nucleation and growth are covered in Ch. 4. Challenge 3 is developed in Ch. 5 alongside the benefits to the complete method allowing specific pattern permutations that are not classically feasible.

Table 3.2. Parameters and preparation conditions.

Control parameters		Measured parameters	
Relative humidity (%)	RH	Liquid droplet diameter (µm)	D_{L}
Ambient temperature (°C)	T_0	Cured pore diameter (µm)	D_{S}
Dew point (°C)	T_{DP}	Area fraction (-)	A_{f}
Peltier temperature (°C)	T_{P}	Droplet number density (mm^{-2})	N_{d}
Subcool temperature [T_{DP} - T_{P}] (°C)	ΔT	Polydispersity (%)	g
Time of applied curing (s)	t_{c}	Interdroplet spacing (µm)	L_{c}
		Voronoi entropy (-)	S

Chapter 4

The physics of condensation: nucleation and growth

The physics of droplet nucleation and growth in the context of the aforementioned temporally arrested breath figure approach is described here. Prior to polymer curing, the liquid-liquid pattern growth of droplets primarily on NOA61 and NOA63 polymer films are analysed at the air-polymer interface. This chapter builds upon the content published in the journal paper 'Temporally arrested breath figure'[185].

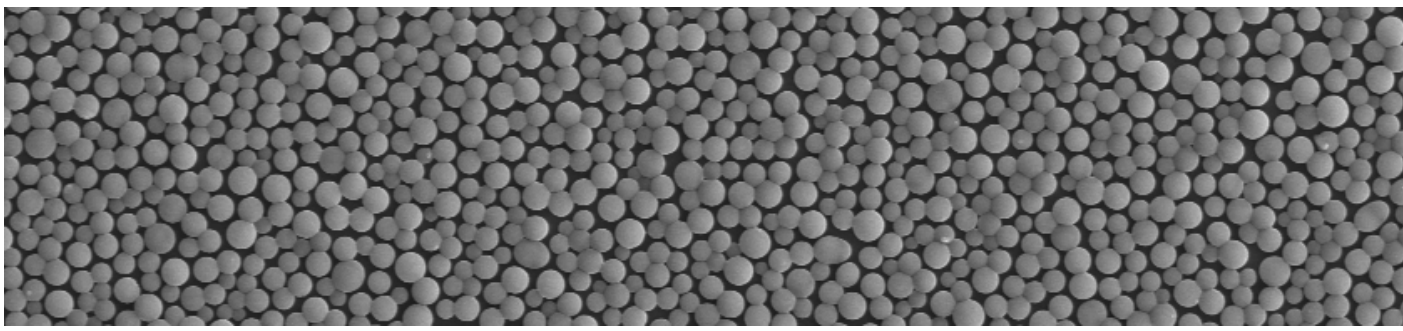

"Thermodynamics is a funny subject.The first time you go through it, you don't understand it at all. The second time you go through it, you think you understand it, except for one or two points. The third time you go through it, you know you don't understand it, but by that time you are so used to the subject, it doesn't bother you anymore."

Arnold Sommerfeld

4.1 Introduction

While mundane in everyday life, the process of condensation, where water vapour in the air (humidity) undergoes a phase transition to liquid water has stoked the curiosity of philosophers for centuries. More generally, the scientific study of phase transformation bears paramount importance across an expanse of scientific and industrial applications, where the physical mechanisms underpinning the processes are similar whether studying the formation of clouds or the deposition of metallic coatings.[80,206,207] The premise of breath figure patterning is contingent upon the initial nucleation, stabilisation and growth of droplets at the air-polymer interface. Understanding the nucleation and subsequent growth mechanisms is thus fundamental for controlling the ensuing pattern, determining the limits to the process and creating the optimal conditions for systematic patterning. Herein, the underlying theory of nucleation and growth of droplets is described alongside experiments to determine the underpinning physics of this system.

Nucleation is defined as the initial random formation of a distinct thermodynamic phase (nucleus) that can irreversibly grow within the body of a metastable parent phase.[93,208] The dominant classical nucleation theory (CNT) is based on Gibb's work on thermodynamic potentials[209] from the late 1800s and was first developed by Volmer and Weber in the early 20th century.[210] It applies continuum thermodynamics and the capillarity assumption to establish a free energy barrier for the formation of a stable nucleation radius. Beyond this critical size, the addition of extra molecules becomes energetically favourable as the free energy associated with the bulk contributions in the new stable phase outweighs the cost of the forming interface. Further, the addition of a surface catalyst of lower interfacial tension (heterogeneous nucleation) decreases the energy barrier to nucleation and increases the rate at which condensation occurs.[211]

Over the last century and a half, notable improvements to CNT by people such as Becker and Döring, Zeldovich, Turnbull and Fisher have led to slight adaptations in the theory, and numerous variations with countless acronyms.[208] For simple systems, CNT can provide good approximations and predictions for phase transitions such as the homogeneous nucleation of water droplets.[212,213] The theory provides a framework for qualitatively analysing the thermodynamic landscape, however, many of the adaptations and diverging theories have arisen from the significant nonphysical predictions of nuclei properties in specific cases.[207,214] While CNT can explain the dependence of steady-state rate on the driving free energy and quantitatively describe time-dependent nucleation behaviour, shortcomings in the theory stem from the significance of nanoscale effects. From the molecular perspective, treatment of small nuclei on the order of angstroms with the bulk, macroscopic properties of the material can be inappropriate.[208] At this length scale, the small number of molecules and sharp curvature can have significant effects on the structure

and interfacial energy, significantly diverging from and misrepresented by these equilibrium properties. Further, in heterogeneous nucleation, the characterisation of interaction energetics between the substrate and nucleating droplet has inherent limitations when described only by the contact angle (such as given by the later discussed general free energy equation), further ignoring the sometimes significant and diffuse interfacial regions at this length scale.[215] In extreme cases, the theory breaks down completely, *e.g.* the high surface tension of mercury vapour condensing predicts a critical nucleus of fewer than 10 atoms, under predicting the necessary supersaturation by a factor of 1000.[216]

The reality of the multiscale condensation process extending from a small assembly of molecules to the growth of droplets in macro dimensions means that specific assumptions and simplifications have to be taken for an application-based experimental approach. Predicting the exact onset and rate of nucleation is challenging given that these events occur at atomistic length scales and on time scales on the order of thermal fluctuations from the vibrational frequency of atoms.[207] With advances in both experimental methods and computational power, the development of new non-classical nucleation pathway theories with intermediate stages is becoming favourable. Density functional theories based on Kohn's electronic density structure and phenomenological diffuse interface models of interfacial regions commensurate with problem length scales are particularly notable.[217] Molecular dynamics simulations and atomistic modelling alongside new experimental tools to interrogate phase change behaviour have rapidly progressed the understanding of these events.[207] The use of environmental-SEM to directly visualise processes occurring in real-time and other light scattering tools to indirectly quantify the kinetics presents new opportunity for study.[218–220]

Despite its many criticisms, the CNT framework is still a conceptually simple and elegant evaluation of the coexisting thermodynamics of a system. From the theory, relative mechanisms can thus be inferred to understand the physics of the model from a more qualitative perspective. While there is specific interest in the nucleation of droplets within this work, this thesis mainly focuses on the characterisation of the growth and modulation of the pattern evolution. Within the context of BF patterning, the subsequent growth of the droplets through continual condensation after the initial nucleation events defines the key characteristics and evolution of the pattern, provided nucleation occurs. The droplet growth, through the continual addition of water molecules adsorbing at the interface can be considered with the dimensionality of the droplet.[152] When a droplet is within a supersaturated system, the kinetic theory of gas states that there is a net flux of molecules (condensation) impinging on the surface, outweighing the evaporative flux of molecules leaving the surface.[93] In the presence of non-condensable gas (*e.g.* air), the limiting factor is the diffusion gradient of water molecules surrounding the droplet, assuming the droplet temperature is homogeneous due to its small size and presence of convection.[189]

Single droplets, growing in isolation from one another, grow in a diffusion-limited regime based on the direct accretion of water monomers to the droplet surface. As the droplets grow closer together, interactions and coalescence between neighbouring droplets rapidly accelerate the average diameter in the breath figure (BF) pattern.

As the physics of condensation is studied in the context of the patterning approach, assuming nucleation events occur, the resultant pattern is revealed primarily from the droplet growth interactions. Nucleation theory and experimental observations are thus first discussed as a conduit to study the relative regimes in droplet growth and the resultant pattern evolution. The core focus of quantitative experimental analysis here regards how the environmental conditions can be tuned to create systematic BF patterns. Microscale *in situ* experimental analysis of condensation is performed on different polymer substrates, with the pattern growth explored in more detail with regard to the substrate and system conditions.

4.2 Physics of droplet nucleation

The onset of condensation, consisting of both the initial droplet nucleation and subsequent growth, is initiated through the temperature of the system/surface dropping to below a threshold value known as the dew point.[93] The vapour in the system is subject to a pressure, P, larger than or equal to the saturation pressure, P_e of the phase. Here, this metastable state is characterised by a thermodynamic driving force where the vapour molecules will eventually condense into a liquid phase of lower energy.

4.2.1 Homogeneous nucleation

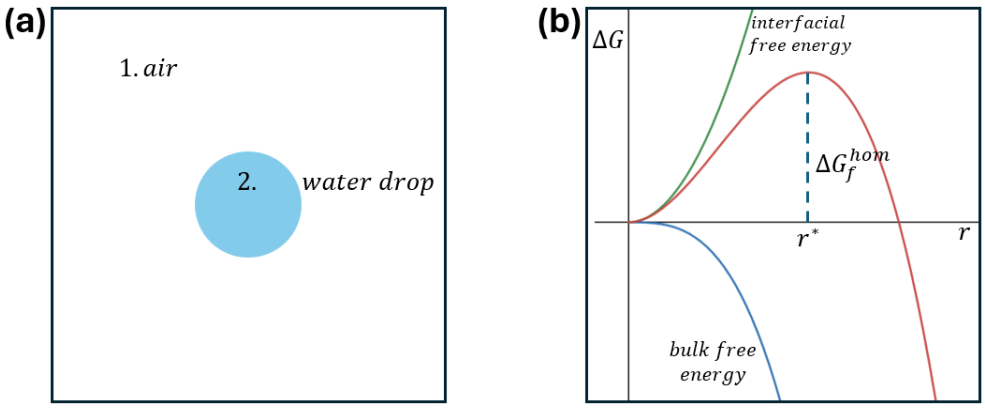

Figure 4.1. (a) Schematic representation of homogeneous nucleation of a water droplet in air, (b) and the relative associated energy terms.

CNT denotes that in the metastable region of supersaturation, transient local variations of water molecule density, termed heterophase fluctuations, become frequent; extreme

perturbations induce nanometre sized clusters of increased density above a threshold diameter producing stable liquid embryos.[93] Based on its capillarity approximation, the homogeneous CNT applies continuum thermodynamics to determine the energy barrier for its formation (ΔG_f^{hom}) and the critical nucleus size (r^*) by balancing the bulk volume and interfacial terms (Fig. 4.1). The energy balance for this transformation can be given as

$$\Delta G_f^{hom} = V_2 \Delta G_v + \gamma_{12} A_{12} = \frac{4}{3}\pi r^3 \Delta G_v + 4\pi r^2 \gamma_{12} \ , \tag{4.1}$$

where V and A are the volumes and surface area of respective phases, r is the radius of the nucleating sphere and γ_{12} is the interfacial tension between the nucleating and parent phases. $\Delta G_v = G_{liquid} - G_{vapour}$ represents the free energy change per unit volume for the formation of the liquid phase from the vapour phase it is forming in (change in internal energy per unit mole), where $\Delta G(T, P, N)$. Providing that the system is supersaturated, ΔG_v is negative, indicating the thermodynamic driving force for the phase change. The second term is the barrier to nucleation in the form of energy required to create a new interface. This is the free energy cost of creating the surface of the nucleus phase given in terms of relative interfacial costs. For a single-component system, this maximum in free energy arises from the summation of the surface and the bulk contributions. The energy cost associated with the nucleus interface formation is proportional to the radius squared, whereas the energy of the bulk decreases proportionally to the radius cubed. Hence, for a nucleus of larger r, the first term dominates leading to the decrease in ΔG_v since it represents the energy decrease upon transition from vapour to liquid (Fig. 4.1b). When r is small, the second term dominates, indicating unlikely nucleation due to the energy cost of the interface outweighing the driving force of the bulk.

The critical radius, r^*, which dictates if an embryo from a fluctuation is stable and grows ($r > r^*$), or unstable and decays ($r < r^*$) is hence given by,

$$\left.\frac{\partial \Delta G_f^{hom}}{\partial r}\right|_{r=r^*} = 0 \Rightarrow r^* = \frac{2\gamma_{12}}{|\Delta G_v|} \ , \tag{4.2}$$

r^* represents the boundary of decaying and growing embryos as shown in Fig. 4.1b. The critical radius can also be written in an adapted form of Kelvin's classical equation for homogeneous nucleation, $r^* = 2\gamma/(RT/v)\ln(P/P_e)$, where R is the universal gas constant for water vapour, T is the temperature, v the specific volume of a water molecule and P is the partial pressure of water in the system and at saturation (P_e). $\ln(P/P_e)$ is also commonly written as $\ln(S)$, where $S = P/P_e$ is the saturation ratio.[146]

The critical free energy of formation can be calculated by substituting Eq. 4.2 into Eq. 4.1.

$$\Delta G_f^* = \frac{16\pi\gamma_{12}^3}{3\Delta G_v^2} \,. \tag{4.3}$$

Considering the standard environmental conditions used throughout, and the nucleating phase being water in the BF process, one can calculate the estimated critical radius for the experimental set-up described in Ch. 3. As the ambient temperature and pressure of the laboratory are used (no closed system control), the temperature fluctuates between 19 - 23 °C, with a relative humidity between 30 - 60 %.[1] Using the August-Roche-Magnus approximation[197] to calculate to the dew point temperature, and considering the low saturation ratio from the small ΔT, the critical radius is estimated to be in the order of 10's of nm.[148]

4.2.2 Heterogeneous nucleation

Solid substrates

In reality, the free energy of formation for homogeneous nucleation is very large, with significant subcooling needed to initiate phase transformation. This has been observed as far back as Fahrenheit in the 18th century, whose observations on the onset of pure water freezing indicated a temperature lower than −40 °C was needed.[208] A surface of lower interfacial tension with the nucleated phase than between that of the two bulk phases can act as a catalyst for nucleation (Fig. 4.2b).

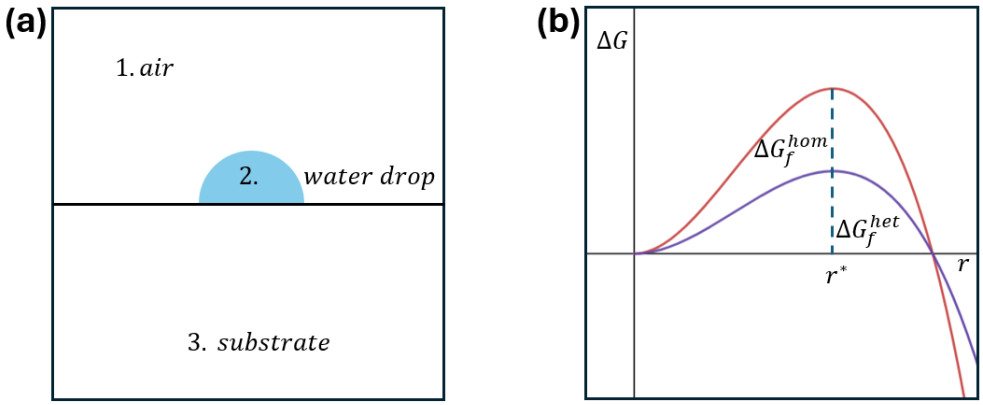

Figure 4.2. (a) Schematic of heterogeneous nucleation of a water droplet on a substrate. (b) The relative free energy change of formation from homogeneous to heterogeneous nucleation.

The presence of an interface can significantly decrease the energy cost of nucleation, making the phase transformation process many orders of magnitude more favourable than

[1] The large variation in standard laboratory conditions corresponds more so to seasonal variations and the inability of a modern, multi-million-pound building to effectively regulate conditions. Variation throughout experimental run time was considered negligible.

homogeneous nucleation.[146] In the new energy balance, a term for the energy of replacing the existing air-substrate interface with a liquid-substrate interface is included.

$$\Delta G_f^{het} = V_2 \Delta G_v + \gamma_{12} A_{12} + (\gamma_{12} - \gamma_{13}) A_{23} \ . \tag{4.4}$$

By deriving the respective volumes and areas, this equation can be re-written as

$$\Delta G_f^{het} = (\frac{4}{3}\pi r^3 \Delta G_v + 4\pi r^2 \gamma) \cdot \left(\frac{2 - 3\cos\theta + \cos^3\theta}{4} \right) \ , \tag{4.5}$$

or more generally,

$$\Delta G_f^{het} = \Delta G_f^{hom} \cdot f(\theta) \ . \tag{4.6}$$

$f(\theta) = (2 - 3\cos\theta + \cos^3\theta)/4$ with $0 \leq f(\theta) \leq 1$. As surfaces become increasingly non-wetting such that $\theta \to 180°$, $f(\theta) = 1$, and the free energy is equal to that of the homogeneous case (Eq. 4.1). As $\theta \to 0°$ and complete wetting occurs, $f(\theta) = 0$ and nucleation is fully catalysed resulting in no barrier to nucleation at the surface. This gives rise to two main modes in heterogeneous condensation, where for wetting surfaces, the formation of a continuous liquid film arises (filmwise condensation) versus in non-wetting cases where discrete droplets form (dropwise condensation).[221]

The critical radius r^* remains unchanged for heterogeneous nucleation and homogeneous nucleation in each case, however, the volume is significantly decreased resulting in a lower nucleation barrier due to the nucleus shape being a function of the wetting angle.[146] Although the critical radius is independent of the surface properties, as previously shown from alternative forms of Eq. 4.2, it is a function of the supersaturation pressure, or level of subcooling given in the experimental set-up. However, the prediction of nucleation onset is even more challenging as the surface roughness or fractal dimension has also been shown to decrease the energy barrier and increase the number of nucleation sites.[222–224]

When the modulus of the solid substrate decreases, the condensation dynamics become more complicated due to the substrate deformability. The nucleating sessile droplet imposes a vertical component from its surface tension at the three-phase contact line, which pulls the substrate around the droplet periphery up into a wetting ridge. Further, the Laplace pressure inside the droplet exerts a force pushing the contact area out.[225] Sokuler *et al.* experimentally showed increased nucleation on soft substrates, with increasing nucleation density on substrates that deformed greater.[226] The decreased nucleation energy barrier facilitated on PDMS with higher shear modulus results from the reduction in free energy due to deformation. The air-water interfacial tension energy term is decreased compared to the rigid case, with this overcompensating from the increase of PDMS-water area and elastic deformation. Phadnis *et al.* derived how softer substrates

can augment phase change behaviour, promoting dropwise condensation with increased nucleation density.[227] Sharma *et al.* performed experiments on PDMS-based organogels with varying both the shear modulus through stoichiometric base:crosslinker ratio and fraction of uncross-linked polymer chains with lubricant addition.[225] Whilst reaching the same conclusion as before where greater deformation results in lower energy barriers for nucleation, they found that the uncrosslinked chains diffused to the interface, forming a lubricating layer. Samples with infused lubricant demonstrated increased nucleation density, however, they also showed minimal dependence with the fraction of lubricant added, speculating that a continuous layer governed this condensation increase.

Liquid substrates

The nucleation on liquid substrates presents an interesting scenario where the surface can be viewed as atomistically smooth with no defects.[148] Eslami *et al.* used the argument of a liquid substrate in condensation analysis to study the problem of soft substrates, defining the liquid as infinitely soft.[147] They conclude a lower energy barrier is present for liquid substrates when comparing to a solid substrate of identical interfacial properties. Large experimental work on the topic has recently been driven by Lubricant Infused Surfaces (LIS) in the use for heat transfer applications.[134,225,228,229] The significant difference with condensation on liquid substrates is the presence of the phase boundaries between the fluid phases characterised by their contact angles and relative interfacial tensions.[148]

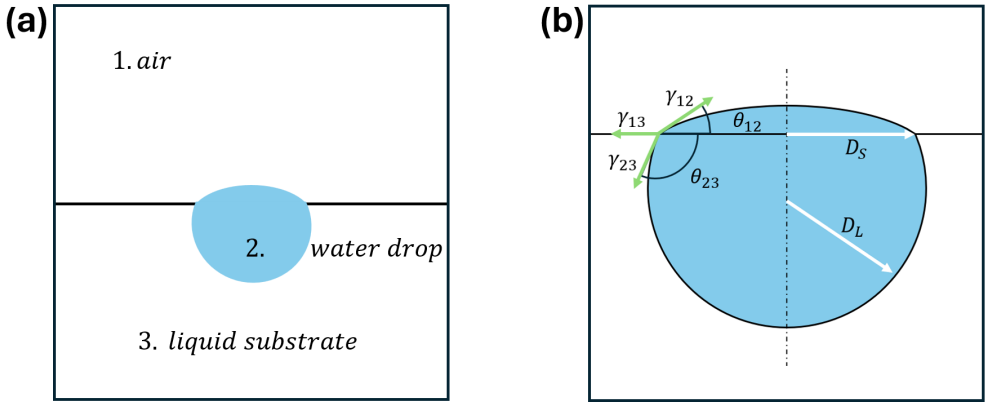

Figure 4.3. (a) Schematic of heterogeneous nucleation of a water droplet on a liquid substrate. (b) Magnified view of the liquid lens showing key parameters and dimensions.

The nucleated phase forms a droplet lens shape at the air-liquid interface (Fig. 4.3a), with the equilibrium shape a function of the relative interfacial tensions (Fig.4.3b). Eq. 4.4 becomes,

$$\Delta G_f = V_2 \Delta G_v + \gamma_{12} A_{12} + \gamma_{23} A_{23} - \gamma_{13} A_{12}^* \,, \tag{4.7}$$

where A_{12} does not always equal A_{23}, resulting in a partially submerged or suspended droplet lens. Further, the substituted air-substrate interface (A_{12}^*) has an area πr^2 where r is the three-phase radius in the plane of the substrate-free surface ($D_S/2$).

A requirement of BF patterning is for dropwise condensation and stable liquid lenses to occur at the air-polymer interface. For liquid lenses of water to be able to form, only partial spreading of the water on the liquid polymer can occur ($S_{23} < 0$), where $S_{23} = \gamma_{13} - (\gamma_{12} + \gamma_{23})$ using the notation as per Fig. 4.3.[230] As a result, due to the relatively high surface tension of water γ_{21}, the condensate forms a liquid lens on all the NOA polymers tested as opposed to spreading into a thin film provided a high enough supersaturation is achieved. With the Bond length of nano/microscale water droplets, $Bo \ll 1$, gravity effects are neglected and the equilibrium droplet shape is a function of the interfacial energies. To minimise the potential energy, the interface with the lowest interfacial energy will be maximised, demonstrating a largely submerged lens as a result of the small water - polymer IFT. Assuming that at the length scale of nucleation, the equilibrium interfacial tensions hold up and describe the shape the the nucleus at the interface, the state of nucleation can be inferred. Lower energy barriers are hence achieved where droplets remain largely submerged *i.e.* $\gamma_{23} < \gamma_{21}$.[134]

While the equilibrium shape of liquid lenses in the absence of gravity is dictated by the balance of interfacial tensions creating a Nuemann triangle,[231] the apparent positive spreading of the polymer on water makes this derivation non-trivial.[232] With the extremely low measured water - NOA IFT, the spreading of polymer on water, S_{32} given by $S_{32} = \gamma_{12} - (\gamma_{13} + \gamma_{23}) > 0$ indicates a thermodynamic propensity to cloak the droplet with a nanoscale layer of polymer. Without further dynamic studies, it is not clear if due to the high polymer viscosity and continuous fast growth kinetics of droplet growth that cloaking does indeed occur.[134] Regardless, a cloaking layer should not affect the overall kinetic scaling trends of the droplet growth which are evaluated within this chapter.[233]

4.2.3 Experimental observations

The reality of condensation is clear when experiments are run using the experimental apparatus described in Ch. 3. When the polymer film is held just above the dew point for a prolonged period of time, no visible nucleation occurs at the interface or throughout the film (Fig. 4.4a). At this temperature, the air does not become supersaturated and no nucleation occurs either homogeneously in the air or at the air-polymer interface. When the film is cooled to below that of the dew point temperature for the environment, the presence of droplets at the air-polymer interface is observed after only a number of seconds (Fig. 4.4b). The low miscibility of water within the liquid polymer suggests it is unlikely that water could homogeneously nucleate within the bulk of the polymer. Further, the relatively thick polymer layer comparative to nucleation length scales indicates that

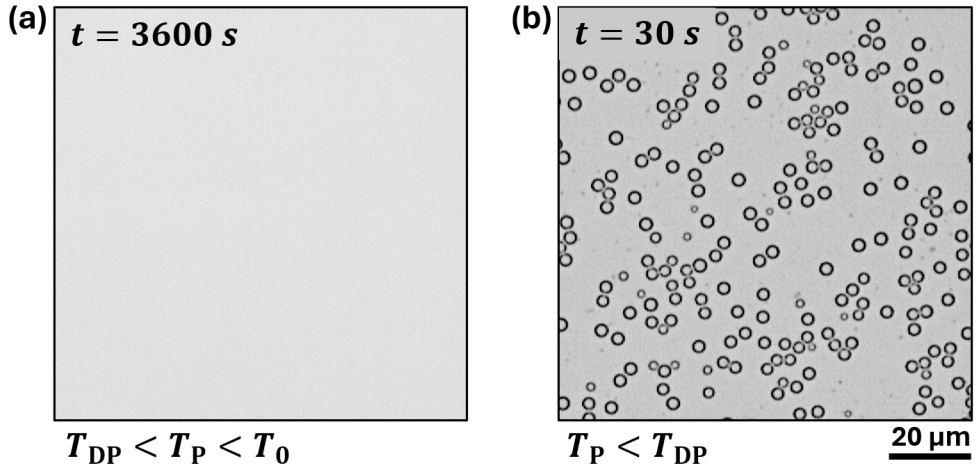

Figure 4.4. NOA61 films held at different temperatures. (a) Peltier is set to below that of the ambient conditions, but slightly above the dew point for 1 hour. (b) Sample image of a NOA61 film after 30 s. The image is focused at the optical plane of the air-polymer interface with the Peltier set below the dew point.

droplets would not nucleate at the bottom glass-polymer interface where there would be lower energies, due to the limited water diffusion.[234] With the polymer layer acting as a subcooled surface, and the saturation dynamics being directly linked with that of the air, the air-polymer interface acts as the most likely region for nucleation.[134,229,235] This is consistent with theoretical and experimental analysis which indicate supersaturated vapour would nucleate at the air-polymer interface.[134,147,148]

The lower energy barrier for heterogeneous nucleation further manifests in an increased nucleation rate. Given as the number of nuclei forming events per unit volume per second, J, is determined by,

$$J = J_0 \exp[-\frac{\Delta G^*}{kT}] \,, \tag{4.8}$$

where J_0 is the pre-exponential factor determined from kinetic considerations, k is the Boltzmann constant, and ΔG^* is the critical free energy as before.[236] Whilst the pre-exponential factor is still dependent on supersaturation, it can be treated as a constant when compared to the significant dependence on exponential terms.[146] The probability of a nucleus forming at a site is thus proportional to $\exp[-\Delta G^*/kT]$. As a result, if ΔG^* is large and positive the probability of forming a nucleus is very low and nucleation will be slow. $\Delta G^* \propto 1/T^2$ so the numerator of the exponential is more T dependent than the denominator. Therefore, with high subcooling a larger number of stable nuclei form (Fig. 4.5).

By varying the level of subcooling on NOA61, the influence on supersaturation can be observed (Fig. 4.5). While these experiments are limited to microscale analysis in the

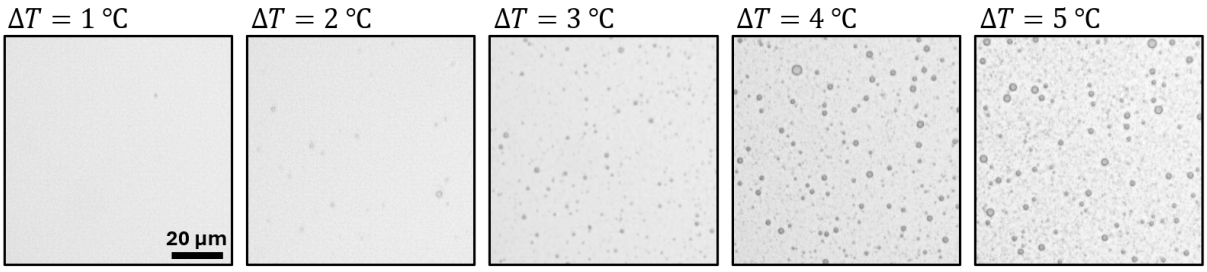

Figure 4.5. Images of nucleation on NOA61 taken at $t = 15$ s for different levels of subcooling.

optically resolvable range, the increasing subcool indicates faster nucleation with higher nucleation density. Snapshots for an equal working time of 15 s, the amount of condensation is almost indistinguishable for subcooling of $\Delta T = 1-2°C$. At the highest subcooling tested, the presence of multiscale nucleation families is clear. Given the lower free energy barrier with increased supersaturation, decreased critical nucleation radii and increased nucleation rates are expected.

The nucleation across different NOA polymer films was tested on the experimental set-up described in Ch. 3 (Fig. 4.6). The first observation comes from the hydrophobised silanised glass control, 'S-Glass'. While some optimised coatings can create readily hydrophobic substrates with minimal contact angle hysteresis, droplets here appear non-circular resulting from contact line pinning as a result of defects and heterogeneities on the glass surface.[230] While these defects can act as specific nucleation sites due to the lower energy barrier associated with the geometry (see Eq. 4.7 argument), they ultimately result in random droplet shapes. The premise of templating on a liquid film ensures the droplet templates produce axis-symmetric equilibrium shapes which can be readily re-organised and self-assembled. This is obvious on the red-outlined polymer films where droplets exhibit a seemingly maximum packing criteria with touching droplet boundaries.

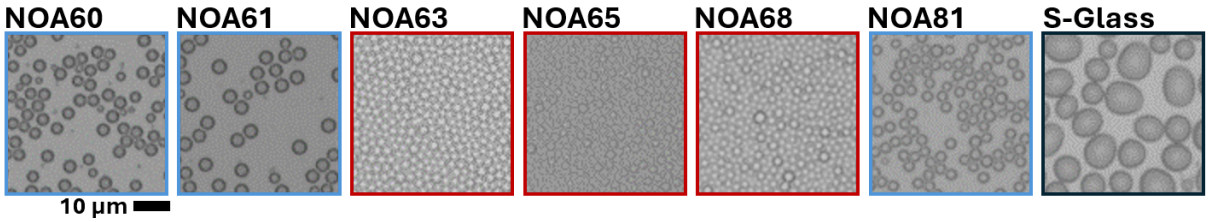

Figure 4.6. Initial nucleation on NOA polymer films tested, including silianised glass for comparison. Blue outlines represent low initial nucleation density with red indicating high nucleation density.

There is a clear difference in nucleation densities between the blue-outlined low density films and red-outlined high density ones. In this case, a correlation exists where the higher viscosity polymers used (NOA63, NOA65 and NOA68) all have significantly higher nucleation densities of droplets. The NOA60, NOA61 and NOA81 polymers all have measured

IFT $>$ 10 mN/m and exhibit a relatively lower nucleation density. For the high viscosity polymers $\mu > 2000$ mPa.s, NOA63 and NOA65 both have measured IFT $<$ 10 mN/m. NOA65, on the other hand, while exhibiting a high nucleation density, has a viscosity between the groups where 300 mPa.s $< \mu_{\mathrm{NOA65}} = 1200$ mPa.s < 5000 mPa.s. The measured IFT is also the largest measured across all the polymers at nearly 14 mN/m. Having the lowest density relative to water, performing pendant drop analysis on NOA65 gave uncertain measurements, with the size of the pendant drop having to be many times larger than the others. Without further validation of the IFT and knowledge of the proprietary polymer compositions, it is difficult to draw conclusive remarks over the variation of nucleation densities on different NOA films.

The difference in nucleation densities between the low and high viscosity polymer films makes it easy to study the disparate regimes when analysing the nucleation and subsequent growth kinetics of the droplets. As a patterning approach, having a consistent nucleation regime with predictable nucleation sites throughout the interface is more desirable. Instead of a stochastic distribution of droplets with different generation families (spatial and size distribution) as seen in NOA61, NOA63 provides a high nucleation density from the first microscopically resolvable point. Fig. 4.7 shows images of condensation nucleation on NOA63 at different time stamps for different levels of subcooling. While the resolution of the optical set-up does not match the scale required to resolve individual droplets, the higher subcool level shows an increase in the condensation rate with the largest droplets in the bottom right image. Across the subcool temperatures, the nucleation density appears fairly consistent at this optical resolving power, with droplets appearing from the onset at very high nucleation density. At subcooling $\Delta T = 5\,^{\circ}\mathrm{C}$, however, individual droplet sites are just about detectable between $t = 30$ s and $t = 45$ s, indicating that while in seemingly almost maximum packing, droplets are initially growing in isolation.

Further study is needed to elucidate the disparate nucleation density regimes observed between the high and low-viscosity NOA polymer films. Previous BF research indicates a correlation between a decreased resultant pore size with increasing molecular weight, M_w, of the polymer chains for consistent conditions.[118,237,238] It could thus be plausible to relate the M_w (and hence viscosity) to a lower free energy barrier for nucleation and increased nucleation density, however other reports suggest no influence of density and distribution with the viscosity.[85,233] Potential thermal-capillary waves in the order of 10's Å resulting from temperature fluctuations could play important roles in nucleation[134] and even polymer functional groups have shown preferential sites for nucleation.[118,189] Further, any potential contaminants or additives at the interface as well as small amounts of adsorbed water can significantly impact the preferential nucleation of new droplets.[239] Without knowledge of the polymer composition and the differences between them, it is difficult to conclude the origin of the nucleation density variation. However, from a patterning

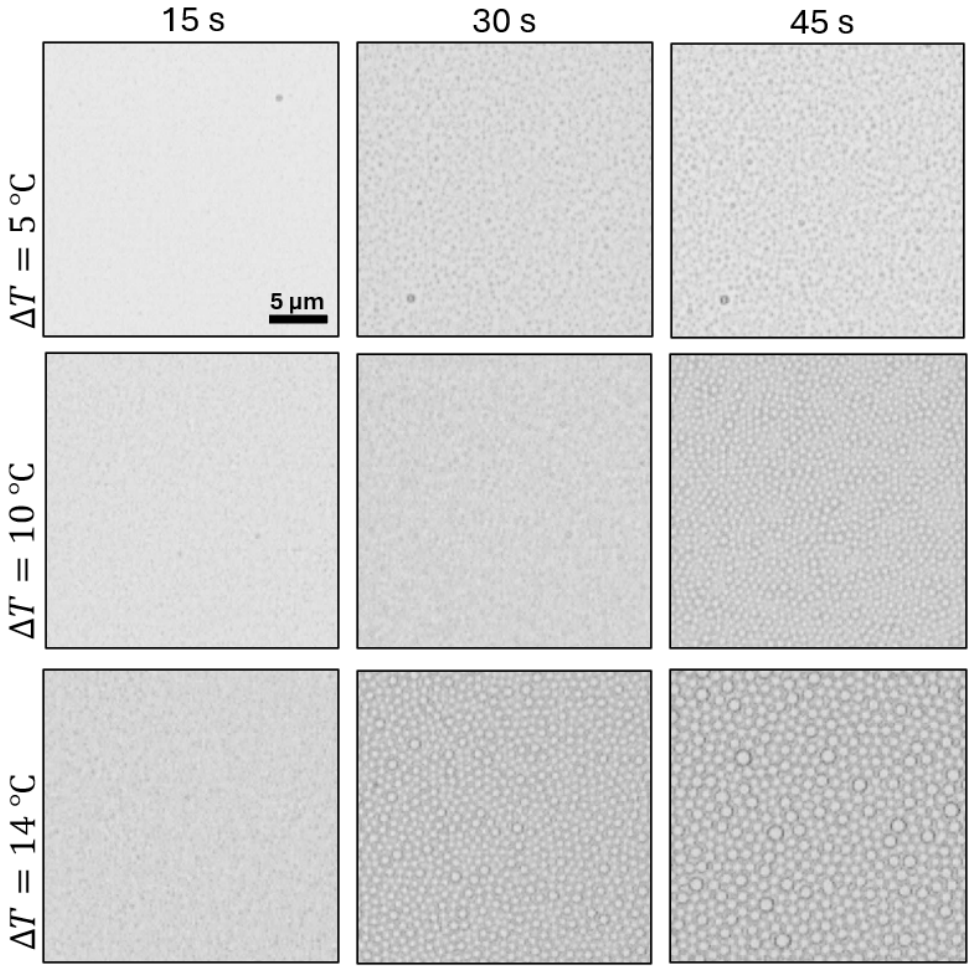

Figure 4.7. Images of nucleation on NOA63 taken at different time intervals for different subcooling levels ΔT.

perspective, it is more beneficial to have a high initial nucleation density of droplets that facilitate systematic and predictable patterning across length scales. Because the main pattern characteristics are determined by the subsequent growth of the droplets, more emphasis is thus placed on the kinetics of droplet growth. With the different films exhibiting two distinct nucleation regimes, taking NOA61 and NOA63 forward presents an opportunity to study the respective growth rates.

4.3 Kinetics of condensation growth

The growth of breath figures has been studied numerically and experimentally on various substrate dimensionalities and materials.[189] This was first explored in detail in the studies of Beysens and Knobler[84,85] analysing the physics of dropwise condensation rather than in the context of the later-derived templating BF approach. Their work was theoretically and experimentally validated, and later corroborated by computational models.[86,87,240] While many different growth regimes have been reported based on the droplet size and packing,

two main stages are considered significant to the experimental work completed here. Early and late-stage droplet growth, correlating to the surface coverage of the droplets and working time duration in these experiments can be summarised; initial growth of isolated droplets in a diffusion-limited regime where as interactions between neighbouring droplets become significant, a crossover into a late stage, coalescent-dominant growth.

Despite the wealth of research on condensation physics, *in situ* analysis or evaluation of the growth mechanism is substantially less studied in breath figure patterning. Constraining successful patterning to monodispersed, non-coalesced droplets, and with an inability to control the arrest within the classical approach, limits the need for study and control of pattern kinetics. As described in Ch. 3, in classical BF patterning there is not necessarily a steady state of condensation with a constant subcooling level ΔT, due to the progression of the solvent evaporation. Further, the evaporation of solvent in tandem with condensing droplets create a new layer of complexity in the process that can affect the overall growth rate.[99] There is thus limited scope for pattern prediction as the average diametric growth is not always a known function of time, $D \neq f(t)$. On the other hand, the temporally arrested breath figure approach facilitates a greater need for understanding of the droplet growth regimes due to the ability to arrest the pattern on demand.

4.3.1 Growth of isolated breath figure droplets

At early stage growth (isolated droplets) of water on viscous oil, Beysens and Knobler showed that for a steady state of condensation, the droplet growth rate is governed by a diffusion-limited regime where droplet-droplet interactions are negligible. Growth occurs through the direct accretion of molecules at the drop surface, as well as diffusion into the drop perimeter through critical droplet nuclei on the substrate.[152] The diameter hence scales with,[206]

$$D \approx (\mathfrak{D}\Delta P C_0 \delta^{-1} t)^{1/3}\,, \tag{4.9}$$

where $\mathfrak{D}$ is the diffusion coefficient for water vapour molecules, ΔP is the saturation pressure difference, C_0 is the concentration of water vapour in air and δ is the length scale of the condensation gradient. Assuming a constant volumetric flux of condensation occurring (steady state conditions), the volume change of a droplet per unit time, dV/dt, is constant. As $V \propto D^3$, for this isolated growth regime, one can view a relationship of $D \propto t^{1/3}$ when analysing 2D images of the growing droplets.[89]

Droplet coalescence is negligible until a critical surface coverage value is reached, beyond which inter-droplet interactions result in temporal and spatio-temporal variations in the surface coverage and geometric configuration.[153] Monitoring the temporal evolu-

tion of condensation droplets thus provides valuable insight into the physical mechanisms governing their growth and spatial organisation. Due to the relatively lower nucleation density previously observed in NOA61 (Fig. 4.5), the growth rate of individual droplets was analysed at a 1 Hz sampling frequency.

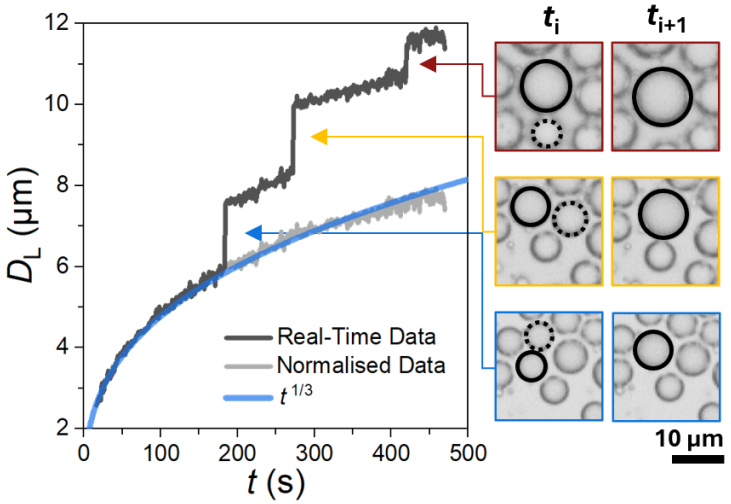

Figure 4.8. Temporal growth of condensation droplets on NOA61 recorded at $RH = 26\%$, $T_0 = 24$ °C, $\Delta T = 14$ °C.

Fig. 4.8 shows the real-time data of a single droplet throughout the analysis period in dark grey. Prior to any coalescence events ($t \lesssim 200$ s), the temporal growth of individual droplets is well predicted by a power law of exponent of 1/3.[85] As the droplet grows closer to neighbouring nucleated droplets, sporadic jumps in diameter are observed due to occasional droplet coalescence, demonstrated by the inset images. By subtracting the rapid droplet diameter increase, the coalescence jumps can be effectively eliminated and the continuous growth shows convergence to the initial power law, $D_L \propto t^{1/3}$. This growth analysis demonstrates the quiescent conditions of the experiment, where constant temperature and no significant airflow result in steady-state conditions.

4.3.2 Growth of highly-packed breath figure droplets

As the surface coverage of droplets increases, coalescence effects from neighbouring droplets significantly impact the average droplet growth rate. With a continuous increase in droplet radius, coalescence occurs from the Laplace pressure exerted by neighbouring droplets draining the viscous boundary separating them.[99] This transitional growth regime occurs when the area fraction of water droplets increases to a point typically beyond 30%.[152] Coalescence between neighbouring droplets rapidly increases the average growth rate in the field of view as this becomes the dominant growth mechanism. Scaling arguments show that for a 3D droplet growing on a 2D constrained substrate by conserving both mass and volume, the area taken up before for two droplets of radius R is $\sim 2 \times R^2$. Upon

coalescence, the droplet has radius $R' \sim 2^{1/3}R$, resulting in $A' \sim 2^{2/3}R^2$. Self-similarity occurs due to an increase in the free surface area from $A' < 2A$.[153,241] With continuous condensation flux, the continuous decrease in area coverage upon coalescence events results in a three-fold increase in the power-law exponent to unity, $D_L \propto t$.[88,153,220,241]

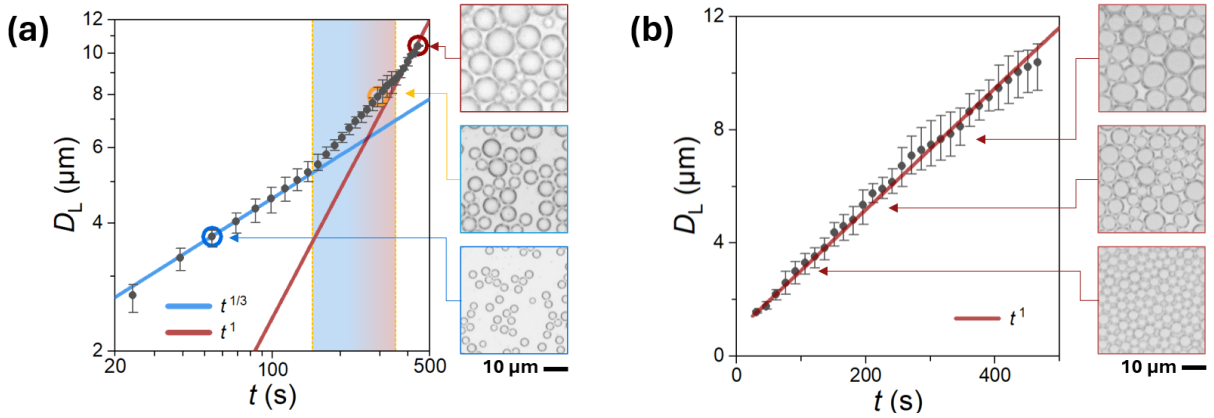

Figure 4.9. Temporal growth of condensation droplets on (a) NOA61 and (b) NOA63. Data recorded at $RH = 26\%$, $T_0 = 24$ °C, $\Delta T = 14$ °C, with the shaded error bands representing the range in mean data across the three repeats.

Further to the single droplet analysis in Fig. 4.8, the average parameters from the complete field of view in the same dataset can be analysed. Fig. 4.9a shows a log-log plot of data for NOA61 from the full frame, downsampled to a 15 s average plot. The mean of three repeats is plotted with an error corresponding to the range in diameter across the repeat window. For $t < 150$ s, a continuation of the 1/3 power law trend is observed across the whole field, indicating growth is predominantly diffusion-limited. This is evidenced in the previous analysis (Fig. 4.8) where the first coalesce occurs just before 200 s. A linear regression plotted in blue shows an adjusted R^2 coefficient of 0.99, and the inset image shows the initially low area coverage of droplets.

For $t > 150$ s, the growth rate increases in a transitional regime as the increased droplet packing leads to more frequent coalescence events between neighbouring droplets.[240] The droplet growth at $t > 350$ s then tends to a power law with exponent of unity with respect to time, demonstrating coalescent-dominating growth manifested by the large droplet number density (see top-right image in Fig. 4.9a). Similar analysis can be completed on a NOA63 film which attains a high nucleation density of droplets from early times. The packing of droplets is already at maximum as the size range becomes optically resolvable. The linear regression again shows a high correlation with an adjusted R^2 coefficient of 0.99, with the inset images showing the consistent droplet packing (Fig. 4.9b).

By quantifying the area coverage and number density of the droplets on NOA63, the coalescent-dominant regime is evident from the start, characterised by the high area coverage A_f and sudden decrease in number of droplets per unit area N_d. By late times, both

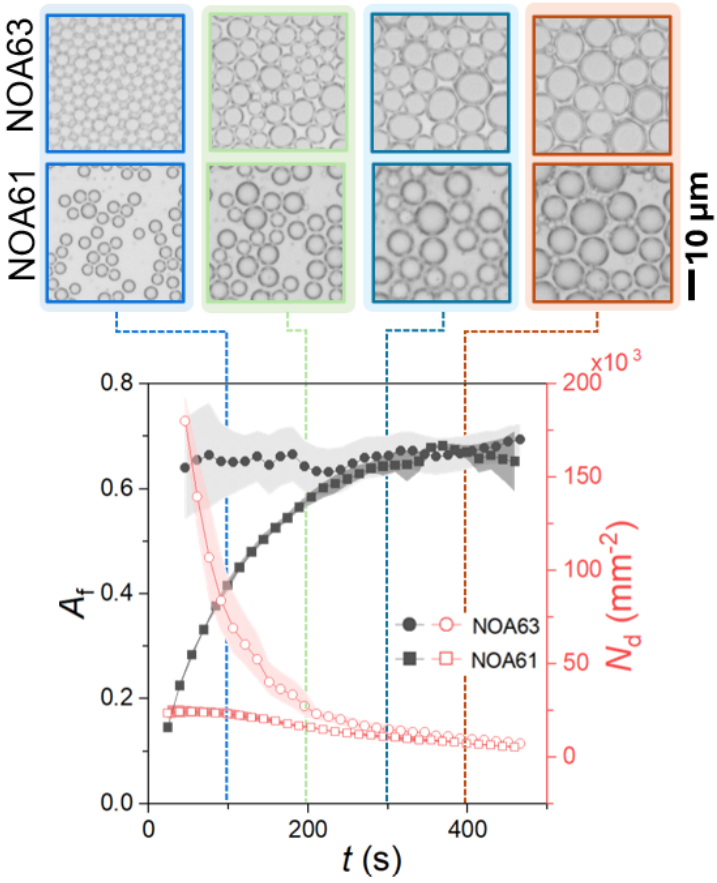

Figure 4.10. Area fraction A_f and number density N_d of condensation droplets calculated for NOA61 and NOA63 with data recorded at $RH = 26\%$, $T_0 = 24$ °C, $\Delta T = 14$ °C. NOA63 is indicated with square markers and NOA61 with circles, with the shaded error bands representing the range in mean data across the three repeats. Representative OM images of the droplets on NOA61 and NOA63 are acquired at corresponding discrete times.

films exhibit a plateau in the $A_f \approx 0.7$ (Fig. 4.10) indicating consistent growth rates at this late stage. The maximum observed packing corresponds to over 70% of the theoretical packing limit in a 2D plane (around $A_f \approx 0.9$), complimenting earlier studies[85] and suggesting this is near optimal packing given the viscous liquid boundaries which stabilise/encapsulate the droplets. Droplet coalescence at such large initial number density N_d yields a quick decrease due to the large number of coalescence occurrences within the frame of view. Conversely, the distinct diffusion-limited and coalescence-dominated regimes of droplet growth observed in NOA61 (Fig. 4.9a) leads to an initially larger increase in area fraction as droplets grow without coalescence, resulting in a smaller decreasing rate of N_d for the same reason (see comparisons in Fig. 4.10). At later times ($t > 350s$), both A_f and N_d on NOA61 films reach similar values to those found for NOA63 during the observable coalescence dominated stage, demonstrating both films tend towards the self-similar growth regime. Video S1 and S2 in the SI of the published paper show examples of droplet growth for NOA61 and NOA63, respectively.[185]

4.4 Thermodynamic control of pattern growth

The self-similar growth of BF patterns on NOA63 that extends from early time (10's s depending on the environmental conditions) to later time (100's s and beyond) suggests that exposure to the UV light will allow arresting patterns of well-predicted pore size and constant surface coverage using this material. Environmental parameters, however, mediate the effective patterning growth resulting from the condensation rate and thus need to be further controlled. In this adapted method, the supplemental handle of substrate temperature control replaces the indirect handle of empirical polymer solution design (polymer type, solvent, concentration) in the classical BF. As the scaling of the growth trend kinetics is independent of the thermodynamics, this section explores how the pattern development can be accelerated or amplified through thermodynamic control.

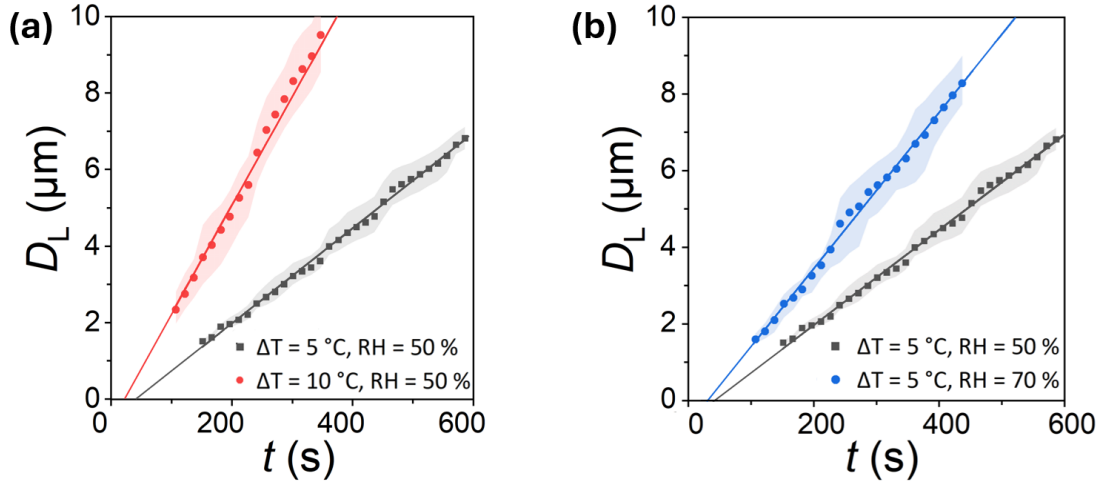

Figure 4.11. Impact of RH and ΔT on temporal growth of templating droplets on NOA63. (a) RH was kept constant at 50% for subcooling levels of $\Delta T = 5$ °C and $\Delta T = 10$ °C (left). (b) For $\Delta T = 5$ °C, the experiments were repeated at RH of 50% and 70% (right). Both graphs have fitted trend lines of $D \propto t$.

The growth rate of the droplet diameter is proportional to the concentration gradient and diffusion coefficient of water molecules in the vicinity of the substrate and the difference in the saturation vapour pressure (Eq. 4.9).[206,242] Modulation of the growth rate can be varied through the relative humidity, however, this is commonly achieved through control of humidified gas flow, increasing the system complexity and causing potential deviation from the theoretical predictions due to hydrodynamic and thermal effects.[152] Therefore, regulation of the substrate temperature at a fixed RH practically attains more predictable patterning across ambient and low humidity conditions. At temperatures close to 20 °C, the saturation pressure difference ΔP_s is proportional to $\Delta T_s^{0.8}$, therefore, increasing the subcooling level at constant relative humidity will increase the growth rate of the droplet diameter (Fig. 4.11a).[148,206] Additionally, the concentration gradient of water molecules can be controlled by modifying the relative humidity and thus the water content of the

surrounding environment (Fig. 4.11b). At a given time, the slower growth results in smaller droplet diameter variation arising from coalescent-effects; this is manifested by the smaller error bars in Fig. 4.11b for $\Delta T = 5$ °C at $RH = 50\%$. The growth rate, reflected largely by the number of coalescence events per unit time thus has implications upon UV curing as will be discussed in the next chapter.

The growth trends of templating droplets remain unchanged, following $D_L \propto t$ for all conditions, indicating that the coalescent-dominated growth regime is upheld throughout, even in the less optimal conditions (less subcooling and low RH). Due to the self-similar nature of the growth regime evident in Fig. 4.11, the data can be collapsed onto one single curve by compensating for the faster growth rates observed at higher subcooling and relative humidity. To this end, a new dimensionless time t/t_0 is defined, where t_0 is an arbitrary initiation time at which average droplet diameters reach 500 nm. The inset plot in Fig. 4.12 demonstrates the relationship between t_0 and the actively controlled subcooling level ΔT at different relative humidity values.

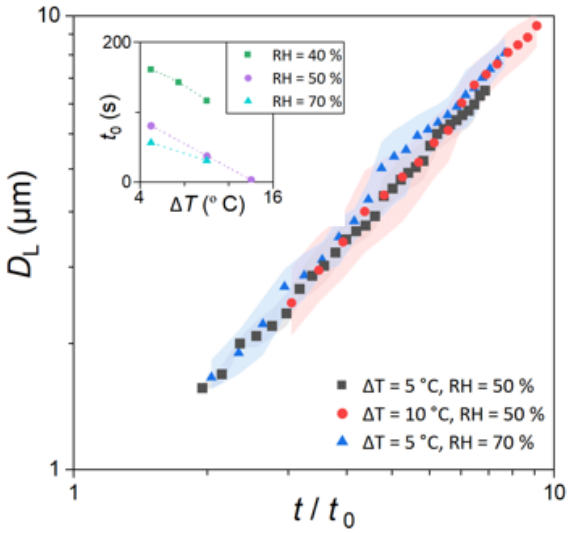

Figure 4.12. Impact of RH and ΔT on temporal growth of templating droplets on NOA63. Droplet diameter growth can be collapsed onto a single power law using the dimensionless time as the new variable. t_0 is an arbitrary initiation time at which average droplet diameters reach 500 nm. Inset graph demonstrates the evolution of t_0 vs. subcooling level at different relative humidity. The shaded error bands represent the range in mean data across the three repeats.

As expected, the initiation time decreases as condensation is enhanced at larger subcooling and higher relative humidity. Plotting the droplet diameters obtained at various environmental conditions (subcooling and relative humidity) versus the new dimensionless t/t_0, all data is predictable by a new single power law $D_L \propto t/t_0$, showing that growth trends remain invariant to input environmental conditions (Fig. 4.12).

4.5 Discussion

From the analysis of droplet nucleation on different substrates, two disparate regimes are observed from the microscale experimental observations. While it is difficult to experimentally interrogate the specifics of nucleation given the short timescale and small length scale of nucleation events, the findings can be characterised on the polymer viscosity. Low nucleation densities and discrete individual droplets at low area fractions are observed on the low viscosity polymers trialled (NOA60, -61 and -81). High nucleation density at initially optically resolvable length scales is observed on the high viscosity films, which also sees a general correlation with lower polymer-water interfacial tensions. For more conclusive remarks on nucleation density across polymer films, known polymers should be trialled that systematically vary IFT and viscosity.

It is seen that increasing the level of supersaturation not only decreases the critical nuclei size but increases the nuclei density. Within this experimental set-up, low viscosity polymers could not attain a similar high nucleation density to the high viscosity polymers even with higher subcooling. Due to the relatively dispersed initial droplet nucleation on NOA61, the area coverage does not reach the maximum packing until late experimental working times, by which point the droplets are relatively large. This limits the application use of the lower viscosity films, with high nucleation density enabling smaller minimum feature sizes and predictable patterning throughout the observable self-similar growth regime.

The role of coalescence also plays the dominant role in pattern re-ordering, occurring during the self-similar regime. For NOA61, the sparse nucleation results in large average droplet spacing. However, as neighbouring droplets grow closer to each other a slight ordering seemingly occurs with the formation of droplet couples, triplets and longer chains (Fig. 4.13). Short range capillary forces attract droplets together due to the minimisation of alike menisci on the floating droplets.[243] However, at the length scales of droplet separation in this study coupled with the polymer viscosity, the polymer substrate deformation is near negligible due to the insignificance of gravity resulting in minimal attraction.

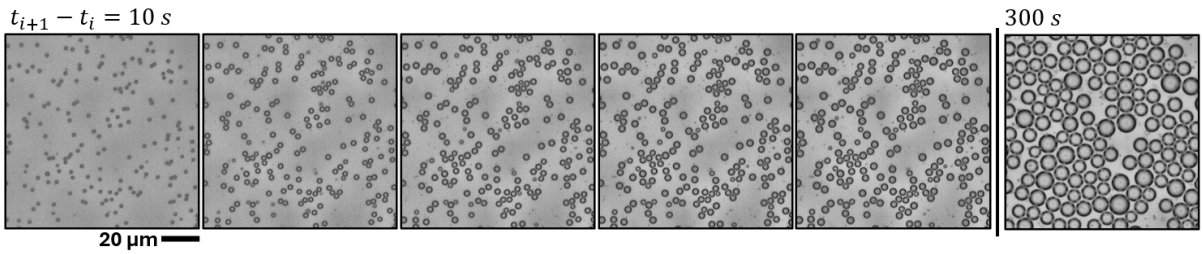

Figure 4.13. Droplet growth on a NOA61 film from $t = 10$ s. The capillary attraction between touching droplets does not facilitate the long-range ordering of droplets.

Whereas on high viscosity polymers, for example NOA63, the droplet rearrangement is

more evident in videos the pattern evolution (see SI in published work from this thesis [185]). The self-similar patterns in the coalescent-dominant regime leads to fast energetics of continual droplet coalescence. Due to the constancy in area fraction, the re-ordering of droplets is further evidenced with a constant packing order. The conformation Voronoi entropy was measured at 125 s, 250 s and 500 s, corresponding to average droplet sizes of 3.4 µm 7.8µm and 14.2 µm, respectively. This value measures the probability of a droplet having a particular number of neighbours, indicated by the colour scheme with droplets having increasing numbers of neighbours going from purple to yellow. The entropy of $S_{vor} = 1.15 \pm 0.02$ throughout indicates the packing order remains constant, evidencing the self-similarity. The entropy obtained between perfect hexagonal order ($S_{vor} = 0$) and complete random packing ($S_{vor} = 1.71$) indicates a relatively poor order compared to classical patterning, but size invariant consistency. While complete hexagonal packing requires a monodisperse droplet size, the small polydsipersity in this regime is constant and small.

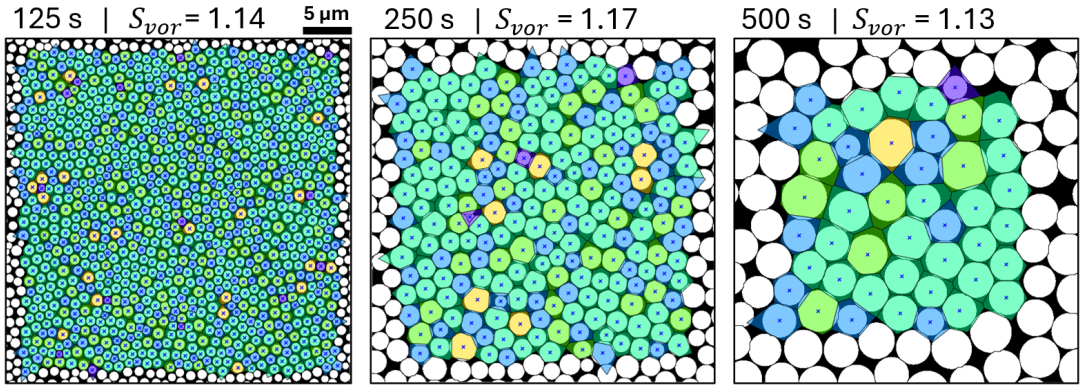

Figure 4.14. Conformation Voronoi entropy measure diagram overlaid on binary masks of thresholded droplets on NOA63. Colour gradient is an inverse rainbow corresponding to the number of neighbouring droplets. The average droplet size doubles across each frame.

4.6 Summary

- Predicting the exact onset and rate of nucleation is challenging given that these events occur at atomistic length scales and on time scales in the order of thermal fluctuations from the vibrational frequency of atoms. The CNT framework, while perhaps becoming increasingly outdated, can provide an overview of the key thermodynamics to infer the results that we are seeing.
- Although the nucleation physics on liquid substrates are still somewhat unclear, the empirical implications for a patterning approach mean key characteristics such as high nucleation densities are more favourable.

- By using a polymer which exhibits a high nucleation density from early onset, the stochastic nature of condensation and nucleation events is transformed into a more predictable pattern growth regime that translates into systematic fabrication means.
- Constraining pattern growth to a coalescent-dominant growth regime, the linear dependence of diameter with time enables easy prediction of the resultant pattern.
- The self-similar pattern growth in the coalescent-dominant phase results in constant area fractional coverage with systematic variation in average diameter in the temporal domain.
- With photocurable polymers, the trends of pattern growth in time can be arrested at discrete intervals, transferring the liquid-liquid observations from this chapter into a porous pattern as will be discussed in Ch. 5.

Chapter 5

Pattern modulation and temporal arrest

The ability to fabricate breath figure patterns of varied morphological arrangements is described in this chapter. Content partially described here has previously been published in the paper '*Exploiting breath figure reversibility for in situ pattern modulation and hierarchical design*'.[186]

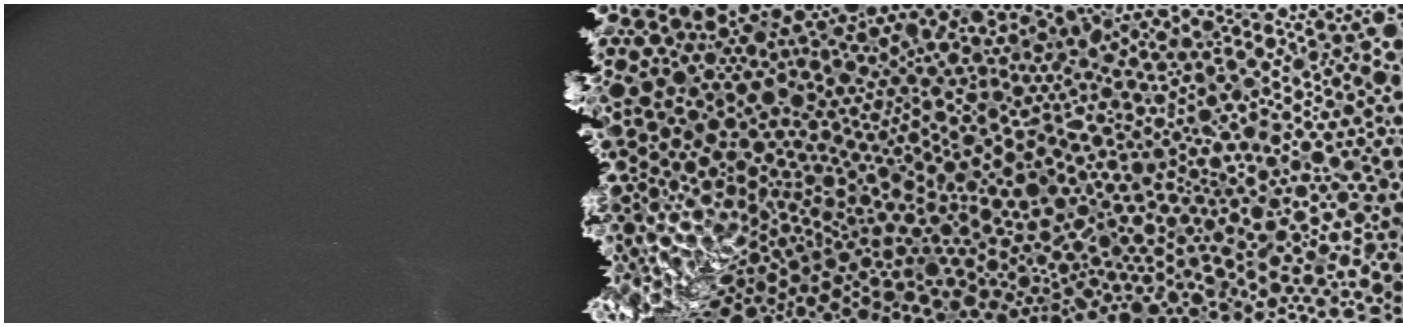

"The role of science, like that of art, is to blend exact imagery with more distant meaning, the parts we already understand with those given as new into larger patterns that are coherent enough to be acceptable as truth."

Edward O. Wilson

5.1 Introduction

Functional patterned surfaces in nature exhibit diverse patterns of varied feature size and arrangement, showcasing examples from highly packed nanoscale structures to multiscale, hierarchical assemblies, including both concave and protruding pattern features.[39,40] The combination of control handles provided by the temporally arrested breath figure (BF) approach not only facilitates prediction and control over the pattern growth rates, but provides access to a breadth of intermediary pattern arrangements that are not feasible with the classical technique. Full exploitation of such biomimetic fabrication methods towards predictive surface patterning thus relies upon the understanding and taming of the underlying complex multiphysics phenomena.[25] Here, the translation of the liquid-liquid breath figure pattern to the cured film is demonstrated. Predictable growth rates observed in Ch. 4 are systematically cured to show the arrested design. Further, the possibility of tuning the standard highly packed surface architecture is explored by exploiting the reversibility of the phase change process that governs the operation. Building on from Ch. 4, translating the thermodynamics governing the BF method into controllable and predictable patterns that are not only low cost, but inherently scalable, provide insight into this technique for biomimetic surface patterning applications.

The classical BF technique enables the fabrication of highly ordered honeycomb-packed pore arrangements. The low viscosity of the polymer-solvent solution facilitates substantial rearrangement of the stabilised droplets through interfacial and thermo-capillary forces, as well as the evaporating front of the solvent.[244] As a result, providing successful fabrication, strikingly ordered films are created of monodisperse features that are hexagonally arranged in the lowest potential energy configuration. While achievement of this monodisperse pattern is only a reality in strict experimental conditions, systematic permutations of the design are more difficult. Spatial modulation of features created through attractive forces is generally inaccessible due to the specific self-assembling mechanisms that create the close-packing. Although pattern modulation can be practised to some extent in the evaporation-driven breath figure approaches,[149,245] full reversibility of the condensation process[239] and access to intermediate patterns are only possible in methods that eliminate solvent evaporation and provide an active polymerisation route.

Recent attempts have been made to further advance the classical BF pattering approach towards modulating pore shape[142,149,178] and generating hierarchical[246–248] structures. The specific pore shape which is primarily dictated by the interfacial tension at the three-phase contact line has been altered through the use of non-aqueous vapors,[142,249] strict temperature/humidity regulation,[149] and employing additives[250] or sacrificial layers[179]. Secondary patterns have been created via consecutive processes such as large-scale re-shaping of the pre-patterned substrates[251] or BF patterning on physically confined 3D[181,247,252,253] sub-

strates. The use of combined techniques with nanoparticles [111,254–256] or other self-assembly and phase separation techniques [105,110,248,257] have also proven successful for the fabrication of hierarchical BF patterns. The reliance upon hybrid approaches, however, further narrows the range of operational working parameters and choice of materials, impairing the simplicity of the classical BF method with little to no deterministic control over the final design.

This chapter delineates the main control parameters in the temporally arrested BF approach alongside the realisation of the final pattern. Sample patterns of predictable pore diameter and area fraction are achieved from the process' combined temperature control and curing dynamics, harnessing the inherent reversibility of the BF phase change. The possibility of inducing and retracting the reversible BF pattern via external temperature control is explored by implementing subsequent regimes of subcooling and superheating. As shown in Fig. 5.1, starting with a high nucleation density polymer such as NOA63, droplet growth can be controlled in the self-similar regime at constant surface coverage from early experimental working times. Evaporation of the pre-established BF pattern is investigated by increasing the Peltier temperature to above the dew point, causing a reduction in the surface coverage. The feasibility of restarting the BF process after evaporation to initiate a secondary condensation regime for the creation of multi-scale patterns is also explored.This approach facilitates *in situ* tuning over the size and spatial arrangement of BF patterns with direct translation to cured patterns via UV curing. The prospect of further pattern permutations such as replica moulding to create protruding features are also investigated.

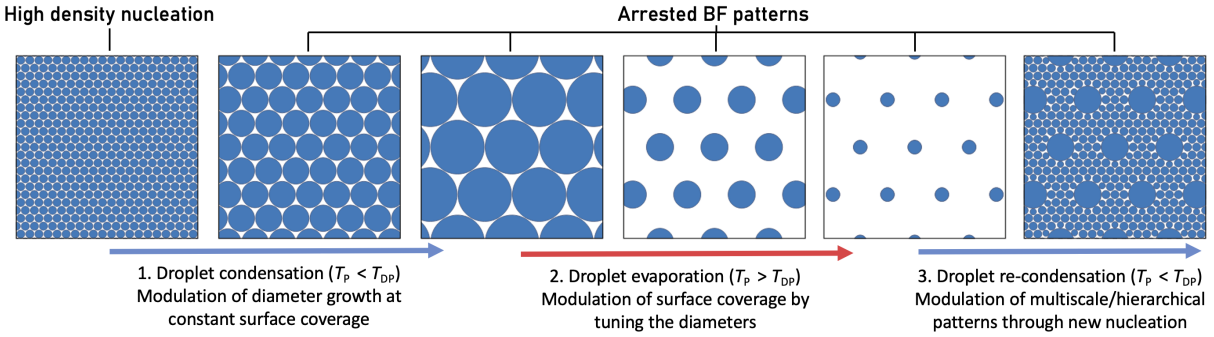

Figure 5.1. Diversity of patterns that occur through subsequent external cooling and heating cycles in the temporally arrested BF. The substrate temperature on the Peltier device, T_P, is set with respect to the dew point temperature, T_{DP}, to alter the patterning regime.

5.2 Temperature controlled patterning regimes

Due to the simplistic experimental set-up centred around the temperature controlled Peltier device, the main handle to modulate the patterning regards the substrate temper-

ature. As described in Ch. 4, a highly packed BF pattern can be established by subcooling the polymer film to below the saturation dew point of the environment. The temperature of the Peltier can be used to vary the growth rate of the pattern when subcooled, and increased to above that of the dew point, thereby starting to evaporate the droplets. As such, permutations of a standard highly packed design can be achieved through temperature modulation.

5.2.1 Size modulation at constant area fraction

Under quiescent conditions of constant temperature and no significant airflow, the growth rates of droplets forming the BF pattern follow the well described drop-wise condensation physics trends:[189] for isolated droplets, diffusion-limited growth increases the droplet volume monotonically, leading to a diametric growth relationship of $D_{\mathrm{L}} \propto t^{1/3}$.[85] However, when droplets pack closely, their growth is accelerated due to the coalescence between neighbours, yielding a self-similar growth regime in which droplet diameters follow $D_{\mathrm{L}} \propto t$.[148]

On the pre-cured liquid polymer film, the pore diameter in the BF pattern can be readily controlled using the temporally arrested BF methodology.[185] The implications of using a film that exhibits a high nucleation density of droplets restrict the pattern growth to the latter coalescent-dominant regime, resulting in a linear increase in average droplet diameter with time. By exposing the liquid pattern to UV irradiation, the liquid pattern characteristics can be translated into a cured film with pores (Fig. 5.2).

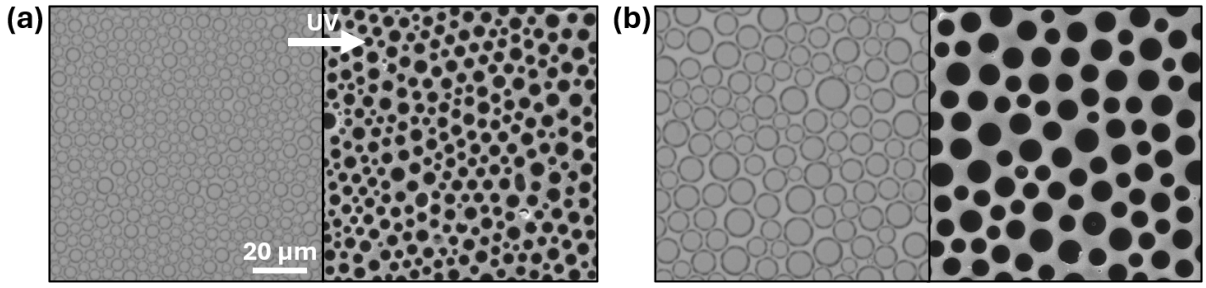

Figure 5.2. Images of pattern transition from (left) liquid droplets on liquid films to (right) pores on solid films at different length scales. The pattern is cured with the UV curing system for 5 s at 650 mW/cm^2 after different experimental working times to attain relative small and large features.

This self-similar regime arises from the rearrangement of coalescing droplets, resulting in a constant area coverage in time. As droplets coalesce, the scaling and self-assembly arguments indicate the decrease in the surface area taken up by the daughter droplet facilitates more droplet growth at a plateaued coverage. Curing different films at discrete time intervals thus produces a systematic increase in the average pore diameter attained in time, with patterns exhibiting a constant area fraction (Fig. 5.3). High-resolution SEM

and LSCM analysis of the cured films show they exhibit the same trends observed in the liquid state, indicating a negligible impact of the curing exposure time, see Sec. 3.3. Fig. 5.3 indicates convergence to the linear trend with droplets less than the previously observed optically resolvable size range.

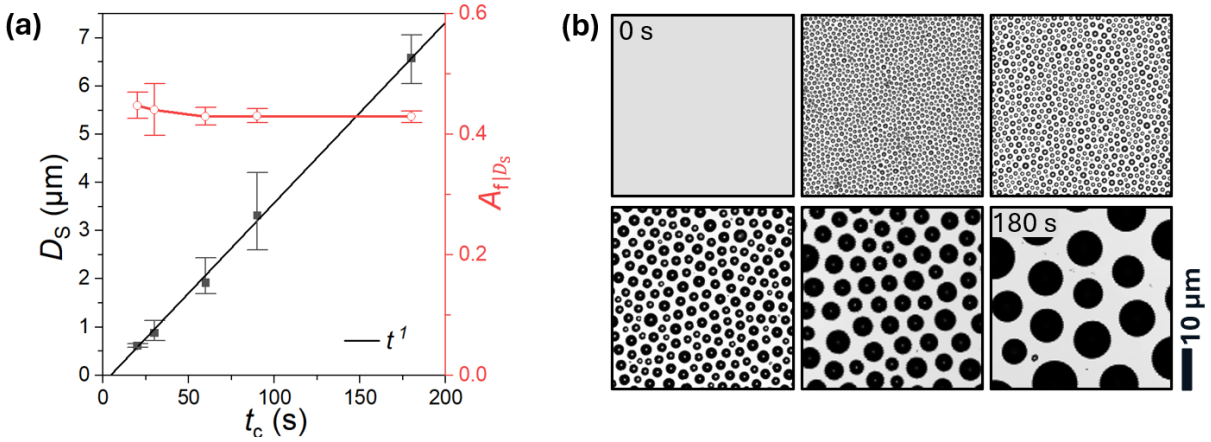

Figure 5.3. Analysis of highly packed NOA63 films cured at discrete condensation working times of 20 s, 30 s, 60 s, 90 s and 180 s. (a) Diametric and area fraction analysis alongside (b) LSCM image examples of the cured films.

The lower $A_{f|D_S}$ here corresponds to the average diameter at the triple line (pore opening), D_S from LSCM analysis of the cured films (Fig. 3.14 from before). This lower value is reflective of the pore morphology, where due to the low polymer-water IFT, the equilibrium shape of the liquid lens results in the majority of the droplet submerged below the surface. Maximum packing analysis using D_L in the liquid state, indicates $A_f \approx 0.7$. At the air-polymer interface in the cured state, $A_{f|D_L} \approx 0.4$, suggesting a pore morphology of $D_S/D_L \approx 0.8 \pm 0.1$. The constant ratio throughout the size domains tested suggests a constant pore shape in time, further reflective of the self-similar growth regime.

5.2.2 Area fraction modulation at constant spacing

At a given relative humidity, the difference between the substrate temperature and the dew point sets the supersaturation level and controls the rate of phase change. For set temperatures below the dew point ($T_P < T_{DP}$), the subcooling defines the linear growth rate of highly-packed BF patterns during the BF formation (Fig. 5.4a). Conversely, on samples with a well-developed BF assembly already established, substrate temperatures above the dew point ($T_P > T_{DP}$) result in evaporation of the droplet pattern (Fig. 5.4b).

As before, with microscopy analysis attaining pattern characteristics at 1 Hz frequency, the evaporation kinetics of evaporating BF patterns on NOA63 at constant superheating levels can be characterised. In the highly packed condensation regime, droplets are pushed by the neighbours and rearrangement occurs due to coalescence. The average size of

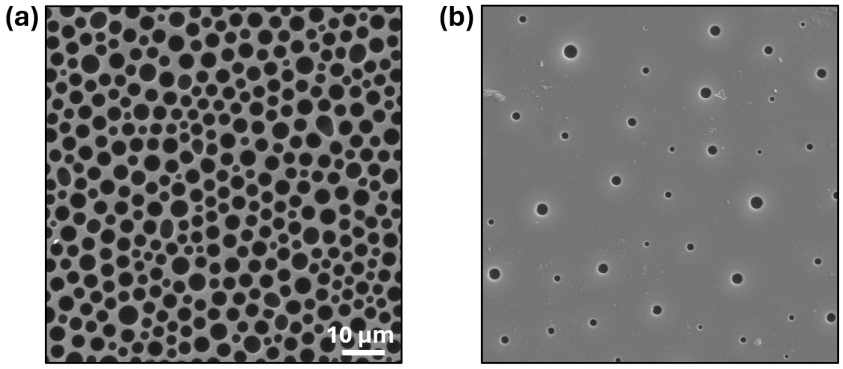

Figure 5.4. Example of (a) a highly packed and (b) sparsely packed cured film.

droplets increases, but the area fraction remains constant due to the self-similarity. Upon evaporation, droplets remain stationary due to the negligible capillary interactions and droplet diffusion in the length and time scales studied here. No coalescence occurs and the radially shrinking droplets maintain a constant interdroplet spacing, $L_c \approx 1.2 \times D_{L_0}$, where D_{L_0} is the maximum droplet diameter attained in the highly packed condensation regime (Fig. 5.5a). This evaporation leads to continuous reduction in the droplet diameters whilst the distance between them is maintained; the area fraction can thus be significantly reduced in a controlled manner by understanding the evaporation kinetics. The images in Fig. 5.5b show a decrease in the area fraction by more than 85% from the initial value.

In cured BF patterns, while pore size modulation at constant high surface packing was achieved via continuous condensation in a subcooled regime, elevating the temperature above the dew point for this evaporation step facilitates a reduction in the area fraction from the radial decrease in the droplet diameter. Due to no coalescence and re-distribution of droplets within the evaporation analysis, the polydispersity in droplet diameter smears the observed trends, especially at later times. It can be seen that the polydispersity during this regime slowly increases from $g \approx 0.1$ to $g \geq 0.2$. Fig. 5.6 demonstrates the smearing effect observed when comparing the reduction in droplet diameter for a single droplet compared to full-field analysis. To ensure that the randomly selected droplet statistically represents the kinetics across the field of view, four other droplets of similar diameters (maximum diameter variation of $\pm$ 5%) were selected across the image frame at the start of the analysis. The identical droplets were then automatically tracked during the evaporation regime with the average plotted. By decreasing the analysis sample size from 100's droplets in the full field analysis, to 5 droplets of approximately equal dimensions, the evaporating kinetics of the droplets can be better studied. All data is presented in square diameter to allow comparison with the available prediction models.

Droplet evaporation occurs in non-saturated environments when surface molecules which have enough energy undergo a phase transition from liquid to gas. At temperatures above the saturation dew point, evaporation occurs through the diffusion and net mass transfer

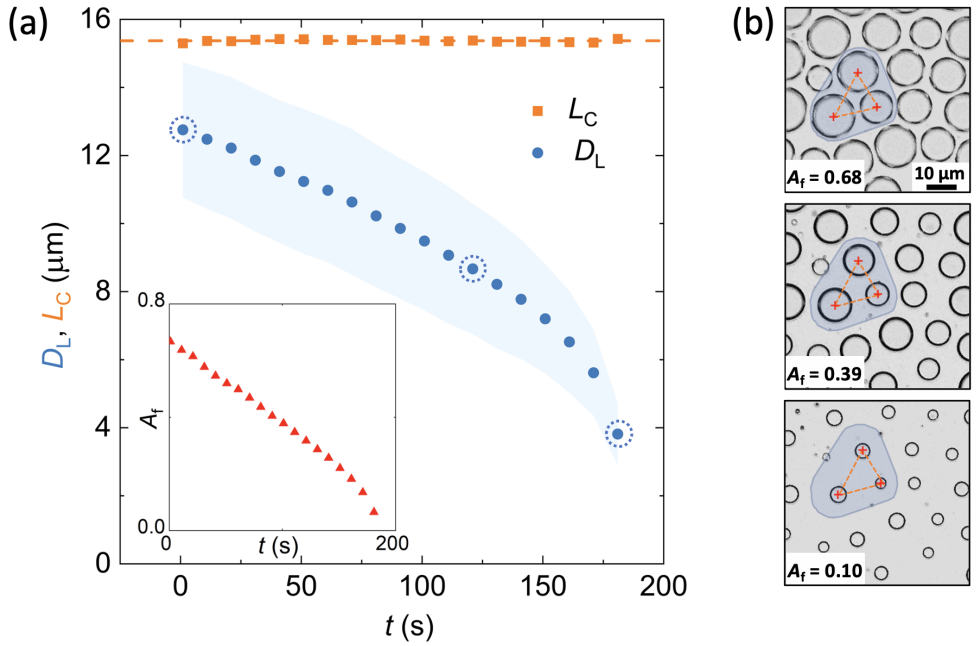

Figure 5.5. Evolution of BF patterns during the evaporation regime with t_0 taken as the time at which the pattern started shrinking. Data was collected at $T_0 = 22\,^{\circ}\mathrm{C}$, $RH = 55\%$ and $\Delta T_H = 5\,^{\circ}\mathrm{C}$. (a) In the evaporation regime, the droplet diameter decreases while the interdroplet spacing remains constant. Shaded area refers to the standard deviation. (b) OM images from initial, intermediate and late stage analysed times (circled on the graph) show the constant interdroplet spacing created from the previous condensation regime.

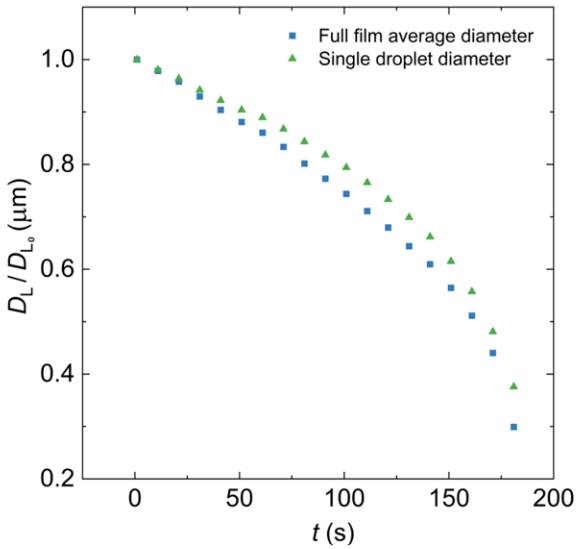

Figure 5.6. Analysis of all droplets in the field of view vs 5 individual droplets plotted as a normalised diameter in time.

of molecules from the liquid bulk to the atmosphere, resulting in a decrease in droplet volume.

$$\frac{\mathrm{d}V}{\mathrm{d}t} = -\frac{\mathfrak{D}}{\rho_o}\int \nabla C \,\mathrm{d}S\,, \tag{5.1}$$

where V is the volume of the lens, $\mathfrak{D}$ is the diffusion coefficient of the vapor, ρ_o is the density of the water, C is the concentration of the vapour in air, and S is the area of the droplet–air interface.

Different evaporation regimes are known to occur that are predominantly a function of the substrate, with the wetting interaction between the droplet and substrate determining the evaporation regime and temporal evolution of contact angle and contact area.[258,259] With the substrate in this case being a deformable fluid, classical hysteresis observed with sessile droplets on solid surfaces cannot occur.[30] The decrease in volume of the droplet has thus been shown to be analogous to that of evaporating sessile droplets on solid substrates.[260,261] The droplets maintain an equilibrium lens shape with consistent contact angles as the overall size decreases - constant contact angle (CCA) evaporation mode.[259]

Previous theoretical and experimental investigations of evaporating droplets in a CCA mode indicate a non-linear decrease in mass given from Eq. 5.1, resulting in a temporal volume relationship of $V^{2/3} \propto t$.[262] Due to the difficulty of directly analysing the evolution of BF droplet volumes or contact angles in time, a more suitable handle tracks the diameter. While at the length scale of these experiments ($D < 10$ µm), the focal plane is too small to properly differentiate between the three-phase contact radius and maximum droplet diameter, measuring the submerged maximum diameter D_L as per previous analysis is still appropriate as a result of the CCA behaviour. Without significant variation in the contact angle in time, a time-dependent linear relationship of $D^2 \propto t$ can be derived.[263]

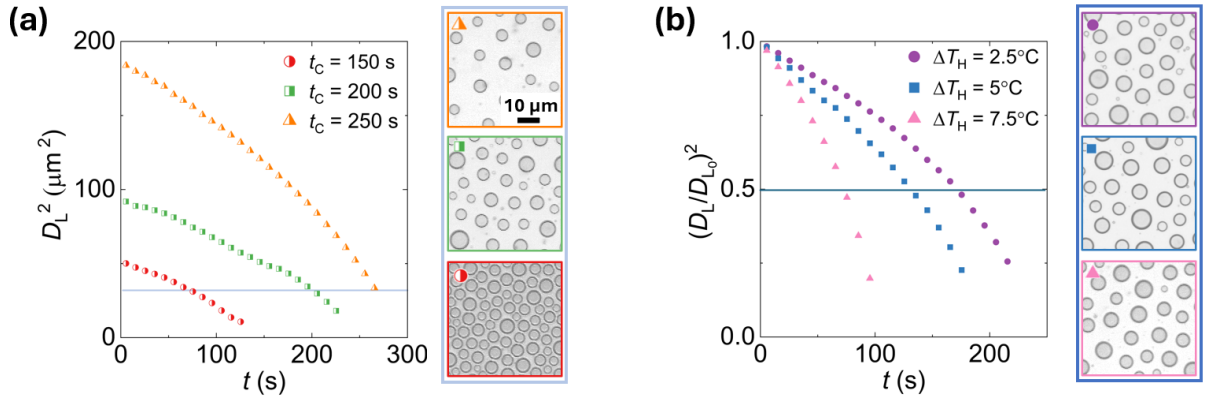

Figure 5.7. Kinetics of BF evaporation analysed for individual droplets averaged over 10 s intervals. (a) The square of droplet diameter monotonically decreases with time. The initial average diameter in the fully packed BF is controlled by varying the duration of the condensation regime t_c, before starting the heating cycle. Data corresponds to $\Delta T_\mathrm{H} = 5$ °C, $T_0 = 19$ °C and $RH = 66\%$. Snapshot images show patterns with similar average square diameter D

For a given Δ and RH, L_c is only a function of the condensation working time from the start of the BF formation in the highly packed condensation process, t_c. Therefore, combining the condensation and the evaporation steps provides a powerful handle for dynamic spatial modulation of BF patterns where both droplet diameter and area fraction can be controlled. Initiating the evaporation at different times from the start of the condensation nucleation allows the generation of BF patterns with different diameters and interdroplet spacing for given subcooling and superheating conditions. Fig. 5.7a shows diverse patterns with similar average droplet diameters but varying interdroplet spacing obtained by tuning t_c. The snapshot images correspond to $D_L^2 = 30\ \mu m^2$, showing that BF patterns can be arrested with different arrangements and area coverage at constant pore diameters. Additional control over the evaporating BF pattern is obtained by adjusting the elevated temperature set by the value of ΔT_H, *i.e.* higher superheating levels yield faster evaporation and smaller final diameters with larger interdroplet spacing at a given time from the start of the evaporation cycle (Fig. 5.7b). Constant average pattern diameter and interdroplet spacing can thus be obtained by arresting varying temperature evaporation cycles at different times, creating effectively identical patterns using different input parameters, see example snapshots of patterns in Fig. 5.7b.

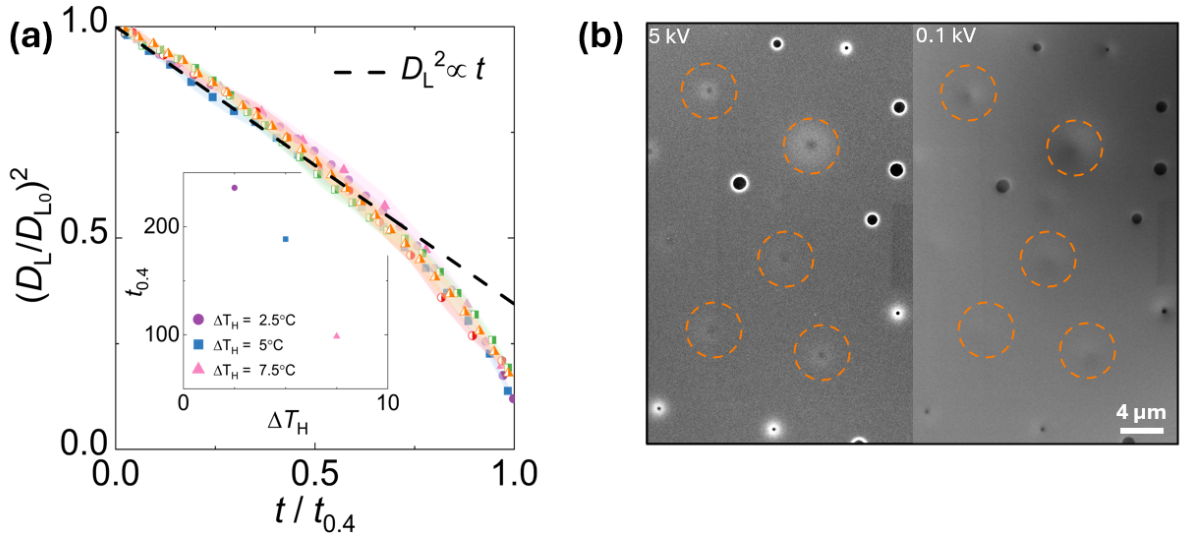

Figure 5.8. (a) Normalising pattern diameters and time allows the collapsing of all data presented in Fig. 5.7. (b) SEM images correspond to the top view morphology of sinking pores observed at late stages of the evaporation cycle. Sample imaged at (left) 5 kV and (right) 0.1 kV show what would have been droplets encapsulated by a thin polymer film right below the interface.

While the trends in droplet diameter reduction appear to be similar in Fig. 5.7b, higher temperatures above the dew point yield faster shrinking of the droplet. Normalising the x-axis by an arbitrary time, $t_{0.4}$, at which the average droplet diameter reaches 40% of its initial value ($D_L/D_{L_0} = 0.4$), accounts for the impact of superheating and in turn collapses all data captured at varied operational and environmental conditions onto a single curve

(Fig. 5.8a). A linear trend, $(D_L/D_{L_0})^2 \propto t/t_{0.4}$, provides a fair prediction of the collapsed data for short evaporation times until $(D_L/D_{L_0})^2 = 0.5$ is reached. At later times, a significant increase in the droplet shrinkage rate with deviation from the predicted linear trend is observed (Fig. 5.8a). At these times, some of the condensation droplets in the field of view appear out of focus, suggesting an increasing frequency of droplets moving downward relative to the focused reference frame at the top interface of the polymer film.[264] This vertical translation is clearly observed in the SEM images of the cured film cross sections as presented in Fig. 5.8b; droplets sink below the interface and eventually become fully encapsulated within the polymer. By varying the accelerating voltage in SEM analysis from 5 kV (left) to 0.1 kV (right), the penetration depth of electrons into the surface decreases.[265] Analysis of the secondary electron signal thus shows increasingly surface-only detail with lower voltages (Fig. 5.8b). Whilst all of these pores are visible with optical microscopy, potential pores that are identified at 5 kV indicate that they are subsurface with analysis at 0.1 kV.

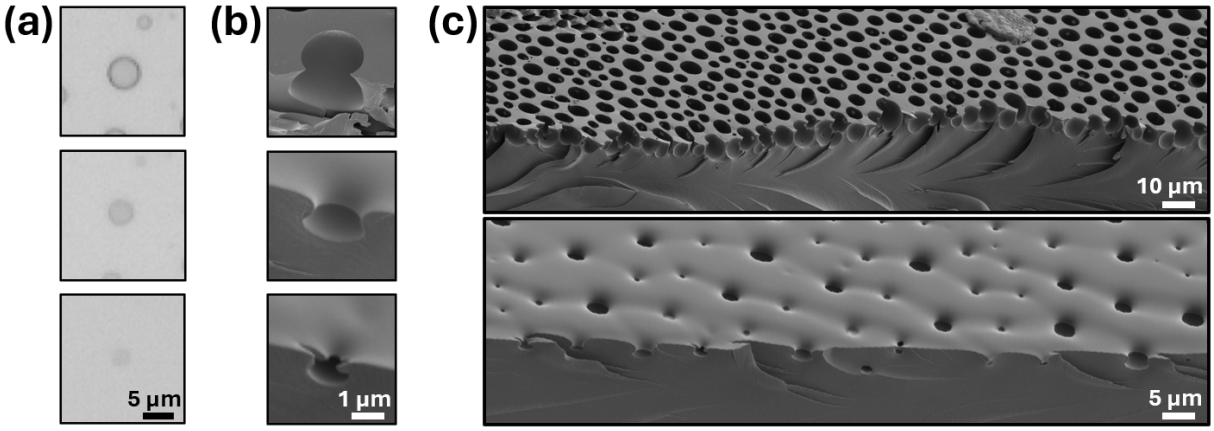

Figure 5.9. Downward translation of droplets out of the optical plane at the air-polymer interface. (a) OM images representing a 10 s interval between each image. (b) SEM imaged cross-sections of droplets at high packing and partially encapsulated states, where (c) the downward motion of droplets deforms the normally flat interface.

As the BF approach is employed here as a surface patterning technique, later evaporation times where initial water droplets are no longer all on the surface are not considered for further analysis. Compared to the condensation regime, at the final stages of evaporation where the downward translation of droplets is observed, the polydispersity in droplet diameters increases up to a maximum value of $g \approx 0.3$. This increase arises from the initial polydispersity in the highly packed droplet population, augmented by the different evaporation rates and translation of droplets within the field. By analysing the moment at which the majority of droplets experience a sudden decrease in contrast and focus (Fig. 5.9a), this can be interpreted as a change in the normal regime and interpreted as the downward translation away from the optical plane. The exact onset is difficult to analyse, particularly at low elevated temperatures where the shift is gradual. Further,

differentiating between tiny droplets in the field of view and stabilised ones presents additional challenges arising from having only top-down *in situ* optical microscopy. The data shows the contrast change occurs at around $D_L/D_{L_0} \approx 0.3$ (Fig. 5.8a), regardless of the maximum droplet diameter or the set temperature. This corresponds to a packing of around 10% of the initial highly packed regime, and an overall area fraction of $A_f \approx 0.1$. The near constant translation moment as a function of size makes sense given the collapsed data sets independent of temperature and size in Fig. 5.8a. Cross-sectional SEM analysis of cured spatially varied scales confirms the encapsulated droplet states observed in Fig. 5.8b. Fig. 5.9b/c shows varied states of sinking droplets, where the overall air-polymer interface goes from planar with sharp contact angles in pores, to deformed with partially encapsulated droplets. While the route onset of droplet encapsulation is unclear without further analysis of the temperature and surface tension gradients within the system, the sinking of droplets below the surface defines the patterning limits as predictable surface features are no longer created.

5.3 Pattern permutations

Beyond the two main temperature-controlled patterning modes, further modulation of the resultant patterning can be created via combinations of the modes and subsequent manipulations to the set-up and cured designs. These subsections elaborate upon existing avenues and potential new routes for the fabrication of patterned films.

5.3.1 Bimodal patterns

Dynamic droplet patterns are transformed into static porous designs only after UV exposure of the photopolymer in the temporally arrested BF approach. Therefore, the reversible condensation and evaporation regimes can be arranged in repeated cycles to attain diverse BF architectures prior to polymer curing.[186] The evaporation regime creates free surface area on the polymer film interface by reducing the area fraction of BF pattern. These free areas can be subsequently re-patterned by generating a new population of droplets as the polymer film is cooled below the dew point again, restarting the condensation phase. In this post-evaporation regime of re-condensation, original droplets grow simultaneously with the formation of new droplet families. Upon UV exposure, the bimodal distribution of the templating droplets creates novel BF designs.

Fig. 5.10 schematically illustrates the experimental procedure with *in situ* microscopy images of the BF patterns produced through a simple combined cycle of condensation, evaporation and re-condensation:

1. An initial subcooling period of condensation is completed to establish highly packed

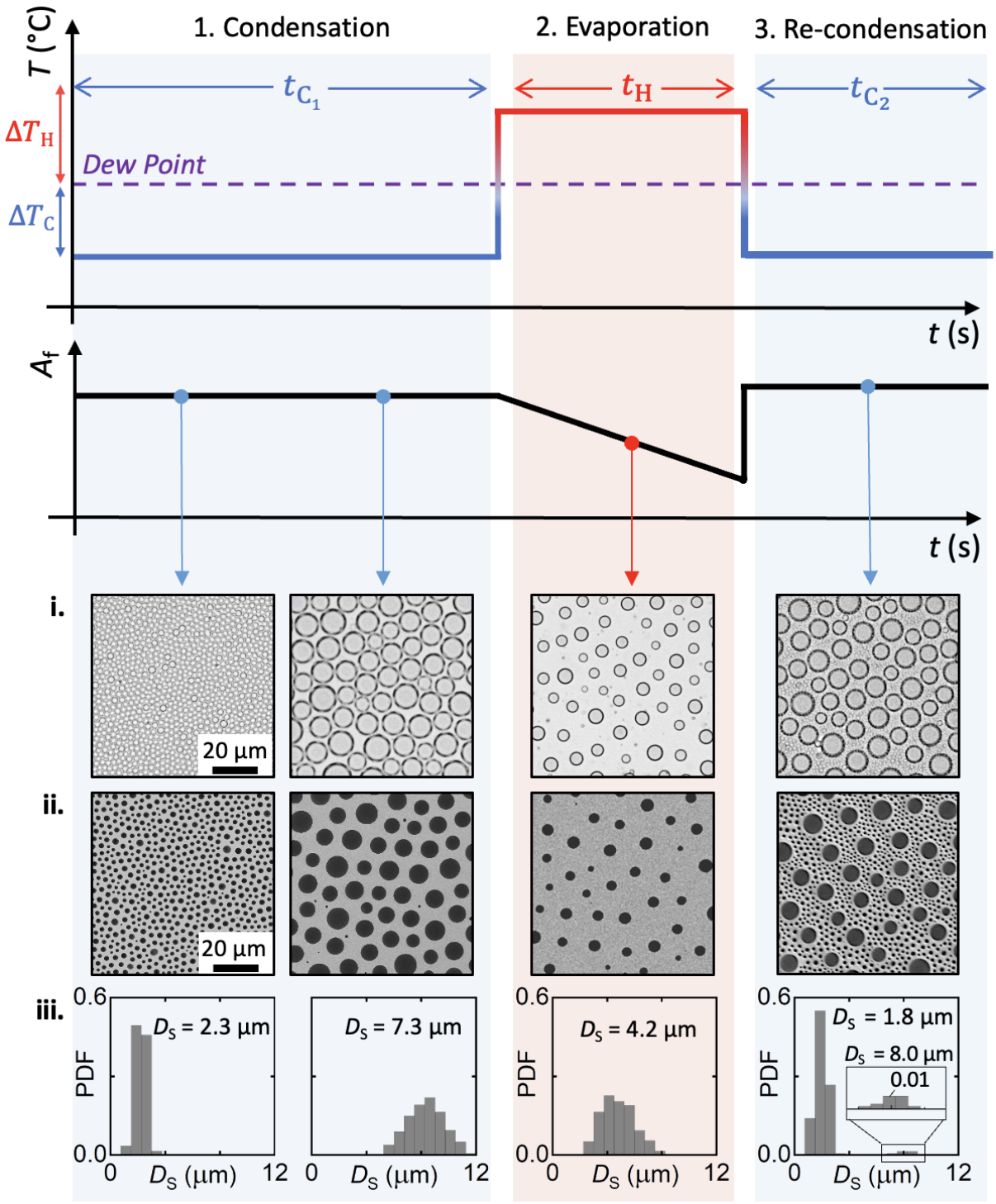

Figure 5.10. Schematic illustration of the complete experimental process followed for hierarchical BF patterning, demonstrating the modulation of temperature around the system dew point and examples of respective patterns obtained. Data was collected at $T_0 = 22°C$, $RH = 36\%$, $\Delta T_C = 10°C$ ($t_{C_1} = 250$ s, $t_{C_2} = 140$ s) and $\Delta T_H = 5°C$ ($t_{H_2} = 250$ s). (i) Real-time OM images capturing the maximum diameters of condensation droplets underneath the interface of the polymer film with air. (ii) SEM images of samples cured at the discrete times showing the pores' openings on the surface of the polymer film. (iii) Probability Density Function of the pore diameters, derived from the SEM images.

BF patterns. This regime dictates the specific interdroplet spacing for the large droplet domains.

2. The system is heated, reducing the droplet packing and modulating the A_f. The droplet diameters decrease in their radial dimension during evaporation whilst maintaining a constant L_c

3. By re-cooling the polymer film, condensation as a result of subcooling is restarted. This re-condensation regime manifests in the appearance of new condensation nucleation sites on the free surface of the polymer, as well as through the growth of the original droplets.

SEM images of the cured films and the corresponding histograms of pore diameters are presented in Fig. 5.10 (ii) and (iii), respectively. The visible diameters on the (i) liquid and (ii) solid films differ as they are associated with the full droplet diameter visible during liquid analysis and the pore opening diameter visible with SEM. The pattern histograms in (iii) show the polydispersity in pore diameters and their distribution at different times, demonstrating the transition from unimodal to bimodal droplet distributions. The active regulation of the substrate temperature allows the control of the overall droplet spacing in the primary regime, modulates the area fraction and facilitates the formation a new droplets. The use of active UV polymerisation enables the translation of these liquid-liquid patterns into cured designs.

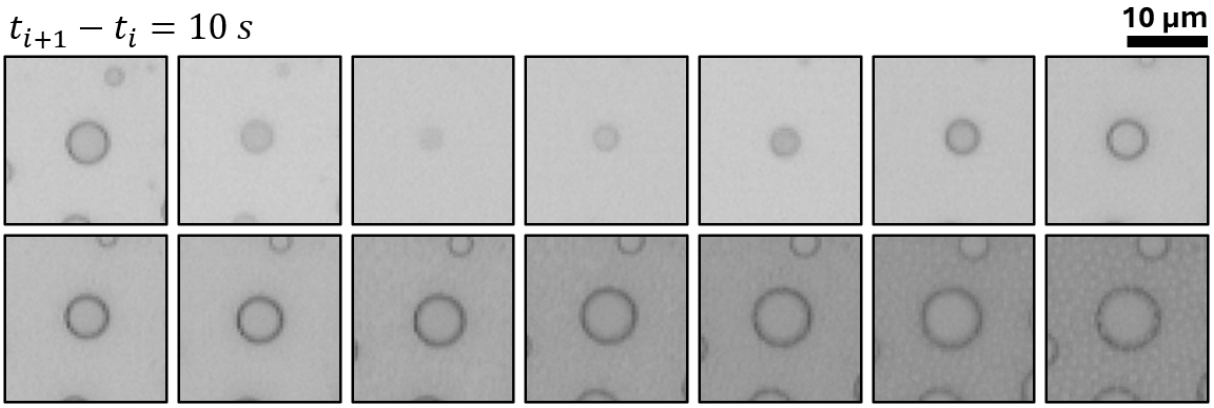

Figure 5.11. Life cycle of a droplet from evaporation to re-condensation. The secondary condensation droplets are observable in the final image.

Limitations to the hierarchical pattern arise with the working time and temperatures used. Whilst near complete evaporation of the droplets in the evaporation regime can lead to droplet sinking and encapsulation beyond $A_f < 0.1$, these droplets can be re-surfaced to attain the equilibrium shape, providing full evaporation has not occurred (Fig. 5.11). Upon reestablishing a subcool temperature, the droplets that does not appear with sharp contrast reappears in-focus, suggesting re-attachment at the air-polymer interface. If the evaporation working time is too long, the droplets become lost and re-organise in the bulk.

Although it is difficult to quantify the actual z-height of the droplet, qualitative results indicate that both the droplet size and thermal gradients affecting the flows within the polymer can have significant effects.

Upon changing the substrate temperature for the re-condensation regime, the effect of nucleation density discussed in Sec. 4.2 is more prominent. Lower nucleation density is more obvious at low supersaturation (smaller ΔT), where preferential nucleation of new droplet families occurs. Droplets tend to nucleate far from the large droplet domains and at a lower nucleation density than initially observed in the primary condensation (Fig. 5.12). The existing large droplet domains create a horizontal gradient in vapour pressure with a reduced vapour pressure which limit new nucleation of droplets at the near interface.[235] An exclusion zone with little to no new nucleation droplets is apparent at early re-condensation times, characteristic of nucleation of films with a low number of nucleation sites.[152] This effect is mitigated to a degree with larger supersaturation levels (*e.g.* $\Delta T > 10\,^{\circ}\mathrm{C}$) where high nucleation density is observed - compare the secondary nucleation densities between Fig. 5.12a vs Fig. 5.12b. Fig. 5.12b shows SEM images of the samples cured at early times with low nucleation density as a result of the saturation. Alongside the evaporating size limit, this prescribes further limits and design guidelines for the creation of bimodal patterns; if the distance between large droplet domains is too small, condensation will favour the continual growth of existing droplets rather than new condensation families. Further, with only low supersaturation, condensation manifests with low nucleation density, meaning effective bimodal patterns are best created by evaporating droplets to near their limit, before re-condensing at high levels of subcooling.

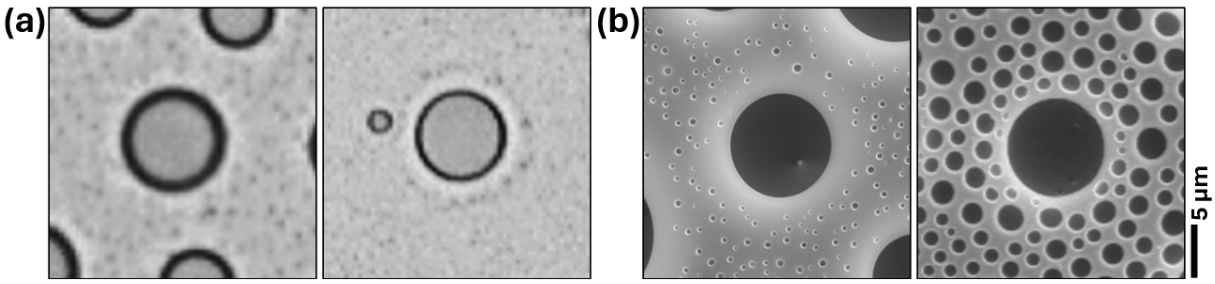

Figure 5.12. (a) Optical microscopy images of new nucleation at low and high supersaturation. (b) SEM images of bimodal samples cured at early and late times of re-nucleation growth regime.

5.3.2 Gradiented patterning

The ability to create gradients in topography opens up new potential applications for the fabricated patterned films and further demonstrates the versatility of the fabrication approach, enabling the fabrication of architecture beyond what is classically attainable self-assembly techniques.[242] The evidenced control over pattern evolution on NOA63 with

substrate temperature control combined with the use of photocurable polymers thus facilitates new capabilities to create feature gradients, as illustrated in Fig. 5.13.

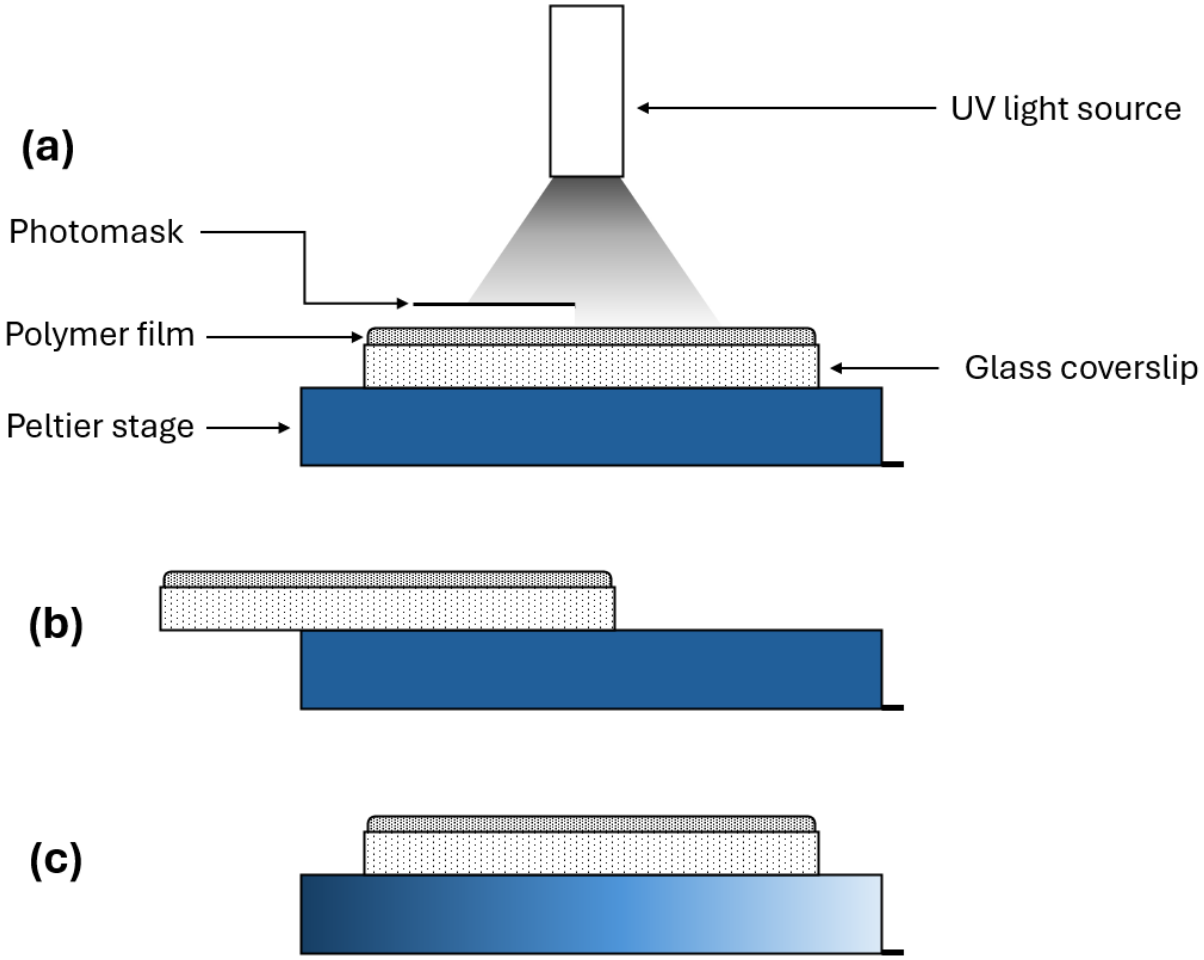

Figure 5.13. Adapted schematic from Fig. 3.10 to show fabrication of gradiented patterns. (a) Use of an opaque photomask to spatially control the curing location, (b) variation of the applied cooling location and (c) variation of the substrate cooling temperature indicated by the colour change.

Photomasking. The strict feature size control attained by the short UV exposure further provides the ability to spatially control the patterning on a single substrate beyond temperature modulation. As a proof of concept, opaque UV photomasks were used to selectively cure sections of the NOA63 films at discrete times. While relatively sharp pattern borders with increased geometrical control over temperature modulation could be attained, experimental difficulties arise with locating the mask above the liquid BF without touching it, whilst limiting the distance to decrease light diffraction upon curing. More details on future perspectives are discussed in Ch. 7.

Temperature gradient. Analysis of the pattern evolution on NOA63 demonstrates good control over the feature sizes through the Peltier temperature handle. Provided that the environmental parameters, namely RH and T_0, can be characterised, the imposed

temperature on the polymer film determines if the droplets grow or shrink. As such, by defining a temperature gradient from the Peltier device across the x-axis of the stage, different growth rates can be harnessed leading to varying feature sizes across a single sample (Fig. 5.13b/c).

Metal strips 1 mm thick were placed partially across the stage and stacked on each other to diffuse the intended cooling. By varying the location of the strips, type of metal, and location of the polymer film, a temperature gradient could be achieved across the surface. The most abrupt gradient (Fig. 5.13b) consists of the polymer film placed only partially on the Peltier device, and varies to more diffuse gradients with increased numbers of offset metal strips. With real-time analysis of the pattern feature parameters, the right-hand side of the polymer (or fastest growing region) could be monitored, and the sample cured at the specified feature size. While the growth of highly packed droplets occurs in a self-similar regime, the temperature difference impacts the growth rate providing a condensation flux imbalance. The coalescent-dominant regime works to smooth the gradient where smaller droplets coalesce into the larger ones (Laplace pressure imbalance), however well-defined gradients can still be achieved. The pattern gradient can hence vary with feature sizes of average $D_S \approx 10$ µm to no features in as little as 100 µm, to the same variation in size over millimetre scale (see differences in Fig. 5.14).

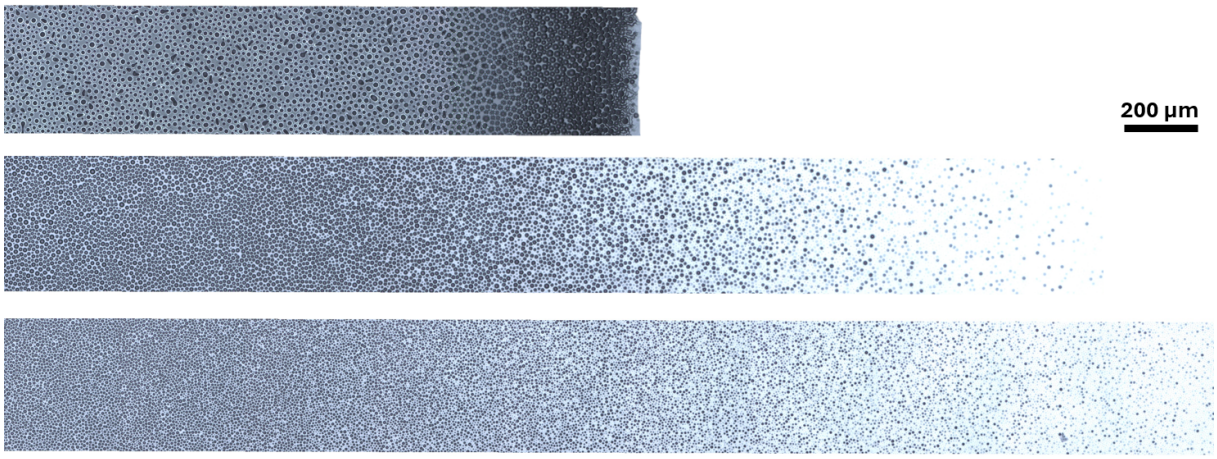

Figure 5.14. Examples of increasingly diffuse pattern gradients created from temperature variation. Patterns ranging from a near binary transition of features to no features over hundreds of µm to gradient transitions over the order of mm.

5.4 Pattern replication

Replication of classical BF patterns has previously been done to create inverse, protruding features on samples using common elastomeric materials such as PDMS.[199,266–268] However, with BF's often created on thin and brittle PS films, each replica is made with a BF pattern which is then commonly dissolved to remove the structure.[199] As a result, the

initial BF pattern is destroyed and one BF patterned sample can make one replica.

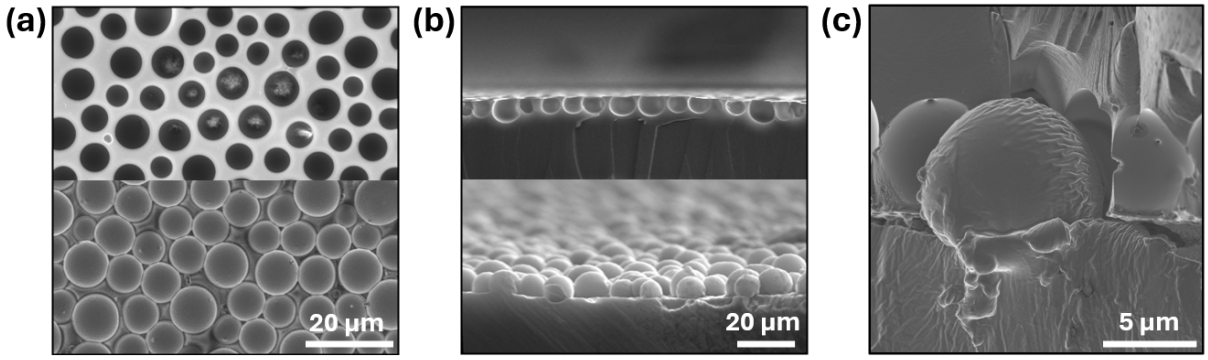

Figure 5.15. Overview of SEM-imaged replicated samples. BF and replication (a) top view and (b) cross-section. (c) Detailed view of BF - PDMS replication prior to separation.

The temporally arrested BF approach is completed on strong cross-linked polymer films meaning the replica can be separated from the mould without causing permanent damage. While a pore shape limit of depth/negative curvature must exist, the pattern can be replicated for samples fabricated in NOA63 without leaving artefacts attached in the BF pore. Successive replicas can thus be created for a singular BF pattern.

Several silicone elastomers were used to replicate the BF patterns before deciding on Sylgard 184 (Dow Corning). Sylgard 184 is a low surface energy material that provides easy release from the BF mould without leaving artefacts.[66] Sylgard 184 is mixed at a 10:1 ratio of base to hardener and is degassed and poured onto the BF as per Sec. 3.3. Fig. 5.15 shows top view and cross-sections of the PDMS - BF mould post curing. The images show good conformation of the PDMS to the BF mould, indicating successful, high fidelity replication of the features. Not only do the protruding replica patterns serve many different applications in their own right, but they can provide new indirect quantitative analysis of the BF geometry that is difficult to attain due to the negative curvature. Fig. 5.16 shows examples of different replicated patterns.

5.5 Discussion

BF patterning harnesses the dynamic templating of droplets to pattern a polymer film. While in the classical BF approach, limited systematic control over the feature characteristics is harnessed, the temporally arrested approach creates new potential for novel patterns. The benefits of a dynamic template (a growing/shrinking water droplet lens) is harnessed via *in situ* arresting through UV exposure, curing and solidifying the transient design. By controlling the experimental time and substrate temperature, patterns are created consisting of highly packed features at varied sizes, spatial variations of differing

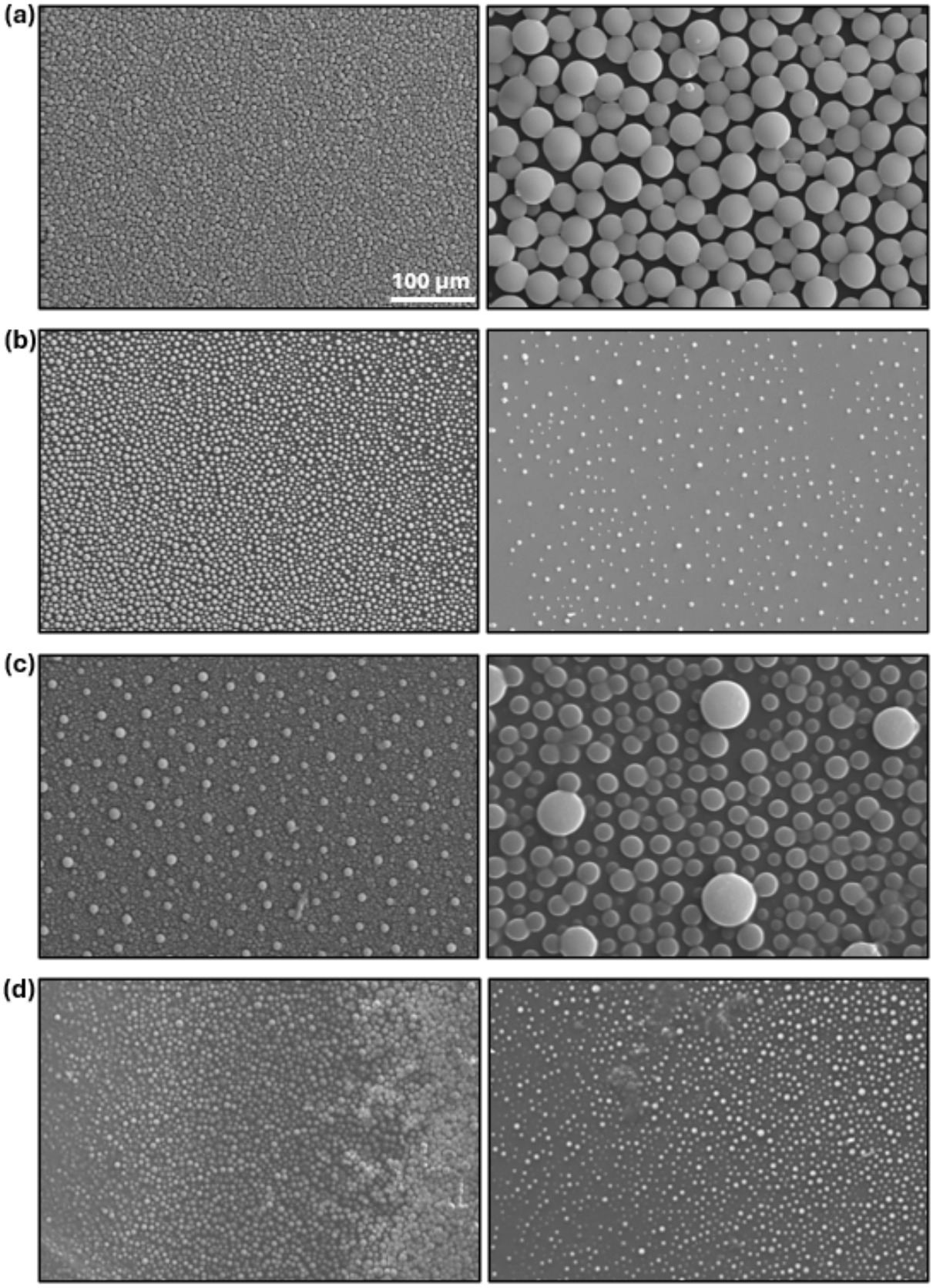

Figure 5.16. Examples showing the range and variation of replicated BF samples. (a) Highly packed, (b) varied spacing, (c) hierarchical patterns and (d) gradiented replica samples.

packing densities and permutations of these combined effects. A wide breadth of pattern configurations can thus be created with the same equipment and experimental design.

Analysis of the transition from liquid BF design to cured pattern indicates minimal influence of the curing mechanism. The transient UV exposure rapidly stabilises the droplets and arrests the pattern evolution in 1 s at 650 mW/cm^2. With continued cooling applied at the time of curing, any potential heating effect from the irradiation is mitigated as much as possible, and no detectable influence is observed for droplets in the optically resolvable size range. As the level of subcool determines the average growth rate of the pattern, it is important to consider the transition time from liquid-liquid pattern to cured design. Lower levels of subcooling implies a slower growth rate of the design. Although this can take longer to reach the desired feature size, the UV exposure is statistically less significant as $t_{curing} \ll t_{condensation}$. With real-time analysis of the pattern characteristics using the developed code, arrest of the design at the desired feature characteristics is thus more accurate with slower growth rates. While not characterised due to the success of NOA63 as a polymer film, viscosity can also impact this cured design. With growth rate a function of coalescence events in this regime, the time taken for coalescence to occur can manifest in the final design with the arrest of partially coalesced droplets. NOA68 produces similar high nucleation density to NOA63, but has a viscosity over 2× that of NOA63. For coalescence to occur, draining of the liquid film separating droplets has to occur which is a function of the droplet size and film viscosity.[99] This is evident in the curing of NOA68, where cured films exhibit a greater number of partially coalesced pores (Fig. 5.17). Not only is the coalescence duration a factor, but qualitative handling and fabrication of BF on the polymers indicates NOA68 films require higher UV doses to stabilise the droplets, despite having the same recommended energy dose on the spec sheet.[191] Experimental design choice thus prioritises fast coalescence and slow growth with rapid polymer curing, facilitating accurate arrest of the desired pattern characteristics.

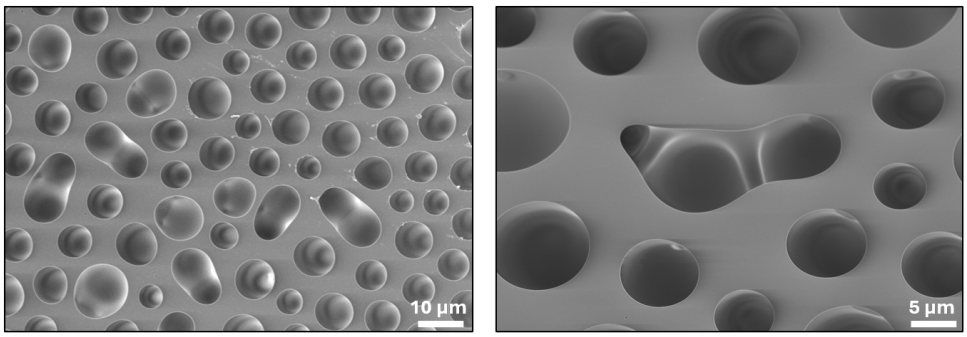

Figure 5.17. Images of cured samples with high amount of partially coalesced droplets arrested.

Whilst the majority of the experimental work has been completed in the optically resolvable range using in-house microscopes for studying the pattern evolution, SEM was used

to view patterns cured before they were detectable. From Ch. 4, the critical radius for nucleation within the system used is calculated to be around 20 nm. The earliest mentions of BF in literature by Rayleigh and Aitken describe the scattering of light from the plano-convex lens of water droplets on a hydrophobic surface.[80,81] Similarly, before the optical microscopy system can resolve any droplets, the liquid film increases in its opacity from the completely transparent unpatterned state. By curing at the onset of colour change, the patterned films have droplets of diameters in the visible light range (> 350 nm) as the light rays detected by our eyes have been scattered by the surface. Fig. 5.18 shows examples of some cured films with pores as small as 100 nm. While evidently possible, the feasibility of arresting the patterning at near-critical nucleation size presents new challenges for fabrication. At this early experimental working time and small length scale, slight variations in substrate temperature can be the difference in observing pattern and no pattern. When cover slips are not completely flush with the Peltier, the non-conformal alignment results in more noticeable variation of patterns as pockets of insulating air consequently delay the nucleation and growth of droplets. Further, the impact of UV curing becomes much more significant as only small amounts of energy result in the evaporation of nanodroplets - an undetectable volume change in large droplet sizes. Best results were thus achieved in high relative humidity environments with near to ambient temperature dew point. At this temperature, using a low subcooling temperature on the Peltier device is essential for maximising the nucleation density at small, potentially pre-coalescent scales. The temperature difference also limits the net evaporation upon curing, enabling an effective transition from the liquid-liquid pattern to cured state.

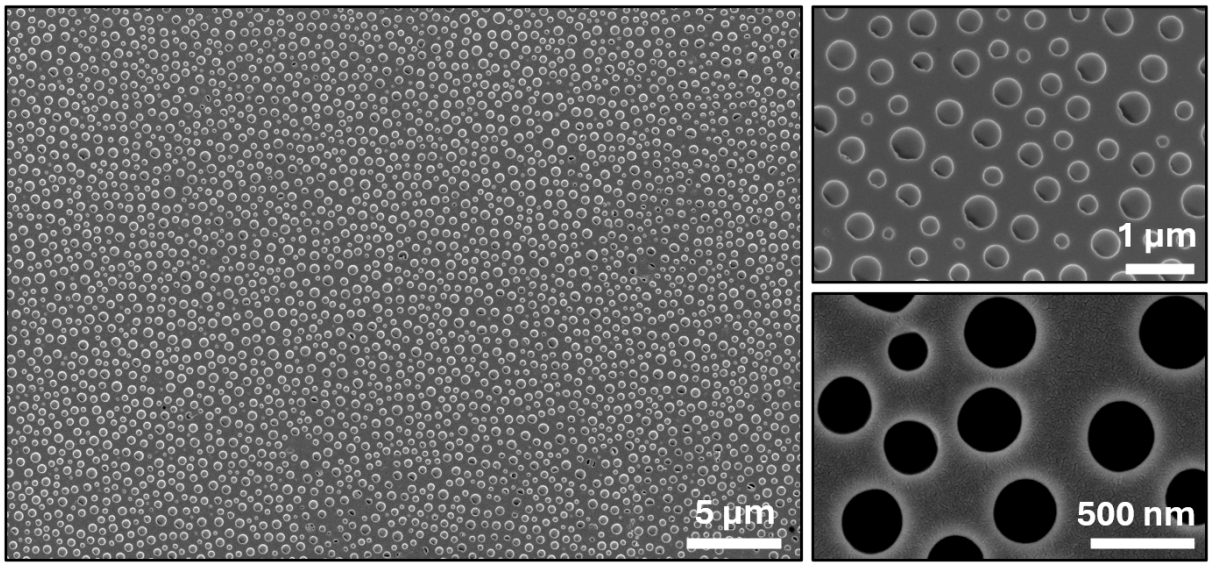

Figure 5.18. Examples of wide-scale patterns consisting of pores of $D_S < 500$ nm.

Not only is the size and spatial configuration of droplets important for surface characterisation, but the pore shape with replica samples can drastically influence the end functionality. Analysis of cured films can be done to elucidate the pore geometry which is difficult in

the liquid state. By infiltrating the pores with fluorescent dye, LSCM can be used to attain a z-stack of the cured pattern and view both the pore diameter D_S and largest diameter D_L simultaneously. Fig. 5.19 highlights both dimensions in a composite flattened image from the z-stack. Analysis shows $D_S/D_L = 0.8$ regardless of the packing (highly packed and partially evaporated droplets). This value is in agreement with combined liquid-liquid analysis and SEM analysis of solid films, where respective area fraction plateaus at highly packed states indicate a ratio of $D_S/D_L = \sqrt{(A_{f|D_S}/A_{f|D_L})} = (0.44/0.7)^{1/2} = 0.8$. The constant ratio, regardless of packing, indicates that droplets are in a constant contact angle regime, maintaining droplet morphology and that minimal polymer shrinkage and curing effects affect the droplet morphology. Ultimately, the ratio is set by the balance of relative interfacial energy differences, allowing potential for future shape manipulation as a result.

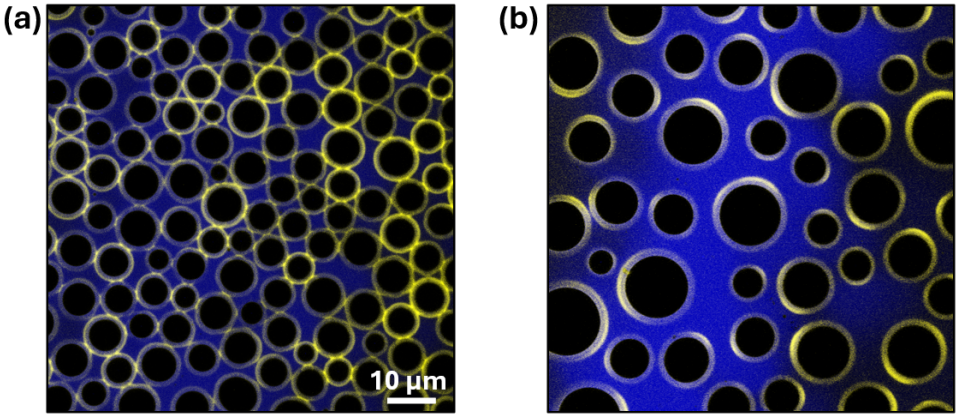

Figure 5.19. Shape analysis using 3D LSCM scans for (a) highly packed and (b) spatially modulated BF samples. The blue corresponds to the reflected wavelength of light highlighting the pore opening whereas the yellow is excited emitted light indicating the maximum pore diameter.

5.6 Summary

- Temperature control via the Peltier device provides the main control handle for varying the pattern evolution. Highly packed size variations and spatially varied permutations can be readily fabricated by setting the temperature below and above the dew point temperature, respectively.
- Photosensitive polymers enable effective temporal arresting of the liquid-liquid pattern. Analysis of cured samples shows negligible curing effects for microscale droplet patterns, facilitating access to a wide array of pattern configurations, a summary of which can be viewed in Fig. 5.20.
- Pattern permutations including bimodal and gradient designs can be readily fabricated by the harnessed control in the temporally arrest breath figure technique.

- Extensive optical microscopy and SEM characterisation demonstrates the design guidelines for effective patterning;
  - ▶ Area fraction of droplets can range from $0.1 < A_{f|D_L} < 0.7$. The high packing limit is a combination of the droplet ordering and viscous boundaries separating the droplets. At low area fractions in evaporative regime, droplets tend to sink and become encapsulated within the polymer.
  - ▶ High relative humidity and large subcooling is needed for nanoscale patterning to ensure high nucleation density and minimal evaporation during UV curing.
  - ▶ Large subcooling upon the re-condensation regime is needed for effective bimodal patterning to enhance the nucleation density of the secondary droplet families.

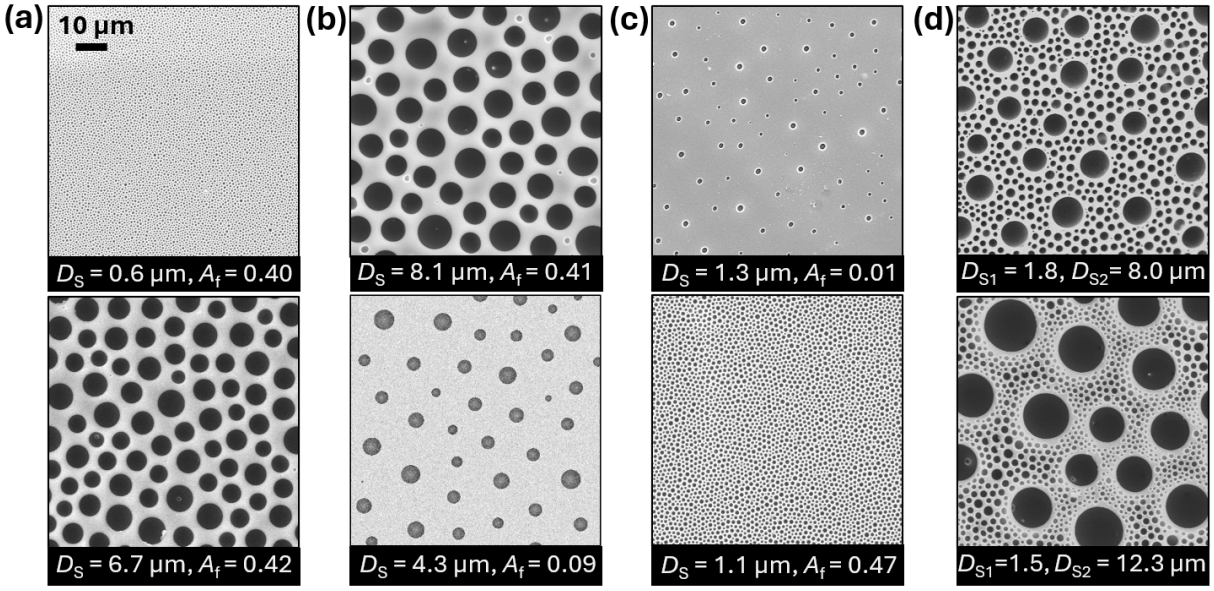

Figure 5.20. SEM images of the cured patterns attainable from the temporally arrested BF process, showing the diversity of the programmed design. (a) Constant area fraction at varying diameters. (b) Constant interdroplet spacing at varying diameters. (c) Constant diameters at varying interdroplet spacing. (d) Varied hierarchical designs. More details are available in the original figure of the published work.[186]

Chapter 6

Wetting behaviour of breath figure patterned surfaces

This chapter concerns the initial characterisation of interfacial wetting behaviour on patterned samples created within this work. Insights delineate how design over size and spacing achieved with the temporally arrest breath figure approach can create tuneable wetting properties.

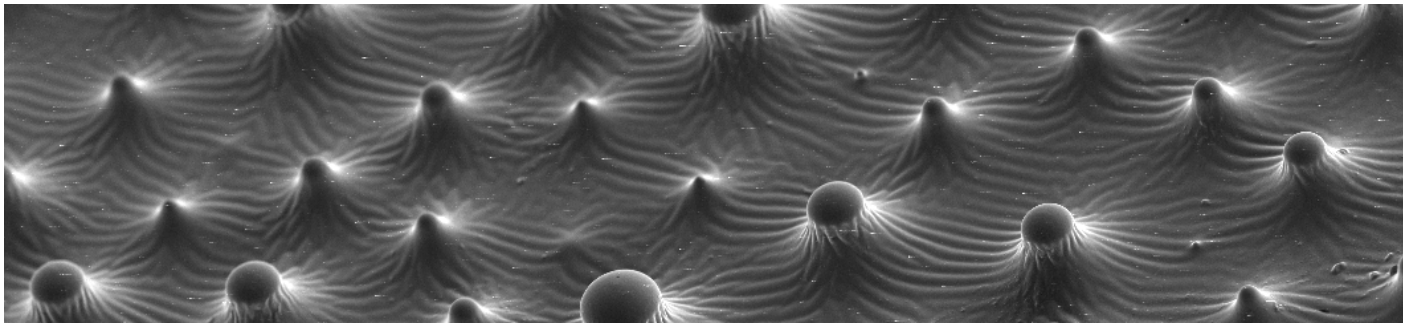

"God made solids, but surfaces were the work of the devil."

Wolfgang Pauli

6.1 Introduction

The wetting interaction of liquids on solid surfaces is not just of fundamental scientific importance, but relevant to a vast variety of industrial applications.[40] With the ability to strictly control the surface morphology through the developed patterning technique, initial characterisation of the wetting behaviour is performed to understand the functional properties of the surfaces, and how modulating the surface features can influence this behaviour in anticipation of future applications.

In such fields where wetting is important, the role of liquid droplets on surfaces is primarily characterised by the contact angle of a static sessile droplet and subsequent dynamic measurements. As a result, sessile droplets are commonly used to probe the key characteristics of surfaces, where the basic interactions tell us information about how the droplet resides on the surface, if it is slippery or adhesive, and even how the droplets will behave in motion.[30] If a surface is significantly rough, air pockets are entrained within the microstructure and remain below a sessile droplet, known as the Cassie-Baxter state.[6] Provided that the total energetic cost of the sum of the liquid-air interfaces is less than the energy gained by the liquid droplet completely conforming to the roughness, the droplet remains in this metastable state resting on top of the roughness features on a surface-air composite interface.[29] As such, a large increase in apparent contact angle is observed from the complementary flat surface. The underside of the droplet bridges the gap between rough features, contacting an extremely low fraction of the solid surface. Control of the surface structure to modulate the subsequent wetting regime is thus significant to any interfacial-related application, where anything from the control of liquid collection to the transport of fluids relies on these interactions.

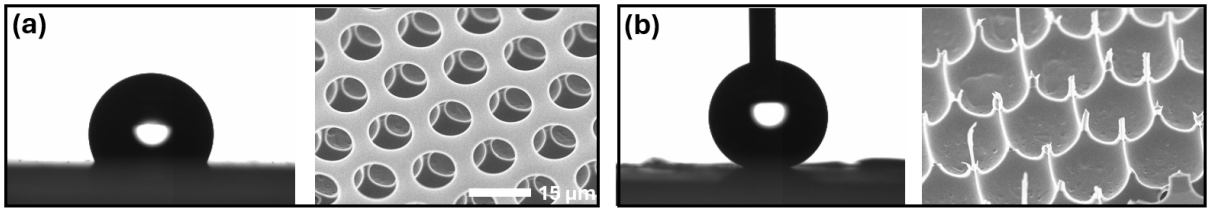

Figure 6.1. 3 µL droplet on (a) classical BF and the corresponding (b) pincushion structure, fabricated on PS-CAB from Ch. 2. The high contact angle on the pincushion with no pinning effects results in the droplet not detaching from the syringe.

Breath figure surfaces are a low-cost and scalable way of fabricating surfaces with specific porosity. Previous research has well demonstrated different states of wetting from BF samples, creating both hydrophilic, hydrophobic and even stimuli-responsive structures.[136,172,269] Due to the combination of chemical and structural optimisation often required for specific wetting scenarios (*e.g.* superhydrophobic surfaces), various methods have included direct synthesis of BF films via low-energy fluorinated polymers[108,172,270]

and various post-fabrication modifications.[162,271] In comparison to the corresponding BF surfaces, pincushion design generated by removal of the top surface level (Sec. 2.4) exhibits significantly reduced solid surface area, thus yielding large water contact angles. Fig. 6.1 shows a 3 µL droplet on a BF sample and the corresponding pincushion film, creating an increase in contact angle from $\theta \approx 116°$, to $\theta > 160°$ where the contact angle cannot be effectively measured due to the extremely low hysteresis and non-wetting behaviour where the droplet will not detach from the deposition needle.

Li *et al.* characterised the dynamic behaviour of impacting water droplets for porous BF and pincushion films of varying size, demonstrating that the spreading of the droplets increases adhesion to the surface and limits the rebounding potential of incident drops.[272] The strong adhesive effects in some BF samples have been demonstrated due to isolated pores with entrapped sealed air pockets engendering a vacuum effect that diminishes droplet movement.[273] While final BF structures can consist of interconnected pores which enable the fabrication of low adhesive pincushion structures (Fig. 6.1), isolated pores such as ones created in this research with NOA polymers engender high adhesion. The attempted removal of droplets creates a negative pressure, facilitating strong adhesion to the surface, which can be used for controlled fluid manipulation and even anti-splashing scenarios.[274] Further, the specific geometry of BF pores residing predominantly below the surface has negative curvature which makes the trapped air pockets particularly stable upon complete submergence.[275,276] This plastron-like trapped air is reminiscent of aquatic insects and can create oil and bubble-repellent surfaces.[26] Replica moulding BF structures with hydrogel materials to create the inverse replica has also demonstrated interesting oleophobic properties.[255,277]

The temporally arrested BF technique enables systematic control over self-similar pore sizes, producing strict design over desirable air-surface fractions. Highly packed porous samples with constant area coverage can be fabricated with the average features sizes ranging across an order of magnitude from 100's nm to 10's µm. Further, the ability to readily modulate the area fraction through evaporation of the pre-established BF pattern as described in Sec. 5.2 facilitates novel scope for modifying the interfacial wetting interactions. As an initial but fundamental analysis of the surface functionality, the wetting behaviour in static and dynamic conditions is characterised in this chapter. For comparison, measurements on replica samples in PDMS are also taken to show the range of wetting capability.

6.2 Experimental Methods

A range of samples using NOA63 were fabricated as previously described in Ch. 3. Different feature size and packing variations were created for BF samples, with further samples

replicated in PDMS to characterise both porous and protruding surface structures.

Surface wettability was characterised by measuring the water contact angle for different volumes of sessile droplets, with a minimum of 5 droplets measured per sample. A lab-made shadowgraphy set-up was created to measure static contact angles using a Nikon D750 DSLR equipped with a Navitar Zoom 1-60135 lens, and a 200 mW LED collimated backlight source (M530L4-C1 - 530 nm, ThorLabs). Analysis was completed on ImageJ software.[201]

Advancing and receding dynamic contact angles[30] were measured using a Theta Tensiometer (Attension, Biolin Scientific) by slowly inflating and deflating a sessile droplet. Contact angles were measured through geometrical analysis of the droplet on the OneAttension software (V4.0.4). Automatic dosing was completed at a flow rate of 0.1 µL/s for both advancing and receding contact angles. As noted in the discussion, droplets of over 20 µL were used at points to attain a large enough baseline diameter for effective measurement of an equilibrium receding contact angle due to strong adhesion.

6.3 Breath Figure Porous samples

6.3.1 Static contact angle

Samples of systematically increasing average pore size were created by varying the condensation working time in the BF approach, creating average pore sizes ranging from sub-micron to $D_S > 5$ µm. In this highly packed growth regime, droplets grow in a self-similar regime at constant area fraction, resulting in a pore coverage of $A_{f|D_S} \approx 0.44$ at the free surface for cured samples (Fig. 6.2a).

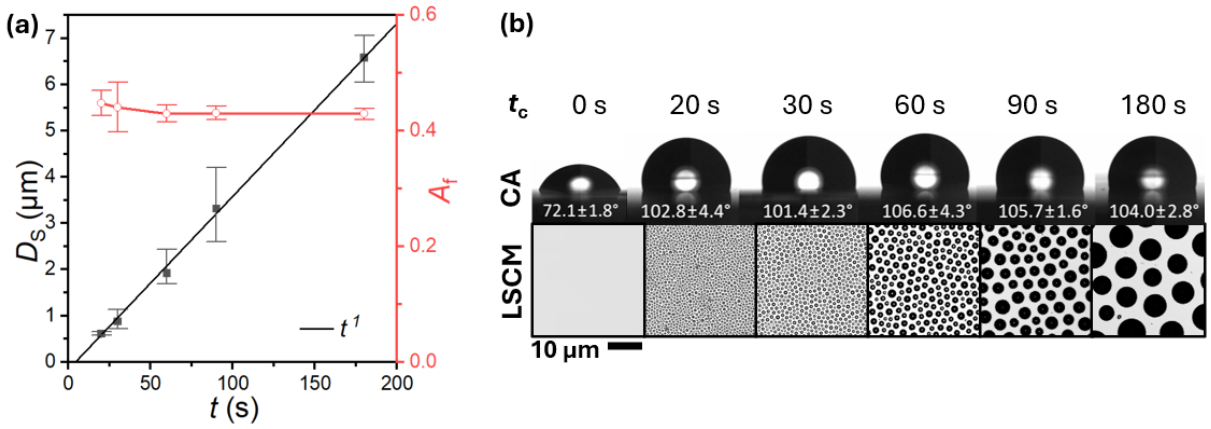

Figure 6.2. (a) Graph reprinted from Ch. 5 showing variation in pore size of fabricated BF samples. (b) Contact angles of 5 µL sessile water droplets were analysed on the respective samples.

5 µL droplets were placed on the surface with their contact angles measured (Fig. 6.2). An

average of $72.1 \pm 1.8°$ (mean $\pm$ standard deviation) was found for flat NOA63 and $104.0 \pm 1.9°$ for highly packed patterned samples. An average contact angle increase of nearly 50% demonstrates an increased hydrophobicity of samples solely through the creation of highly packed pores. Microscopic imaging of the sessile droplets on the patterned surface further showed no significant in-homogeneity along the contact line on the solid surface across the feature sizes tested (Fig. 6.3). No macroscale pinning effects from perimeter pores were noticeable, indicating valid analysis with the droplet radius much larger than the characteristic scale of porosity.

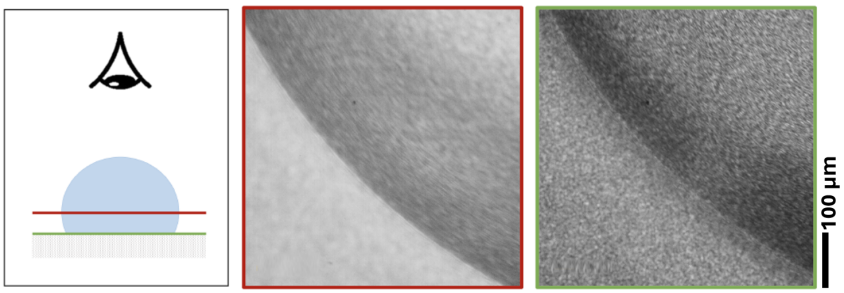

Figure 6.3. Top view optical microscopy image of a 3 µL water droplet on a BF patterned surface with large pores ($D_S > 5$ µm). The contact line on the surface (green framed image) is masked by the maximum droplet diameter (red framed image) when viewed from the top and can be imaged only through high magnification objective with a thin focal plane (high numerical aperture).

The constant contact angle value regardless of the pore size suggests the droplets must be in the Cassie-Baxter regime, with air trapped within the pores. The observed apparent contact angle can be modelled based on the equation,

$$\cos\theta_{CB} = f_1 \cos\theta_1 + f_2 \cos\theta_2 \,, \tag{6.1}$$

where f_1 and f_2 are the solid and air fractions respectively. θ_1 and θ_2 are the intrinsic contact angles of the solid and air surfaces, where $\theta_2 = 180°$ as water forms a spherical droplet in air. Further, $A_{f|D_S} = f_2$, relating to the air fraction from the pore coverage in previous analysis, resulting in the solid fraction $f_1 = 1 - f_2$. Eq. 6.1 is thus commonly simplified to,

$$\cos\theta_{CB} = f_1 \cos\theta - (1 - f_1) \,. \tag{6.2}$$

This equation assumes that the liquid bridges over the porous features and does not penetrate inside. It is assumed that the liquid only contacts the flat free surface of the BF structure, and the meniscus of the liquid bridge also remains flat where the pore diameter is much greater than the meniscus curvature.[29]

For the fabricated highly packed surfaces, the fraction of solid sample in contact with a droplet is given by, $f_s = 1 - A_{f|D_S} \approx 0.56$. For an equilibrium contact angle on flat NOA63,

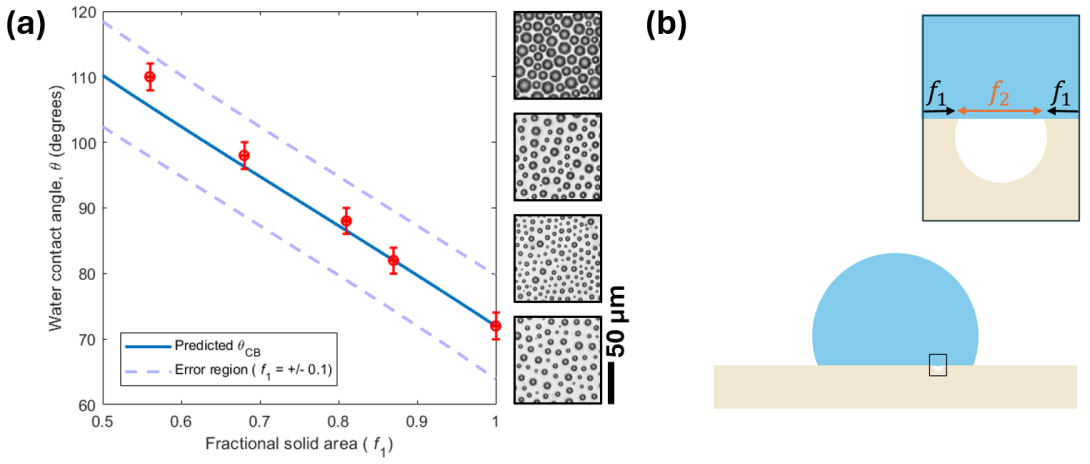

Figure 6.4. (a) Data plotted alongside Cassie-Baxter prediction for BF surfaces of varied fractional area. (b) Schematic of respective fractional quantities.

$\theta = 72.1°$, the predicted contact angle assuming a Cassie-Baxter state is $\theta_{CB} = 105.5°$, indicating a good approximation for the regime.

BF surfaces with decreasing pore fractional area can be fabricated to view the effects on contact angle as $f_1 \to 1$ (flat NOA surface). Fig. 6.4a shows the predicted Cassie-Baxter contact angle and overlaid data points corresponding to tested samples. The dashed lines represent a fractional area tolerance of $f_1 \pm 0.1$ and the data points are plotted with the standard deviation in measured contact angles. The Cassie-Baxter prediction is in good agreement with the data, suggesting that all the samples are in that regime (Fig. 6.4b).

6.3.2 Dynamic contact angle

While the static contact angles are well predicted for the BF films, the dynamic contact angles paint a more interesting picture. Due to the isolated pore structure, it is well-known that these samples create highly adhesive surfaces.[273] Advancing contact angles can be measured by pumping liquid into a sessile droplet, measuring an equilibrium angle as the baseline diameter increases (Fig. 6.5a). Receding contact angles are measured in the same manner upon withdrawal of the liquid. Due to the high adhesion of these surfaces,[273] little confidence in receding data is given; large droplets greater than 20 µL are needed to provide a large enough contact diameter for an equilibrium receding contact angle to be measured. A constant contact radius is observed until very low contact angles are achieved, at which point there is little to no volume to effectively measure the receding angle. Further, the effects of the vertical location of the syringe cannot be neglected (see inset images in Fig. 6.5b).[278] Despite the difficulty in measurements of receding contact angles, qualitative behaviour in differences of varying area fraction is readily observed (Fig. 6.5a).

Flat NOA has a static contact angle of 72.1° and advancing / receding angles of $78.9 \pm 0.4°$

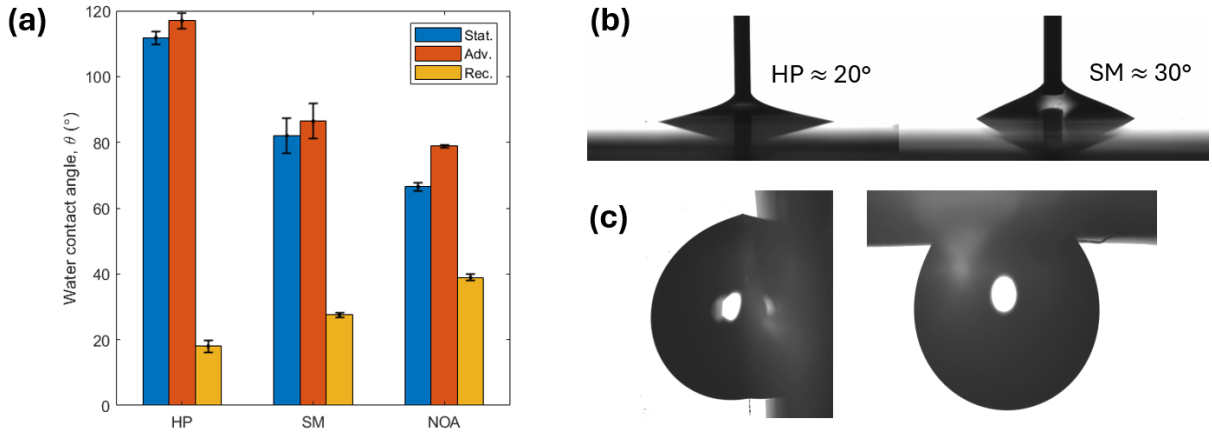

Figure 6.5. (a) Static, advancing and receding contact angles on varied BF surfaces. (b) Visualisation of receding contact angles for the highly packed (HP) ($A_{f|D_L} \approx 0.7$) and spatially modulated (SM) ($A_{f|D_L} \approx 0.2$) samples at constant spacing. For scale, the tip used is 27 g. (c) Manifestation of the high adhesive properties showing adhesion at angles.

/ $38.8 \pm 1.0°$, respectively (Fig.6.5). The sample exhibits moderate hysteresis, calculated by the difference between the dynamic contact angles at 40°. The pinning of the triple line (droplet perimeter at the vertex between liquid-solid-air boundary) manifested in the macroscopic analysis of the dynamic contact angle is a result of intermolecular interactions from chemical and physical irregularities.[230] The highly packed surface has a significantly higher observable hysteresis, primarily arising due to the densely packed pores providing a lower surface fraction f_1 and higher static contact angle. The large number of pores which entrap air also exert a negative pressure on the droplet when receding, manifesting in small receding contact angles from the high adhesion. By analysing dynamic contact angles on a surface with similar average pore diameter (≈ 5 µm), but lower area fraction of pores, the measured hysteresis decreases by around 40% from near 100° to around 60° (see Fig. 6.5a). By maintaining the same pore size, the vacuum effect per pore should be similar, with the lower hysteresis stemming from the decreased number of pores. The increasing solid contact from highly packed pores to flat surface which should equate to greater adhesive force contributions from van der Waal's forces is outweighed by the counteracting pore effect, manifesting in 'stuck' droplets on inclined planes (Fig. 6.5c).

6.4 Breath figure replica samples

6.4.1 Static contact angle

The BF samples produce a simplistic, co-planar system that is well predicted by the Cassie-Baxter equation. The replica samples, however, are 3D representations that are no longer represented by a free surface and pore diameter. Instead, the larger 'pores'

manifest in 3D protrusions which extend in both diameter and height. This 3D variation results in a wetting regime that is not assumed within a singular plane due to the wetting behaviour on individual protrusions.

A modified Cassie-Baxter equation can be used which incorporates a roughness factor, r^*, defining the ratio of actual surface area in contact to the projected area,[29,32]

$$\cos\theta_{CB} = r^* f_1 \cos\theta - (1 - f_1)\,. \tag{6.3}$$

The surface can be modelled in a similar way to previous Voronoi tessellation (Sec. 3.4) in which the projected area of highly packed features consists of Voronoi polygons separated by the bisecting distance between neighbouring features. For simplicity, the surface is approximated by hexagonally arranged homogeneous features of average measured diameter, separated by the average measured interdroplet spacing. A sessile droplet partially wets the features and forms a spherical cap contact, with the meniscus spanning the distance between features (Fig. 6.6a).[277] On one characteristic feature, the height of the spherical wetting cap, h, can be approximated through analysis of the intrinsic material contact angle on flat PDMS (Fig. 6.6a.ii) with the relationship $\sin(\theta - \pi/2) = (R - h)/R$, where R is the feature radius. The feature wetting radius r_2 is given by $r_2^2 = 2Rh - h^2$ and the roughness factor, r^*, and solid area fraction, f_1 can be calculated by,

$$r^* = \frac{\text{area of contact by droplet}}{\text{projected area}} = \frac{2\pi Rh}{\pi r_2^2}\,, \tag{6.4}$$

$$f = \frac{\text{projected area of contact}}{\text{area of hexagonal base feature}} = \frac{\pi r_2^2}{A} = \frac{8\pi r_2^2}{3\sqrt{3}L_c^2}\,. \tag{6.5}$$

Again, these equations assume a homogeneous ordered micropatterned surface, where the use of these equations is somewhat misleading. Here we assume consistent exposure of the droplet to features that are at a constant height (constant level of penetration). Unlike in the flat BF surfaces, $f_1 \neq 1 - f_2$ due to feature curvature.[32] $r*$ is a function of the wetting and thus varies with increased penetration, where $r^* \rightarrow \theta_{wenzel}$ upon full penetration.

After measuring the intrinsic contact angle on the PDMS material to be 117°, the droplet area in contact can be calculated through calculating the area of the spherical cap with Eq. 6.4/6.5.[277] For the highly packed surface being analysed, $D_{\mathrm{L}} = 11.7$ and $L_c = 15.9$, the roughness and solid fraction values equal 1.38 and 0.52, respectively. The angle for a 5 µL sessile droplet on the patterned surface of $145.8 \pm 1.7°$ is reasonably well predicted by Cassie-Baxter angle for the surface of $\theta_{CB} = 144°$. For a range of highly packed samples tested (1.3 µm $\leq D_{\mathrm{L}} \leq$ 10.0 µm), near constant static angles are observed at $143.5 \pm 1.6°$.

As the area fraction of BF samples can be modulated by evaporating a pre-established

droplet array, samples were fabricated with approximately equal average interdroplet spacing of (mean ±range/2) 16.2±0.7 µm. Fig. 6.6b plots the predicted Cassie-Baxter contact angle for the observable range of average feature diameter, with the same f_1 ±0.1 tolerance as the previous model.

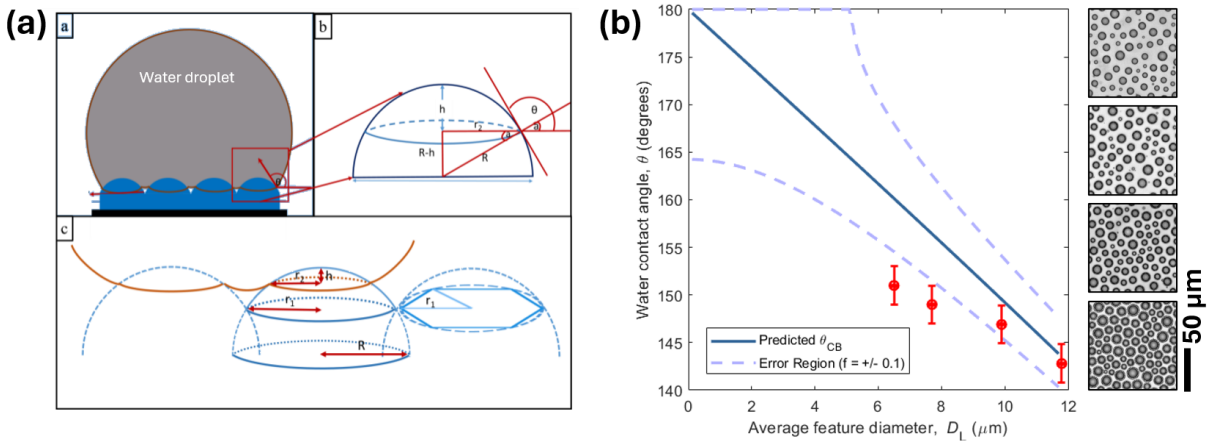

Figure 6.6. (a) Respective parameters used, adapted from Arora *et al.*[277] for (b) the Cassie-Baxter prediction of wetting on PDMS replica surfaces. Replicas have constant $L_c \approx 16.2$ µm and varied A_f through evaporation of the pattern, hence the average D_L is plotted.

Due to the nature of the replication being the counter of the BF surface, the opposite trends to the BF results are observed. Decreasing the area fraction through a decrease in the average feature size D_L increases the contact angle. As the average feature size decreases for a constant interdroplet spacing, the area fraction of solid decreases, resulting in a higher contact angle measured. This is evidenced by superhydrophobic angles over 150° observed at the smallest feature diameter. Experimental values for the lower packed surfaces tend to deviate from the predicted trend as assumptions become less valid. The curvature of the liquid meniscus increases as the feature spacing increases, and the 3D height variation of features varies with the previously described templating droplet sinking.

6.4.2 Dynamic contact angle

Similar dynamic analysis is completed on the PDMS replicas. Fig. 6.7 shows the opposite effects of the BF samples, as evaporating the pattern decreases the solid area fraction; higher hysteresis is observed on the spaced samples relative to the highly packed, measuring 134.3° and 93.1°, respectively. This is significantly higher than the flat PDMS, exhibiting a small hysteresis of only 16.4°. While the sticky behaviour does not arise from individual entrapped air pockets like the pores in the BF samples, the level of pinning here depends on the wetting behaviour on individual features. Due to the spherical cap nature of the protrusions, resistance to receding motion is partially governed by how

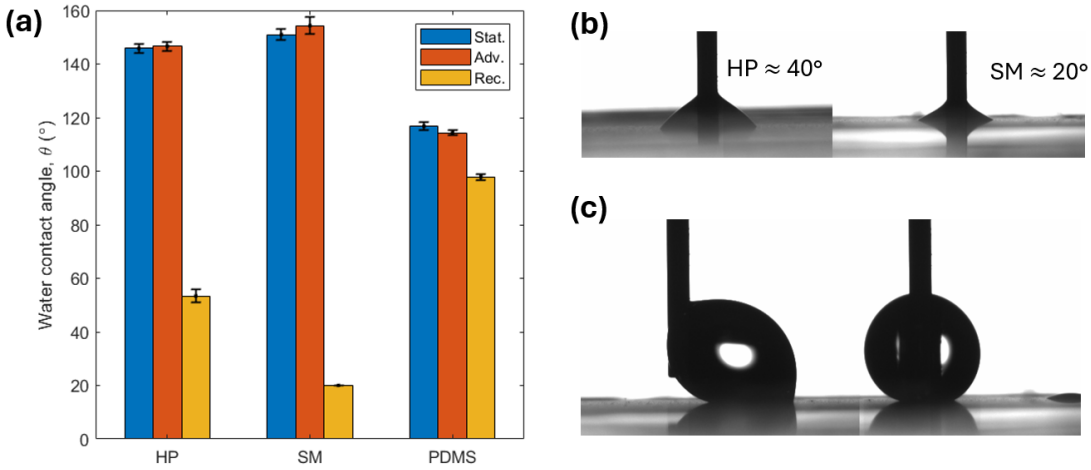

Figure 6.7. (a) Static and dynamic contact angles on varied PDMS replica surfaces. (b) Visualisation of receding contact angles for the highly packed (HP) ($A_{f|D_L} \approx 0.7$) and spatially modulated (SM) ($A_{f|D_L} \approx 0.2$) samples at constant spacing. (c) Despite high adhesion, droplet still moves when pulled by a capillary. For scale, the tip used is 27 g.

far down the protrusion curvature the sessile droplet wets.[29] Further, with increasingly spaced feature samples, the curvature of the meniscus bridging the gap between features increases, manifesting in the larger receding angles observed in Fig. 6.7.

6.5 Droplet evaporation

With the difficulty in analysing receding contact angles by conventional active deflation of a sessile droplet,[30] comparative sessile droplets evaporation tests were performed on BF patterned surfaces and their PDMS replicas.[278] 5 µL droplets were left to evaporate in ambient laboratory conditions, with the baseline and contact angle tracked throughout. As the experimental set-up is much simpler with no inserted syringe pumping the droplet in this study, the difference between size variation of features in highly packed samples was studied compared to a flat control surface. Sessile droplets on hydrophobic and superhydrophobic surfaces undergo different regimes of constant contact angle (CCA) and constant contact radius (CCR) during evaporation.[262,279] While CCA is indicative of continuous sliding of the contact line on slippery surfaces, CCR is characteristic of sticky coatings that induce significant pinning and stick-slip effects of the contact line on the surface. The relatively high hysteresis observed for dynamic contact angles indicates that the droplet is expected to evaporate in an initial CCR regime with a continuous decrease in droplet volume. The droplet perimeter will be largely pinned until reaching the natural receding angle, upon which the baseline area will decrease.[278]

For both highly packed (HP) BF samples, a similar receding contact angle of around 20° is observed at the onset of the baseline decrease (highlighted in Fig. 6.8). For flat NOA, the angle is only marginally higher at 25°, however, the overall evaporation time

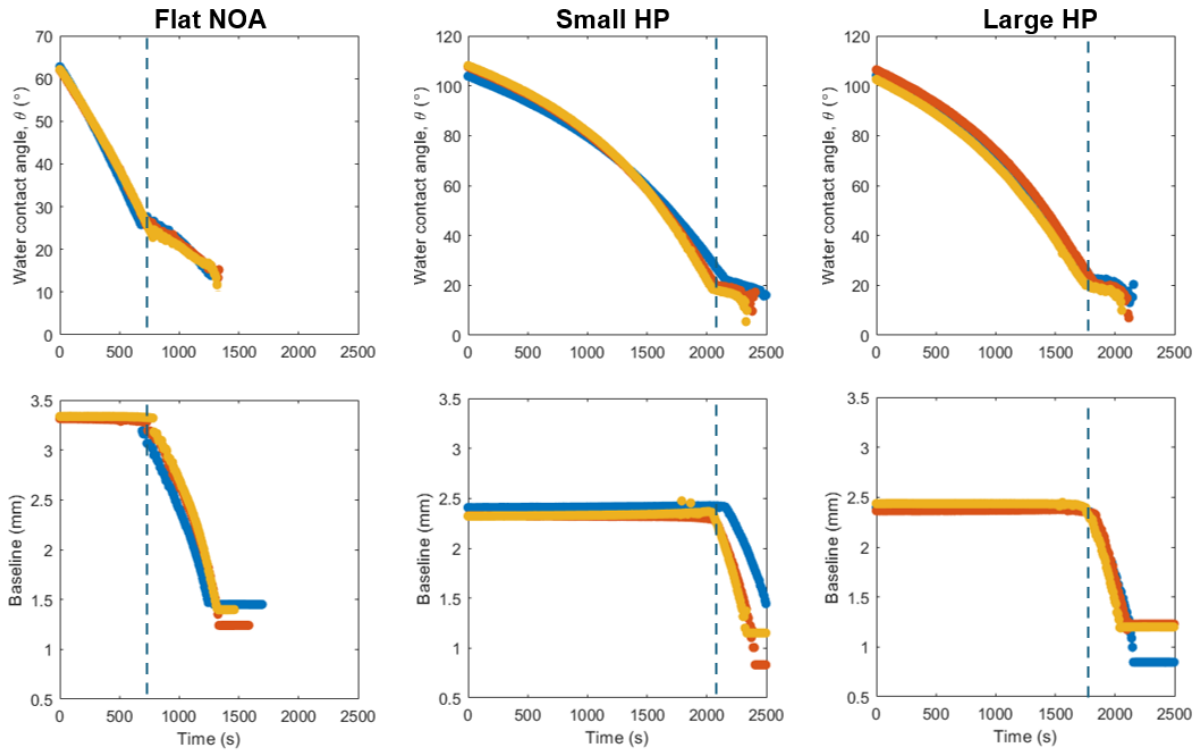

Figure 6.8. Evaporation of 5 µL water droplets on flat and highly packed (HP) NOA BF samples, with the different colours representing three independent repeats. Hashed line represents onset of baseline diameter decrease. Respective feature sizes for small vs large highly packed BF samples are roughly 1 µm vs 10 µm.

is much shorter at 1300 s. The time at which the sessile droplet is in a constant contact radius regime is over half the time of the patterned films, primarily arising due to the lower intrinsic contact angle on the flat film with the greater initial contact area. No significant difference manifests across the size variation in the highly packed surfaces, with the decreasing angle appearing near constant irrespective of pore size and thus contained volume of trapped air. The 20° angle for highly packed patterned films is similar to the receding angle found previously, however the evaporating angle undergoes a CCR mode at a smaller angle than the previously found 38.9° value. The size of the evaporating sessile droplet was also separately varied from 3 µL to 7 µL, with no significant difference in the angles found.

All of the PDMS replica samples exhibit a similar CCR evaporation mode, with the contact line pinned until reaching the receding angle (Fig. 6.9). There is a more significant variation in the receding evaporating angle between the size variation of highly packed surfaces. A smaller angle of around 60° is found, compared to 75° for the larger feature surface, indicating a higher level of pinning and adhesion with the smaller features. An interesting change in the data is observed near the start of analysis on the small feature sample ($D_L \approx 1$ µm). An approximate 7% increase in the baseline length occurs at the same time as a small decrease in the contact angle (yellow and red lines). This passive

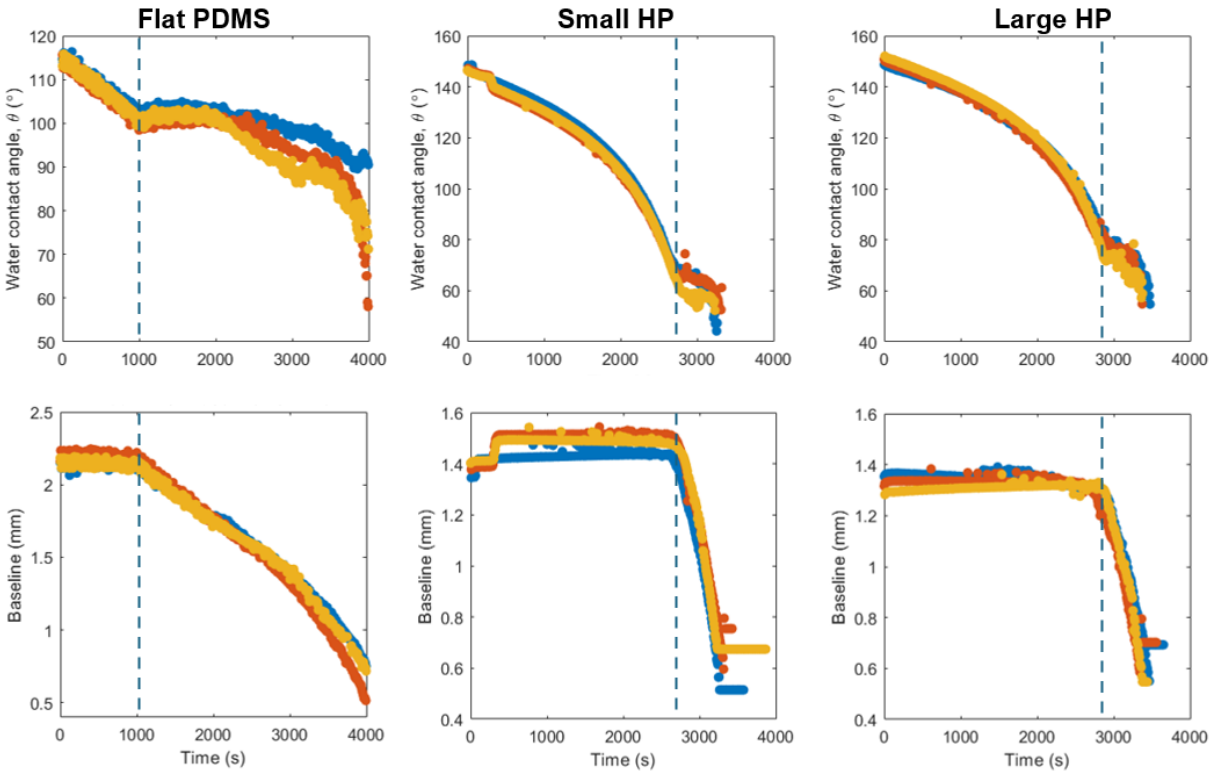

Figure 6.9. Evaporation of 5 µL water droplets on flat and highly packed (HP) PDMS replica samples. Hashed line represents onset of baseline diameter decrease. Respective feature sizes for small vs large are roughly 1 µm vs 10 µm.

jump is clearly visible in the live view of the droplet shape, indicating a sudden transition in the wetting regime, for example, as the droplet partially penetrates the gaps between the surface features.[9] With small features, depending on how far down the sessile droplet wets the protrusions, only a small change is needed for the menisci to touch the bottom surface and partially penetrate the topography. Different failure modes of Cassie-Baxter state evaporating droplets depend on the overall energy landscape, as the droplet can explore intermediate equilibrium conformations that are neither complete Cassie-Baxter or Wenzel regimes.[280,281] As the radius of the evaporating droplet gets smaller, the local Laplace pressure enlarges and can drive the menisci to protrude deeper. A sufficiently large Laplace pressure (as the droplet size decreases) can also drive menisci to slide down along the sides of the features. It is also true that even without sufficient Laplace pressure exerted at only very small droplet sizes, a global interfacial energy analysis could show that partial penetration of the droplet is likely. Wetting transitions can also occur due to a number of external properties, such as vibrations[282] or even through capillary condensation of the sessile droplet into the topography.[79] These results indicate that while the PDMS replicas show increased hydrophobicity and superhydrophobicity relative to the BF samples, the BF samples with entrapped air tend to be in a more stable Cassie-Baxter state.

6.6 Discussion

As tested samples could not be destructively characterised through SEM analysis, the evaluation of the key surface pattern characteristics is estimated optically. Due to the film transparency, it is hence difficult to attain values for the top surface level of the BF, in particular D_S (see discussion in Sec. 3.4). Despite this, the static analysis of the BF samples matches well with predictions. Evaporated, spatially modulated BF samples are less well predicted, however, the results show a further handle to module the wetting behaviour, as seen with the decreased/increased hysteresis effects for pores vs protrusions, respectively.

The good predictability of the Cassie-Baxter equation indicates that the surfaces are in the Cassie-Baxter regime, meaning droplets rest on a composite surface-air interface.[30] The dominating effect of the wetting behaviour hence originates from the area fraction and volume of trapped air. In the fabricated BF samples, isolated pores result in trapped pockets of air where the meniscus of a sessile water droplet is assumed flat when modelling the Cassie-Baxter regime. However, in practice due to the capillary pressure of the water droplet, a small meniscus will form as shown in Fig. 6.10i. In a larger pore, a larger volume of sealed air would exert a smaller Laplace pressure on the sessile droplet, and the larger pore diameter would result in a higher meniscus curvature. Upon droplet removal (Fig. 6.10ii), this would manifest in a lower air expansion ratio and lower negative pressure indicating that the larger pores are less adhesive.[273] While for flat surfaces, the force from van der Waals interactions between the droplet contact area determines the adhesion and hysteresis, the observed adhesion is created by the counteracting pore volumes exerting a negative pressure. The adhesive effects in the PDMS protruding surfaces can be viewed from the depth of penetration of the droplet on the curved features. This is further evidenced by the apparent wetting transition observed for small PDMS pillars, manifesting as a jump in the contact area and a decrease in the contact angle as water penetrates the feature gaps. Hence, the adhesive force can be readily controlled by varying the BF pattern, indicating an effective way to fabricate surfaces with different adhesion.

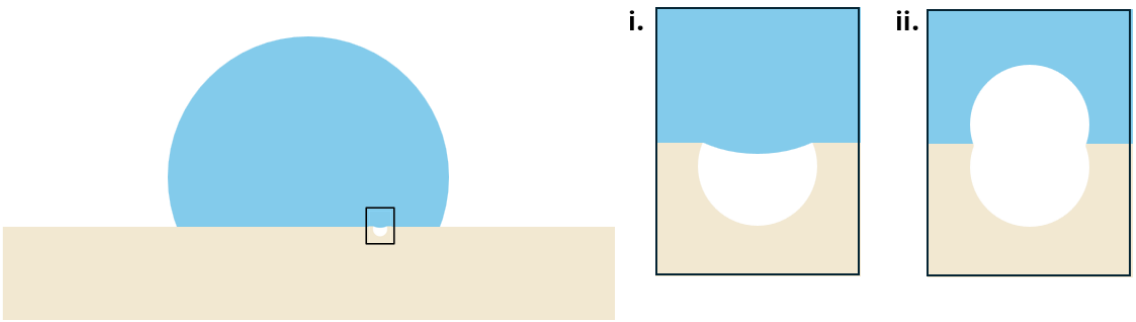

Figure 6.10. Schematic of a sessile droplet on a breath figure surface. (i) Resting Cassie-Baxter state and (ii) negative pressure produced upon droplet removal.

The apparent stability of the Cassie-Baxter state in BF surfaces is greater than that of the PDMS replicas. In fact, the negative curvature of the porous surface is commonly used morphology where the re-entrant design manifests in many oleophobic surfaces in nature.[283] The re-entrant curvature enhances the stability of the composite air interfaces,[283,284] beyond that described by the use of the classical Cassie-Baxter fractional surface area (Eq. 6.1). Like the partial penetration behaviour observed for evaporating droplets on small highly packed PDMS protruding surfaces (Fig. 6.9), the discovery of numerous metastable wetting states beyond the binary Cassie-Baxter and Wenzel regimes demonstrates the insufficiency to describe complex wetting scenarios.[284] Emphasised by Tuteja *et al.*, it is the local surface curvature that plays a key role in driving wetting. Surfaces with re-entrant curvature result in liquids with significantly lower surface tensions than water unable to readily penetrate the topography.[283,285]

The wetting behaviour of fluids with surface tension less than water can be measured by depositing sessile droplets in the same manner on both flat and patterned surfaces. Silicone oil (40 mN/m), sodium dodecyl sulfate (SDS) solution (33 mN/m), ethanol (22.1 mN/m) and toluene (28.4 mN/m) were used as probing fluids. Ethanol and toluene were used as polar and non-polar volatile solvents. Results in Tab. 6.1 show an increase in contact angle for all fluids tested from the flat to patterned samples. The angular increase for SDS solution is well predicted by the Cassie-Baxter equation for the average pore size $D_{\mathrm{L}} \approx 2$ µm). Further, both ethanol and toluene solvents which completely wet the flat surface (measurements unable to be taken) produce a significant increase in the apparent contact angle on the patterned surface.

Table 6.1. Contact angles of low surface tension fluids on highly packed breath figure patterns ($D_{\mathrm{L}} \approx 2$ µm).

Fluid	Surface tension (mN/m)	Flat contact angle θ°	Patterned contact angle θ°
Silicone oil	40	11.9 ± 0.7	52.5 ± 2.9
SDS solution	33	24.8 ± 3.3	84.6 ± 1.6
Ethanol	22.1	0†	46.6 ± 1.9
Toluene	28.4	0†	33.6 ± 1.8

†Complete wetting resulting in no measurable contact angle

The tuneable wetting response based upon the porous or protruding architecture provides scope for varied applications. The short fabrication time over seconds or minutes, as well as the ability to modulate the pattern morphology *in situ* further facilitates the potential for programmable surfaces for specific control and manipulation of fluids. More in depth wetting analysis including pore-scale visualisation of the wetting effects with use of immersion lenses in optical set-ups and LSCM fluorescent analysis will provide more conclusive remarks.[79,286,287]

6.7 Summary

- Fabrication of highly packed breath figure samples with varied pore sizes exhibit predictable static wetting behaviour as a result of Cassie-Baxter analysis of constant solid-air fraction. An increase of contact angle of over 40% is observed from flat NOA film to highly packed sample.
- Spatially modulated BF samples tend towards the properties of the flat film as the $A_f \rightarrow 0$, as expected.
- Non planar PDMS surfaces show the opposite trend, where increasing the spacing between features (lowering A_f) results in increased hydrophobicity, with some samples reaching contact angles over 150°.
- Higher hysteresis effects are observed on the spatially modulated PDMS samples relative to the highly packed samples.
- The partial wetting transition observed in the small highly packed PDMS samples show that the PDMS Cassie-Baxter state is less stable, and the design of larger features is favourable for greater hydrophobic properties.
- Preliminary results with common low surface tension fluids show omniphobic properties of the BF re-entrant patterning.
- As demonstrated in the next and final chapter, the initial studies on wetting show variable behaviour dependent on the tuneable pattern morphology, promising potential for future applications of these patterns.

Chapter 7

Overview: applications, conclusions and future perspectives

The overall discussions of the thesis work are presented alongside concluding remarks. Current ongoing application-driven collaborations and initial results are also summarised to provide perspectives for future work.

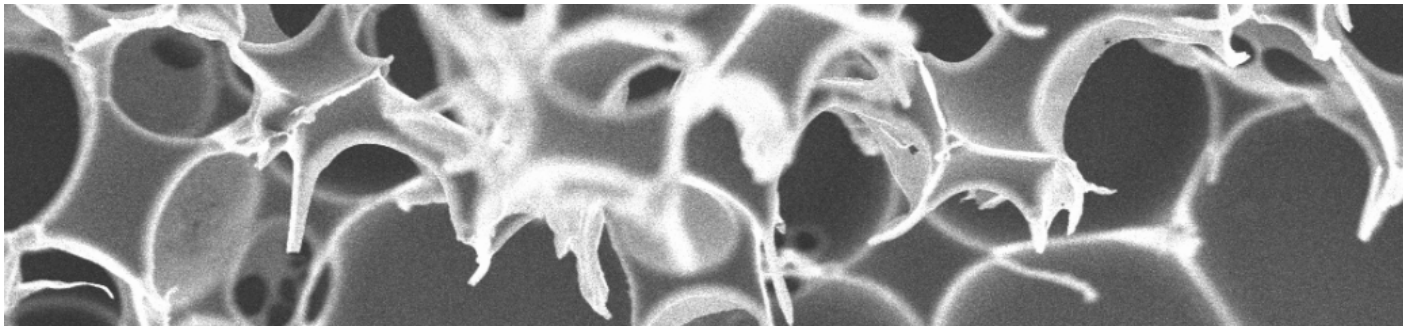

"We can only see a short distance ahead, but we can see plenty there that needs to be done."

Alan Turing

7.1 Overview

The surface of any object is the outermost exterior face, representing a physical boundary between the object and its environment. As such, the properties at this boundary dictate its interactions with the environment and determine the overall performance. As we have seen abundant in nature, nano and microscale patterning offers age-old optimisation strategies that we are only now beginning to fully explore. The development of new fabrication and low-cost manufacturing routes with good control will enable the broader use of biomimetic patterned surfaces with further commercial exploitation.

Since the development of the breath figure templating method in the mid-1990s, significant interest regarding the technique has been observed with the study of huge numbers of varied polymer architectures and applications across a number of fields. The extraordinary order of these patterns exemplifies the potential for bottom-up and self-assembly-driven techniques for the creation of micropatterned surfaces. While the simplicity of the passive approach can create almost counterintuitive perfect ordering, it is the same simplicity that limits the effectiveness of the surfaces for diverse applications. The described adapted methodology in this work is hence an attempt to increase the reliability and systematic adaptability of the approach.

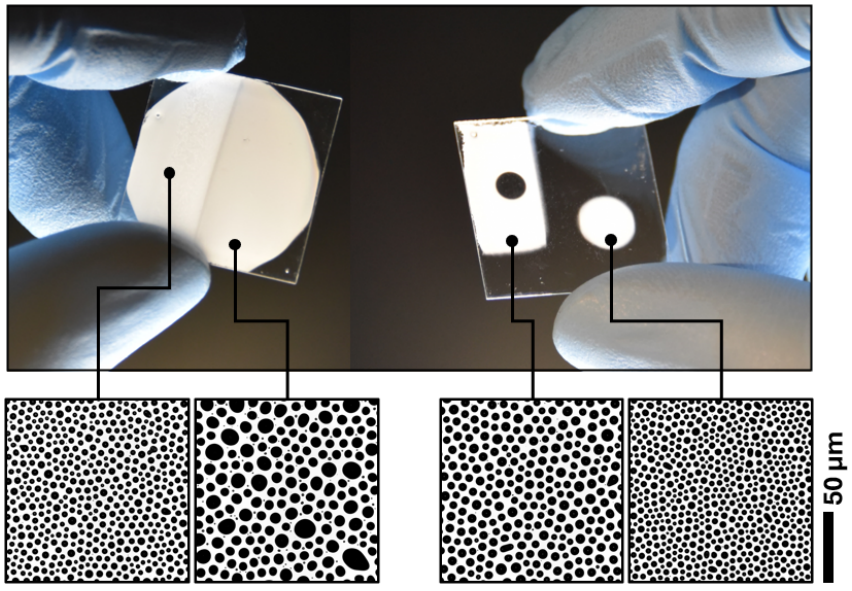

Figure 7.1. Spatially varied gradient topography BF samples from the combined use of UV photomasking and substrate temperature variation.

While Ch. 1 & 2 introduce the inspiration, rationale and methods for surface patterning, Ch. 3 presents the temporally arrested breath figure method in full alongside the experimental techniques used. The majority of time on the project was spent analysing the evolution of the droplet pattern in the liquid state (Ch. 4), ensuring it is possible to modulate and actively design the final cured structure. Overall good control over the size

and morphological arrangement of the pattern was achieved. This is evidenced in Ch. 5 by the creation of systematically varied highly packed patterns with average feature sizes varying from hundreds of nanometres to tens of microns, all with near-constant feature morphology and polydispersity.[185] Further patterns were created varying in packing density coverage from $A_{f|D_L} \approx 0.7$ to $A_{f|D_L} \approx 0.1$, through subsequent evaporation of the established BF pattern.[186] The ability to extend the modulation level through temperature gradients and photomasking is also briefly introduced towards the end of this work with the overall effect on wetting and interfacial properties characterised in Ch. 6. As can be seen in Fig. 7.1, spatially varied and gradiented feature design can offer potential new samples for undiscovered applications.

Tuning of the fabricated patterns was touched upon at the end of this work, facilitating new ways to alter the potential interfacial behaviour. With more analysis of the sinking effects of droplets upon late evaporation, control of the pore morphology or replicate feature could unlock new geometries, including increasingly re-entrant designs (Fig. 7.2a vs. (Fig. 7.2b) for omniphobic applications. Further, Fig. 7.2c - e shows how control of the replicating conditions can also create features varying from smooth high fidelity replicas, wrinkled secondary features and nanoparticle infiltrated hierarchical geometries. Additional study is needed to facilitate a better understanding of the level of control harnessed with these modulations and the corresponding change in interfacial properties.

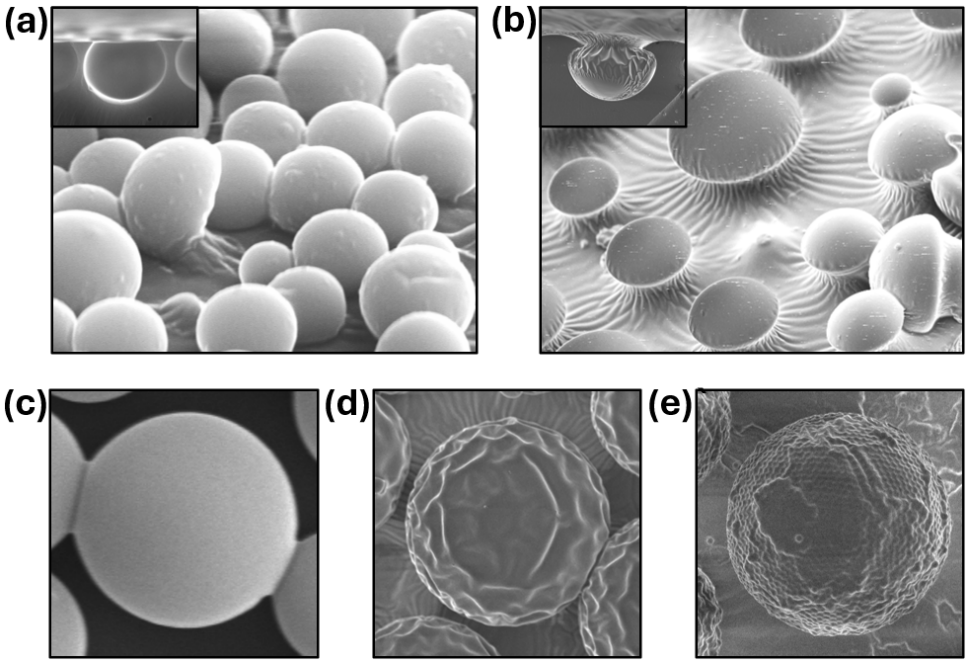

Figure 7.2. (a) Standard BF morphology replica and (b) partially sunken pore morphology and replica. Further modification of replica features from (c) standard replication, (d) wrinkling instability and (e) nanoparticle infiltration. Average feature sizes correspond to $D_L \approx 10$ µm.

What has not been covered here is potential future avenues for application-driven use

of the patterned surfaces created. The breadth of patterned designs which can be fabricated, ranging from the highly packed, spatially modulated and bimodal BF designs to the inverse PDMS replica surfaces, exhibit widely contrasting topography which can be applied to many different open-ended applications. While this feeds into some of the ongoing collaborative work that is discussed below, further opportunities relating to anti-reflectance photonic applications[288] and perforated through-pore filtration membranes[177] could all be promising studies. The cross-linked polymer BFs in this study are also significantly stronger than many of the classically made films, overwhelmingly composed of brittle polystyrene-derivatives. The robust films hence not only have more controlled pore distributions, but exhibit mechanical and solvent resistance, making them appealing to a wide range of industrial applications. The ability to readily control the film thickness independently of droplet growth kinetics makes films created via this method more adaptable to a range of applications where the coating thickness is important. With this in mind, the following final sections elaborate upon three ongoing collaborations employing fabricated surfaces for diverse applications, showcasing potential future perspectives of this research. Each subsection presents the application challenge and preliminary data summarised so far.

7.2 Ongoing application-driven collaborations

7.2.1 Directional wetting analysis on non-homogeneous surfaces

Work in collaboration with Maximilian Dreisbach (PhD student), Jochen kriegseis and Alexander Stroh of the Institute of Fluid Mechanics, Karlsruhe Institute of Technology, Germany.

Spatial gradients in topography can give rise to variable wetting effects and the directional manipulation of incident droplets.[289] Surfaces in nature exhibit similar structures to control the direction of liquids crucial for their survival.[40,43] For example, the overlapping structured peristome of pitcher plants resembles asymmetric re-entrant geometries, which engender low adhesive unidirectional flow.[289] For survival in arid conditions, Namib desert beetles have rough bumps on their elytra to be able to harvest and guide water from the atmosphere.[290] While artificial surfaces tend to manipulate droplets through external stimuli (*e.g.* electric fields), the ability to passively manipulate droplets based on topography is essential for optimising new functional and responsive materials.[291]

This collaboration tests gradiented patterned samples created in this work at Leeds on the state-of-the-art imaging facilities at Karlsruhe Institue of Technology. Gradiented BF patterns were created with NOA68 on the set-up described in Sec. 5.3, using stacked metal strips to diffuse and create a temperature gradient across the polymer film. The pattern

growth on the 'cool' side of the film was analysed in real-time and the film was cured when $D_L \approx 10$ µm. A subsequent pattern gradient was created based on the diffused temperature gradient from the number of offset metal strips. Cured BF patterns were replicated in PDMS following the pre-established procedure and were the primary interest in testing. A single camera was used to image an impacting droplet with both standard contact angle shadowgraphy side-on views and bottom-up perspectives. Droplets of 2.1 mm diameter impacted the substrate with a downward velocity of 0.69 m/s, corresponding to a Weber number of $We = 6.9$.

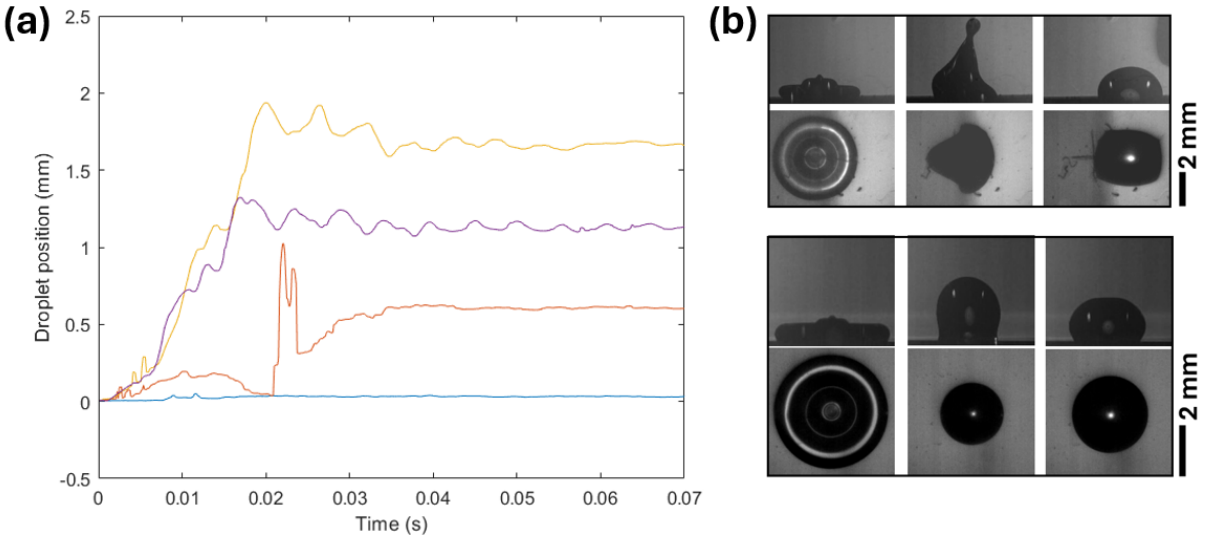

Figure 7.3. (a) Graph of central droplet contact position on varying gradient pattern samples plotted as the mean of three repeats in time. (b) Side-on and bottom-up views of impacting droplets on the largest gradient pattern (top) and controlled homogeneous pattern (bottom).kit

Fig. 7.3a shows data tracking the central coordinates of the contact line for the impacting droplets on different patterned samples as a function of time. For flat patterned highly packed BF films, while the protruding features are not completely hexagonally ordered (See Sec. 4.5), an impacting droplet has no lateral translation, producing an axisymmetric impact shape (bottom images in Fig. 7.3b). The largest surface pattern gradient exhibits clear forcing of the impacting droplet to the non-patterned side. The patterned side has a stable enough Cassie-Baxter state that the droplet does not wet the surface and rebounds, compared to the non-patterned area which exhibits pinning and 'sticky' behaviour. What is interesting is that the patterned side produces high adhesion on placed sessile droplets as observed in Ch. 7, yet the impacting droplet is able to rebound and translate almost completely off of the patterns. Within 35 ms after impact, the droplet has shifted to a new equilibrium position for all the patterned samples tested. Modulation of the pattern can hence attain precise manipulation and retention of droplets.

7.2.2 Biomaterials for biofilm inhibition

Work and secondment opportunity in collaboration with Desmond van den Berg and Benjamin Hatton of the Functional and Adaptive Surfaces group, University of Toronto, Canada.

Surface adherent bacteria can proliferate and colonise surfaces, forming biofilms that are up to 1000 times more resistant to chemical bactericides such as antibiotics.[292] Bacterial colonisation hence poses significant challenges ranging from device failure of biomedical implants to infection spread from contaminated touch. Patterned surfaces are able to limit bacterial attachment and delay subsequent biofilm growth as a function of the surface structure, limiting requirements for intervention.[293] The understanding of how different pattern morphologies impact bacterial attachment is hence necessary for further application.

Two bacterial strains were chosen for analyzing the initial attachment and subsequent biofilm formation on flat control, small packed and large packed breath figure surfaces: gram-negative *Pseudomonas aeruginosa* (PAO1, wild-type stain; serotype O5) and gram-positive *Staphylococcus aureus* (KR3). Both bacterial strains were prepared by obtaining a single colony from a tryptic soy agar (TSA) plate and streaked using the four-quadrant method on a new agar plate before incubation at 37 °C overnight. Precultures were prepared by transferring a colony from these plates using a sterile loop into 10 mL of tryptic soy broth (TSB) medium at 37 °C overnight in aerobic conditions. Inoculations of both strains were prepared by adding 1% of the bacterial suspension to fresh TSB, which resulted in a cell density of $2.7 \times 10^7 \pm 0.2 \times 10^7$ and $3.2 \times 10^6 \pm 0.4 \times 10^6$ for *P. aeruginosa* and *S. aureus*, respectively as confirmed through serial dilution and plating via the Miles and Misra method in triplicate.[294]

Each microstructured surface (PDMS and NOA polymer samples) was placed in a 35 x 10 mm petri dish and sterilized via UV irradiation for 3 minutes. Following disinfection, each dish was filled with 5 mL of the prepared bacterial suspension and incubated at 37 °C under aerobic conditions for 1, 6, and 18 h. After each time point, the samples were rinsed in 5 mL of DI water 10 times by vertical dipping, and submerged in 3 mL of 2% glutaraldehyde (v/v) in 1X PBS for 10 min. All samples were then submerged in 0.05% Tween-20 (v/v) in 1X PBS for 10 min. Attached microbes were stained with Sytox Green (1 µL suspended in 10 mL of 1X PBS) by submersion in 3 mL of 1X PBS and 100 µL of the prepared stain solution. After staining, all samples were placed on glass slides and dried for 30 min at 37 °C before being imaged.

Fig. 7.4 shows preliminary fluorescent microscopy images of adhered *S. aureus* cells to breath figure surfaces after 2 and 6 hours respectively. Images are taken at the free surface level at different magnifications. Initial data indicates a clear trend with significantly

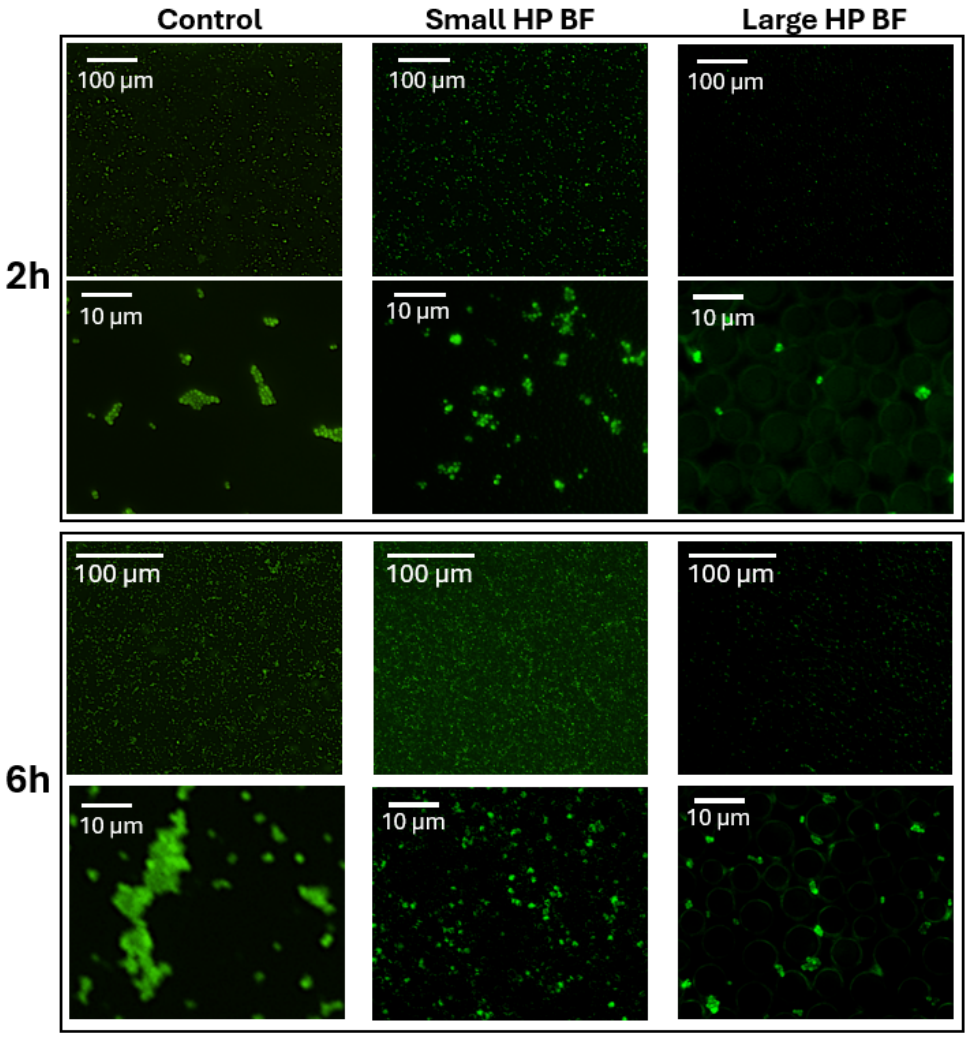

Figure 7.4. Fluorescent images of stained *S. aureus* cells on control and breath figure surfaces (both small highly packed $D_L \approx 1$ µm and large highly packed $D_L \approx 6$ after 2 hour and 6 hour exposures).

lower bacterial attachment after 6 hours on the patterned films. 2 hour studies do not show significant difference in density between all samples, with large highly packed samples showing consistently lower number of adhered cells at later times. The larger pores seemingly disrupt the ability for bacteria to aggregate and colonise at the same rate as the flat control group. Further studies aim to test surfaces of feature sizes concomitant with bacteria.

7.2.3 Cryogenic quenching heat transfer enhancement through micropatterning

Work in collaboration with Marco Graffiedi (PhD student) and Matteo Bucci of the Nuclear Science and Engineering department at the Massachusetts Institute of Technology, USA.

Cryogenic fluids such as liquid hydrogen, liquid oxygen and liquid methane are commonly used fluids for propulsion and thermal management systems in space exploration.[295] The transport, handling and storage of these fluids pose significant challenges as the surface temperature of equipment is typically much higher than that of the saturation temperature of the fluid, resulting in vigorous boiling of the liquid through initial surface contact. Upon transfer of these fluids, an initial flux of fluid is commonly spent in a 'chill-down' regime to cool the surfaces of the new system. However, the heat transfer rate during this boiling regime is extremely low due to the insulating effects of the vapour film, demonstrating process efficiencies as low as 8%.[296] The vaporised cryogen has to be vented to the environment before the full liquid transfer can commence.

Low effusivity coatings and increased surface roughness have all been used to enhance the heat transfer of the process during liquid-to-vapour phase change.[297,298] This work demonstrates the possibility of improving the quenching thermal efficiency through the use of microporous surfaces to increase the Leidenforst temperature and critical heat flux.[295] The quenching thermal efficiency can be improved through early suppression of the film boiling regime, shortening the overall chill-down time.

Different breath figure pattern morphologies, including small, large highly packed and spatially modulated samples were tested by measuring the temperature across the film during contact with a jet of liquid nitrogen. Fabricated samples had to be created on steel substrates with mounting points for securing the sample and installing thermocouples. Coating adhesion of the patterned polymer layer to the steel was optimised through initial plasma cleaning of the steel and annealing of the sample post-fabrication, where preliminary tests showed good adhesion of the coating to the substrate. Samples were mounted to the designed rig where three temperature points were probed continuously during the experiment and the process was recorded on a high-speed camera at 550 fps.

Results indicate that the micropatterned samples effectively reduce the chill down time up to a factor of 5, as shown in Fig. 7.5. The micropattern suppresses the film boiling regime, promoting the wetting of the surface. The large highly packed sample performs the best, however further investigation of the wetting dynamics and coating thickness is required.

7.3 Conclusions and future outlook

This work presents an adapted breath figure templating approach to facilitate greater patterning control whilst maintaining experimental simplicity. The respective chapters summarise each key element of the working process, documenting the progression from the rationale and initial inspiration through to the final ongoing collaborations that validate the use of these surfaces in future applications.

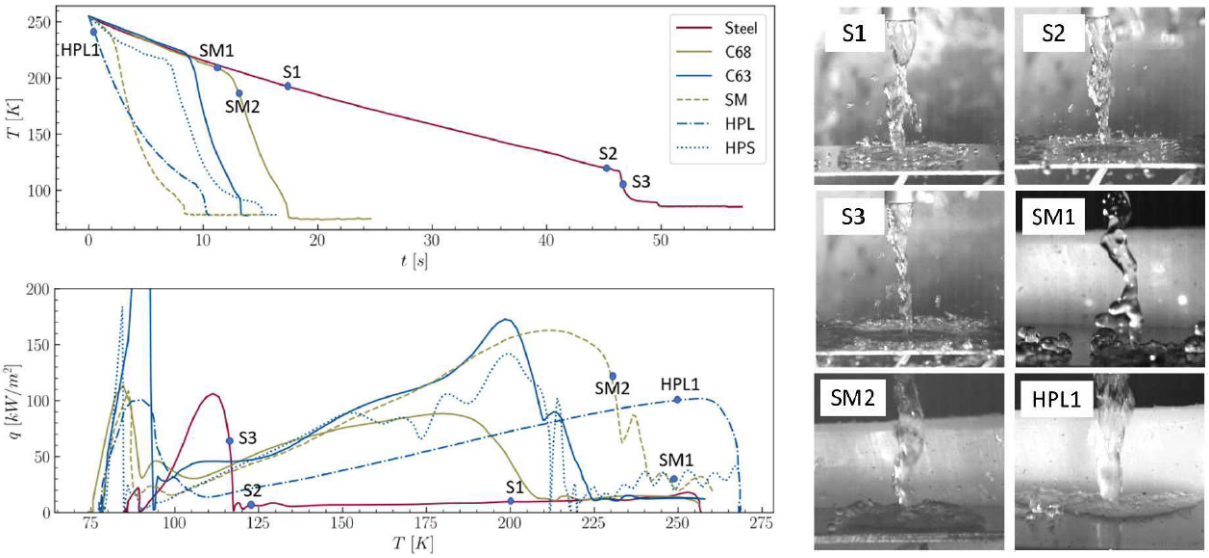

Figure 7.5. Top plot shows the temporal evolution of temperature for the respective coatings tested. The bottom plot shows the corresponding boiling curve, with inset images showing high speed stills at respective marked points. Adapted from Graffiedi *et al.*[299]

- The current landscape of fabrication methods for bio-inspired and biomimetic design of functional surfaces has been discussed, highlighting the applicability of self-assembly techniques for scalable fabrication.
- The literature surrounding classical breath figure patterning is summarised with the use of classically fabricated examples to highlight limitations to the process.
- The temporally arrested breath figure approach was introduced in full indicating how the de-coupled control handles provide new capabilities for pattern formation.
- Droplet condensation studies highlight the ability to readily predict and control the ensuing pattern provided a polymer exhibiting high initial nucleation density is used.
- Quasi-instantaneous arrest of patterns is demonstrated via use of UV curing. Translation of modulated pattern designs are highlighted as a new capability of this technique.
- Initial wetting properties on porous and replica patterns is characterised to demonstrate the behaviour of the surfaces.
- Potential future avenues and new applications of the manufactured surfaces are highlighted.

Bibliography

[1] Evans, C. J.; Bryan, J. B. "Structured", "Textured" or "Engineered" Surfaces. *CIRP Annals* **1999**, *48*, 541–556.

[2] Mate, C. M.; Carpick, R. W. *Tribology on the Small Scale - A Modern Textbook on Friction, Lubrication, and Wear*, 2nd ed.; Oxford University Press, 2019; Chapter 2. Surface.

[3] Stout, K. J.; Blunt, L. *Three Dimensional Surface Topography*, 2nd ed.; Penton Press, 2000; Chapter Part VI -.

[4] Hruby, J.; Trusty, D. *From Cooking Vessels to Cultural Practices in the Late Bronze Age Aegean*, 1st ed.; Oxbow Books, 2017.

[5] Galilei, G. *Discourses about two new sciences*; Translation published by Macmillan (1914), 1638.

[6] Cassie, A. B. D.; Baxter, S. Wettability of porous surfaces. *Transactions of the Faraday Society* **1944**, *40*, 546–551.

[7] Wenzel, R. N. Resistance of solid surfaces to wetting by water. *Industrial Engineering Chemistry* **1936**, *28*, 877–996.

[8] Barthlott, W.; Neinhuis, C. Purity of the sacred lotus, or escape from contamination in biological surfaces. *Planta* **1997**, *202*, 1–8.

[9] Bhushan, B. In *Springer Handbook of Nanotechnology*, 3rd ed.; Bhushan, B., Ed.; Springer, 2010; Chapter 8, pp 231–270.

[10] Bartell, F. E.; Shepard, J. . W. The Effect of Surface Roughness on Apparent Contact Angles and on Contact Angle Hysteresis. I. The system Paraffin–Water–Air. *Journal of Physical Chemistry* **1953**, *57*, 211–215.

[11] Dettre, R. H.; Johnson, R. E. Contact angle hysteresis explained. *The Journal of Physical Chemistry* **1965**, *69*, 1437–1788.

[12] Barthlott, W.; Ehler, N. Raster-Elektronenmikroskopie der Epidermis-Oberflächen von Spermatophyten. *Tropische und Subtropische Pflanzenwelt* **1977**, *19*, 366–467.

[13] Busscher, H. J.; Stokroos, I.; Golverdingen, J. G.; Shakenraad, J. M. Cells and Materials Adhesion and Spreading of Human Fibroblasts on Superhydrophobic Fep-Teflon. **1991**, *1*, 243–249.

[14] Busscher, H. J.; Stokroos, I.; Van Der Mei, H. C.; Rouxhet, P. G.; Schakenraad, J. . M. Preparation and characterization of superhydrophobic FEP-Teflon surfaces. *Journal of Adhesion Science and Technology* **1992**, *6*, 347–356.

[15] Onda, T.; Shibuichi, S.; Satoh, N.; Tsujii, K. Super-Water-Repellent Fractal Surfaces. *Langmuir* **1996**, *12*, 2125–2127.

[16] Shibuichi, S.; Onda, T.; Satoh, N.; Tsujii, K. Super Water-Repellent Surfaces Resulting from Fractal Structure. *Journal of Physical Chemistry* **1996**, *3654*, 19512–19517.

[17] Lang, A. W. The speedy secret of shark skin. *Physics Today* **2020**, *73*, 58–59.

[18] Hasan, J.; Crawford, R. J.; Ivanova, E. P. Antibacterial surfaces: The quest for a new generation of biomaterials. *Trends in Biotechnology* **2013**, *31*, 295–304.

[19] Ivanova, E. P.; Hasan, J.; Webb, H. K.; Truong, V. K.; Watson, G. S.; Watson, J. A.; Baulin, V. A.; Pogodin, S.; Wang, J. Y.; Tobin, M. J.; Löbbe, C.; Crawford, R. J. Natural Bactericidal Surfaces: Mechanical Rupture of Pseudomonas aeruginosa Cells by Cicada Wings. *Small* **2012**, *8*, 2489–2494.

[20] Autumn, K.; Gravish, N. Gecko adhesion: Evolutionary nanotechnology. *Philosophical Transactions of the Royal Society A: Mathematical, Physical and Engineering Sciences* **2008**, *366*, 1575–1590.

[21] Nosonovsky, M.; Bhushan, B. *Multiscale Dissipative Mechanisms and Hierarchical Surfaces: Friction, Superhydrophobicity, and Biomimetics*; Heidelberg: Springer Press, 2008.

[22] Chan, L. W.; Morse, D. E.; Gordon, M. J. Moth eye-inspired anti-reflective surfaces for improved IR optical systems visible LEDs fabricated with colloidal lithography and etching. *Bioinspiration and Biomimetics* **2018**, *13*, 041001.

[23] Hayles, A.; Hasan, J.; Bright, R.; Palms, D.; Brown, T.; Barker, D.; Vasilev, K. Hydrothermally etched titanium: a review on a promising mechano-bactericidal surface for implant applications. *Materials Today Chemistry* **2021**, *22*, 100622.

[24] House of Lords, U. *Catapults : bridging the gap between research and industry*; 2021.

[25] Brun, P.-T. Fluid-Mediated Fabrication of Complex Assemblies. *JACS Au* **2022**, *2*, 2417–2425.

[26] Schroeder, T. B.; Houghtaling, J.; Wilts, B. D.; Mayer, M. It's Not a Bug, It's a Feature: Functional Materials in Insects. *Advanced Materials* **2018**, *30*, 1705322.

[27] Young, T. III. An essay on the cohesion of fluids. *Philosophical Transactions of the Royal Society of London* **1805**, *95*, 65–87.

[28] Furmidge, C. Studies At Phase Interfaces I. the Sliding of Liquid Drops on Solid Surfaces and a Theory for Spray Retention. *Journal of Colloid Science* **1962**, *17*, 309–324.

[29] Shirtcliffe, N. J.; Mchale, G.; Atherton, S.; Newton, M. I. An introduction to superhydrophobicity. *Advances in Colloid and Interface Science* **2010**, *161*, 124–138.

[30] Quéré, D. Wetting and Roughness. *Annual Review of Materials Research* **2008**, *38*, 71–99.

[31] De Gennes, P. G. Wetting: Statics and dynamics. *Reviews of Modern Physics* **1985**, *57*, 827–863.

[32] Milne, A. J.; Amirfazli, A. The Cassie equation: How it is meant to be used. *Advances in Colloid and Interface Science* **2012**, *170*, 48–55.

[33] Pease, D. C. The significance of the contact angle in relation to the solid surface. *Journal of Physical Chemistry* **1945**, *49*, 107–110.

[34] Gao, L.; McCarthy, T. J. How Wenzel and Cassie Were Wrong. *Langmuir* **2007**, *23*, 3762–3765.

[35] Bhushan, B.; Jung, Y. C.; Koch, K. Micro-, nano- And hierarchical structures for superhydrophobicity, self-cleaning and low adhesion. *Philosophical Transactions of the Royal Society A: Mathematical, Physical and Engineering Sciences* **2009**, *367*, 1631–1672.

[36] Wang, D.; Sun, Q.; Hokkanen, M. J.; Zhang, C.; Lin, F. Y.; Liu, Q.; Zhu, S. P.; Zhou, T.; Chang, Q.; He, B.; Zhou, Q.; Chen, L.; Wang, Z.; Ras, R. H.; Deng, X. Design of robust superhydrophobic surfaces. *Nature* **2020**, *582*, 55–59.

[37] Nishino, T.; Meguro, M.; Nakamae, K.; Matsushita, M.; Ueda, Y. The lowest surface free energy based on -CF3 alignment. *Langmuir* **1999**, *15*, 4321–4323.

[38] Barthlott, W.; Mail, M.; Bhushan, B.; Koch, K. Plant surfaces: Structures and functions for biomimetic innovations. *Nano-Micro Letters* **2017**, *9*, 1–40.

[39] Arzt, E.; Quan, H.; McMeeking, R. M.; Hensel, R. Functional surface microstructures inspired by nature – From adhesion and wetting principles to sustainable new devices. *Progress in Materials Science* **2021**, *119*, 100823.

[40] Leng, X.; Sun, L.; Long, Y.; Lu, Y. Bioinspired superwetting materials for water manipulation. *Droplet* **2022**, *1*, 139–169.

[41] Ensikat, H. J.; Ditsche-Kuru, P.; Neinhuis, C.; Barthlott, W. Superhydrophobicity in perfection: The outstanding properties of the lotus leaf. *Beilstein Journal of Nanotechnology* **2011**, *2*, 152–161.

[42] Almonte, L.; Pimentel, C.; Rodríguez-Cañas, E.; Abad, J.; Fernández, V.; Colchero, J. Rose petal effect: A subtle combination of nano-scale roughness and chemical variability. *Nano Select* **2022**, *3*, 977–989.

[43] Bhushan, B.; Her, E. K. Fabrication of superhydrophobic surfaces with high and low adhesion inspired from rose petal. *Langmuir* **2010**, *26*, 8207–8217.

[44] Romero-Montero, A.; Rosas-Melendez, S. A.; Valencia-Bermúdez, J. L.; Nuñez-Tapia, I.; Piña-Barba, M. C.; Melgoza-Ramírez, L. J.; Leyva-Gómez, G.; Del Prado-Audelo, M. L. Oil/water separation by super-hydrophobic wastepaper cellulose-candelilla wax cryogel: a circular material-based alternative. *Frontiers in Materials* **2023**, *10*, 1–10.

[45] Helbig, R.; Nickerl, J.; Neinhuis, C.; Werner, C. Smart skin patterns protect springtails. *PLoS ONE* **2011**, *6*, 2–7.

[46] Darmanin, T.; Guittard, F. Superhydrophobic and superoleophobic properties in nature. *Materials Today* **2015**, *18*, 273–285.

[47] Domingues, E. M.; Arunachalam, S.; Nauruzbayeva, J.; Mishra, H. Biomimetic coating-free surfaces for long-term entrapment of air under wetting liquids. *Nature Communications* **2018**, *9*, 1–11.

[48] Vu, H. H.; Nguyen, N. T.; Kashaninejad, N. Re-Entrant Microstructures for Robust Liquid Repellent Surfaces. *Advanced Materials Technologies* **2023**, *8*, 2201836.

[49] Elbourne, A.; Crawford, R. J.; Ivanova, E. P. Nano-structured antimicrobial surfaces: From nature to synthetic analogues. *Journal of Colloid and Interface Science* **2017**, *508*, 603–616.

[50] Watson, G. S.; Watson, J. A.; Hu, S.; Brown, C. L. Micro and nanostructures found on insect wings - designs for minimising adhesion and friction. *International Journal of Nanomanufacturing* **2010**, *5*, 112–128.

[51] Linklater, D. P.; Juodkazis, S.; Ivanova, E. P. Nanofabrication of mechano-bactericidal surfaces. *Nanoscale* **2017**, *9*, 16564–16585.

[52] Dickson, M. N.; Liang, E. I.; Rodriguez, L. A.; Vollereaux, N.; Yee, A. F. Nanopat-

terned polymer surfaces with bactericidal properties. *Biointerphases* **2015**, *10*, 021010.

[53] Hawi, S.; Goel, S.; Kumar, V.; Pearce, O.; Ayre, W. N.; Ivanova, E. P. Critical Review of Nanopillar-Based Mechanobactericidal Systems. *ACS Applied Nano Materials* **2022**, *5*, 1–17.

[54] Falconnet, D.; Csucs, G.; Michelle Grandin, H.; Textor, M. Surface engineering approaches to micropattern surfaces for cell-based assays. *Biomaterials* **2006**, *27*, 3044–3063.

[55] Biswas, A.; Bayer, I. S.; Biris, A. S.; Wang, T.; Dervishi, E.; Faupel, F. Advances in top–down and bottom–up surface nanofabrication: Techniques, applications future prospects. *Advances in Colloid and Interface Science* **2012**, *170*, 2–27.

[56] Liu, T. L.; Kim, C.-j. C. Turning a surface superrepellenteven to completely wetting liquids. *Science* **2014**, *346*, 1096–1100.

[57] Cao, Y.; Jana, S.; Bowen, L.; Tan, X.; Liu, H.; Rostami, N.; Brown, J.; Jakubovics, N. S.; Chen, J. Hierarchical Rose Petal Surfaces Delay the Early-Stage Bacterial Biofilm Growth. *Langmuir* **2019**, *35*, 14670–14680.

[58] Fan, Z.; Cui, D.; Zhang, Z.; Zhao, Z.; Chen, H.; Fan, Y.; Li, P.; Zhang, Z.; Xue, C.; Yan, S. Recent progress of black silicon: From fabrications to applications. *Nanomaterials* **2021**, *11*, 1–26.

[59] Pozzato, A.; Zilio, S. D.; Fois, G.; Vendramin, D.; Mistura, G.; Belotti, M.; Chen, Y.; Natali, M. Superhydrophobic surfaces fabricated by nanoimprint lithography. *Microelectronic Engineering* **2006**, *83*, 884–888.

[60] Zhao, H.; Park, K. C.; Law, K. Y. Effect of surface texturing on superoleophobicity, contact angle hysteresis, and "robustness". *Langmuir* **2012**, *28*, 14925–14934.

[61] Cao, Y.; Su, B.; Chinnaraj, S.; Jana, S.; Bowen, L.; Charlton, S.; Duan, P.; Jakubovics, N. S.; Chen, J. Nanostructured titanium surfaces exhibit recalcitrance towards Staphylococcus epidermidis biofilm formation. *Scientific Reports* **2018**, *8*, 1–13.

[62] Ta, V. D.; Dunn, A.; Wasley, T. J.; Li, J.; Kay, R. W.; Stringer, J.; Smith, P. J.; Esenturk, E.; Connaughton, C.; Shephard, J. D. Laser textured superhydrophobic surfaces and their applications for homogeneous spot deposition. *Applied Surface Science* **2016**, *365*, 153–159.

[63] Peter, A.; Lutey, A. H.; Faas, S.; Romoli, L.; Onuseit, V.; Graf, T. Direct laser in-

terference patterning of stainless steel by ultrashort pulses for antibacterial surfaces. *Optics and Laser Technology* **2020**, *123*, 105954.

[64] Lasagni, A. F.; Alamri, S.; Aguilar-Morales, A. I.; Rößler, F.; Voisiat, B.; Kunze, T. Biomimetic surface structuring using laser based interferometric methods. *Applied Sciences (Switzerland)* **2018**, *8*, 1260.

[65] Skoulas, E.; Manousaki, A.; Fotakis, C.; Stratakis, E. Biomimetic surface structuring using cylindrical vector femtosecond laser beams. *Scientific Reports* **2017**, *7*, 1–11.

[66] Xia, Y.; Whitesides, G. M. Soft Lithography. *Angewandte Chemie* **1998**, *37*, 550–575.

[67] Jetter, R.; Riederer, M. Epicuticular crystals of nonacosan-10-ol: In-vitro reconstitution and factors influencing crystal habits. *Planta* **1994**, *195*, 257–270.

[68] Koch, K.; Bhushan, B.; Barthlott, W. Multifunctional surface structures of plants: An inspiration for biomimetics. *Progress in Materials Science* **2009**, *54*, 137–178.

[69] Dent, F. J.; Tyagi, G.; Esat, F.; Cabral, J. T.; Khodaparast, S. Tuneable Topography and Hydrophobicity Mode in Biomimetic Plant-Based Wax Coatings. *Advanced Functional Materials* **2024**, *34*, 2307977.

[70] Su, B.; Li, M.; Shi, Z.; Lu, Q. From superhydrophilic to superhydrophobic: Controlling wettability of hydroxide zinc carbonate film on zinc plates. *Langmuir* **2009**, *25*, 3640–3645.

[71] Guo, X.; Liu, L.; Zhuang, Z.; Chen, X.; Ni, M.; Li, Y.; Cui, Y.; Zhan, P.; Yuan, C.; Ge, H.; Wang, Z.; Chen, Y. A New Strategy of Lithography Based on Phase Separation of Polymer Blends. *Scientific Reports* **2015**, *5*, 1–12.

[72] Hatton, B.; Mishchenko, L.; Davis, S.; Sandhage, K. H.; Aizenberg, J. Assembly of large-area, highly ordered, crack-free inverse opal films. *Proceedings of the National Academy of Sciences of the United States of America* **2010**, *107*, 10354–10359.

[73] Yuan, L.; Wang, Y.; Mema, R.; Zhou, G. Driving force and growth mechanism for spontaneous oxide nanowire formation during the thermal oxidation of metals. *Acta Materialia* **2011**, *59*, 2491–2500.

[74] Chen, L.; Guo, Z.; Liu, W. Outmatching superhydrophobicity: Bio-inspired reentrant curvature for mighty superamphiphobicity in air. *Journal of Materials Chemistry A* **2017**, *5*, 14480–14507.

[75] Bang, J.; Jeong, U.; Ryu, D. Y.; Russell, T. P.; J Hawker, C. Block copolymer nanolithography: Translation of molecular level control to nanoscale patterns. *Advanced Materials* **2009**, *21*, 4769–4792.

[76] O'Connell, R. A.; Porter, A. E.; Higgins, J. S.; Cabral, J. T. Phase behaviour of poly(2, 6-diphenyl-p-phenylene oxide) (PPPO) in mixed solvents. *Polymer* **2019**, *180*, 121652.

[77] Siddique, R. H.; Donie, Y. J.; Gomard, G.; Yalamanchili, S.; Merdzhanova, T.; Lemmer, U.; Hölscher, H. Bioinspired phase-separated disordered nanostructures for thin photovoltaic absorbers. *Science Advances* **2017**, *3*, e1700232.

[78] Wang, L.; Shu, L.; Hu, Q.; Jiang, X.; Yang, H.; Wang, H.; Rao, L. Mechanism of self-recovery of hydrophobicity after surface damage of lotus leaf. *Plant Methods* **2024**, *20*, 1–14.

[79] Arunachalam, S.; Ahmad, Z.; Das, R.; Mishra, H. Counterintuitive Wetting Transitions in Doubly Reentrant Cavities as a Function of Surface Make-Up, Hydrostatic Pressure, and Cavity Aspect Ratio. *Advanced Materials Interfaces* **2020**, *7*, 2001268.

[80] Aitken, J. Breath Figures. *Proceedings of the Royal Society of Edinburgh* **1893**, *20*, 94–97.

[81] Rayleigh Breath figures. *Nature* **1911**, *86*, 416–417.

[82] Baker, T. Breath Figures . *The London, Edinburgh, and Dublin Philosophical Magazine and Journal of Science* **1922**, *44*, 752–765.

[83] Spurr, R. T.; Butlin, J. G. Breath figures. *Nature* **1957**, *179*, 1187.

[84] Beysens, D.; Knobler, C. M. Growth of Breath Figures. *Physical Review Letters* **1986**, *57*, 1433–1436.

[85] Knobler, C. M.; Beysens, D. Growth of breath figures on fluid surfaces. *Europhysics Letters* **1988**, *6*, 707–712.

[86] Meakin, P. Dropwise condensation: The deposition growth and coalescence of fluid droplets. *Physica Scripta* **1992**, *1*, 31–41.

[87] Family, F.; Meakin, P. Kinetics of droplet growth processes: Simulations, theory, and experiments. *Physical Review A* **1989**, *40*, 3836–3854.

[88] Briscoe, B. J.; Galvin, K. P. Growth with coalescence during condensation. *PHYSICAL REVIEW A* **1991**, *43*, 1906–1917.

[89] Briscoe, B. J.; Galvin, K. P. Breath figures. *Journal of Physics D: Applied Physics* **1990**, *23*, 1265–1266.

[90] Yabu, H. Fabrication of honeycomb films by the breath figure technique and their applications. *Science and Technology of Advanced Materials* **2018**, *19*, 802–822.

[91] François, B.; Pitois, O.; François, J. Polymer films with a self-organized honeycomb morphology. *Advanced Materials* **1995**, *7*, 1041–1044.

[92] Widawski, G.; Rawiso, M.; François, B. Self-organized honeycomb morphology of star-polymer polystyrene films. *Nature* **1994**, *369*, 387–389.

[93] Carey, V. P. *Liquid-Vapor Phase-Change Phenomena*; CRC Press, 2020; Chapter 5, pp 153–200.

[94] Srinivasarao, M.; Coolings, D.; Philips, A.; Patel, S. Three-Dimensionally Ordered Array of Air Bubbles in a Polymer Film. *Science* **2001**, *292*, 79–83.

[95] Stenzel, M. H.; Davis, T. P. Formation of Honeycomb-Structured, Porous Films via Breath Figures with Different Polymer Architectures. *Journal of Polymer Science Part A: Polymer Chemistry* **2006**, *44*, 2363–2375.

[96] Hernández-Guerrero, M.; Stenzel, M. H. Honeycomb structured polymer films via breath figures. *Polymer Chemistry* **2012**, *3*, 563–577.

[97] Zhang, A.; Bai, H.; Li, L. Breath Figure: A Nature-Inspired Preparation Method for Ordered Porous Films. *Chemical Reviews* **2015**, *115*, 9801–9868.

[98] Wan, L. S.; Zhu, L. W.; Ou, Y.; Xu, Z. K. Multiple interfaces in self-assembled breath figures. *Chemical Communications* **2014**, *50*, 4024–4039.

[99] Rodríguez-hernández, J.; Bormashenko, E. *Breath Figures: Mechanisms of Multi-Scale Patterning and Strategies for Fabrication and Applications of Microstructured Functional Porous Surfaces*; Springer, 2020.

[100] Escalé, P.; Rubatat, L.; Billon, L.; Save, M. Recent advances in honeycomb-structured porous polymer films prepared via breath figures. *European Polymer Journal* **2012**, *48*, 1001–1025.

[101] Bormashenko, E. Breath-figure self-assembly, a versatile method of manufacturing membranes and porous structures: Physical, chemical and technological aspects. *Membranes* **2017**, *7*, 45.

[102] Battenbo, H.; Cobley, R. J.; Wilks, S. P. A quantitative study of the formation of breath figure templated polymer materials. *Soft Matter* **2011**, *7*, 10864–10873.

[103] Pitois, O.; François, B. Formation of ordered micro-porous membranes. *European Physical Journal B* **1999**, *8*, 225–231.

[104] Li, J.; Li, Y.; Chan, C. Y. K.; Kwok, R. T. K.; Li, H.; Zrazhevskiy, P.; Gao, X.; Sun, J. Z.; Qin, A.; Tang, B. Z. An Aggregation-Induced-Emission Platform for Direct Visualization of Interfacial Dynamic Self-Assembly. *Angewandte Chemie International Edition* **2014**, *53*, 13518–13522.

[105] Falak, S.; Shin, B.; Huh, D. Modified Breath Figure Methods for the Pore-Selective Functionalization of Honeycomb-Patterned Porous Polymer Films. *Nanomaterials* **2022**, *12*, 1055.

[106] Ferrari, E.; Fabbri, P.; Pilati, F. Solvent and substrate contributions to the formation of breath figure patterns in polystyrene films. *Langmuir* **2011**, *27*, 1874–1881.

[107] Dickson, J. L.; Psathas, P. A.; Salinas, B.; Luna-barcenas, G.; Hwang, H. S.; Lim, K. T.; Johnston, K. P. Formation and Growth of Water-in-CO 2 Miniemulsions. *Langmuir* **2003**, *19*, 4895–4904.

[108] De León, A. S.; Del Campo, A.; Fernández-García, M.; Rodríguez-Hernández, J.; Muñoz-Bonilla, A. Fabrication of structured porous films by breath figures and phase separation processes: Tuning the chemistry and morphology inside the pores using click chemistry. *ACS Applied Materials and Interfaces* **2013**, *5*, 3943–3951.

[109] De León, A. S.; Del Campo, A.; Fernández-García, M.; Rodríguez-Hernández, J.; Muñoz-Bonilla, A. Tuning the pore composition by two simultaneous interfacial self-assembly processes: Breath figures and coffee stain. *Langmuir* **2014**, *30*, 6134–6141.

[110] Muñoz-Bonilla, A.; Ibarboure, E.; Papon, E.; Rodriguez-Hernandez, J. Self-organized hierarchical structures in polymer surfaces: Self-assembled nanostructures within breath figures. *Langmuir* **2009**, *25*, 6493–6499.

[111] Böker, A.; Lin, Y.; Chiapperini, K.; Horowitz, R.; Thompson, M.; Carreon, V.; Xu, T.; Abetz, C.; Skaff, H.; Dinsmore, A. D.; Emrick, T.; Russell, T. P. Hierarchical nanoparticle assemblies formed by decorating breath figures. *Nature Materials* **2004**, *3*, 302–306.

[112] Gurr, P. A.; Zhang, Z.; Hao, X.; Hughes, T. C.; Qiao, G. G. Highly Ordered Honeycomb Film Formation of Linear Polymers by the Breath Figure Technique. *Australian Journal of Chemistry* **2016**, *69*, 1130–1139.

[113] Peng, J.; Han, Y.; Yang, Y.; Li, B. The influencing factors on the macroporous formation in polymer films by water droplet templating. *Polymer* **2004**, *45*, 447–452.

[114] Zander, N. E.; Orlicki, J. A.; Karikari, A. S.; Long, T. E.; Rawlett, A. M. Super-Hydrophobic Surfaces via Micrometer-Scale Templated Pillars. *Chemistry of Materials* **2007**, *11*, 6145–6149.

[115] Bolognesi, A.; Mercogliano, C.; Yunus, S. Self-Organization of Polystyrenes into Ordered Microstructured Films and Their Replication by Soft Lithography. *Langmuir* **2005**, *21*, 3480–3485.

[116] Hernández-Guerrero, M.; Davis, T. P.; Barner-Kowollik, C.; Stenzel, M. H. Polystyrene comb polymers built on cellulose or poly(styrene-co-2-hydroxyethylmethacrylate) backbones as substrates for the preparation of structured honeycomb films. *European Polymer Journal* **2005**, *41*, 2264–2277.

[117] Stenzel, M. H. Formation of regular honeycomb-patterned porous film by self-organization. *Australian Journal of Chemistry* **2002**, *55*, 239–243.

[118] Saunders, A. E.; Dickson, J. L.; Shah, P. S.; Lee, M. Y.; Lim, K. T.; Johnston, K. P.; Korgel, B. A. Breath figure templated self-assembly of porous diblock copolymer films. *Physical Review E - Statistical, Nonlinear, and Soft Matter Physics* **2006**, *73*, 031608.

[119] Ghannam, L.; Manguian, M.; François, J.; Billon, L. A versatile route to functional biomimetic coatings: Ionomers for honeycomb-like structures. *Soft Matter* **2007**, *3*, 1492–1499.

[120] Tian, Y.; Ding, H.; Jiao, Q.; Shi, Y. Influence of Solvents on the Formation of Honeycomb Films by Water Droplets Templating. *Macromolecular Chemistry and Physics* **2006**, *207*, 545–553.

[121] Zheng, Y.; Kubowaki, Y.; Kashiwagi, M.; Miyazaki, K. Process optimization of preparing honeycomb-patterned polystyrene films by breath figure method. *Journal of Mechanical Science and Technology* **2011**, *25*, 33–36.

[122] Cobo, F. N.; Faria-Tisher, P. C.; Duarte, J. L.; Carvalho, G. M. Preparation and characterization of microporous cellulose acetate films using breath figure method by spin coating technique. *Cellulose* **2017**, *24*, 4981–4995.

[123] Gliemann, H.; Almeida, A. T.; Petri, D. F. S.; Schimmel, T. Nanostructure formation in polymer thin films influenced by humidity. *Surface and Interface Analysis* **2007**, *39*, 1–8.

[124] Tian, Y.; Jiao, Q.; Ding, H.; Shi, Y.; Liu, B. The formation of honeycomb structure in polyphenylene oxide films. *Polymer* **2006**, *47*, 3866–3873.

[125] Bormashenko, E.; Balter, S.; Aurbach, D. On the Nature of the Breath Figures Self-Assembly in Evaporated Polymer Solutions: Revisiting Physical Factors Governing the Patterning. *Macromolecular Chemistry and Physics* **2012**, *213*, 1742–1747.

[126] Bunz, U. H. F. Breath figures as a dynamic templating method for polymers and nanomaterials. *Advanced Materials* **2006**, *18*, 973–989.

[127] Daly, R.; Sader, J. E.; Boland, J. J. Existence of micrometer-scale water droplets at solvent/air interfaces. *Langmuir* **2012**, *28*, 13218–13223.

[128] Daly, R.; Sader, J. E.; Boland, J. J. The dominant role of the solvent-water interface in water droplet templating of polymers. *Soft Matter* **2013**, *9*, 7960–7965.

[129] Casper, C. L.; Stephens, J. S.; Tassi, N. G.; Chase, D. B.; Rabolt, J. F. Controlling surface morphology of electrospun polystyrene fibers: Effect of humidity and molecular weight in the electrospinning process. *Macromolecules* **2004**, *37*, 573–578.

[130] Huang, C.; Thomas, N. L. Fabricating porous poly(lactic acid) fibres via electrospinning. *European Polymer Journal* **2018**, *99*, 464–476.

[131] Ghasemi, S. M.; Besharati, M. Ethyl cyanoacrylate ordered porous films prepared via in-situ polymerization and static breath figures process. *Polymers for Advanced Technologies* **2020**, *31*, 3104–3113.

[132] Dell'Aversana, P.; Banavar, J. R.; Koplik, J. Suppression of coalescence by shear and temperature gradients. *Physics of Fluids* **1996**, *8*, 15–28.

[133] Onder, O. C.; Nazeer, M. A.; Yilgör, E.; Yilgör, I. Spontaneous formation of microporous poly(lactic acid) coatings. *Progress in Organic Coatings* **2018**, *125*, 249–256.

[134] Anand, S.; Rykaczewski, K.; Subramanyam, S. B.; Beysens, D.; Varanasi, K. K. How droplets nucleate and grow on liquids and liquid impregnated surfaces. *Soft Matter* **2014**, *11*, 69–80.

[135] Cheng, C. X.; Tian, Y.; Shi, Y. Q.; Tang, R. P.; Xi, F. Porous polymer films and honeycomb structures based on amphiphilic dendronized block copolymers. *Langmuir* **2005**, *21*, 6576–6581.

[136] Wang, C.; Mao, Y.; Wang, D.; Qu, Q.; Yang, G.; Hu, X. Fabrication of highly ordered microporous thin films by PS-b-PAA self-assembly and investigation of their tunable surface properties. *Journal of Materials Chemistry* **2008**, *18*, 683–690.

[137] Li, X.; Wang, Y.; Zhang, L.; Tan, S.; Yu, X.; Zhao, N.; Chen, G.; Xu, J. Fabrication of honeycomb-patterned polyalkylcyanoacrylate films from monomer solution by breath figures method. *Journal of Colloid and Interface Science* **2010**, *350*, 253–259.

[138] Bormashenko, E.; Pogreb, R.; Stanevsky, O.; Bormashenko, Y.; Stein, T.; Gaisin, V.-Z.; Cohen, R.; Gendelman, O. V. Mesoscopic Patterning in Thin Polymer Films Formed under the Fast Dip-Coating Process. *Macromolecular Materials and Engineering* **2005**, *290*, 114–121.

[139] Maruyama, N.; Karthaus, O.; Ijiro, K.; Shimomura, M.; Koito, T.; Nishimura, S.; Sawadaishi, T.; Nishi, N.; Tokura, S. Mesoscopic pattern formation of nanostructured polymer assemblies. *Supramolecular Science* **1998**, *5*, 331–336.

[140] Nishikawa, T.; Nishida, J.; Ookura, R.; Nishimura, S. I.; Wada, S.; Karino, T.; Shimomura, M. Mesoscopic patterning of cell adhesive substrates as novel biofunctional interfaces. *Materials Science and Engineering C* **1999**, *10*, 141–146.

[141] Young, J. F. Humidity Control In The Laboratory Using Salt Solutions - A Review. *Journal of Applied Chemistry* **1967**, *17*, 241–268.

[142] Ding, J.; Zhang, A.; Bai, H.; Li, L.; Li, J.; Ma, Z. Breath figure in non-aqueous vapor. *Soft Matter* **2013**, *9*, 506–514.

[143] Bai, W.; Xiao, X.; Cai, L.; Xu, Y.; Lin, J. Fabrication of morphology-controlled nano/microstructural polyfluorene in mixed nonsolvent vapor atmospheres. *Reactive and Functional Polymers* **2014**, *76*, 13–18.

[144] Kojima, M.; Hirai, Y.; Yabu, H.; Shimomura, M. The effects of interfacial tensions of amphiphilic copolymers on honeycomb-patterned films. *Polymer Journal* **2009**, *41*, 667–671.

[145] Servoli, E.; Ruffo, G. A.; Migliaresi, C. Interplay of kinetics and interfacial interactions in breath figure templating - A phenomenological interpretation. *Polymer* **2010**, *51*, 2337–2344.

[146] Sigsbee, R. A.; Pound, G. M. Heterogeneous Nucleation from the Vapor. *Advances in Colloid and Interface Science* **1967**, *1*, 335–390.

[147] Eslami, F.; Elliott, J. A. Thermodynamic investigation of the barrier for heterogeneous nucleation on a fluid surface in comparison with a rigid surface. *Journal of Physical Chemistry B* **2011**, *115*, 10646–10653.

[148] Nepomnyashchy, A. A.; Golovin, A. A.; Tikhomirova, A. E.; Volpert, V. A. Nucleation and growth of droplets at a liquid-gas interface. *Physical Review E* **2006**, *74*, 021605.

[149] Daly, R.; Sader, J. E.; Boland, J. J. Taming Self-Organization Dynamics to Dramatically Control Porous Architectures. *ACS Nano* **2016**, *10*, 3087–3092.

[150] Bormashenko, E.; Frenkel, M.; Vilk, A.; Legchenkova, I.; Fedorets, A.; Aktaev, N.; Dombrovsky, L.; Nosonovsky, M. Characterization of Self-Assembled 2D Patterns with Voronoi Entropy. *Entropy* **2018**, *20*, 956.

[151] Wu, X.; Wang, S. Regulating MC3T3-E1 cells on deformable poly(ϵ-caprolactone) honeycomb films prepared using a surfactant-free breath figure method in a water-miscible solvent. *ACS Applied Materials and Interfaces* **2012**, *4*, 4966–4975.

[152] Beysens, D. Dew nucleation and growth. *Comptes Rendus Physique* **2006**, *7*, 1082–1100.

[153] Beysens, D. The formation of dew. *Atmospheric Research* **1995**, *39*, 215–237.

[154] Limaye, A. V.; Narhe, R. D.; Dhote, A. M.; Ogale, S. B. Evidence for convective effects in breath figure formation on volatile fluid surfaces. *Physical Review Letters* **1996**, *76*, 3762–3765.

[155] Liu, W.; Xie, M.; Li, C.; Xie, H.; Hong, R.; Chen, Y.; Li, Z.; Zeng, G. Highly ordered water droplet arrays on a volatile solvent surface. *Colloids and Surfaces A: Physicochemical and Engineering Aspects* **2020**, *590*, 124487.

[156] Karthaus, O.; Maruyama, N.; Yabu, H.; Koito, T.; Akagi, K.; Shimomura, M. Pattern formation in polymer films by non-linear processes. *Macromolecular Symposia* **2000**, *160*, 137–142.

[157] Yamazaki, H.; Ito, K.; Yabu, H.; Shimomura, M. Formation and control of line defects caused by tectonics of water droplet arrays during self-organized honeycomb-patterned polymer film formation. *Soft Matter* **2014**, *10*, 2741–2747.

[158] Schatz, M. F.; Neitzel, G. P. Experiments on Thermocapillary Instabilities. *Annual Review of Fluid Mechanics* **2001**, *33*, 93–127.

[159] Bormashenko, E.; Balter, S.; Pogreb, R.; Bormashenko, Y.; Gendelman, O.; Aurbach, D. On the mechanism of patterning in rapidly evaporated polymer solutions: Is temperature-gradient-driven Marangoni instability responsible for the large-scale patterning? *Journal of Colloid and Interface Science* **2010**, *343*, 602–607.

[160] Wu, B.; Zhang, W.; Gao, N.; Zhou, M.; Liang, Y.; Wang, Y.; Li, F.; Li, G. Poly (ionic liquid)-Based Breath Figure Films: A New Kind of Honeycomb Porous Films with Great Extendable Capability. *Scientific Reports* **2017**, *7*, 13973.

[161] Ponnusamy, T.; Lawson, L. B.; Freytag, L. C.; Blake, D. A.; Ayyala, R. S.; John, V. T. In vitro degradation and release characteristics of spin coated thin films of PLGA with a "breath figure" morphology. *Biomatter* **2012**, *2*, 77–86.

[162] Fukuhira, Y.; Yabu, H.; Ijiro, K.; Shimomura, M. Interfacial tension governs the formation of self-organized honeycomb-patterned polymer films. *Soft Matter* **2009**, *5*, 2037–2041.

[163] De Gennes, P. G. Instabilities during the evaporation of a film: Non-glassy polymer + volatile solvent. *European Physical Journal E* **2001**, *6*, 421–424.

[164] Gau, H.; Herminghaus, S. Ripening of Ordered Breath Figures. *Physical Review Letters* **2000**, *84*, 4156–4159.

[165] Noor, N.; Koll, J.; Abetz, C.; Notzke, H.; Abetz, V. Continuous Production of

Macroporous Films: An Alternative to Breath Figure Assembly. *Scientific Reports* **2017**, *7*, 1–9.

[166] Yamazaki, H.; Kohashi, S.; Ito, K.; Ijiro, K.; Shimomura, M. Production technology and applications of honeycomb films. *Polymer Journal* **2021**, *54*, 107–120.

[167] Farbod, F.; Pourabbas, B.; Sharif, M. Direct breath figure formation on PMMA and superhydrophobic surface using in situ perfluoro-modified silica nanoparticles. *Journal of Polymer Science Part B: Polymer Physics* **2013**, *51*, 441–451.

[168] Huang, C.; Kamra, T.; Chaudhary, S.; Shen, X. Breath figure patterns made easy. *ACS Applied Materials and Interfaces* **2014**, *6*, 5971–5976.

[169] Huang, C.; Shen, X.; Liu, X.; Chen, Z.; Shu, B.; Wan, L.; Liu, H.; He, J. Hybrid breath figure method: A new insight in Petri dishes for cell culture. *Journal of Colloid and Interface Science* **2019**, *541*, 114–122.

[170] Chen, S.; Gao, S.; Jing, J.; Lu, Q. Designing 3D Biological Surfaces via the Breath-Figure Method. *Advanced Healthcare Materials* **2018**, *7*, 1–18.

[171] Kojima, M.; Nakanishi, T.; Hirai, Y.; Yabu, H.; Shimomura, M. Photo-patterning of honeycomb films prepared from amphiphilic copolymer containing photochromic spiropyran. *Chemical Communications* **2010**, *46*, 3970–3972.

[172] Yabu, H.; Takebayashi, M.; Tanaka, M.; Shimomura, M. Superhydrophobic and lipophobic properties of self-organized honeycomb and pincushion structures. *Langmuir* **2005**, *21*, 3235–3237.

[173] Liu, M.; Zhang, X.; Wang, D.; Cheng, J.; Pang, X.; Qu, W.; Li, C.; Li, S. Facile fabrication of superhydrophobic surface from fluorinated poss acrylate copolymer via one-step breath figure method and its anti-corrosion property. *Polymers* **2019**, *11*, 1953.

[174] Li, L.; Zhong, Y.; Li, J.; Chen, C.; Zhang, A.; Xu, J.; Ma, Z. Thermally stable and solvent resistant honeycomb structured polystyrene films via photochemical cross-linking. *Journal of Materials Chemistry* **2009**, *19*, 7222–7227.

[175] Park, J. M.; Lee, Y. H.; Park, H.; Kim, H. D. Preparation and properties of UV-curable fluorinated polyurethane acrylates. *Journal of Applied Polymer Science* **2014**, *131*, 40603.

[176] Maniglio, D.; Ding, Y.; Wang, L.; Migliaresi, C. One-step process to create porous structures in cross-linked polymer films via breath-figure formations during in situ cross-linking reactions. *Polymer* **2011**, *52*, 5102–5106.

[177] Cong, H.; Wang, J.; Yu, B.; Tang, J. Preparation of a highly permeable ordered

porous microfiltration membrane of brominated poly(phenylene oxide) on an ice substrate by the breath figure method. *Soft Matter* **2012**, *8*, 8835–8839.

[178] Peng, Y.; Guo, X.; Liang, R.; Mou, Y.; Cheng, H.; Chen, M.; Liu, S. Fabrication of Microlens Arrays with Controlled Curvature by Micromolding Water Condensing Based Porous Films for Deep Ultraviolet LEDs. *ACS Photonics* **2017**, *4*, 2479–2485.

[179] Mei, L.; Wang, G.; Deng, J.; Xiao, J.; Guo, X. Tunable fabrication of concave microlens arrays by initiative cooling-based water droplet condensation. *Soft Matter* **2019**, *15*, 9150–9156.

[180] Yabu, H.; Jia, R.; Matsuo, Y.; Ijiro, K.; Yamamoto, S.-a.; Nishino, F.; Takaki, T.; Kuwahara, M.; Shimomura, M. Preparation of Highly Oriented Nano-Pit Arrays by Thermal Shrinking of Honeycomb-Patterned Polymer Films. *Advanced Materials* **2008**, *20*, 4200–4204.

[181] Ding, J.; Gong, J.; Bai, H.; Li, L.; Zhong, Y.; Ma, Z.; Svrcek, V. Constructing honeycomb micropatterns on nonplanar substrates with high glass transition temperature polymers. *Journal of Colloid and Interface Science* **2012**, *380*, 99–104.

[182] Bolognesi, A.; Galeotti, F.; Moreau, J.; Giovanella, U.; Porzio, W.; Scavia, G.; Bertini, F. Unsoluble ordered polymeric pattern by breath figure approach. *Journal of Materials Chemistry* **2010**, *20*, 1483–1488.

[183] Ma, H.; Hao, J. Ordered patterns and structures via interfacial self-assembly: superlattices , honeycomb structures and coffee rings. *Chemical Society Reviews* **2011**, *40*, 5457–5471.

[184] Tanaka, M.; Takebayashi, M.; Shimomura, M. Fabrication of Ordered Arrays of Biodegradable Polymer Pincushions Using Self-Organized Honeycomb-Patterned Films. *Macromolecular Symposia* **2009**, *279*, 175–182.

[185] Dent, F. J.; Harbottle, D.; Warren, N. J.; Khodaparast, S. Temporally Arrested Breath Figure. *ACS Applied Materials and Interfaces* **2022**, *14*, 27435–27443.

[186] Dent, F. J.; Harbottle, D.; Warren, N. J.; Khodaparast, S. Exploiting breath figure reversibility for in situ pattern modulation. *Soft Matter* **2023**, *19*, 2737.

[187] Blaschke, J.; Lapp, T.; Hof, B.; Vollmer, J. Breath Figures: Nucleation, Growth, Coalescence, and the Size Distribution of Droplets. *Physical Review Letters* **2012**, *109*, 068701.

[188] Kuo, C.-T.; Lin, Y.-S.; Liu, T.-K.; Liu, H.-C.; Hung, W.-C.; Jiang, I.-M.; Tsai, M.-S.; Hsu, C.-C.; Wu, C.-Y. Dynamics of single-layer polymer breath figures. *Optics Express* **2010**, *18*, 18464–18470.

[189] Beysens, D. *The Physics of Dew, Breath Figures and Dropwise Condensation*; Heidelberg: Springer, 2022; Vol. 994.

[190] Sticker, D.; Geczy, R.; Häfeli, U. O.; Kutter, J. P. Thiol-Ene Based Polymers as Versatile Materials for Microfluidic Devices for Life Sciences Applications. 2020.

[191] Norland Products Norland Optical Adhesives - Technical Data Sheets.

[192] Hoyle, C. E.; Lee, T. Y.; Roper, T. Thiol-enes: Chemistry of the past with promise for the future. *Journal of Polymer Science, Part A: Polymer Chemistry* **2004**, *42*, 5301–5338.

[193] Worthington, A. M. II. On Pendent drops. *Proceedings of the Royal Society of London* **1881**, *212*, 362–377.

[194] Berry, J. D.; Neeson, M. J.; Dagastine, R. R.; Chan, D. Y.; Tabor, R. F. Measurement of surface and interfacial tension using pendant drop tensiometry. *Journal of Colloid and Interface Science* **2015**, *454*, 226–237.

[195] McHale, G.; Afify, N.; Armstrong, S.; Wells, G. G.; Ledesma-Aguilar, R. The Liquid Young's Law on SLIPS: Liquid-Liquid Interfacial Tensions and Zisman Plots. *Langmuir* **2022**, *38*, 10032–10042.

[196] Emslie, A. G.; Bonner, F. T.; Peck, L. G. Flow of a viscous liquid on a rotating disk. *Journal of Applied Physics* **1958**, *29*, 858–862.

[197] Alduchov, O. A.; Eskridge, R. E. Improved Magnus form approximation of saturation vapor pressure. *Journal of applied meteorology* **1996**, *35*, 601–609.

[198] Llorente, O.; Agirre, A.; Calvo, I.; Olaso, M.; Tomovska, R.; Sardon, H. Exploring the advantages of oxygen-tolerant thiol-ene polymerization over conventional acrylate free radical photopolymerization processes for pressure-sensitive adhesives. *Polymer Journal* **2021**, *53*, 1195–1204.

[199] Yabu, H.; Shimomura, M. Simple fabrication of micro lens arrays. *Langmuir* **2005**, *21*, 1709–1711.

[200] Murphy, D. B.; Davidson, M. W. *Fundamentals of Light Microscopy and Electronic Imaging*, 2nd ed.; John Wiley and Sons, 2012.

[201] Schneider, C. A.; Rasband, W. S.; Eliceiri, K. W. NIH Image to ImageJ: 25 years of image analysis. *Nature Methods* **2012**, *9*, 671–675.

[202] Matlab R2023b Image Processing Toolbox™. 2023.

[203] Aurenhammer, F. Voronoi Diagrams-A Survey of a Fundamental Geometric Data Structure. *ACM Computing Surveys* **1991**, *23*.

[204] Webb, R. H. Confocal optical microscopy. *Reports on Progress in Physics* **1996**, *59*, 427–471.

[205] Wang, Z.; Guo, W.; Li, L.; Luk'yanchuk, B.; Khan, A.; Liu, Z.; Chen, Z.; Hong, M. Optical virtual imaging at 50 nm lateral resolution with a white-light nanoscope. *Nature Communications 2011 2:1* **2011**, *2*, 1–6.

[206] Beysens, D.; Steyer, A.; Guenoun, P.; Fritter, D. How Does Dew Form? *Phase Transitions* **1991**, *31*, 219–246.

[207] Karthika, S.; Radhakrishnan, T. K.; Kalaichelvi, P. A Review of Classical and Nonclassical Nucleation Theories. *Crystal Growth and Design* **2016**, *16*, 6663–6681.

[208] Adamson, A. W.; Gast, A. P. *Physical Chemistry of Surfaces*, 6th ed.; John Wiley Sons Inc., 1997.

[209] Gibbs, J. W. *On the equilibrium of heterogeneous substances*; 1878.

[210] Volmer, M.; Weber, A. Nucleus Formation in Supersaturated Systems [translation]. *Zeitschrift für Physikalische Chemie* **1926**, *1*, 277–301.

[211] Cantor, B.; Nabarro, F. R. Heterogeneous nucleation and adsorption. Philosophical Transactions of the Royal Society A: Mathematical, Physical and Engineering Sciences. 2003; pp 409–417.

[212] Kashchiev, D. Analysis of experimental data for the nucleation rate of water droplets. *Journal of Chemical Physics* **2006**, *125*.

[213] Sharaf, M. A.; Dobbins, R. A. A comparison of measured nucleation rates with the predictions of several theories of homogeneous nucleation. *The Journal of Chemical Physics* **1982**, *77*, 1517–1526.

[214] Laaksonen, A.; Napari, I. Breakdown of the capillarity approximation in binary nucleation: A density functional study. *Journal of Physical Chemistry B* **2001**, *105*, 11678–11682.

[215] Cahn, J. W.; Hilliard, J. E. Free energy of a nonuniform system. I. Interfacial free energy. *The Journal of Chemical Physics* **1958**, *28*, 258–267.

[216] Martens, J.; Uchtmann, H.; Hensel, F. Homogeneous Nucleation of Mercury Vapor. *Journal of physical chemistry* **1987**, *91*, 2489–2492.

[217] Becke, A. D. Perspective: Fifty years of density-functional theory in chemical physics. *Journal of Chemical Physics* **2014**, *140*.

[218] Lecointre, P.; Laney, S.; Michalska, M.; Li, T.; Tanguy, A.; Papakonstantinou, I.;

Quéré, D. Unique and universal dew-repellency of nanocones. *Nature Communications 2021 12:1* **2021**, *12*, 1–9.

[219] Zhang, L.; Iwata, R.; Zhao, L.; Gong, S.; Lu, Z.; Xu, Z.; Zhong, Y.; Zhu, J.; Cruz, S.; Wilke, K. L.; Cheng, P.; Wang, E. N. Nucleation Site Distribution Probed by Phase-Enhanced Environmental Scanning Electron Microscopy. *Cell Reports Physical Science* **2020**, *1*.

[220] Fritter, D.; Knobler, C. M.; Beysens, D. A. Experiments and simulation of the growth of droplets on a surface (breath figures). *Physical Review A* **1991**, *43*, 2856–2869.

[221] El Fil, B.; Kini, G.; Garimella, S. A review of dropwise condensation: Theory, modeling, experiments, and applications. 2020.

[222] Ucar, I. O.; Erbil, H. Y. Dropwise condensation rate of water breath figures on polymer surfaces having similar surface free energies. *Applied Surface Science* **2012**, *259*, 515–523.

[223] Mu, C.; Pang, J.; Lu, Q.; Liu, T. Effects of surface topography of material on nucleation site density of dropwise condensation. *Chemical Engineering Science* **2008**, *63*, 874–880.

[224] Katselas, A.; Parin, R.; Neto, C.; Katselas, A.; Parin, R.; Neto, C. Quantification of Nucleation Site Density as a Function of Surface Wettability on Smooth Surfaces. *Advanced Materials Interfaces* **2022**, *9*, 2200246.

[225] Sharma, C. S.; Milionis, A.; Naga, A.; Lam, C. W. E.; Rodriguez, G.; Del Ponte, M. F.; Negri, V.; Raoul, H.; D'Acunzi, M.; Butt, H. J.; Vollmer, D.; Poulikakos, D. Enhanced Condensation on Soft Materials through Bulk Lubricant Infusion. *Advanced Functional Materials* **2022**, *32*.

[226] Sokuler, M.; Auernhammer, G. K.; Roth, M.; Liu, C.; Bonacurrso, E.; Butt, H. J. The softer the better: Fast condensation on soft surfaces. *Langmuir* **2010**, *26*, 1544–1547.

[227] Phadnis, A.; Rykaczewski, K. Dropwise Condensation on Soft Hydrophobic Coatings. *Langmuir* **2017**, *33*, 12095–12101.

[228] Anand, S.; Paxson, A. T.; Dhiman, R.; Smith, J. D.; Varanasi, K. K. Enhanced Condensation on Lubricant-Impregnated Nanotextured Surfaces. *ACS Nano* **2012**, *6*, 10122–10129.

[229] Sun, J.; Jiang, X.; Weisensee, P. B. Enhanced Water Nucleation and Growth

Based on Microdroplet Mobility on Lubricant-Infused Surfaces. *Langmuir* **2021**, *37*, 12790–12801.

[230] De Gennes, P. G.; Brochard-Wyart, F.; Quere, D. *Capillarity and Wetting Phenomena*; Springer: New york, 2004.

[231] Marchand, A.; Das, S.; Snoeijer, J. H.; Andreotti, B. Contact angles on a soft solid: From young's law to neumann's law. *Physical Review Letters* **2012**, *109*, 1–5.

[232] Semprebon, C.; McHale, G.; Kusumaatmaja, H. Apparent contact angle and contact angle hysteresis on liquid infused surfaces. *Soft Matter* **2017**, *13*, 101–110.

[233] Weisensee, P. B.; Wang, Y.; Qiang, H.; Schultz, D.; King, W. P.; Miljkovic, N. Condensate droplet size distribution on lubricant-infused surfaces. *International Journal of Heat and Mass Transfer* **2017**, *109*, 187–199.

[234] Xiao, R.; Miljkovic, N.; Enright, R.; Wang, E. N. Immersion condensation on oil-infused heterogeneous surfaces for enhanced heat transfer. *Scientific Reports* **2013**, *3*.

[235] Kajiya, T.; Schellenberger, F.; Papadopoulos, P.; Vollmer, D.; Butt, H. J. 3D Imaging of Water-Drop Condensation on Hydrophobic and Hydrophilic Lubricant-Impregnated Surfaces. *Scientific Reports* **2016**, *6*, 1–10.

[236] Varanasi, K. K.; Hsu, M.; Bhate, N.; Yang, W.; Deng, T. Spatial control in the heterogeneous nucleation of water. *Applied Physics Letters* **2009**, *95*, 094101.

[237] Matsuyama, H.; Ohga, K.; Maki, T.; Teramoto, M. The effect of polymer molecular weight on the structure of a honeycomb patterned thin film prepared by solvent evaporation. *Journal of Chemical Engineering of Japan* **2004**, *37*, 558–591.

[238] Bormashenko, E.; Pogreb, R.; Stanevsky, O.; Bormashenko, Y.; Gendelman, O. Formation of honeycomb patterns in evaporated polymer solutions: Influence of the molecular weight. *Materials Letters* **2005**, *59*, 3553–3557.

[239] Lavielle, N.; Beysens, D.; Mongruel, A. Memory Re-Condensation. *Langmuir* **2023**, *39*, 2008–2014.

[240] Steyer, A.; Guenoun, P.; Beysens, D.; Knobler, C. M. Two-dimensional ordering during droplet growth on a liquid surface. *Physical Review B* **1990**, *42*, 1086–1089.

[241] Viovy, J. L.; Beysens, D.; Knobler, C. M. Scaling description for the growth of condensation patterns on surfaces. *Physical Review A* **1988**, *37*, 4965–4970.

[242] Huang, J.; Hao, H.; Huang, Y.; Yu, B.; Ren, K.; Jin, Q.; Ji, J. Gradient Porous Structure Templated by Breath Figure Method. *Langmuir* **2021**, *37*, 6016–6021.

[243] Vella, D.; Mahadevan, L. The "Cheerios effect". *American Journal of Physics* **2005**, *73*, 817–825.

[244] Zheng, Y.; Tang, J.; Li, W.; Yu, J.; Bin Wei; Li, X.; Shi, J.; Miyazaki, K. Control of the pore size of honeycomb polymer film from micrometers to nanometers via substrate-temperature regulation and its application to photovoltaic and heat-resistant polymer films. *Nanotechnology* **2020**, *31*, 015301.

[245] Thong, A. Z.; Wei Lim, D. S.; Ahsan, A.; Wei Goh, G. T.; Xu, J.; Chin, J. M. Non-close-packed pore arrays through one-step breath figure self-assembly and reversal. *Chemical Science* **2014**, *5*, 1375–1382.

[246] Muñoz-Bonilla, A.; Fernández-García, M.; Rodríguez-Hernández, J. Towards hierarchically ordered functional porous polymeric surfaces prepared by the breath figures approach. *Progress in Polymer Science* **2014**, *39*, 510–554.

[247] Park, J. S.; Lee, S. H.; Han, T. H.; Kim, S. O. Hierarchically ordered polymer films by templated organization of aqueous droplets. *Advanced Functional Materials* **2007**, *17*, 2315–2320.

[248] Escalé, P.; Save, M.; Billon, L.; Ruokolainen, J.; Rubatat, L. When block copolymer self-assembly in hierarchically ordered honeycomb films depicts the breath figure process. *Soft Matter* **2016**, *12*, 790–797.

[249] Zhang, A.; Du, C.; Bai, H.; Wang, Y.; Wang, J.; Li, L. Formation of breath figure arrays in methanol vapor assisted by surface active agents. *ACS Applied Materials and Interfaces* **2014**, *6*, 8921–8927.

[250] Wan, L. S.; Ke, B. B.; Zhang, J.; Xu, Z. K. Pore shape of honeycomb-patterned films: Modulation and interfacial behavior. *Journal of Physical Chemistry B* **2012**, *116*, 40–47.

[251] Ge, W.; Lu, C. Hierarchical honeycomb patterns with tunable microstructures: controllable fabrication and application as replication templates. *Soft Matter* **2011**, *7*, 2790–2796.

[252] Connal, L. A.; Qiao, G. G. Honeycomb coated particles: porous doughnuts, golf balls and hollow porous pockets. *Soft Matter* **2007**, *3*, 837–839.

[253] Kim, J. H.; Seo, M.; Kim, S. Y. Lithographically patterned breath figure of photoresponsive small molecules: dual-patterned honeycomb lines from a combination of bottom-up and top-down lithography. *Advanced Materials* **2009**, *21*, 4130–4133.

[254] Deleuze, C.; Derail, C.; Delville, M. H.; Billon, L. Hierarchically structured hybrid

honeycomb films via micro to nanosized building blocks. *Soft Matter* **2012**, *8*, 8559–8562.

[255] Arora, J. S.; Cremaldi, J. C.; Holleran, M. K.; Ponnusamy, T.; Sunkara, B.; He, J.; Pesika, N. S.; John, V. T. Hierarchical patterning of hydrogels by replica molding of impregnated breath figures leads to superoleophobicity. *Nanoscale* **2016**, *8*, 18446–18453.

[256] Zhu, P.; Kong, T.; Zhou, C.; Lei, L.; Wang, L. Engineering Microstructure with Evaporation-Induced Self-Assembly of Microdroplets. *Small Methods* **2018**, *2*, 1800017.

[257] Bertrand, A.; Bousquet, A.; Lartigau-Dagron, C.; Billon, L. Hierarchically porous bio-inspired films prepared by combining "breath figure" templating and selectively degradable block copolymer directed self-assembly. *Chemical Communications* **2016**, *52*, 9562–9565.

[258] Birdi, K. S.; Vu, D. T.; Winter, A. *A Study of the Evaporation Rates of Small Water Drops Placed on a Solid Surface*; 1989; Vol. 93; pp 3702–3703.

[259] Picknett, R. G.; Bexon, R. The evaporation of sessile or pendant drops in still air. *Journal of Colloid and Interface Science* **1977**, *61*, 336–350.

[260] Li, N.; Shen, Y.; Wang, X.; Miao, Z.; Kang, F.; Xu, J.; Cheng, Y. Theoretical and Numerical Studies of Liquid Lens Evaporation with Coupled Fields. *Industrial and Engineering Chemistry Research* **2022**, *61*, 17379–17389.

[261] Sun, W.; Yang, F. Evaporation of a Volatile Liquid Lens on the Surface of an Immiscible Liquid. *Langmuir* **2016**, *32*, 6058–6067.

[262] Erbil, H. Y.; McHale, G.; Newton, M. I. Drop evaporation on solid surfaces: Constant contact angle mode. *Langmuir* **2002**, *18*, 2636–2641.

[263] Mchale, G.; Rowan, S. M.; Newton, M. I.; Banerjee, M. K. Evaporation and the Wetting of a Low-Energy Solid Surface. *Journal of physical chemistry B* **1998**, *102*, 1964–1967.

[264] Subramanian, S. G.; Nair, S.; DasGupta, S. Evaporation mediated translation and encapsulation of an aqueous droplet atop a viscoelastic liquid film. *Journal of Colloid and Interface Science* **2021**, *581*, 334–349.

[265] Joy, D. C.; Pawley, J. B. High-resolution scanning electron microscopy. *Ultramicroscopy* **1992**, *47*, 80–100.

[266] Kim, D. H.; Lin, Z.; Kim, H. C.; Jeong, U.; Russell, T. P. On the replication of

block copolymer templates by poly(dimethylsiloxane) elastomers. *Advanced Materials* **2003**, *15*, 811–814.

[267] Wu, C. Y.; Chiang, T. H.; Hsu, C. C. Fabrication of microlens array diffuser films with controllable haze distribution by combination of breath figures and replica molding methods. *Optics Express* **2008**, *16*, 19978.

[268] Vohra, V.; Yunus, S.; Attout, A.; Giovanella, U.; Scavia, G.; Tubino, R.; Botta, C.; Bolognesi, A. Bifunctional microstructured films and surfaces obtained by soft lithography from breath figure arrays. *Soft Matter* **2009**, *5*, 1656–1661.

[269] Kabuto, B. T.; Hashimoto, Y.; Karthaus, O. Thermally Stable and Solvent Resistant Mesoporous Honeycomb Films from a Crosslinkable Polymer **. *Advanced Functional Materials* **2007**, *17*, 3569–3573.

[270] Kamei, J.; Yabu, H. On-Demand Liquid Transportation Using Bioinspired Omniphobic Lubricated Surfaces Based on Self-Organized Honeycomb and Pincushion Films. *Advanced Functional Materials* **2015**, *25*, 4195–4201.

[271] Ting, W.-h.; Chen, C.-c.; Dai, S. A.; Suen, S.-y.; Yang, I.-k.; Liu, Y.-l.; Chen, F. M. C.; Jeng, R.-j. Superhydrophobic waxy-dendron-grafted polymer films via nanostructure manipulation. *Journal of Materials Chemistry* **2009**, *19*, 4819–4828.

[272] Li, Z.; Ma, X.; Kong, Q.; Zang, D.; Guan, X.; Ren, X. Static and Dynamic Hydrophobic Properties of Honeycomb Structured Films via Breath Figure Method. *Journal of Physical Chemistry C* **2016**, *120*, 18659–18664.

[273] Heng, L.; Meng, X.; Wang, B.; Jiang, L. Bioinspired design of honeycomb structure interfaces with controllable water adhesion. *Langmuir* **2013**, *29*, 9491–9498.

[274] Kim, W.; Eun, J.; Jeon, S. Applied Surface Science Anti-splashing properties of sticky superhydrophobic surfaces. *Applied Surface Science* **2021**, *542*, 148617.

[275] Chen, B.; Wada, T.; Yabu, H. Underwater Bubble and Oil Repellency of Biomimetic Pincushion and Plastron-Like Honeycomb Films. *Langmuir* **2020**, *36*, 6365–6369.

[276] Han, K.; Heng, L.; Jiang, L. Multiphase Media Antiadhesive Coatings: Hierarchical Self-Assembled Porous Materials Generated Using Breath Figure Patterns. *ACS Nano* **2016**, *10*, 11087–11095.

[277] Arora, J. S.; Cremaldi, J. C.; Holleran, M. K.; Ponnusamy, T.; He, J.; Pesika, N. S.; John, V. T. Hydrogel Inverse Replicas of Breath Figures Exhibit Superoleophobicity Due to Patterned Surface Roughness. *Langmuir* **2016**, *32*, 1009–1017.

[278] Erbil, H. Y. Determination of the peripheral contact angle of sessile drops on solids

from the rate of evaporation. *Journal of Adhesion Science and Technology* **1999**, *13*, 1405–1413.

[279] Erbil, H. Y. Evaporation of pure liquid sessile and spherical suspended drops: A review. *Advances in Colloid and Interface Science* **2012**, *170*, 67–86.

[280] Tsai, P.; Lammertink, R. G.; Wessling, M.; Lohse, D. Evaporation-triggered wetting transition for water droplets upon hydrophobic microstructures. *Physical Review Letters* **2010**, *104*, 2–3.

[281] Moulinet, S.; Bartolo, D. Life and death of a fakir droplet: Impalement transitions on superhydrophobic surfaces. *European Physical Journal E* **2007**, *24*, 251–260.

[282] Bormashenko, E.; Pogreb, R.; Whyman, G.; Bormashenko, Y.; Erlich, M. Vibration-induced Cassie-Wenzel wetting transition on rough surfaces. *Applied Physics Letters* **2007**, *90*, 5–7.

[283] Tuteja, A.; Choi, W.; Mabry, J. M.; Mckinley, G. H.; Cohen, R. E.; Prausnitz, J. M. Robust omniphobic surfaces. *Proceedings of the National Academy of Sciences of the United States of America* **2008**, *105*, 18200–18205.

[284] Nosonovsky, M.; Bhushan, B. Why re-entrant surface topography is needed for robust oleophobicity. *Philosophical Transactions of the Royal Society A: Mathematical, Physical and Engineering Sciences* **2016**, *374*.

[285] Kota, A. K.; Kwon, G.; Tuteja, A. The design and applications of superomniphobic surfaces. *NPG Asia Materials 2014 6:7* **2014**, *6*, e109–e109.

[286] Papadopoulos, P.; Deng, X.; Mammen, L.; Drotlef, D.-M.; Battagliarin, G.; Li, C.; Müllen, K.; Landfester, K.; del Campo, A.; Butt, H.-J.; Vollmer, D. Wetting on the Microscale: Shape of a Liquid Drop on a Microstructured Surface at Different Length Scales. *Langmuir* **2012**, *28*, 8392–8398.

[287] Vieira, A.; Cui, W.; Jokinen, V.; Ras, R. H.; Zhou, Q. Through-drop imaging of moving contact lines and contact areas on opaque water-repellent surfaces. *Soft Matter* **2023**, *19*, 2350–2359.

[288] Galeotti, F.; Trespidi, F.; Pasini, M. Breath Figure-Assisted Fabrication of Nanostructured Coating on Silicon Surface and Evaluation of Its Antireflection Power. *Journal of Nanomaterials* **2016**, *2016*, 1–8.

[289] Li, C.; Kim, B.; Yoon, J.; Sett, S.; Oh, J. Advances in Directional Wetting Surfaces for Enhanced Fluid Control: A Comprehensive Review. *Advanced Functional Materials* **2024**, *34*, 1–30.

[290] Lei, J.; Guo, Z. A fog-collecting surface mimicking the Namib beetle: Its water collection efficiency and influencing factors. *Nanoscale* **2020**, *12*, 6921–6936.

[291] Dai, H.; Dong, Z.; Jiang, L. Directional liquid dynamics of interfaces with superwettability. *Science Advances* **2020**, *6*, 1–10.

[292] Sharma, D.; Misba, L.; Khan, A. U. Antibiotics versus biofilm: an emerging battleground in microbial communities. *Antimicrobial Resistance Infection Control* **2019**, *8*, 1–10.

[293] Pellegrino, L.; Kriem, L. S.; Robles, E. S.; Cabral, J. T. Microbial Response to Micrometer-Scale Multiaxial Wrinkled Surfaces. *ACS Applied Materials and Interfaces* **2022**, *14*, 31463–31473.

[294] Miles, B. Y. A. A.; Misra, S. S. The estimation of the bactericidal power of blood. *Epidemiolgy and Infection* **1931**, *38*, 732–749.

[295] Hu, H.; Xu, C.; Zhao, Y.; Shaeffer, R.; Ziegler, K. J.; Chung, J. N. Modification and enhancement of cryogenic quenching heat transfer by a nanoporous surface. *International Journal of Heat and Mass Transfer* **2015**, *80*, 636–643.

[296] Shaeffer, R.; Hu, H.; Chung, J. N. An experimental study on liquid nitrogen pipe chilldown and heat transfer with pulse flows. *International Journal of Heat and Mass Transfer* **2013**, *67*, 955–966.

[297] Li, Z.; Yu, D.; Cui, J.; Feng, P.; Feng, F. Influences of brass surface morphology on leidenfrost effect during liquid nitrogen cooling. *Applied Sciences (Switzerland)* **2021**, *11*.

[298] Chung, J. N.; Darr, S. R.; Dong, J.; Wang, H.; Hartwig, J. W. Heat transfer enhancement in cryogenic quenching process. *International Journal of Thermal Sciences* **2020**, *147*, 106117.

[299] Graffiedi, M.; Dent, F. J.; Khodaparast, S.; Bucci, M. Cryogenic Quenching Process Enhancement Through Coating and Microstructure Optimization. *Journal of Physics: Conference Series* **2024**, *2766*, 012139.